**POLITECNICO DI MILANO**

Scuola di Ingegneria Industriale

Corso di Laurea Magistrale

in Ingegneria Energetica

# Numerical Simulation and Economic Analysis of Adiabatic Underwater CAES for the Enhancement of an Offshore Wind Farm

*Relatore:*

Prof. Stefano CAMPANARI

*Co-relatore:*

Prof. Marco ASTOLFI

Prof. Eliodoro CHIAVAZZO

Ing. Giulio GUANDALINI

Prof. Paolo SILVA

Tesi di Laurea Magistrale di:

Silvia DI MICHELE Matr. 863808

Nicola FRASCELLA Matr. 850480

Anno Accademico 2016 – 2017

"…Fatti non foste a viver come bruti
Ma per seguir virtute e canoscenza…"

*Dante Alighieri, La Divina Commedia, Inferno, XXVI, vv. 119-120*

# *Ringraziamenti*

*Il primo ringraziamento va a tutto il team che ci ha seguito e permesso di lavorare a questa tesi con continui spunti e fiducia nelle nostre idee. Ringraziamo i prof. Campanari e Silva per il tempo che ci hanno dedicato, seguendo gli sviluppi e i piccoli traguardi raggiunti passo dopo passo, per i molteplici suggerimenti e per averci mostrato, un po' più da vicino, cosa significhi passione nella ricerca e soprattutto come possano nascere idee da quattro chiacchiere a menti aperte. Ringraziamo particolarmente il prof. Astolfi, per la sua totale disponibilità e il suo pronto intervento, senza il quale non saremmo potuti essere così orgogliosi della nostra tesi. Ma soprattutto ringraziamo l'ing. Guandalini, che dal primo all'ultimo giorno di questa avventura non ha mai smesso di dedicarci il suo tempo, di condividere le sue idee e di credere in noi. Un ringraziamento speciale va al Prof. Silva per averci ricordato come le soddisfazioni più grandi si trovino fuori dal laboratorio, e a cui facciamo i nostri più sinceri auguri. Grazie anche tutti gli altri professori che in questi cinque anni ci hanno inspirato e a Chi illumina di saggezza il mondo.*

*Molta gratitudine va anche all'agente scelto Eustachio Sabatelli e a Carolina Molin, che con la loro onestà hanno reso possibile concludere al meglio questo lavoro, ritrovando il pc perduto.*

*Infine un sincero ringraziamento a tutte le persone che ci hanno sostenuto, alle nostre splendide famiglie, ai nostri parenti vicini e lontani, agli amici che hanno condiviso con noi questi anni così intensi e agli amici di sempre, quelli che nonostante siamo stati costretti ad abbandonare per sessioni di studio matte e disperatissime, non hanno mai smesso di esserci e di volerci bene. Grazie alle nostre metà, per tutte le piccole cose di ogni giorno.*

# *Index*

# *Abstract*


## INTRODUCTION

*The increasing interest and investment in energy storage systems, in terms of research and development, is strongly related to their role in flattening power profiles, especially in relation to the increasing renewable share in the energy sector. The expected goal is to improve the dispatchability of intermittent sources of renewable energy, matching the instantaneous demand and helping to solve the grid control issues.*

*In this work, it will be introduced a techno-economic analysis of an Under-Water Adiabatic Compressed Air Energy Storage system (UW-A CAES), coupled to an Offshore Wind farm.*

*The standard Compressed Air Energy Storage (CAES) system, well known in literature and already experimented in a few large-scale applications, belongs to the macro category of large-scale mechanical storage. With its high reliability, economic feasibility, and low environmental impact, it is a promising method for large-scale energy storage. The Adiabatic CAES pre-compresses ambient air, using for example low-cost electricity from the power grid at off-peak times, pumps it into an underground cavern or a storage tank at a high pressure, and utilizes it later to generate electricity through an expansion in turbine when required. The Adiabatic configuration allows to replace fuel combustion, necessary to heat up the air before the expansion in turbine, with thermal energy taken from compressed air and stored in a Thermal Energy Storage (TES) system. The main originality of UW-CAES lies in the possibility of operating with an isobaric air storage, obtained by placing the air storage underwater and exploiting the hydrostatic pressure by the water column to keep its pressure constant. So, in the discharging processes, the pressure at turbine inlet is constant rather than variable as it would be with conventional cavern storages. A possible application of this concept is the coupling with offshore wind turbines, a technology that has experienced large growth worldwide and is expected to be deployed in the future also on high depth seas, whose growth is limited by grid issues due to intermittency of the source. Large scale energy storage systems have been identified as a potential solution to this challenge.*

### Thesis's Objective

This Thesis work intends to provide:

- The whole UW A-CAES design in nominal conditions.
- The UW A-CAES Off-design to investigate the performances in the operative range changing boundary conditions and available power to be stored.
- The UW A-CAES sizing coupling to the Off-shore Wind farm.
- The economic assessment of the whole system, UW A-CAES coupled to the Off-shore Wind farm.

# METHODOLOGY

## UW A-CAES design

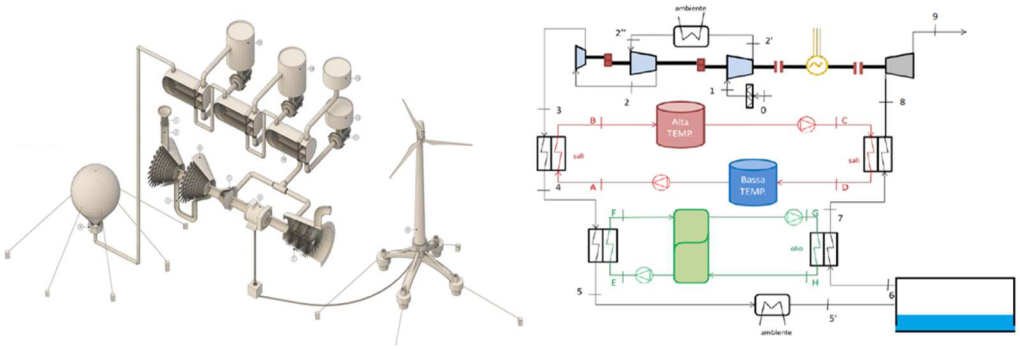


***Figure a: CAD system conceptual layout on the left and schematic process sketch on the right***

The UW-CAES is represented in Figure a. The designed components included in the system are:

1. The power unit for compressed air, made either by axial and centrifugal compressors.
2. Eventual seawater intercoolers in the compression phase.
3. The heat storage and heat exchange devices, constituted by three thermal storage units combined at different temperatures, sequentially through salt, oil and seawater fluid media.
4. The underwater modular compressed air tank, conceived as a network of tanks with free capacity.
5. The axial turbine, designed to work always at full load thanks to the constancy of the air flow rate and of the TIT guaranteed by the thermal storage.

The system design peculiarities are the followings:

1. The UW-CAES allows to store air at constant pressure, thanks to the underwater tank with openings that allow water in and out to balance the air pressure.
2. The total compression heat recovery, through the thermal energy storage (TES), in discharging phase, avoiding an additional combustion in order to keep the system emission-free.
3. The application of the same heat exchangers to both the charging and discharging phase, avoiding a duplication and implying a reduced investment cost but a challenging design.

The cases studied in the work fall within the storage pressure range of 60 to 100 bar, that implies storage depths from 600 to 1000 meters. The whole system has been

coded on MatLab, with the possibility to cover a wide range of cases, widening the scope of the application.

The compression train has been identified as the key component of the system. Peculiarity of the compression design is that it is designed for a fixed compression ratio and given electric power, being unknown the resulting mass flow rate and efficiency. The fixed compression ratio is a direct consequence of the storage pressure imposed to the underwater tank, while the fixed electric power that has to be absorbed by the compression train is an input to the CAES design, dependent on the offshore wind power production. An additional compression phase boundary condition is the maximum compression outlet temperature (COT) that can be reached, directly related to the medium chosen for the thermal storage. In this work, we considered the adoption of standard solar salts for the first (hottest) thermal storage, featuring an upper limit temperature of 600°C to avoid cracking phenomena.

The preliminary configuration, number, type and compression ratio of the compressors, has been evaluated taking into account the required storage pressure together with the COT limit, optimizing the UW A-CAES efficiency. The configuration, in almost the totality of the studied cases, turns out to be composed by two intercooled axial compressors followed by a centrifugal one. The choice of a centrifugal compressor as last component is motivated by the flexibility and robustness of the machine, operating at the higher temperatures, as well as the lower volumetric flow rates and the higher compressor ratios available per stage.

The compression design employs the Balje diagram to evaluate the compression train performances and to verify the types of machine that have to be installed, starting from the following input data:

1. Nominal Power
2. Storage Pressure
3. Compression train configuration
4. Maximum COT

All the other parameters necessary to the calculations, such as environment conditions and all the working fluids and components characteristics are defined in the thesis work.

The Balje diagram has been digitalized on MatLab as shown in Figure b.

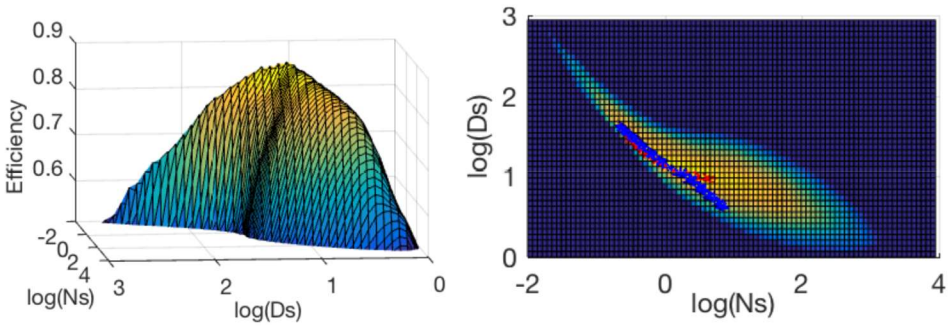


***Figure b: Digitalized Balje map, 3D view and Ns-Ds view with the two methods highlighted***

Two methods have been implemented to evaluate the performances of compressors. Both of them are based on the middle stage optimization, that means to fix the revolving compressor speed equal to the optimal one for the middle-stage of each unit.

The "Fixed Diameter method" has been defined keeping constant the mean diameter of each compressor, and is described by the blue points in Figure b (on the right) as an application example. Alternatively, the "Variable Diameter method" aims to define the optimal single stage efficiency, imposing the appropriate value of each stage diameter to follow the Cordier maximum function; the method is described for an application by the red points in Figure b (right). Several kinds of configurations have been discussed in the thesis, as a "Single Shaft" configuration (optimized for both the methods, resulting in interesting evidences described in the thesis); however, the chosen and implemented configuration is a "Multiple Shaft" one, with three shafts that can guarantee higher efficiencies imposing the optimal revolving speed to each section of the compressor train. All the methods and configurations have been verified in this thesis with respect to the reference values for the efficiency of commercial compressors, revealing how the Balje efficiency data result slightly lower with respect to the nowadays reference values; efficiencies have therefore been corrected to consider more realistic values (the correction is around 4.5%, with top isentropic efficiencies of 92%). In Figure c is possible to highlight the validity of the "Variable Diameter method" combined with the "Multiple Shaft" configuration with the standard Balje data.

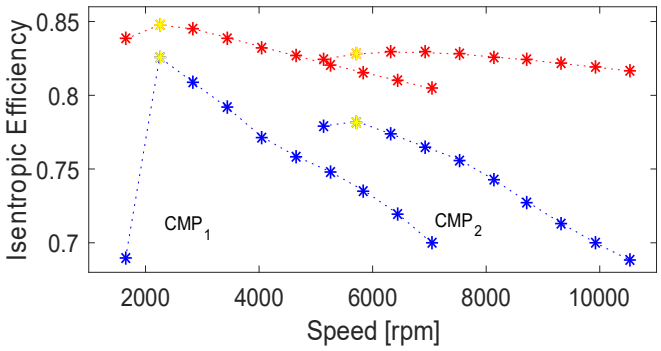


***Figure c: The "Multiple Shaft" configuration with the "Variable Diameter" method in red and the "Fixed Diameter" method in blue. It is verified that the mid-stage Ns in yellow allows the highest compressors efficiencies.***

The Multiple shaft configuration could be built using either a separated electric motor to drive each shaft or using a single motor with gearboxes to allow different revolving speeds on each compressor. Considering possible future developments of this thesis, the configuration with multiple motors on each shaft is considered more promising, since it may allow to work with variable revolving speed on each shaft and to widen the plant off-design flexibility.

## UW A-CAES Off-design

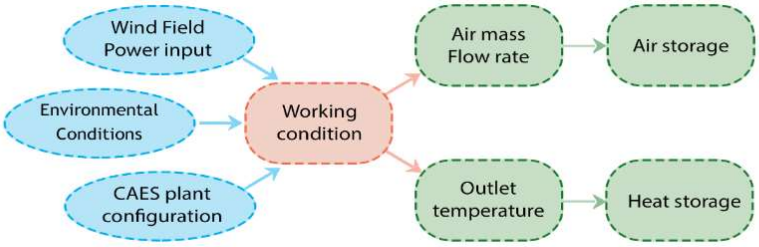


***Figure d: Off-design algorithm input and output***

Since the system requires to work with variable input power from the wind plant and it is also largely sensible to the environment conditions, the off-design modelling becomes even more relevant (Figure d). The variable stator angle at the inlet of the first compressor, alias variable Inlet Guide Vanes (IGV) has been implemented. The conditions which have to be always verified are the conservation of the volumetric flow rate for the inlet of the axial compressors (working in choked conditions) and the characteristic curve defined in its reference map for the centrifugal compressor. To enhance the controllability of the whole system, it has been implemented the variable inlet stator angles at all three compressor trains; however, it has been demonstrated that

exploitation of IGV on all trains does not enhance the process performance (round trip efficiency) in a significative way. The main issue is related to the necessity of avoiding the stall region in all compressor stages, where the first axial compressor results to be the limiting one. An example of the off-design behaviour is illustrated in Figure e respectively for the axial and centrifugal compressors, increasing the input power to the compression train together with the arrow directions. To work at partial loads implies a compression ratio reduction (from B to A) for the first compressor. Note that, being the required final pressure constant, the first reduction shall be compensated by an increase of pressure ratio on the others (D to C on the left Figure e and F to E on the right one). It has been highlighted how the operative range always available falls between 80% and 103% of the nominal power, reaching wider values only in particular environmental conditions. Such a low flexibility does not allow a wide regulation region at partial loads, requiring a wise utilization logic behind its use. Besides using variable stator angles or rotational speed as suggested in the thesis, a possible alternative to increase such range could be to use more compression trains in parallel.

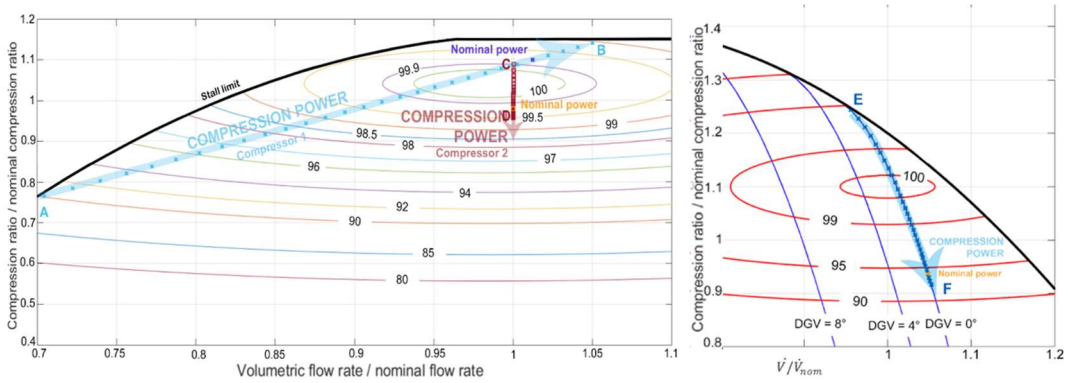


***Figure e: Off-design trend to the axial compressors on the left and to the centrifugal one on the right***

## Off-shore Wind Field integration

The thesis develops a test case where it is considered to locate the system in the windy locations offshore the south-west Sardinia coast. Thanks to the Spanish harbour weather forecast company, Puertos, which has provided the hourly data of wind speed for four following years, and through the SAM (NREL) software for wind turbine modelling, after a wide comparison it has been selected the Siemens SWT-2.3 MW-108m turbine as a reference case. Considering four wind farms of about 30 MW each, the total offshore wind field capacity is slightly more than 120 MW. Figure f shows the yearly fluctuating power from the wind field in blue and the CAES integration, resulting in a load levelling, in red.

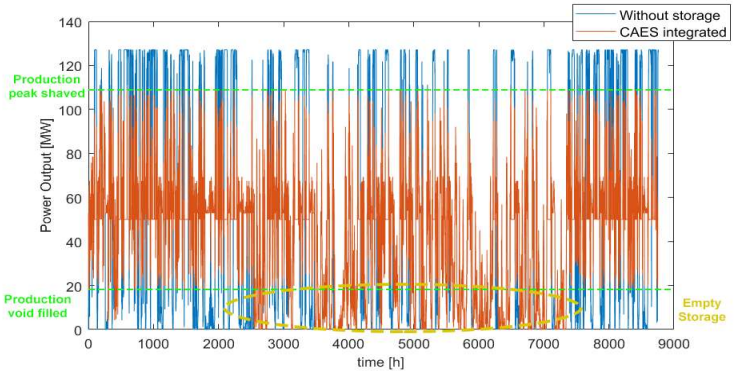


***Figure f: Yearly fluctuating power output with and without the storage system. reference case defined by: storage pressure of 80 bar, TDF (Turbine Dimension Factor) = $\dot{m}_T^{nom}/\dot{m}_C^{nom} = 1$, unlimited capacity for each storage unit, Pnom,compression =75 MW***

The thesis highlights that the UW-CAES unavailable hours are due to the thermal storage. The first heat tank used during the discharging phase has been identified as the scarce resource in most conditions, yielding an operative stall, where the stored air is no longer exploitable. The solution found is the activation of an additional aftercooler storage system with a bypass valve, to allow the exploitation of the upper storages when the first one is empty. The resulting thermal and air storages behaviour is showed in the left of Figure g for an example case study. Furthermore, the moving mean built by hourly values from a quarter of year is used to take care of the seasonality of the wind resource, giving the possibility to change the compressor and turbine activation threshold following the wind field mean power production, Figure g (right). The purpose is to avoid an unjustified charging of the CAES during months when the production is high for a wide period, resulting in an over-dimensioning of the reservoirs.

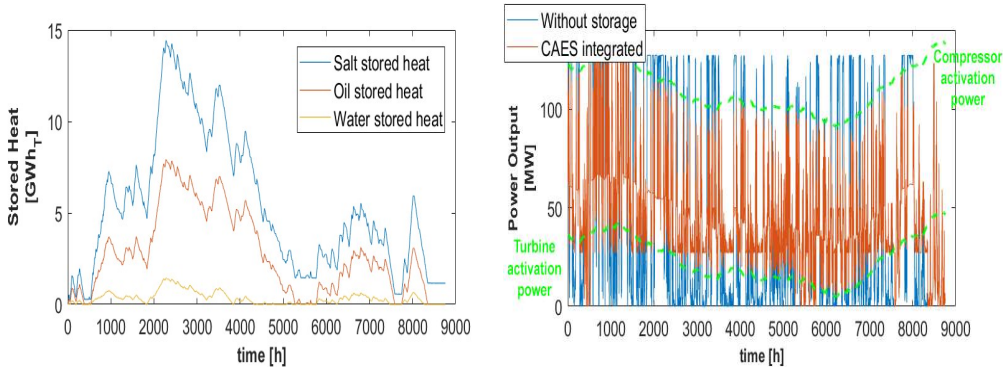


***Figure g: The yearly thermal storage trend on the left and moving mean of power output implemented on the right both for a particular case study with TDF (Turbine Dimension Factor)= $\dot{m}_T^{nom}/\dot{m}_C^{nom} = 0.5$, and Pnom,compression=75 MW***

Obviously, all results are strongly dependent on the compression and expansion sizing, as well as on the site selection and the yearly data analysed. The dimensioning of

the components has been evaluated taking into account also the economic assessment, following initially an arbitrage logic (air compression when electric prices are low, air expansion when electric prices are high) based on the Italian energy market data, and then a peak shaving logic to investigate the storage potential in terms of grid advantages. The arbitrage turns out to be not economically attractive because with a largely fluctuating power input it is only seldom possible to follow the economic trend while contemporary keeping balanced the thermal storages. The peak-shaving logic, which is the ultimate purpose of the UW-CAES system, is then discussed in detail. The system high investment cost has driven to find an appropriate incentive, with the peak shaving logic, to allow the breakeven point at the end of the system life cycle.

## RESULTS

The thermal energy storage results to be the primary cause to the high investment cost. Indeed, keeping the thermal storage capacity unlimited, the working fluid inventory required in the discharging phase is of the order of magnitude of ten thousand tons for about 650 hours of capacity, excessive both for its mass and for its cost. The cost share is shown in the pie charts for the extreme applications with the smallest and the biggest turbomachinery respectively, Figure h.

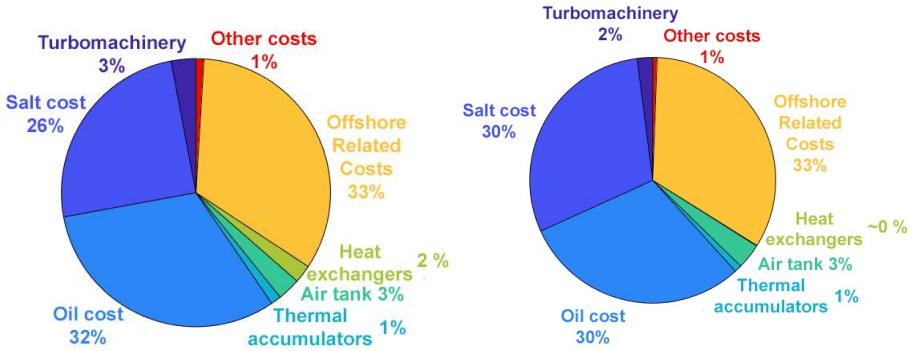


***Figure h: Share of the investment costs, case with 650h storage capacity for a storage pressure of 80 bar, on the left for smallest configuration, Total cost: 198 M€ (Pnom,cmp=25 MW, TDF(Turbine Dimension Factor)= $\dot{m}_T^{nom}/\dot{m}_C^{nom} = 0.4$), on the right for the biggest one, Total cost: 622 M€ ( Pnom,cmp=75 MW, TDF(Turbine Dimension Factor)= $\dot{m}_T^{nom}/\dot{m}_C^{nom} = 1$).***

For this reason, a sensitivity analysis on the thermal storage capacity has been performed in the thesis and the following results are the ones related to the thermal storage maximum capacity of 250 hours (more than 10 days). Additionally, the offshore installation cost has been evaluated following the oil and gas references, as the 50 % of the system cost, and represents the first voice in terms of cost. The optimal sizing of the compression train (in relation to the offshore wind plant power output) and the expander (in relation to the compression train), have been evaluated considering, among the other parameters, the round-trip efficiency, the standard deviation of the total power output of

the wind park with the UW CAES vs. its average power (which gives an idea of the degree of dispatchability of the overall system), the investment cost, and the energy storage incentive (in €/MWh referred to the electricity generated by the turbine) required to allow the breakeven point at the end of the system life cycle .

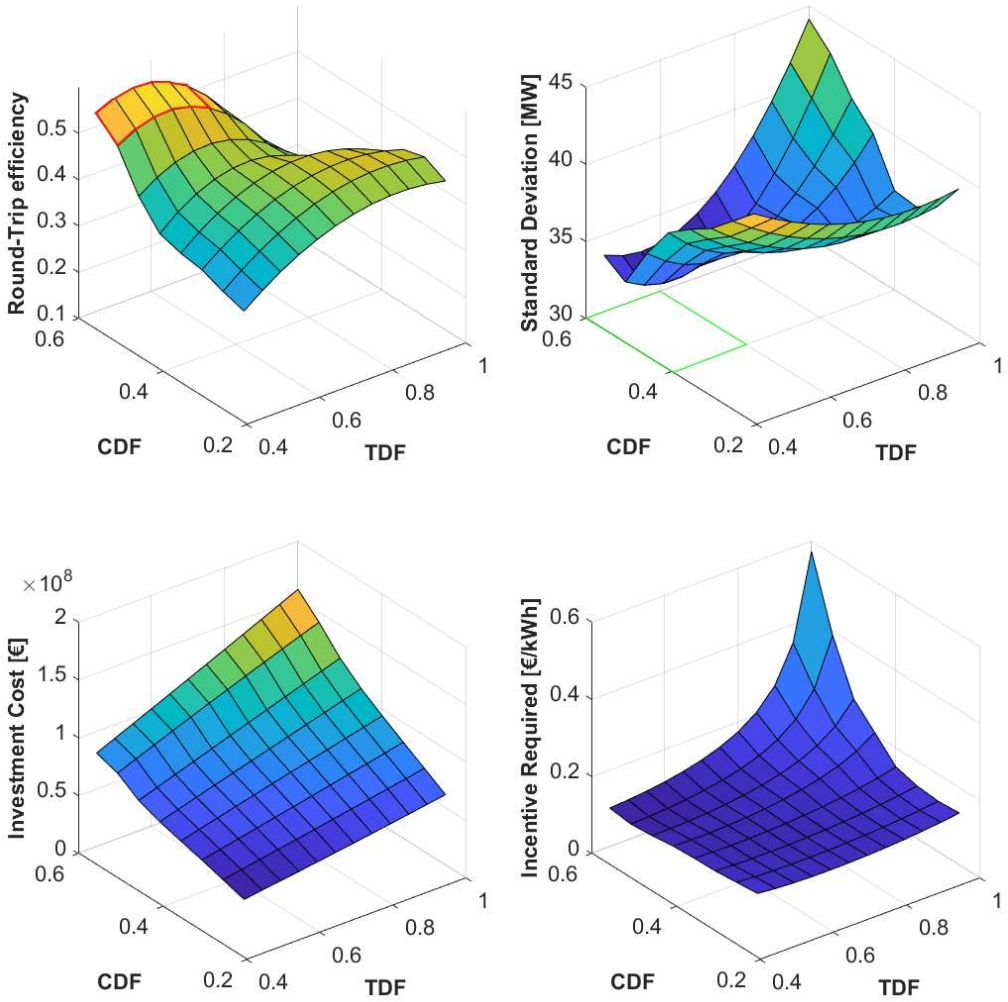


***Figure i: Main results with thermal storage limited to 250 hours, CDF stands for the compression size in terms of power with respect to the wind field, while TDF is the turbine size related to the compression one in terms of air mass flow rate.***

The following considerations can be drawn:

- The round-trip efficiency, that reached 70 % with the unlimited thermal storage, is reduced to a maximum value of 55% in the red lined area, for a compressor size 0.6 times the wind field power and a turbine size in the range from 0.4 to 0.6 with respect to the compression size (Figure i on the top-left).
- The same range of value results the best one in term of standard deviation reduction, that represents how much the load has been levelled thanks to the

storage system integration; as a reference value, the standard deviation of the wind plant without the storage results equal to 48.6 MW. So, with the exception of the region highlighted in green, in the rest of the mapped area the standard deviation abatement is very limited (Figure i, on the top-right), indicating that the system is not effective for the peak-shaving purpose.

- Considering the investment cost, a reduction of one order of magnitude can be appreciated with respect to the unlimited thermal storage simulation, with a more balanced share of cost among the system components (Figure i on the bottom-left).
- By the point of view of the required incentive, it can be noticed an overall improvement with respect to the unlimited thermal storage case, with the incentive (or extra-price) to be assigned to the energy obtained by the turbine around 0.11 $€/kWh$ in the flat area of the diagram (Figure i on the bottom-right); a value not far from incentives nowadays already applied to other renewable solutions.

  Further discussion and results can be found in the thesis.

In conclusion, the UW-CAES system demonstrates promising results with some limits, highlighted by the thesis, which can be summarised in three main categories: the low flexibility of the compression train, the thermal storage cost and the difficult balance among the storage levels, and last but not least, the off-shore implementation in term of cost. It results also interesting analysing the system behaviour in different locations and boundary conditions, as it has been initially discussed at the end of this work. Other possible further developments include: the implementation of parallel compression trains to work in a wider operative range, the analysis of the investment cost resulting from different installation options (e.g. installing the turbomachinery and thermal storage system on ground, connected with offshore deep tanks, with a challenging underwater pipeline sizing, due to the fluctuation in the charging phases and the consequent pressure stress).

Furthermore, the incentives required for system economical applicability are in some cases lower than 0.1 $€/kWh$, a value comparable to nowadays renewable incentives. Moreover, the advantage of such technology consists in the use of well-known elements, such as turbomachinery, heat exchangers and thermal storage units. Among other large-scale energy storage solutions, the UW-Compressed Air Energy Storage systems could be able to complement the classic pumped-hydro units in the grid balancing role in an increasingly renewable-based forward-looking perspective.

***KEYWORDS****: Large-Scale Storage, Underwater CAES, Offshore Wind Power, Thermal Storage, Incentives, Economic Analysis.*

# 1. INTRODUCTION

The global energy consumption in the last 200 years has seen a huge increase, driven mainly by the fossil fuels (Figure 1.1). The industrial revolution propelled urbanization and industrialization as the predominant paths to economic and social modernization. However, these paths promoted the rapid growth of fossil fuel consumption and produced significant amounts of carbon dioxide ($CO_2$) and other greenhouse gas (GHG) emissions. Moreover, the world population, in 2017 of 7.6 billion, is projected to increase by 1 billion over the next 10 years and to reach 9.8 billion by 2050, according to UN report [1]. Growing population and increasing standards of living for many people in developing countries will place even more demand on energy resources. Indeed, as the last BP Energy Outlook underlines, nearly two thirds of the increase in global energy demand is for power generation, as the world economy continues to electrify [2].

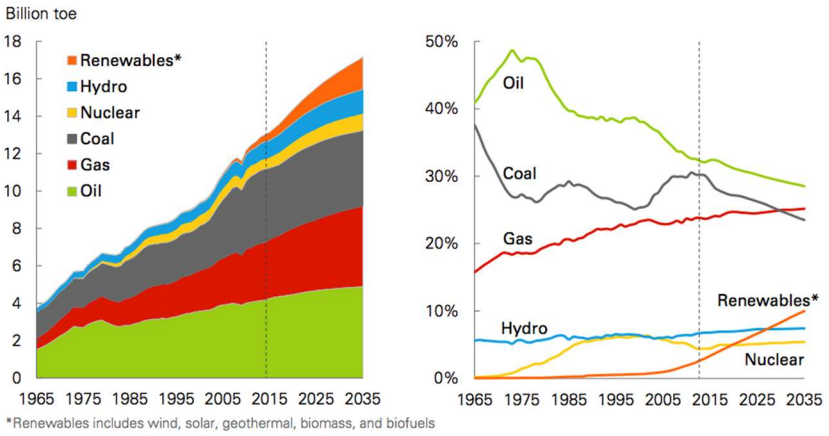


***Figure 1.1: Global primary energy consumption by fuel on the left and shares of primary energy on the right*** [2]

The greenhouse gas emissions have increased since the pre-industrial era, driven largely by economic and population growth. This has led to a huge increase of atmospheric concentrations of carbon dioxide [3] (Figure 1.2) and, according to more

than 97% of the climate scientists [4], climate-warming trends over the past century, highlighted by the global mean surface warming (Figure 1.3), are extremely likely due to human activities.

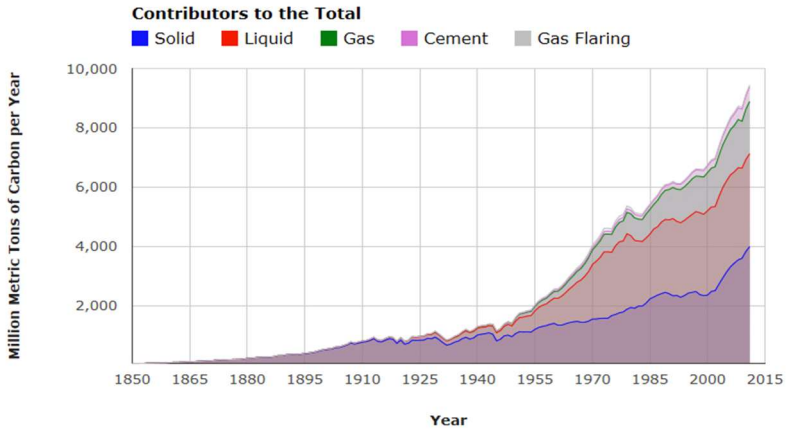


***Figure 1.2: Global carbon emissions trend*** [5]

Projections of greenhouse gas emissions vary over a wide range, depending on both socio-economic development and climate policy as shown in Figure 1.3. Climate change has the characteristics of a collective action problem at the global scale and only through the coupling of adaptation and mitigation strategies could be possible to contribute to climate-resilient pathways for sustainable development [6]. Among the mitigation drivers, there are the increase in energy efficiency and the switch to renewable and non-carbon-based fuels.

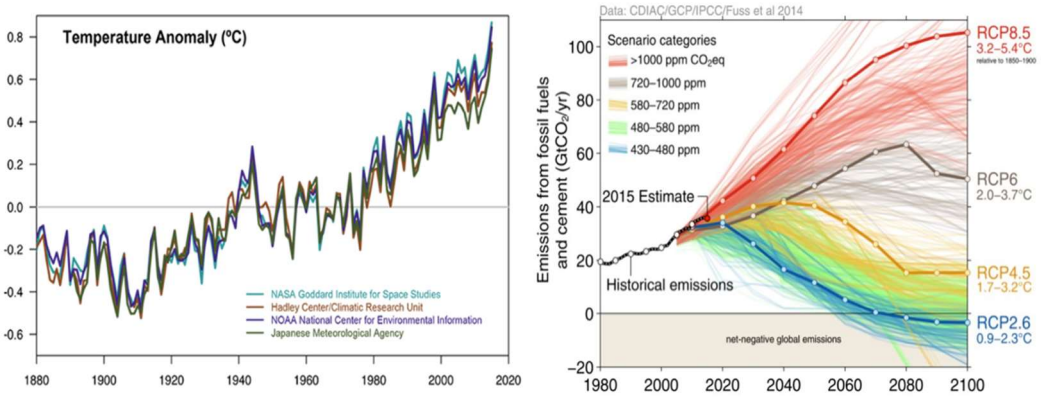


***Figure 1.3 Temperature data from four international science institutions [7] and Figure 1.4 CO2 emission forecast considering different scenarios [8]***

The cost-effectiveness of renewable power generation technologies has reached historic levels. Biomass for power, hydropower, geothermal and onshore wind can now all provide electricity competitively compared to fossil fuel-fired power generation, Figure 1.5. The installed costs for onshore wind power, solar PV and concentrating solar power (CSP) have continued to fall, while their performances have improved [9].

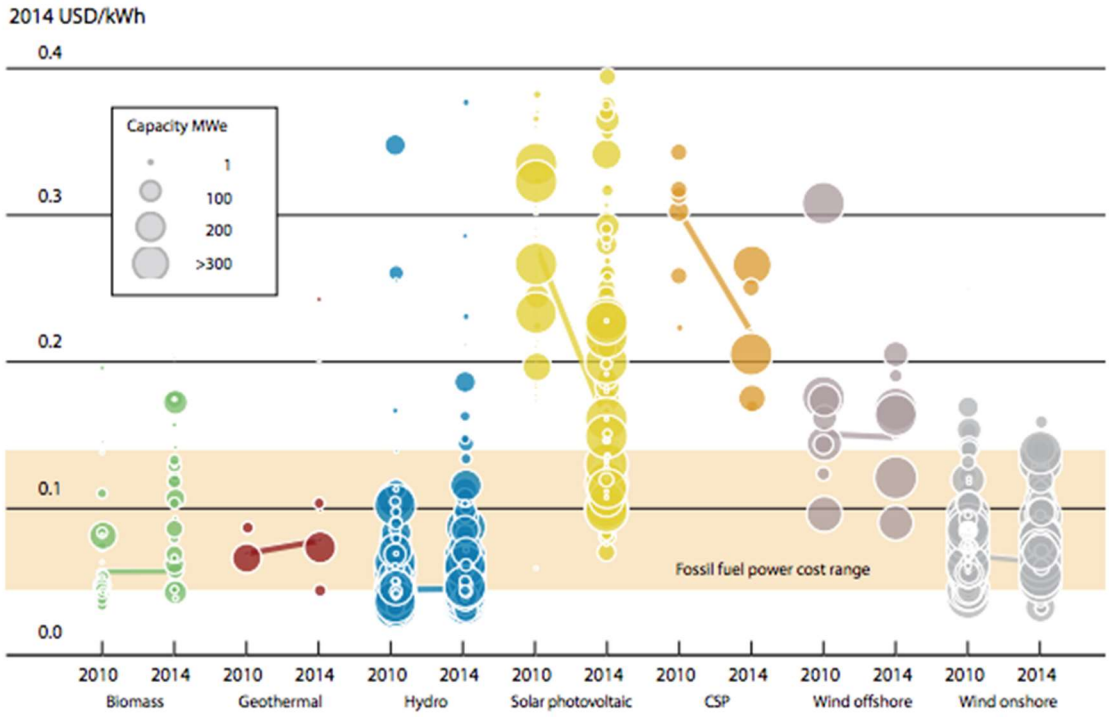


***Figure 1.5: The levelized cost of electricity from utility-scale renewable technologies, 2010 and 2014, IRENA Renewable cost database (2014)***

Among the renewable sources, wind energy is one of the fastest-growing energy sources in the world (Figure 1.6). According to the 2017 BP Statistical Review of World Energy, wind provided more than half of renewables growth while solar energy contributed almost a third despite accounting for only 18% of the total [10]. Offshore wind power shares the same benefits of onshore wind power relative to conventional power sources, but at higher costs; however offshore winds are generally stronger and more constant than onshore winds. As a result, turbines are expected to operate at their maximum capacity for a larger percentage of their time, and the constancy of wind speed provides a more constant source of power to the electrical grid [11]. Indeed,

renewable sources and wind in particular are intermittent and unstable in nature, varying considerably according to the time of day and the season of the year, and hence creating many grid integration and power fluctuation issues, which disturb the stability of the grid.

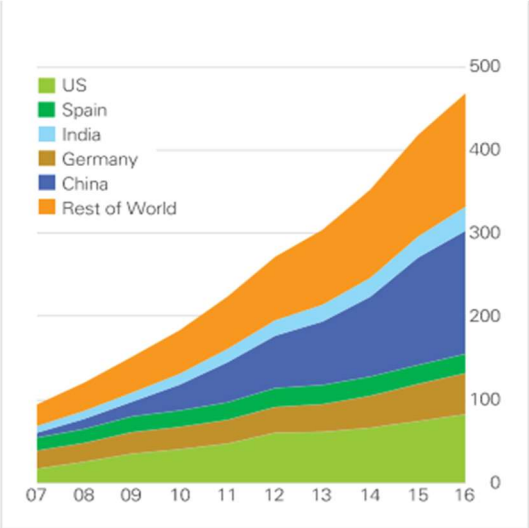


***Figure 1.6: Installed wind generation capacity, (Gigawatts cumulative installed capacity)*** [10]

In this context, the deployment of energy storage becomes an indispensable instrument in order to improve the grid flexibility and to deliver services to the energy system, in an increasing renewable integration. The diverse storage approaches currently deployed around the world could be divided in macro groups of storage: The Chemical, the Electrical, the Electrochemical, the Mechanical and the Thermal Energy Storage [12]. Among them, the mechanical Compressed Air Energy Storage (CAES) covers the large scale power range (Figure 1.7) and has received significant attention as a result of its relatively low capital and maintenance costs, broad geographical coverage and low environmental impacts [13].

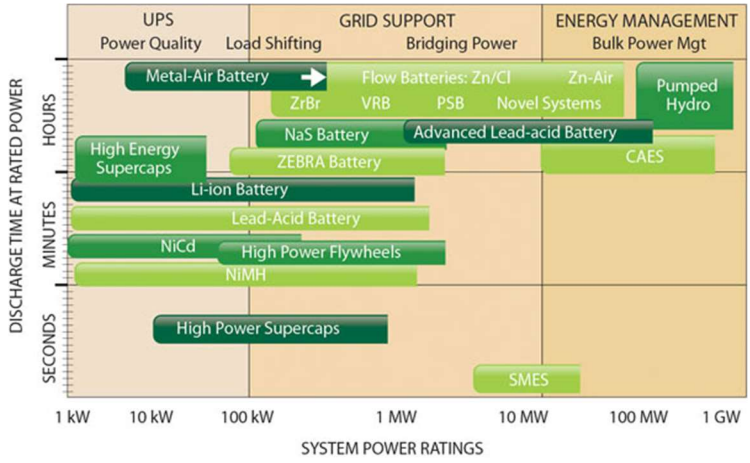


***Figure 1.7: Summary chart of storage technologies, as a function of nominal power and energy storage capacity***

The world's first utility-scale CAES plant was installed at Huntorf, in Germany in 1978, to provide load following service, storing the energy from nuclear power industry. It has been later updated to a buffering use against the intermittence of wind energy. It employs two salt dome caverns to store the compressed air at constant volume with a pressure range from 48 to 66 bar. With a rated power of 290 MW, the Huntorf CAES plant's round-trip efficiency is about 42%.

The large-scale CAES plant in McIntosh Alabama started operation in 1991. With 26 hours of full power guaranteed, it is used to store off peak power with a nominal power of 110 MW. The plant utilizes a single salt dome cavern with a pressure range from 45 to 74 bar. The improvement with respect to the Huntorf plant is the recuperator to reuse part of the heat energy from the exhaust of the gas turbine section, reducing fuel consumption of 22-25% and obtaining a round-trip efficiency of 54% .

In a current development status, RWE Power, General Electric, Zublin and DLR are now working on the world first large-scale A-CAES demonstration project, called Adele, in Germany. This plant is provided by a TES system with molten salt and thermal oil, with actually a natural gas based added combustor and GT heat recovery system. The turbine power output is about 260 MW and the storage capacity is in the range from 1 to 2 GWh. This huge size of heat storage capacity is

one of the main challenges in terms of cost and size, without any existing industrial example. The compression train is made by the axial LP unit and the radial HP compressor. The aim is to reach the 70% cycle efficiency developing down-scalable solutions. The system potential is high but the cost reduction is the main target [14].

There are a lot of other demonstration project studied as the LAES facility in UK, re-founded in 2014; the Iowa Stored Energy Park project with the intention to build a 270 MW CAES plant to be coupled to a wind farm; the Norton Energy Storage project with the intention to build a system with total huge capacity from 270 to 2700 MW, and many other projects but none of them come into being, mainly due to the economic perspective [15].

This work will investigate the modelling and simulation of an Adiabatic Underwater CAES system, which couples the TES, Thermal Energy Storage, to the CAES, while the underwater location takes advantage of the hydrostatic pressure associated with water depth as its motive force. Moreover, the UW-CAES system will be coupled to an offshore wind farm in the south-west coast of Sardinia and this thesis will introduce the economic assessment of the whole system considering the arbitrage and the peak shaving logics.

The second chapter will introduce the whole UW A CAES system design; the third one will focus on the compressor design as the key component of the system and the 4$^{th}$ chapter will investigate the compressor's off-design behaviour.

In the 5$^{th}$ chapter the offshore wind plant will be described and in the 6$^{th}$ one it will be discussed the integration between the UW ACAES and the wind plant. The 7$^{th}$ chapter will introduce the economic assessment of the system together with the relevant results, while the 8$^{th}$ chapter will consider the effect of variations in the boundary conditions. The concluding chapter will summarise the thesis main results with some further development cues.

# 2. UW CAES SYSTEM

Compressed Air Energy Storage is one of the most promising methods for the combination of Renewable Energy Source (RES) based plants with electricity supply, and has a large potential to compensate the fluctuating nature of renewable energies. An example is the coupling with a wind power field as treated in chapter 5. In a CAES system, when there is no demand or when is convenient, the off-peak power from the grid or the electricity generated from renewable sources is used to compress air, pumping it into an underground cavern or into a large sized storage tank at high pressure. Whenever there is a power requirement, this high pressurised air from the underground reservoir or tank is retrieved and used to drive the turbine, producing power from the generator [16]. The Underwater CAES system deploys the hydrostatic pressure by the water column to obtain an isobaric storage. The main advantages of UW-CAES system are constant energy output profile, scalable design and geographical adaptability. In such a system the storage pressure is constant [17].

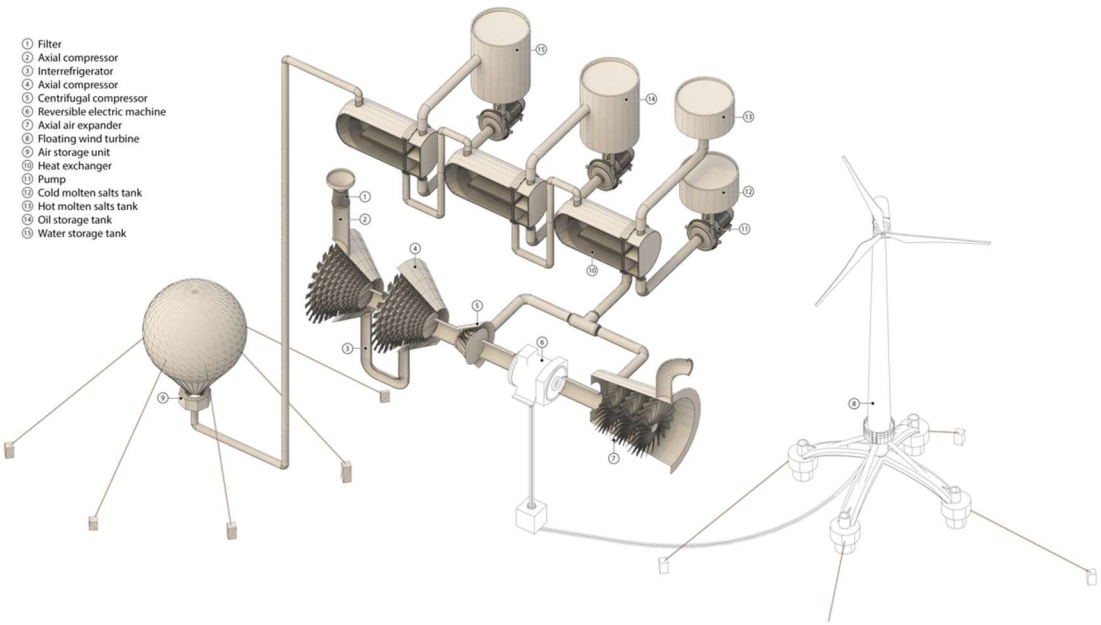


***Figure 2.1: CAD representation of the UW-CAES system***

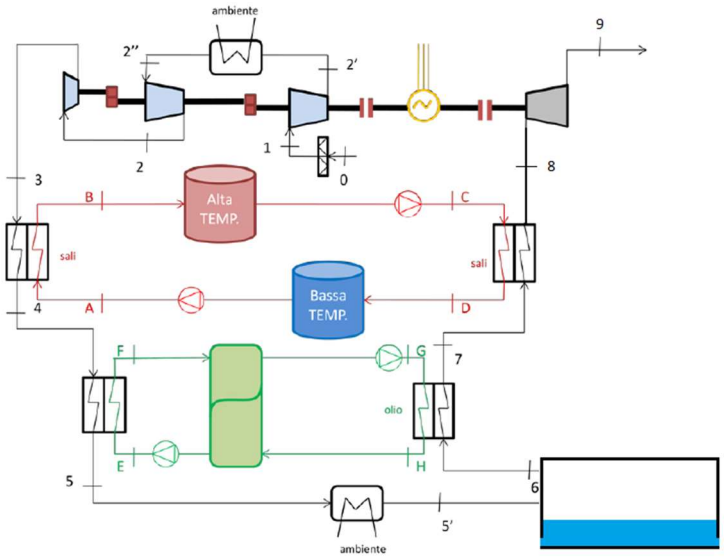


***Figure 2.2: Schematic representation of the UWCAES system***

The UW-CAES is represented by Figure 2.1 and the process is outlined in Figure 2.2. The components included in the system are:

1. The power unit for compressed air, made both by axial and centrifugal compressors.
2. Eventual intercoolers in the compression phase.
3. The heat storage and heat exchange devices.
4. The underwater compressed air tank.
5. The axial turbine.
6. The necessary electric and mechanical equipment.

In the charging phase, air is compressed to high pressures by multi-stage compressors, using the electricity produced by the offshore wind power plant (points 0 to 3 in the figure). When air is compressed, the heat exchange device, between the axial compressors, absorbs the heat released by the compressed air, using seawater (points 2' to 2''). The compressed air, at the compression train outlet, is cooled down by the heat exchange line, that is composed by the air/salt (points 3 to 4), air/oil (points 4 to 5) and air/seawater (points 5 to 5') heat exchangers and, finally, stored in the underwater air storage chamber (points 5' to 6). The thermal energy storage (TES) is performed by the

first molten salts storage, made by the dual, hot and cold, tanks system (A-D), the following thermocline storage system with diathermic oil (E-H) and the eventual additional atmospheric water storage tank. Decoupling in this way the compression and expansion phases, the air flow can be heated again in the heat exchange line, made by the same heat exchanger devices, just crossed in reverse (points 6 to 8; the schematic Figure 2.2 is just a representative tool, Figure 2.1 is more realistic where the heat exchangers are the $10^{th}$ component). Finally, it is possible drive a multi-stage expansion turbine to generate electric power (points 8 to 9).

The system peculiarity with respect to a standard CAES are the following:

- The UWCAES allows to store air at constant pressure, thanks to the underwater tank with openings that allow water in and out to balance the air pressure.
- The total compression heat recovery, through the thermal energy storage (TES), in discharging phase, avoiding an additional combustion step.
- The application of the same heat exchangers to both the charging and the discharging phase, implying a reduced investment cost but a challenging design.

The whole system has been coded on MatLab, with the possibility to cover a wide range of cases, widening the scope of the application.

The model is able to:

1. Size compressors, heat exchangers, turbine, thermal storage and air tanks.
2. Calculate the mass flow rate of salts, oil and water to and from the thermal storage, as well as the heat transfer rates.
3. Evaluate the design and off-design performances, for different available powers from the wind field and for different ambient condition.

The calculations depend on several parameters, that have to be provided to the model, such as:

1. The air tank depth of installation, directly related to the air pressure at the storage tank.
2. The nominal power in input to the compression phase, related to the wind field activity.
3. Limits and available components for the compressor train.
4. Properties of the heat storage fluids.
5. The maximum temperature at the compression outlet, dependent on the heat storage limitations (e.g. salts cracking temperature).
6. Environmental conditions (temperature and pressure).

All the assumed values are introduced in detail in the related chapters.

The code is able to give answers for several sizes and required air storage pressures, but this analysis will be limited in a range that goes from 60 bar to 100 bar. Indeed, from a previous thesis [18], it is already known that operating in value lower than 40 bar is not convenient and, on the other side, becomes hard to move farther the upper limit, due to the increasing depth of installation, linked to the following relation (2.1) between water hydrostatic pressure and depth.

$$p_{hydro} = p_{atm} + \rho_{water}\, gz \qquad \textit{(2.1)}$$

Where $p_{hydro}$ [Pa] is the hydrostatic pressure, $p_{atm}$ [Pa] is the atmospheric pressure, $\rho_{water}$ [kg/m$^3$] is the seawater density, approximately 1025 kg/m$^3$ for sea water, g [m$^2$/s] is the acceleration due to gravity and z [m] is the resulting depth. Increasing the pressure of 1 bar means to increase the depth of 10 meters, so the operative defined range is working in a depth range that goes from 600 to 1000 meters. For example, this range of value is confirmed to be available in the south-west region of Sardinia [19].

In the following section, details for each component will be provided.

## 2.1. COMPRESSION TRAIN

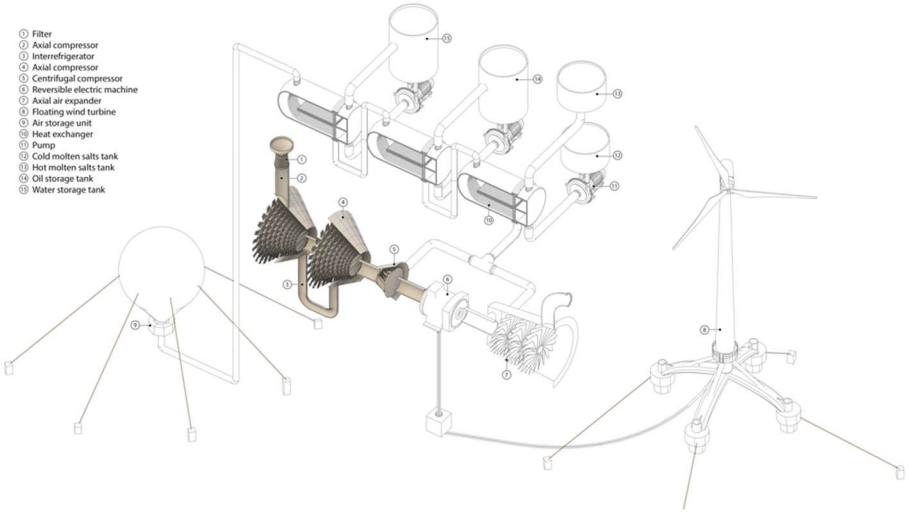


***Figure 2.3: Compression train in the UW CAES system***

The first component of the whole system is the compression train (Figure 2.3). Its size has to be designed in relation to the wind farm and to the desired pressure for the air storage chamber. Peculiarity of the design of the system is that it is designed for fixed compression ratio (β) and given electric power, being unknown the mass flow rate and the efficiency. For this reason, it is possible to have several compression train configurations. The system uses both axial and centrifugal compressors. The axial compressors are used at low pressures while the centrifugal for higher ones. The outlet temperature is fixed by a technological limit, i.e. the downstream salt heat exchanger max temperature, that will be investigated in the next paragraph. So, the studied pressure range, together with the COT (compressor outlet temperature) limit, determines the compression train configuration, that is, in almost every case studies, defined by:

- The multistage low-pressure axial compressor with off-design control through IGV (Inlet Guide Vane) system.
- The seawater-cooled intercooler.
- The multistage high-pressure axial compressor.
- The single stage centrifugal compressor at the end of the compression train.

During the charging phase, the air firstly passes through the filter, necessary to avoid blade erosion effect and to reduce the fouling effect on the compression units[20].

Then, we have the axial compression made by two machines, together with the intercooler in between. The intercooler advantage is certainly to reduce the compression work decreasing air temperature and its specific volume; however, its main advantage is to reduce the COT, the compression train outlet temperature, that has to be limited due to the salt operative properties. The specific application of the UW-CAES guarantees the availability of low temperature water: indeed the working fluid is seawater at 14 °C with pinch point $\Delta T_{pp} = 15$ °C. The last centrifugal compressor is used without the intercooler before it, to guarantee an adequate outlet temperature to the thermal storage, i.e. about 600 °C.

The following data are all assumed to evaluate the compression phase design:

***Table 2-1: Operational data for preliminary compressor design***

| | | |
|---|---|---|
| Ambient temperature | 15 | °C |
| Ambient pressure | 1.01325 | bar |
| Filter, pressure drop | 1 | % |
| Intercooler, pressure drop | 2 | % |
| Intercooler, $\Delta T_{pp}$ | 15 | °C |
| Intercooler, seawater inlet temperature | 14 | °C |
| Axial compressor isentropic efficiency | 86.5 | % |
| Centrifugal compressor isentropic efficiency | 81.5 | % |
| Electrical efficiency | 0.97 | % |
| Organic efficiency | 0.98 | % |

The whole system has been designed coding on MatLab, with REFPROP (Reference Fluid Thermodynamic and Transport Properties Database) and CoolProp programs to evaluate the thermodynamic properties.

The compression phase design algorithm is divided into two steps: the preliminary step aims to define the configuration to be applied, while the further detailed step provides stages and rows operating conditions, as well as a more accurate compression nominal efficiency. The decisive input data, necessary to define the nominal configuration and the thermodynamic property of each stage, are:

1. The required pressure at the underwater air storage tank, that is evaluate in a range between 60 and 100 bar, defined ‘p storage’ in the chart below.
2. The maximum compression outlet temperature, that is directly related to the selected salt type chosen for the thermal storage, defined ‘T max’ in the chart below.
3. The nominal power that the compression train has to absorb.

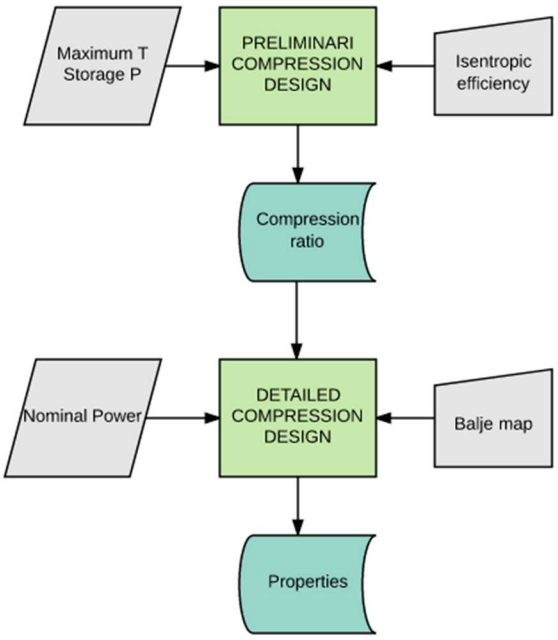


***Figure 2.4: Structure of the algorithm for compressor design***

The “preliminary” and “detailed” compression phase design will be detailed in the next chapter “Compression Phase Design”.

As a consequence of the wind power fluctuation, the CAES system, combined to the offshore wind plant, will operate in off design for most of the operational time. The

compression off design has been developed by implementing the “Inlet guide vane system” (IGV) to increase the operative range by the control of the input air flow. The compression’s off-design will be described in the related chapter “Compression phase Off design”.

## 2.2. THERMAL ENERGY STORAGE (TES)

The thermal energy storage is one of the key point of the Adiabatic CAES as evident from pilot projects such as Adele [21]. Through the thermal storage, it is possible to decouple the compression and expansion phase avoiding an additional combustion process. As a matter of fact, it is not possible to store pressurized air at high temperature, especially in the underwater system. Hence, by combining the air storage to the thermal storage, it is possible to store heat during the charging phase and release it during the discharging one.

Sensible heat storage is achieved by raising the temperature of a material: liquids such as water, oil-based liquids, molten salts, or solids such as rocks, metals, and others. The amount of heat stored is a function of the heat capacity and is linearly dependent on the temperature increase. The larger the difference between the high-temperature and low-temperature system, the higher is the heat stored by the material. All of the currently installed thermal energy storage systems, in solar thermal electric plants store energy, use sensible heat [22]. Alternatives are latent heat based thermal storages, that exploit also the phase change of the storage medium. They have usually higher thermal capacities but lower flexibility and, so, they will not be considered in this work.

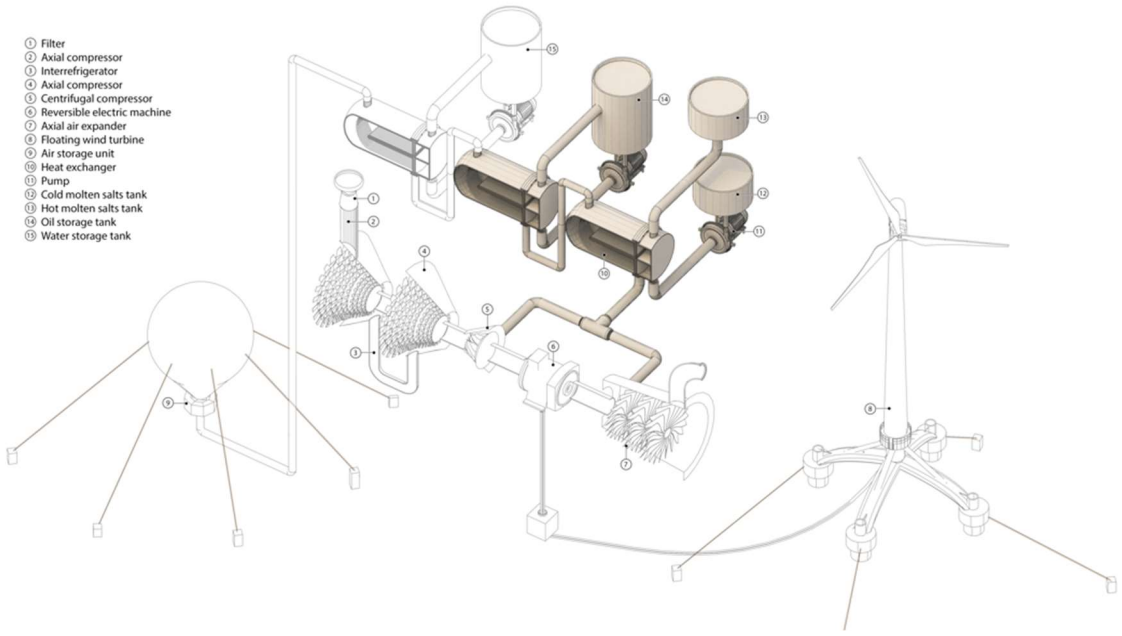


***Figure 2.5: Thermal energy storage by salt and oil together with the relative heat exchangers, in the UW CAES system***

The CAES system, as shown in the Figure 2.5, uses two level of thermal storage, the high temperature storage with molten salt and the low temperature storage with diathermic oil. The chosen salt for the thermal storage is the Solar Salt with the composition of 60% $NaNO_3$ and 40% of $KNO_3$. This fluid is liquid in both the charge and discharge states, so there are minimal heat-transfer limitations, making the heat-exchanger design relatively straight-forward [23]. Solar salt and oil are widely used nowadays for the CSP thermal storage. Their properties are described in the Table 2-2.

***Table 2-2: Solar Salt and diathermic oil properties***

| Properties | Salt | Oil |
|---|---|---|
| Density [kg/$m^3$], @300°C | 1899 | 900 |
| Cp, heat capacity [kJ/kg K] | 1.495 | 2.387 |
| Lower temperature limit [°C] | 220 | 55 |
| Upper temperature limit [°C] | 600 | 345 |

The lower temperature limit represents, for the molten salts their freezing temperature, while for the oil the temperature under which it is difficult to handle it because of the oil viscosity. The upper temperature limit is due to thermal cracking process for both fluids. The upper bound of the salt temperature limits the air COT, Compressor Outlet Temperature, to a maximum of 625 °C, considering that the system could work in over temperature conditions only for a limited amount of time.

The configuration is made by the dual tank salt storage, that is the wider developed and commercialized solution [23], and by the thermocline oil tank, made by one single tank where the hot fluid is usually pumped in the upper part of the tank, gradually displacing the colder fluid in the bottom. A thermal gradient is created and due to buoyancy effects, in an ideal case it is stabilized and preserved [24].

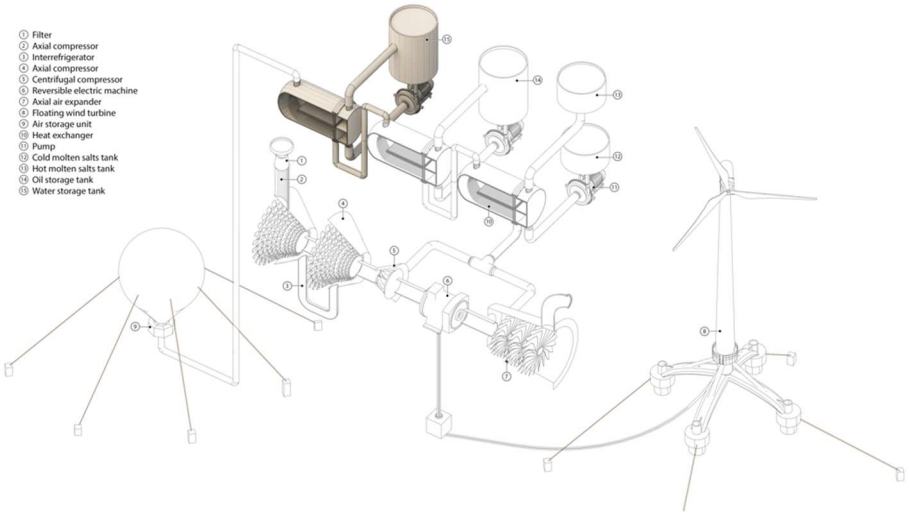


***Figure 2.6: Additional seawater heat recovery together with its heat exchanger in the UW CAES system***

The possibility to activate the additional heat recovery through the seawater atmospheric storage tank has been implemented (Figure 2.6). In this way the aftercooler, located after the air/oil heat exchanger, can be used to store additional low-temperature thermal energy through seawater in a dedicated tank. This kind of solution will be useful to extend the CAES dispatchability, partially overcoming the risk to have not enough thermal energy stored to be able to expand the air in turbine, as discussed in chapter 5. Due to the atmospheric pressure, the maximum temperature for the seawater

storage is related to the evaporation phenomena, indeed this temperature has been fixed to 70°C, considering a safety factor and the lower oil temperature.

The operational data for the thermal storage tanks are summarized in the following Table 2-3. The temperature losses are considered as a percentage of the thermal energy stored.

***Table 2-3: TES working properties***

| | Salt | Oil | Seawater |
|---|---|---|---|
| Hot side temperature [°C] | 600 | 270 | 70 |
| Cold side temperature [°C] | 270 | 55 | 14 |
| Temperature loss [$(Q_{i+1} - Q_i)$ / hour] | $0.001 \cdot Q_i$ | $0.001 \cdot Q_i$ | $0.001 \cdot Q_i$ |

### 2.2.1. TES Sizing

The TES tank sizing turns out to be one of the critical issue to the system. Indeed, the TES size will influence the operational hours of the CAES system. If only one of the thermal storage tanks will not be able to guarantee enough thermal energy, the CAES cannot be activated. On the other side, the cost of the TES system without any sizing limitation will be unsustainable.

For example, analysing the case study with the storage pressure equal to 100 bar and the nominal power absorbed by the compression phase equal to 80 MW, it is easy to evaluate the needed working fluid quantity and the size of the tank, varying the storage hours ensured (Figure 2.7). The height of the tank has been fixed to 15 meters, taking as reference the size of the Andasol project [25]. In relation to the wind trend and to the compression train sizing, it could be needed to store up to 500 hours, that are 20 days; in this case we are speaking of orders of magnitude of 10’000 tons for each working fluid. The cost of these quantities of salt and oil become the main issue and the tanks size unfeasible. The storage hours will become an optimization variable to guarantee the correct working of the CAES system, with a trade-off between acceptable efficiency range and the system economic sustainability.

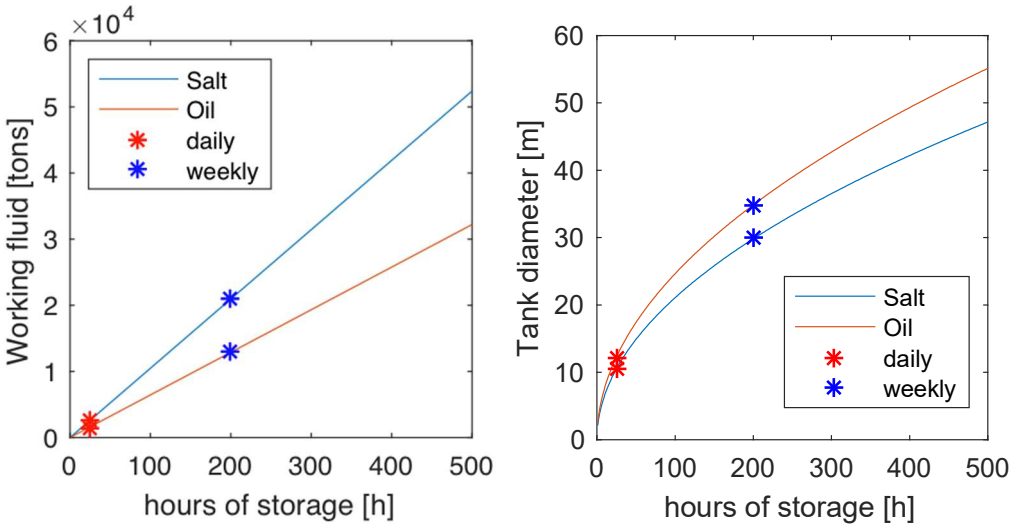


***Figure 2.7: Case study reference: P nominal compression = 80MW, storage pressure = 100. The left figure represents the fluids quantity needed to cover up to 500 hours of storage, while the right figure, the related tank diameter, with daily and weekly cases highlighted.***

On the other hand, considering to store energy on a shorter time horizon, i.e. daily and weekly, as shown in Figure 2.7, the diameter size is reduced to about 10 m and 30 m with few thousand tons of fluids. This size is compatible to the one of storage for solar CSP [22].

## 2.3. HEAT EXCHANGERS

The heat exchangers, despite of the schematic representation, are used in both the cooling and heating direction. The charging and discharging phases have been decoupled in the Figure 2.2 only for modelling purpose but they exploit the same devices. We have defined the 'Cooling To Storage' (CTS) phase to identify the heat exchange process to cool down the air flow after the compression, passing through the air/salt, air/oil and air/seawater heat exchanger, to the air underwater storage tank (points 3 to 5' in the Figure 2.2). On the other hand, we have called the 'Heating From Storage' (HFS) phase, to identify the heat exchange process to heat up the air flow from the underwater tank, getting through the air/seawater, air/oil and air/salt heat exchangers, to the expansion phase (points 5' to 8). The heat exchangers have been

designed in relation to the compression phase, that is the most sensitive because working often in off design.

### 2.3.1. Heat Exchanger Formulation

The heat exchangers selected are the Shell-and-Tube types: they operate with one fluid flowing inside the tubes (i.e. water) while the other flows outside transversely to the length of the tubes (i.e. air). The relation used to size the heat exchangers are the following.

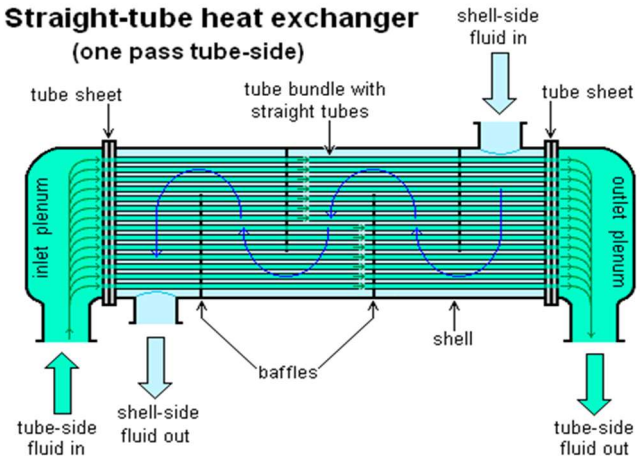


***Figure 2.8: Shell & Tube heat exchanger***

$$\dot{Q} = \dot{m}\bar{c_p}\Delta T_i \tag{2.2}$$

$$\dot{Q} = UA\Delta T_{ml} \tag{2.3}$$

Where $\dot{Q}$ is the heat transfer rate [kW], $\dot{m}$ is the air mass flow rate [kg/s], $\bar{c_p}$ is the average specific heat capacity [kJ/kgK], $\Delta T_i$ is the temperature variation between inlet and outlet section [K]. U [kW/m$^2$K] is the overall heat exchange coefficient, A [m$^2$] is the heat exchange surface and $\Delta T_{ml}$ is the mean logarithmic change in temperature defined in the following equation 2.4.

$$\Delta T_{ml} = \frac{\Delta T_{in} - \Delta T_{out}}{\ln\left(\frac{\Delta T_{in}}{\Delta T_{out}}\right)} \tag{2.4}$$

$$\Delta T_{in} = T_{h,in} - T_{c,out} \tag{2.5}$$

$$\Delta T_{out} = T_{h,out} - T_{c,in} \tag{2.6}$$

To guarantee an energy balanced heat exchanger, the heat capacity has been kept constant between the air and the working fluid (equation 2.7), and to limit the heat exchanger cost the ΔT has been fixed to 25 °C. This implies a fixed value to the inlet and outlet air temperature, as shown in Figure 2.9 for a case study. So, it is, possible to evaluate the nominal heat transfer rate $\dot{Q}$, for each unit, and the relative surface A.

$$\dot{C}_{air} = \dot{m}_{air} \cdot c_{p,air} = \dot{m}_f \cdot c_{p,f} = \dot{C}_f \tag{2.7}$$

$$\dot{Q} = \dot{C}_{air} \cdot \Delta T_{air} = \dot{C}_f \cdot \Delta T_f \tag{2.8}$$

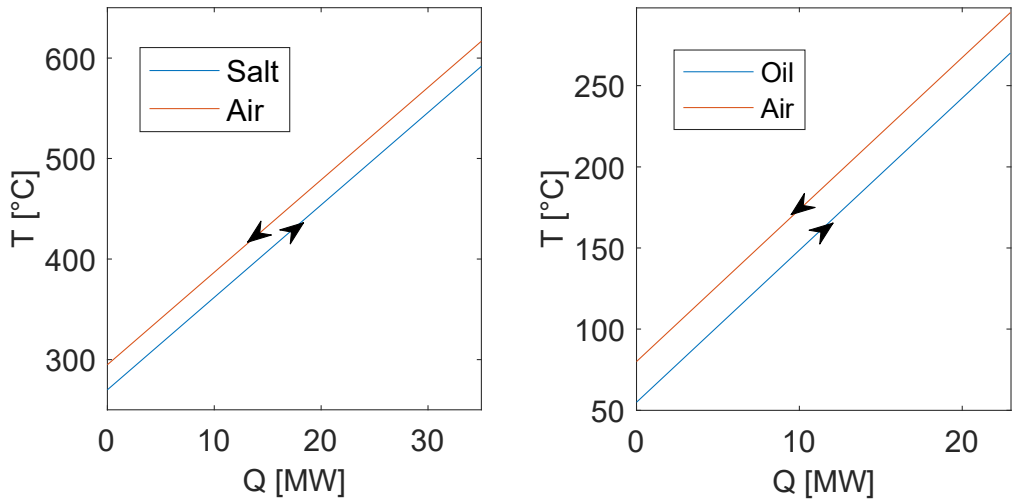


***Figure 2.9: Case study: Compression nominal Power = 80 MW, Storage pressure = 100 bar. The left figure represents the nominal TQ diagram for the Air/Salt heat exchanger, the right one is the nominal TQ diagram for the Air Oil one.***

These equations are valid to all the heat exchangers, despite of the working fluid.

### 2.3.2. Assumption & Heat Exchanger Design

To design the heat exchangers, a lot of assumptions have been made for the heat transfer problem formulations, notably in the area of energy balances, rate equations and boundary conditions. They are summarized in the following list.

1. The heat exchanger has been designed in relation to the compression phase in the nominal condition, and will operate under steady-state condition, i.e. operate with constant flow rates and fluid temperatures, both at the inlet and within the heat exchanger.
2. Heat losses to and from the surroundings are neglected.
3. Uniform distribution of fluid temperature over every cross section of the exchanger.
4. No phase change, since we are only dealing with liquid working fluid (molten salt, oil or liquid water) on one side and air on the other side of the exchanger, in any operating conditions.
5. The working fluids employed in the heat exchangers are assumed to be of constant specific heat capacities. While the specific heat capacity coefficient on air side is calculated through REFPROP.
6. The overall heat transfer coefficients are assumed constant, thus independent of temperature, time and position, in the heat exchangers.
7. The flow velocity and temperature of both fluids at the inlet of the heat exchanger on each fluid side is considered uniform over the flow cross section.
8. The fluid flow rate is uniformly distributed through the exchanger on each fluid side in each pass.

The working fluids properties, together with the heat exchangers operative conditions, are defined in the following table 2-4 [26] [23].

***Table 2-4: Thermo- physical properties of the working fluid used in the heat exchanger***

| Properties | Salt | Oil | Water |
|---|---|---|---|
| ΔT pinch point, air / working fluid [°C] | 25 | 25 | 10 |
| Pressure drop | 1% | 1% | 1% |
| Cp, heat capacity [kJ/kgK] | 1.495 | 2.387 | 4.186 |
| U, overall heat transfer coefficient $[W/m^2K]$ | 700 | 400 | 300 |
| T in, working fluid [°C] | 270 | 55 | 14 |
| T out, working fluid [°C] | 600 | 270 | 70 |
| T in, air [°C] | 625 | 295 | 80 |
| T out, air [°C] | 295 | 80 | 24 |

The resulting surfaces for each shell & tube heat exchanger depends on the case studied. Taking as reference the nominal input power to the compression phase equal to 80 MW and the storage pressure equal to 100 bar, the results are described in the following Table 2-5.

***Table 2-5: Resulting heat exchangers surface in the case study with compression nominal power of 80 MW and P storage of 100 bar***

| | Salt | Oil | Water |
|---|---|---|---|
| $\dot{Q}$, heat transfer rate [kW] | 35910 | 22960 | 6268 |
| A, surface $[m^2]$ | 2052 | 2296 | 2089 |

### 2.3.3. Heat Exchanger Off Design

The CAES system will operate in off design in most of the operative time, implying different working conditions with respect to the nominal case. In particular, in off design the heat exchangers will vary their heat transfer rate $\dot{Q}$ according to the working fluid mass flow rate. Consequently, also the fluids' outlet temperatures will change.

The heat exchange off-design inputs are:

1. The air mass flow rate, derived by the sizing of the compression train with respect to the wind farm and recalculated through the compression off design

analysis. Once it is defined by the off-design simulation, it is known in the "Cooling To Storage" process and it is kept constant.

2. The air heat capacity, that can be calculated through REFPROP.
3. The air COT, Compressor Outlet Temperature, derived by the compression off-design analysis.
4. The heat exchanger surfaces, derived by the heat exchanger design in the nominal case.
5. The overall heat exchange coefficient, thanks to the relation (2.9).
6. The working fluid inlet and outlet temperatures, that have to be kept constant to guarantee the TES working configuration without overcoming the thermodynamic fluid properties limits.

$$U_{off} = U_{nom} \cdot \left(\frac{\dot{V}_{off}}{\dot{V}_{nom}}\right)^{0.75} \tag{2.9}$$

By the formulation introduced (2.2) (2.3), it is possible to calculate the air temperature at the outlet of each heat exchanger and the related heat transfer rate $\dot{Q}$. An example of off-design application with nominal power of 80 MW and storage pressure of 100 bar is shown in Figure 2.10. The heat transfer rate is, of course, dependent on the air mass flow rate, that can vary working in off design conditions thanks to the IGV system (see chapter 4).

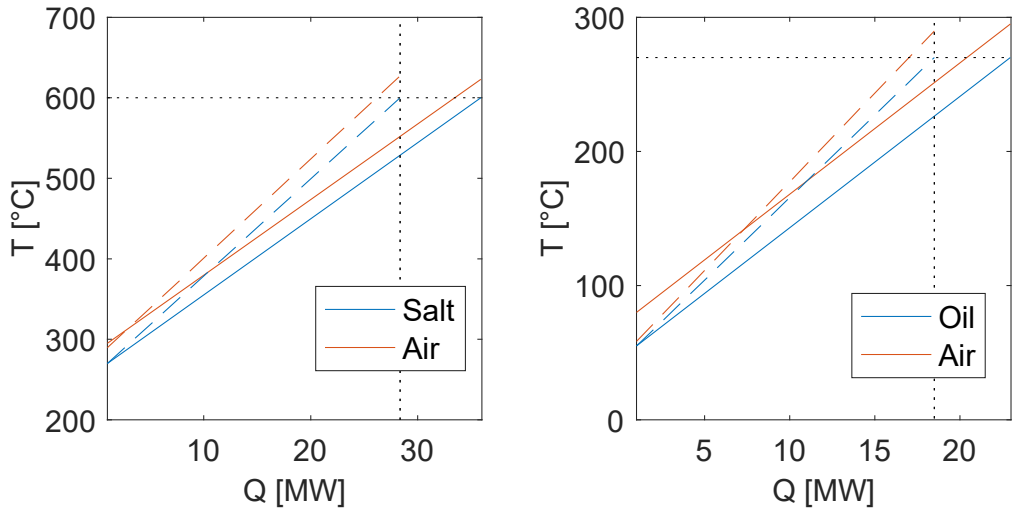


***Figure 2.10: Heat exchanger off-design for case study P=80 MW and storage pressure=100 bar.***

### 2.3.4. Discharging Process: "Heating From Storage"

The turbine will be dimensioned in relation to the offshore wind farm production to guarantee the full load operational condition. Its size can be defined with respect to the compression nominal size, i.e. in the range from 0.4 to 1. The air mass flow rate, in the discharging phase, will be related to the turbine chosen configuration, and it will be always lower (or equal in then limit case) with respect to the charging phase.

In the Heating From Storage (HFS) phase the working fluids temperature differences are kept constant. Since the air flow rate is lower, it results in oversized heat exchangers for the HFS process and, consequently, lower air-working fluid $\Delta T$ at the air side outlet. This choice allows to exploit the unpredictable excess energy with a larger machine, while the turbine, that is operated in a low-power conditions, has a smaller investment cost. This means that we are able to reach the desired TIT, Turbine Inlet Temperature, necessary to the expansion phase.

## 2.4. UNDERWATER AIR TANK

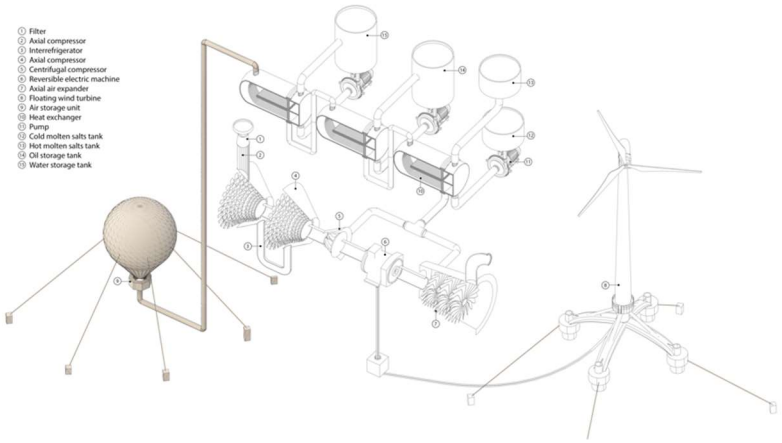


***Figure 2.11: Tank in UW-CAES system. Only representative sketch to highlight where we are during the process, the modelled tank will be like in the Figure 2.12.***

Traditional Compressed Air Energy Storage (CAES) utilizes geologic formations such as solution mined salt domes or confined aquifers in order to store large volumes of compressed air. In underwater compressed energy storage, the air is compressed in a container located underwater. Several approaches to UW-CAES are under development including the utilization of distensible air container also referred to as Energy Bag, similar to the one in Figure 2.11 [27]. One developer, Hydrostor Inc. completed installation of a grid connected UW-CAES system in November 2015. This system is deployed within Lake Ontario [28]. However, also other kind of underwater storage are being developed. While Hydrostor's balloons use water pressure to deliver a novel form of compressed air energy storage (CAES), the Fraunhofer project, called StEnSEA (Stored Energy in the Sea), is essentially a variant of pumped hydro, and it is another approach to offshore energy storage which utilizes large concrete spherical structures mounted to waterbed [29].

The underwater tank in our system is simplified as a rigid modular tank. As shown in the Figure 2.12, the reservoirs are containers made of common and ordinary materials like concrete and steel with openings at the base to guarantee the seawater access, to keep the air pressure constant and equal to the hydrostatic one (2.1).

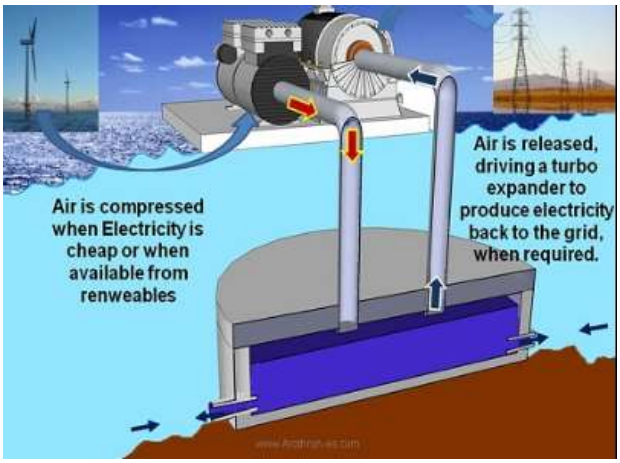


***Figure 2.12: Underwater tank system*** [30]

The tank geometry has been simplified as a hemispherical volume of 10.000 $m^3$, taking as reference a previous work [18]. Considering the coupling of the CAES to the wind field, as discussed in chapter 5, the air volume that requires to be stored is an output value, so, thanks to this kind of modular tank we can evaluate how many tanks are needed. To evaluate the minimum wall thickness necessary to avoid the floating of the tanks, the forces balance has been calculated. The most restrictive condition occurs when the tank if full of air, and the balance in this condition is defined by the following relations. Where $\rho$ is the fluid density [kg/$m^3$], $g$ is the acceleration due to gravity [m/$s^3$], $r_{ext}$ is the outer radius and $r_{int}$the internal one [m].

$$P_{tank,concrete} + P_{air} - P_{water} = 0 \tag{2.10}$$

$$P_{tank,concrete} = \rho_{concrete} \cdot \frac{2}{3} \cdot \pi \cdot (r_{ext} - r_{int})^3 \cdot g \tag{2.11}$$

$$P_{water} = \rho_{water} \cdot \frac{2}{3} \cdot \pi \cdot {r_{ext}}^3 \cdot g \tag{2.12}$$

$$P_{air} = \rho_{air} \cdot \frac{2}{3} \cdot \pi \cdot {r_{int}}^3 \cdot g \tag{2.13}$$

Since we are dealing with pressurized air, its density is relevant, the $P_{air}$ cannot be neglected (2.13). The concrete available to be used in marine environments is the Marine Concrete, with higher durability [31]. The densities involved in the balance are summarised in the following Table 2-6.

***Table 2-6: Densities involved in the forces balance, considering a storage pressure of 100 bar.***

| | |
|---|---|
| $\rho_{concrete}$ [kg/$m^3$] | 2290 |
| $\rho_{water}$ [kg/$m^3$] @ 100 bar, 4°C | 1025 |
| $\rho_{air}$ [kg/$m^3$] @100 bar, 14°C | 127 |

The equation (2.10) results in a balance driven by the change in densities among the medium involved. Combining the previous equations, it is possible to derive the concrete volume required to sink the assumed air volume, through the relation (2.14).

$$\rho_{concrete} \cdot \frac{V_c}{V_{air}} + \rho_{air} = \rho_{water} \cdot \left(\frac{V_c}{V_{air}} + 1\right) \qquad (2.14)$$

The volume ratio $\left(\frac{V_c}{V_{air}}\right)$ is a function of $\rho_{air}$, so it depends on the depth of installation. In the following Table 2-7, some results:

***Table 2-7: Volume ratio to sink the tank for some case studies***

| | |
|---|---|
| $\left(\frac{V_c}{V_{air}}\right)$ *@ Storage Pressure 120 bar* | 0.67 |
| $\left(\frac{V_c}{V_{air}}\right)$ *@ Storage Pressure 100 bar* | 0.70 |
| $\left(\frac{V_c}{V_{air}}\right)$ *@ Storage Pressure 80 bar* | 0.73 |

For example, considering the storage pressure of 100 bar, the concrete volume has to be 0.70 times the inlet air tank volume to not float. Since this implies large concrete volumes, could be also possible to use more tanks with lower wall thickness. As we can see from the Figure 2.13, the equation (2.10) is balanced with a wall thickness of 3.29

m, that implies a huge amount of concrete, while imposing 0.5 m of wall thickness, requires more than 200 tanks to store 10000 $m^3$ of air.

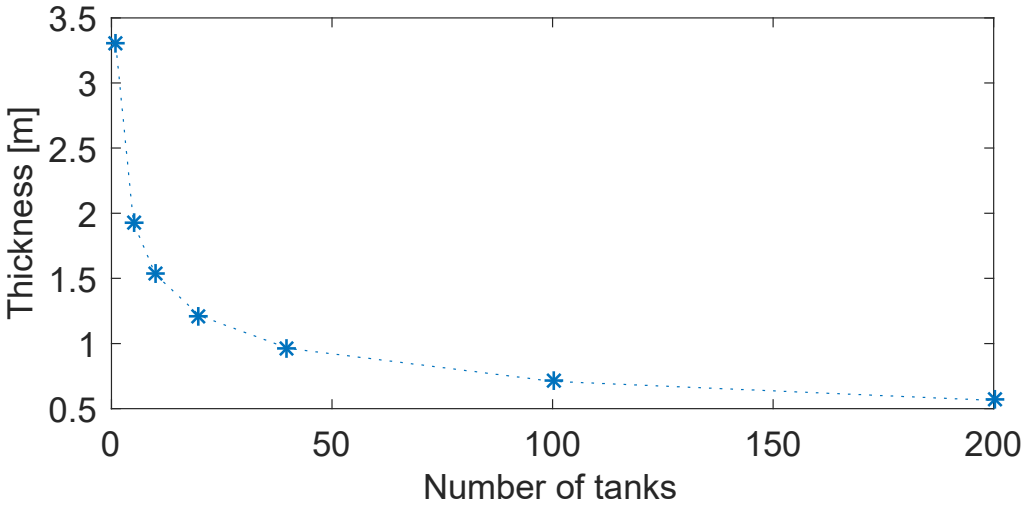


***Figure 2.13: Concrete wall thickness related to the number of tanks to sink the tanks, considering the case study at the storage pressure of 100 bar***

A better solution could be to use anchorage's system with a feasible wall thickness. To estimate the tank's cost, we have considered the inlet volume of 10000 $m^3$ and a wall thickness of 0.4 m with an appropriate anchorage's system.

### 2.4.1. Pipeline sizing

Considering the piping loss in the underwater system, has been taken as a reference the offshore pipe design of oil & gas sector [32][33]. The principal factors governing the pipe size to be used are the nature of the fluid, the flow velocity and pressure drop. The sizing criteria are different depending on whether the pipe is carrying a single-phase liquid, a single-phase gas or a two-phase mixture of liquid and gas. We are dealing with just pressurised air. For a straight pipe, the pressure drop is given by the equation.

$$\Delta P = \lambda \frac{\rho V^2}{2} \frac{L}{D} \tag{2.15}$$

Where λ is the Moody friction factor, ρ is the density of the fluid, V is the average velocity of the fluid in the pipe, L is the length of pipe and D is the inside diameter. The Moody friction factor can be read from a Moody diagram, which shows the friction factor plotted against the Reynolds number, Re, for various relative roughness values, ε / D.

$$\mathrm{Re} = \frac{\rho V D}{\mu} \tag{2.16}$$

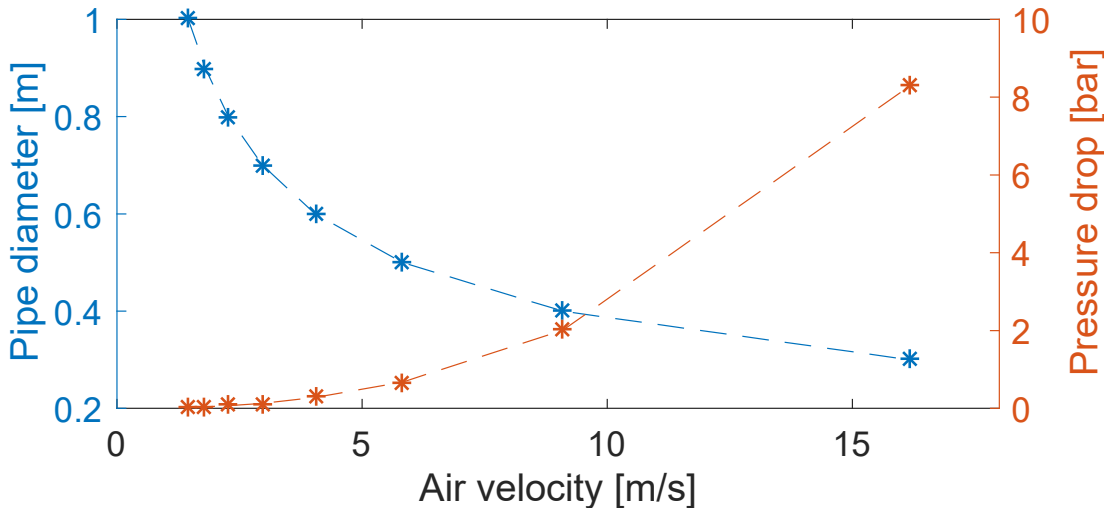


***Figure 2.14: Pipeline sizing parameters, considering a case study with storage pressure of 100 bar***

For a case study with the pressure tank of 100 bar, the results are showed in the Figure 2.14. It is evident how the pressure drop is not so relevant for air velocities until 10 m/s, where the pressure drop range is from 0.1% to 2 %. So, the pressure drop in the pipeline is not a limiting factor from the thermodynamic point of view and the pipeline size selection could be made just considering the structural limits, taking into consideration the fluctuation of the charging and discharging phases that could led to mechanical resistance problems, due to under- and over-pressure zone inside the pipelines.

## 2.5. TURBINE

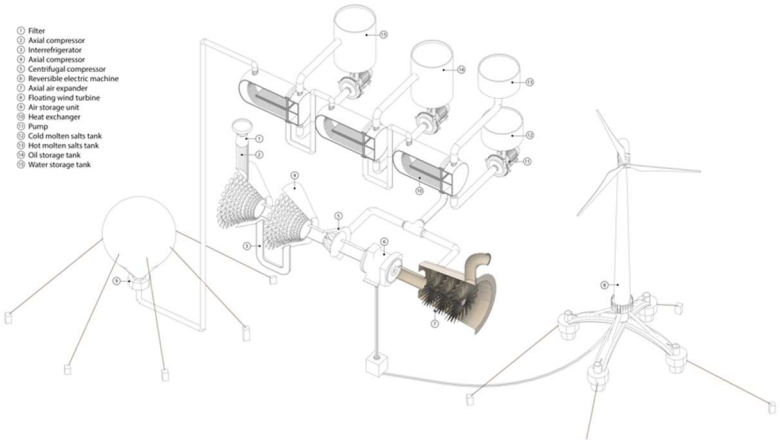


***Figure 2.15: Turbine in the UW CAES system***

The turbine has been sized to operate always at full load, thanks to the constant air mass flow rate and to the heat storage that provides a heat source to guarantee a constant TIT, Turbine Inlet Temperature. The turbine size will be defined in the related 5$^{th}$ chapter considering the wind field behaviour. The assumed data to define the turbine design are summarized in the following Table 2-8.

***Table 2-8: Assumed data for the turbine design***

| | |
|---|---|
| Isentropic efficiency, $\eta_{is}$ | 0.94 |
| Minimum outlet temperature [°C] | 5 |
| Maximum peripheral speed u [m/s] | 400 |
| Reaction grade, $\chi$ | 0.5 |

The minimum outlet temperature is imposed to avoid freezing phenomena on the turbine blades, and the ideal reaction grade (Figure 2.16) implies that the head coefficient of one stage (2.17) is equal to 1, where $L_{eu}$ is the work per unit of flowing mass transferred from the flow to the blades of the machine. In this way, a change in enthalpy of 160 kJ/kg has been determined as a maximum value for each stage.

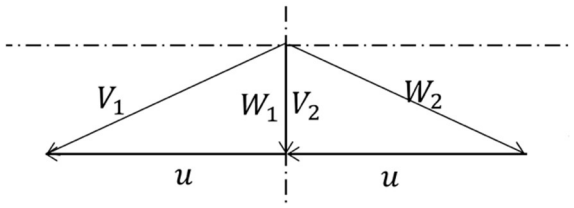


***Figure 2.16: Optimized ideal reaction stage, $\chi = 0.5$***

$$\varphi = \frac{L_{eu}}{u^2} = \frac{u\Delta V_t}{u^2} \tag{2.17}$$

The geometry of the turbine, i.e. diameter and blade height, has been finally calculated through the following equations [34].

$$\dot{m} = \rho \cdot Va \cdot \pi \cdot Dm \cdot h \tag{2.18}$$

$$u = \omega \cdot \frac{Dm}{2} \tag{2.19}$$

$$V_a = u \cdot \tan\alpha \tag{2.20}$$

# 3. COMPRESSION PHASE DESIGN

As anticipated before, the compressors design aim, is to define a compression train capable to answer to several fixed conditions with appropriate working features.

The conditions a priori defined are:

1. The nominal power, given by the wind field, that has to be absorbed by the compression train;
2. The underwater tank pressure, that requires a certain compression train outlet pressure;
3. The Outlet temperature of the compression train, that is limited due to the presence of the Salt Heat Exchanger.

The design initial phase identifies the "Preliminary configuration": number and type of compressors needed, number of intercoolers needed and the nominal compression ratio of each compressor, minimizing the CAES system efficiency.

The second phase is a deeper analysis developed at stage level, through the Balje diagram. Its aim is to define the compressors efficiency stage by stage, so the real outlet thermodynamic conditions together with the compressors size and the optimized rotational speed, as in 3.2. This second step is focused on assessing feasibility of the compressor with respect to the specifications.

## 3.1. PRELIMINARY CONFIGURATION

### 3.1.1. Parameter definition

The preliminary configuration is defined through an optimization, in order to share the total expansion ratio on each compressor, with the maximum CAES system efficiency (3.1), defined as:

$$\eta_{round\ trip}^{nom} = \frac{\dot{m}\ \Delta h_T^{nom}}{\dot{m}\ \Delta h_C^{nom}} \tag{3.1}$$

The input data are:

- The required pressure at the underwater tank;
- The average isentropic efficiency of the axial and radial compressors respectively equal to 0.865 and 0.815 [20].
- The limited final outlet temperature, due to the presence of the salt heat exchanger, indeed the chosen salt is Solar Salt with the operative temperature range from 300 °C to 600 °C [23].
- Turbine isentropic efficiency equal to 0.94 [20].
- Pressure loss. Equal to 1% for the filter, for the heat exchangers and for the intercoolers.

Moreover, in this phase, it is decided to place a centrifugal compressor after the axial ones. Centrifugal compressors in general are used for higher pressure ratios and lower flow rates compared to lower stage pressure ratios and higher flow rates in axial compressors [35].

First, a compression ratio of at least 3 is decided, to guarantee the right sizing to the eventual centrifugal compressor. It will be confirmed as the right configuration in the subsequent analysis through the Balje diagram.

The centrifugal compressor could work with higher rotational speed and, at the cost of a lower isentropic efficiency, it allows higher isentropic enthalpy difference in a single stage, with higher single stage compression ratio. This means that has a lower size and thus a lower costs.

The expected output data from this code is the nominal total compression ratio (3.2) for each compressor, together with the nominal configuration, number and type of compressors and intercoolers.

$$\beta = \frac{Pout}{Pin} \tag{3.2}$$

### 3.1.2. Intercooler

The possibility to activate or not the intercoolers has been integrated in the optimization. The intercoolers aim is to decrease the compression work required, affecting also the outlet compression temperature. It is required to keep under control the compression outlet temperature particularly for high pressure tank cases (approximately from 60 bar) when the risk to overcome the cracking temperature is higher.

The employed cooling fluid is seawater, with the temperature of 14 °C in the nominal case. The pinch point is fixed at 15°C, that implies, in the activated intercooler cases, an outlet air temperature of 29°C. Due to this reason, the code will prefer to place the intercooler as soon as possible during the compression phase, to not limit too much the outlet compression temperature, in order to keep high the CAES efficiency (3.1). This is a particular issue of this system: a trade-off exists between lower compression work, that implies lower outlet temperature, and heat storage efficiency, that requires higher outlet temperature.

### 3.1.3. Preliminary design applying example

This example aims to show the results of the preliminary design for a single specific case of study, the storage tank pressure equal to 100 bar.

The implemented code gives a uniquely determined result for the last axial and centrifugal compressors, due to the technical limits imposed.

On the other hand, in the first phase of compression, if we leave to the code the possibility to have as much axial compressors and intercoolers between them, as it would, the results would obviously tend to an isothermal compression, as shown in Figure 3.1.

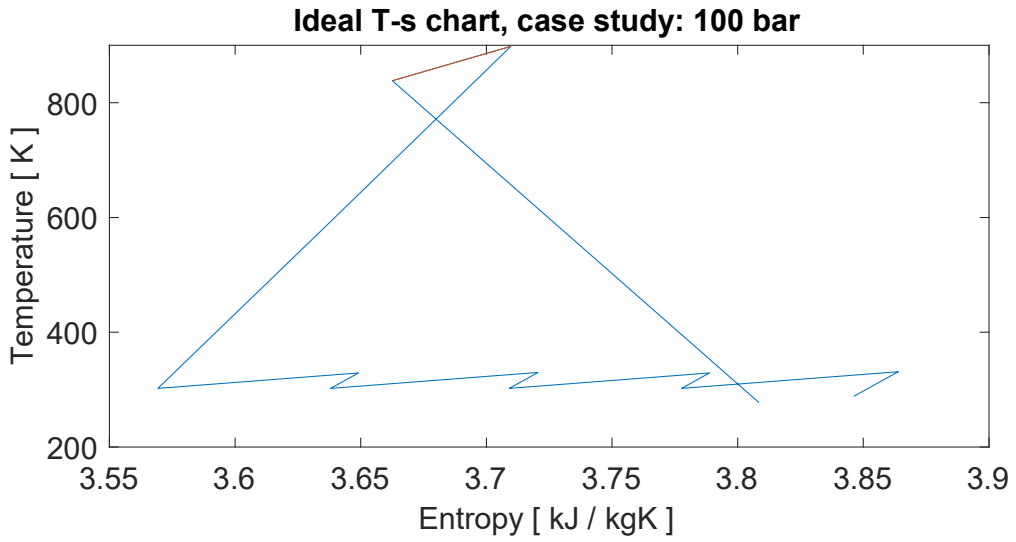


***Figure 3.1: Example of preliminary ideal T-s chart: compression and expansion are plotted as sequential steps, although they are shifted in time.***

The red line stands for the temperature and pressure losses during the heat exchanger line between the compression phase and the expansion one.

Taking into consideration the mentioned example, the ideal isentropic preliminary CAES efficiency is equal to 0.79. While the configuration results made by the first four small compressors with $\beta$ between 1.3 and 1.5, four intercoolers, the bigger axial compressor with $\beta = 9.14$, and the last centrifugal compressor with $\beta = 3.5$.

The resulting nearly isothermal compression is analytically correct but not feasible, because of the costs and also due to the, too small, size of each compressor. Indeed, to cover a compression ratio of 1.3, one single stage is enough. So, we have to introduce realistic applicability limits to the code. The right sizing, for this case study, results in a combination of the last two, already determined, compressors, together with only one other axial compressor, instead of the isothermal compressors sequence, as shown in the Figure 3.2.

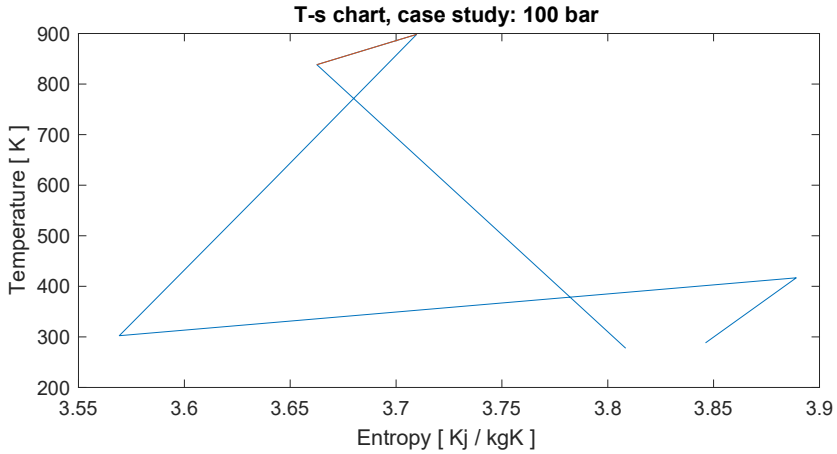


***Figure 3.2: Example of preliminary T-s chart: two axial intercooled compressions followed by centrifugal compression and expansion***

So, with a tank pressure of 100 bar, the chosen configuration is made by a first axial compressor with $\beta = 3.15$, a second axial compressor with $\beta = 9.14$, and the one last centrifugal compressor with $\beta = 3.5$, while the isentropic preliminary CAES efficiency is equal to 0.77.

## 3.2. DETAILED DESIGN OF COMPRESSION TRAIN

Once the preliminary design data are determined it is possible to go on with the detailed design stage by stage, developed through the dimensional analysis.

When the concept of dimensional analysis in fluid mechanics is applied to turbomachines, it provides a greater depth of understanding of performances and classification of machines [36]. This approach provides to the designer information as the best type of machine for an application. In addition, it provides parameters to determine the size of the machine and it also aids in the selection of the optimum rotational speed.

This is the formal procedure whereby the group of variables representing some physical situation is reduced to a smaller number of dimensionless groups.

Through the dimensional analysis technique, the dimensionless similarity parameters specific speed Ns, specific diameter Ds, Reynolds number Re, and Mach

number Ma, are derived. They serve as convenient parameters for presenting the performance criteria of turbomachines. These four parameters are sufficient to describe completely the performance of geometrically similar turbomachines. For a given volume flow rate and a given isentropic enthalpy change through a turbomachine, specific speed Ns is a number indicative of the revolving speed of the machine and specific diameter Ds is a number indicative of the rotor diameter or size of the machine. Reynolds number expresses the ratio of inertia force to viscous force and reflects the properties of the fluid and the speed of the machine. It is difficult to present the performance of any machine as a function of four parameters at one time. Fortunately, two of these variables, namely Reynold's number Re and Mach number Ma, have only a secondary effect on turbomachine performance; and more significantly, if the Reynolds number is above 10^6 for turbines and compressors or above 10^7 for pumps the effect of Reynolds number is almost negligible, which eliminates this variable. If the Mach number of the machine is less than or near 1.0, the compressibility effects are low, eliminating this variable too; so, turbomachine performance can be presented as a function of two parameters, specific speed, Ns and specific diameter, Ds [37].

$$N_s = \frac{N * \sqrt{\dot{V}}}{\Delta h^{3/4}} \tag{3.3}$$

$$D_s = \frac{D * \Delta h^{1/4}}{\sqrt{\dot{V}}} \tag{3.4}$$

Hence, these two parameters are function of volume flow rate (3.5) and isentropic enthalpy change (3.6), defined stage by stage.

$$\dot{V} = \frac{\dot{m}}{\rho} \tag{3.5}$$

$$\Delta h_{is} = h_{is,out} - h_{in} \tag{3.6}$$

Indeed, these parameters are already defined from the preliminary design, since the total compression ratio and the configuration made by axials and centrifugal compressors were already established.

In an axial-flow compressor, the air passes from one stage to the next, each stage raising the pressure slightly. By producing low-pressure increases on the order of 1.1:1 to 1.4:1, very high efficiencies can be obtained. The use of multiple stages permits overall pressure increases of up to 40:1 in some aerospace applications, and a pressure ratio of 30:1 in some industrial applications [38].

So, we have imposed a maximum compression ratio equal to 1.3 to the axial compressors. This limiting value provides the stages number for each axial compressor and the real single stage compression ratios.

By contrast, centrifugal compressors range in size from pressure ratios of 3:1 per stage to as high as 12:1 on experimental models [39].

Discussion here will be limited to pressure ratios around 3, since this type is prevalent in the petrochemical industry and, primarily, is the fitting type for our studied system.

So, thanks to the information regarding the number of stages and single stage compression ratio, together with the starting isentropic efficiency, the volume flow rate and the isentropic enthalpy change for each stage are known.

### 3.2.1. Balje diagram

In the 1950s, Cordier (1955) carried out an intensive empirical analysis of “good turbomachines” using extensive experimental data. He attempted to correlate the data in terms of Ns, Ds and efficiency. He found that turbomachines, which for their type had good to excellent efficiencies, tended to group along a definable curve when plotted with their values of Ns vs. Ds. He further found that the efficiencies of these machines grouped into a definable, if rough, curve as function of Ds. Machines whose efficiencies could be classified as poor for a particular type of device were found to scatter away from the locus of excellent machine in Ds-Ns coordinates [36]. Cordier curve (Figure

3.3) was, in effect, a practical guideline to both design layout and effective selection of good machinery for a specified purpose. This concept was further developed by Balje (1981) (Figure 3.4).

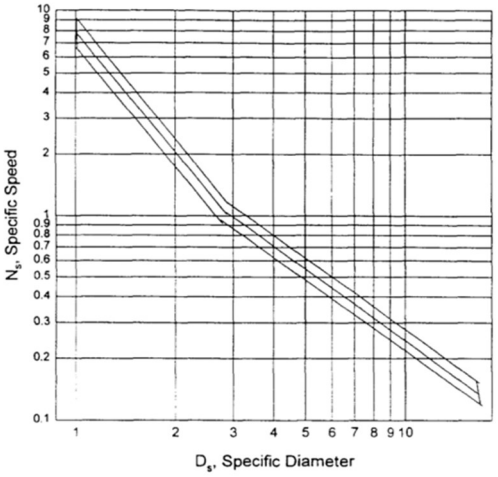


***Figure 3.3: Cordier diagram of maximum efficiency***

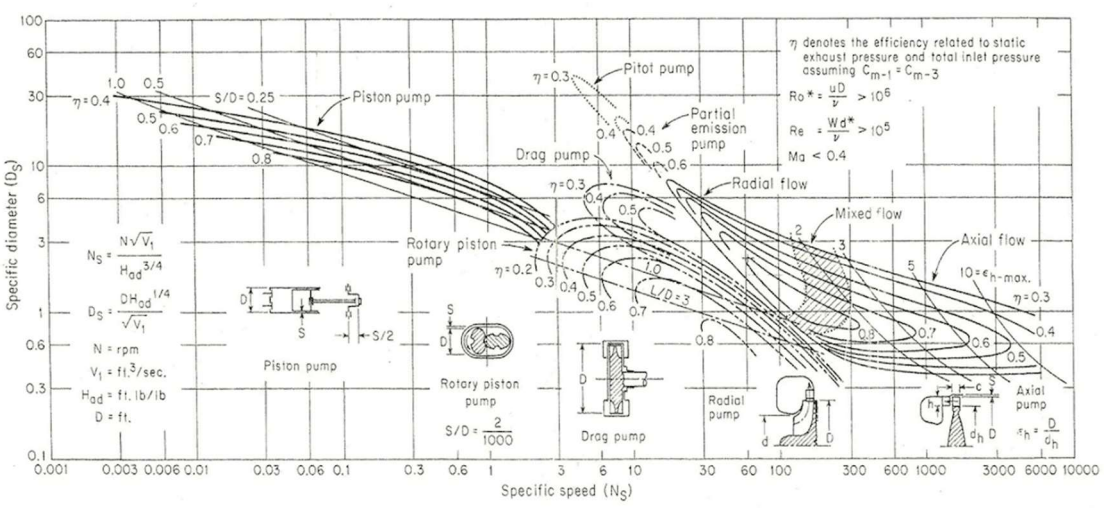


***Figure 3.4: Ns-Ds diagram for single stage compressors, O.E. Balje***

Ns – Ds diagrams are used to estimate the performances of a turbomachine for a specific application. If a certain efficiency level of operation is desired for a turbine, pump or compressor, the head across the machine is calculated. For a turbine, this head is the total isentropic head drop available and for pumps or compressors it is the isentropic head rise associated with the pressure ratio; the volume flow is then

determined. For pumps or compressors, the volume flow is the inlet flow and the state conditions are usually known. While for turbines the volume flow is the exit one. Now, since it was assumed that a certain minimum efficiency was desired it is possible to determine, on the Ns – Ds diagram, the lowest value of Ns that provides this efficiency. Substituting this value into the Ns equation, the required revolving speed is found out. For most applications, the rotational speed will already be determined by such considerations as stress levels, maximum bearing or gear speeds. When the shaft speed is known, the Ns can be calculated and the potential performance determined. This procedure is much simpler than evaluating the entire detailed equations that govern turbomachinery performances. The Ds value from the Ns – Ds diagram will allow the determination of the machine rotor diameter which of course is indicative of the size of the unit [37].

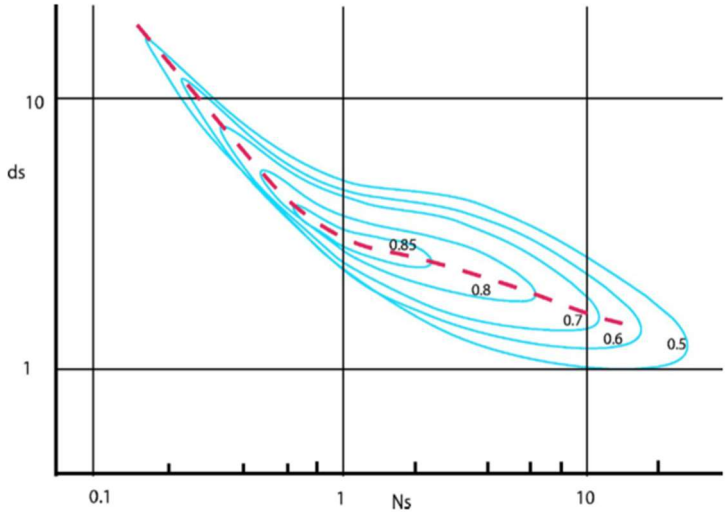


***Figure 3.5: Ns-Ds diagram in International System of Units*** [40]

In our code, we have developed the digitizing graph data through Scanit, a program for extracting data from scientific graphs, particularly from line and scatter plots [41], and MatLab, that provides the possibility to interpolate with bi-harmonic spline interpolation.

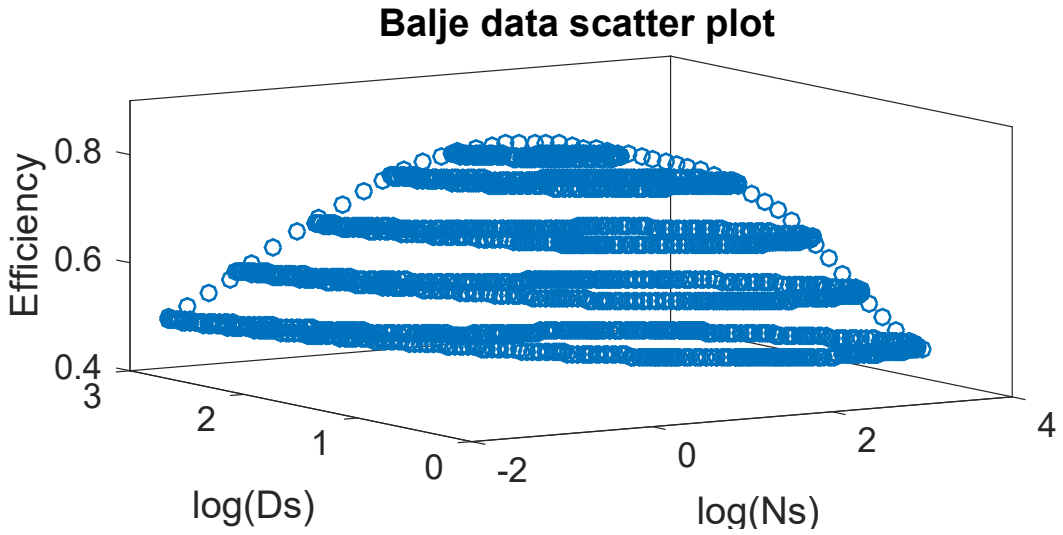


*Figure 3.6: Scatter plot of Balje map data extracted through Scanit*

In Figure 3.6 it is presented the scatter plot of the acquired data through Scanit, while Figure 3.7 is the interpolation on the Ns-Ds view and Figure 3.8 shows the interpolation on the three dimensions, where the axes are logarithmic.

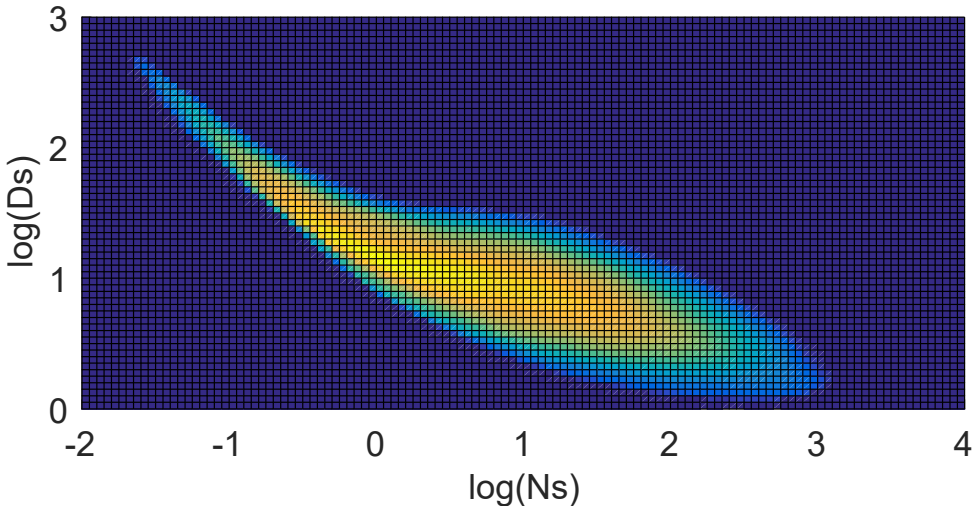


*Figure 3.7: Digitized Balje map, Ns-Ds view*

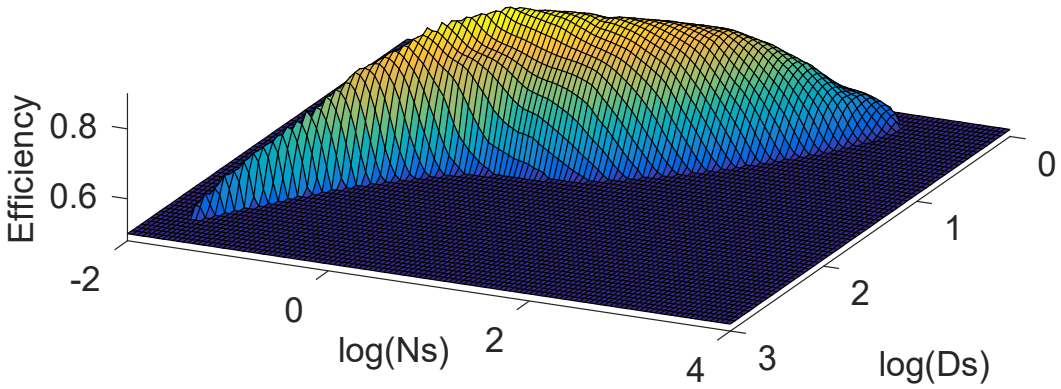


***Figure 3.8: Digitized Balje map***

Moreover, it has been derived the Cordier function, that relates the maximum stage efficiency to the Ns (Figure 3.9) and, it has been also derived, a function to link the specific diameter Ds to Ns on the maximum efficiency line, Figure 3.10.

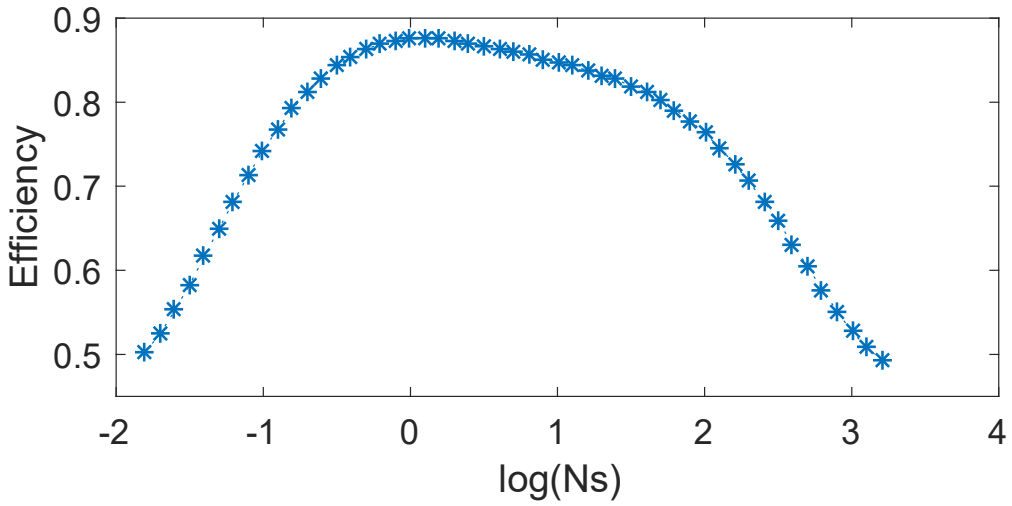


***Figure 3.9: Efficiency on the Cordier maximum line with respect to the Ns***

$$\eta_{Cordier} = 0.0019 * (\ln(N_s))^6 - 0.0088 * (\ln(N_s))^5 - 0.0041 * (\ln(N_s))^4 + 0.0496 * (\ln(N_s))^3 - 0.0778 * (\ln(N_s))^2 + 0.0116 * \ln(N_s) + 0.8751 \quad (3.7)$$

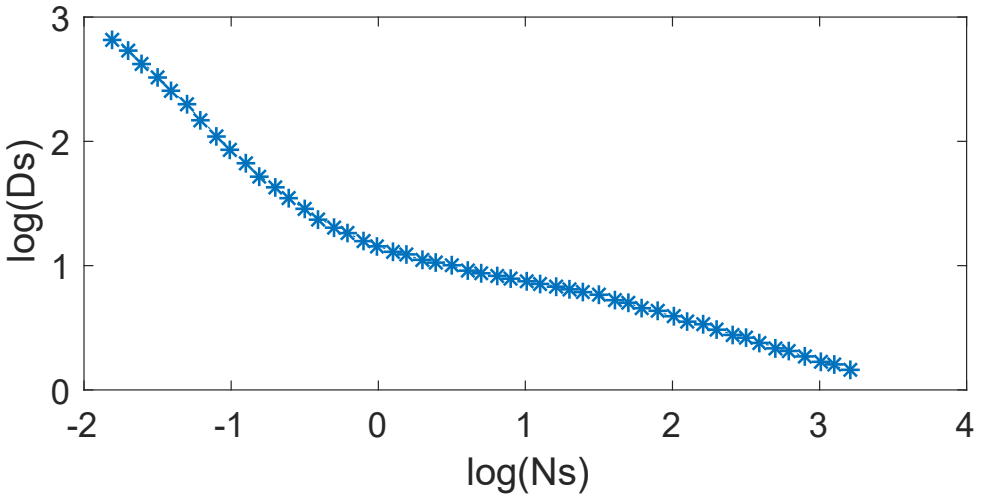


***Figure 3.10: Specific diameter on the Cordier function related to specific speed Ns***

$$ln(Ds) = -0.0028 * (\ln(N_s))^6 + 0.0192 * (\ln(N_s))^5 - 0.0204 * (\ln(N_s))^4 - 0.1135 \ldots * (\ln(N_s))^3 + 0.2752 * (\ln(N_s))^2 - 0.4316 * \ln(N_s) + 1.1566 \quad (3.8)$$

### 3.2.2. Algorithm

Two methods were developed to evaluate the compressors performance. Both of them based on the middle stage optimization:

- The first method has been defined keeping constant the mean diameter of each compressors, we called it 'fixed diameter method'.
- On the other hand, the second one aims to define the optimal single stage efficiency, imposing the appropriate value of each single stage diameter to have the maximum possible efficiency for each stage, we called it 'variable diameter method'.

**Fixed diameter method**

Analysing the first method, the preliminary step of the proposed algorithm is to choose the maximum efficiency condition for the mid-point compression stage for each compressor. This means to start identifying on the Ns-Ds chart the maximum efficiency,

obtaining the Ns and Ds values associated to the best efficiency condition. At this point we can evaluate the optimal revolving speed N (3.9) and the optimal size D (3.10) for the mid-point stage. Now the calculated mid-point optimal N and D are fixed as the optimal speed and size for each compressor's unit.

$$N = \frac{N_s * \Delta h^{3/4}}{\sqrt{\dot{V}}} \tag{3.9}$$

$$D = \frac{D_s * \sqrt{\dot{V}}}{\Delta h^{1/4}} \tag{3.10}$$

Once the optimal values are fixed for the compressors unit, it is possible to calculate the specific speed Ns and the specific diameter Ds for each single stage, since all the necessary parameters are defined.

So, thanks to the MatLab interpolation function interp2, that returns interpolated values of a function of two variables at specific query points using linear interpolation, we can extrapolate each stage efficiency related to its Ns and Ds, using the digitized Balje map, Figure 3.8.

**Variable diameter method**

The variable diameter method has been developed to find a more efficient solution for the compressors design. Indeed, the algorithm has been developed using the Cordier function, that relates Ns and Ds to the maximum efficiency line. In this way, the single stage efficiency can be the optimal one for each of them.

As in the previous method, the first step is to define the maximum efficiency point coordinates, Ns and Ds, on the Balje map. Then we have to define the middle stage for each compressor and proceed calculating its optimal speed. At this point, the optimal speed for the middle stage is imposed to be the optimal speed for the whole compressor machine. Now, we can calculate the specific speed Ns for each stage, through the optimal speed just imposed. With the previous defined function of the efficiency and

specific diameter related to the specific revolving speed, it is possible to calculate the right size of each stage that allows to reach the maximum efficiency for each of them.

In the following chart (Figure 3.11), we can see in blue the fixed diameter method points for each stage example, and in red the variable diameter ones.

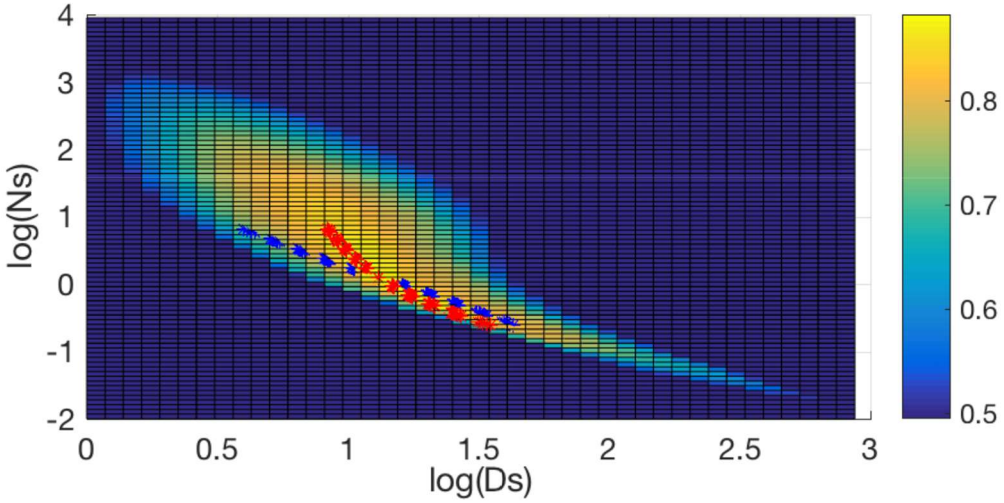


***Figure 3.11: Results stage by stage for fixed diameter method (blue) and variable diameter method (red)***

To verify the validity of the introduced methods, we have developed a sensitivity analysis on a single axial compressor.

As a reference, the axial-flow compressor in most advanced gas turbines is a multistage compressor consisting of 17 to 22 stages with an exceedingly high-pressure ratio. It is not uncommon to have pressure ratios in industrial gas turbines in the 17 to 20:1 range, with some units having pressure ratios in the 30:1 range [42], see Table 3-1 and Figure 3.12.

***Table 3-1: Typical values for axial compressors***

| Type of Application | Type of Flow | Inlet Relative Velocity Mach Number | Pressure Ratio per Stage | Efficiency per Stage |
|---|---|---|---|---|
| Industrial | Subsonic | 0.4–0.8 | 1.05–1.2 | 88–92% |
| Aerospace | Transonic | 0.7–1.1 | 1.15–1.6 | 80–85% |
| Research | Supersonic | 1.05–2.5 | 1.8–2.2 | 75–85% |

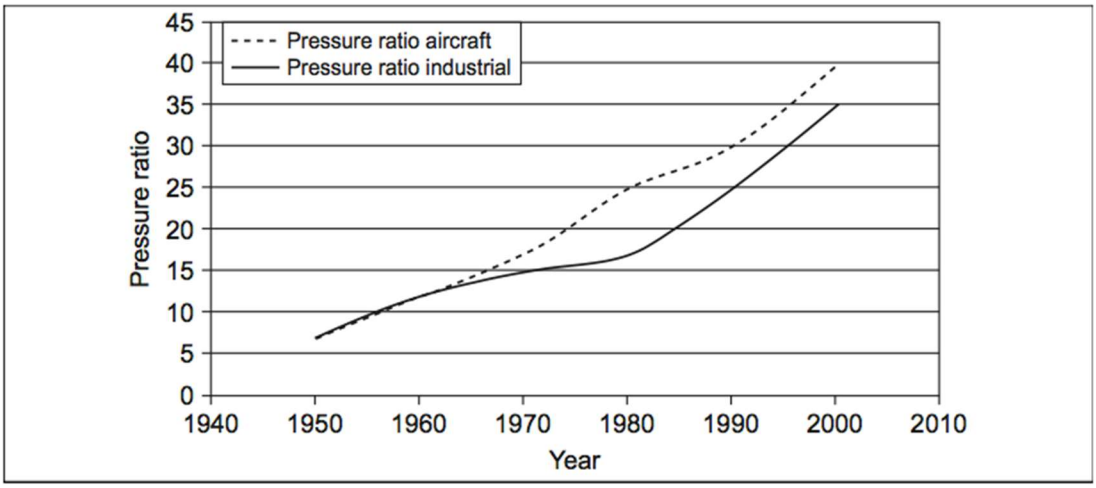


***Figure 3.12: Pressure ratio development***

Following these reference data, we have tried our code on the single axial compressor, optimizing it with both introduced methods, and comparing the outcomes with the literature ranges.

It has already been explained that the optimized stage is the middle one, so this choice can be validated through the following diagrams, obtained for an axial compressor with a compressor ratio of 12. The red line is representative of the variable diameter method, while the blue one of the fixed diameter method. The yellow spot is representative of the compressor's efficiency reached by the middle stage optimization.

The first diagram (Figure 3.13) confirms how the rotational speed chosen as the fixed rotational speed to the whole compressor is, actually, the one that can guarantee the maximum adiabatic efficiency to the compressor. This is true for both the methods. It is shown on the following efficiency vs revolving speed diagram, where the revolving speed is expressed in round per minute [rpm].

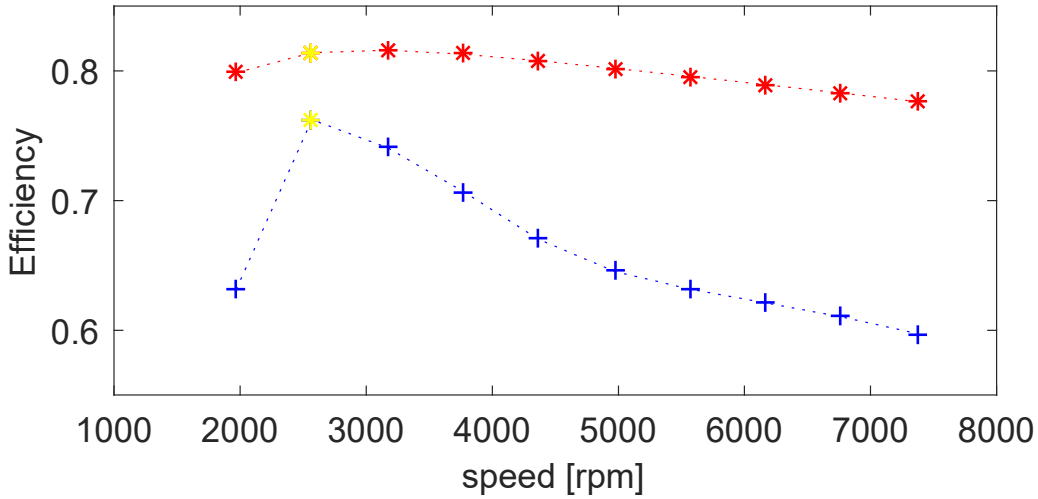


*Figure 3.13: efficiency versus revolving speed in case of axial compressor with $\beta = 12$*

The following diagram (Figure 3.14) represents the efficiency for each stage, and it can confirm that going away from the middle stage the efficiency tends to decrease, consistently with the algorithms described.

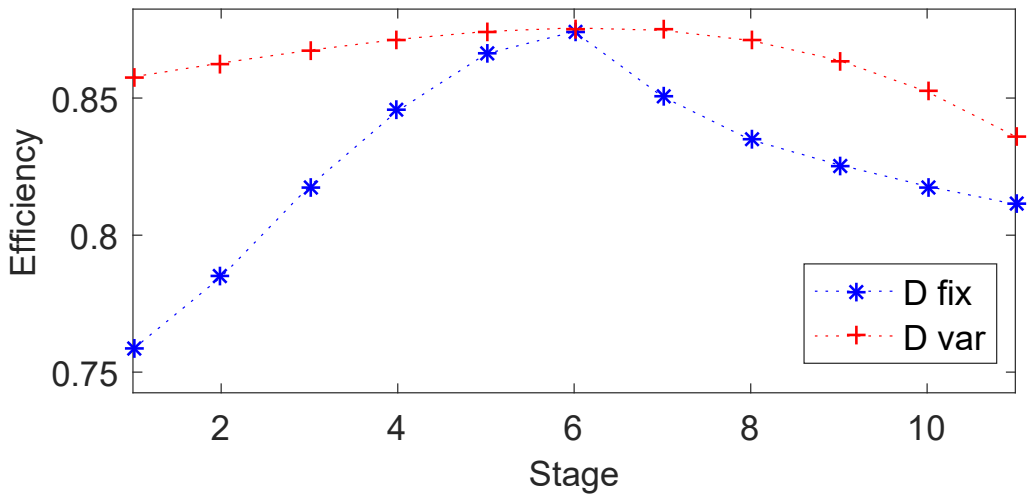


*Figure 3.14: single stage efficiency with the middle stage optimization, $\beta = 12$*

At the end, we can also see how the adiabatic efficiency is related to the compressor's number of stages, and thus to the total compression ratio: the former is clearly decreasing with the number of stages needed to cover the compression ratio (Figure 3.15). In the diagram, we have total adiabatic efficiency versus compression

ratio. It can be noted as, correctly, the previous maximum efficiency corresponds to the value of 12 on the abscissa, compression ratio.

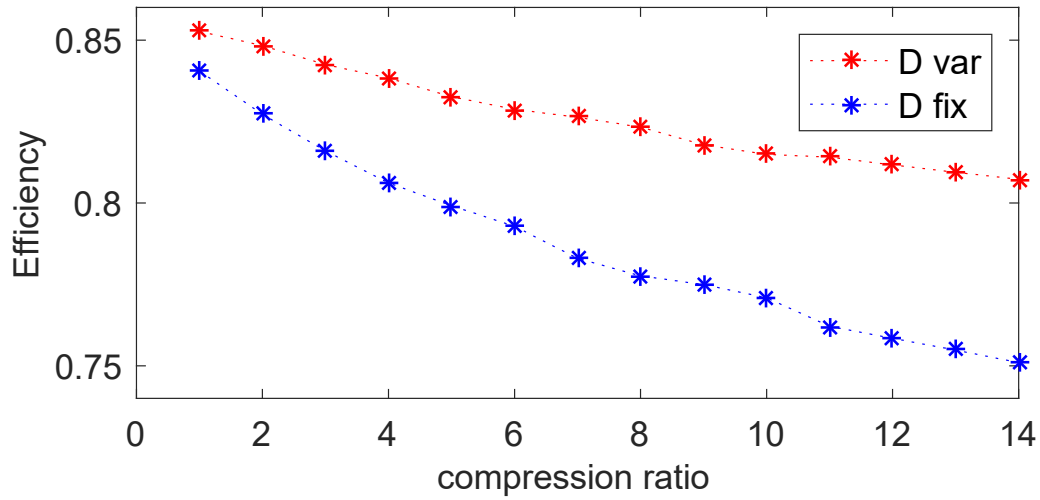


***Figure 3.15: adiabatic compressor efficiency by varying the compression ratio***

The middle stage optimization validity has been confirmed, and the variable diameter method can always ensure higher efficiency values, but in the case shown, with a compression ratio of 12 the adiabatic efficiency is only 82% in the best case. This value seems to be lower compared to nowadays compressor's efficiency and the problem could be that the Balje map employed is quite old and it has never been updated in terms of efficiency values.

Indeed, through the function of the compressor's adiabatic efficiency with respect to the polytropic one, we can see the expected value taking the polytropic efficiency to 0.9, and $\gamma$ =1.4 for air; $\eta_{ad}$ results equal to 0.86, considering the following relation (3.11):

$$\eta_{ad} = \frac{T_0 * \left(\beta^{\frac{\gamma-1}{\gamma}} - 1\right)}{T_0 * \left(\beta^{\frac{\gamma-1}{\gamma * \eta_{pol}}} - 1\right)} \qquad (3.11)$$

Considering the corrected efficiency data on the Balje map, with efficiency values multiplied by 1.05, 5 % more, the result is the expected one, with an efficiency of 0.86 for the axial compressor with $\beta = 12$, as it is shown in the following charts.

First of all the shape of the Balje interpolation is, correctly, the same, just with higher value of efficiency (Figure 3.16).

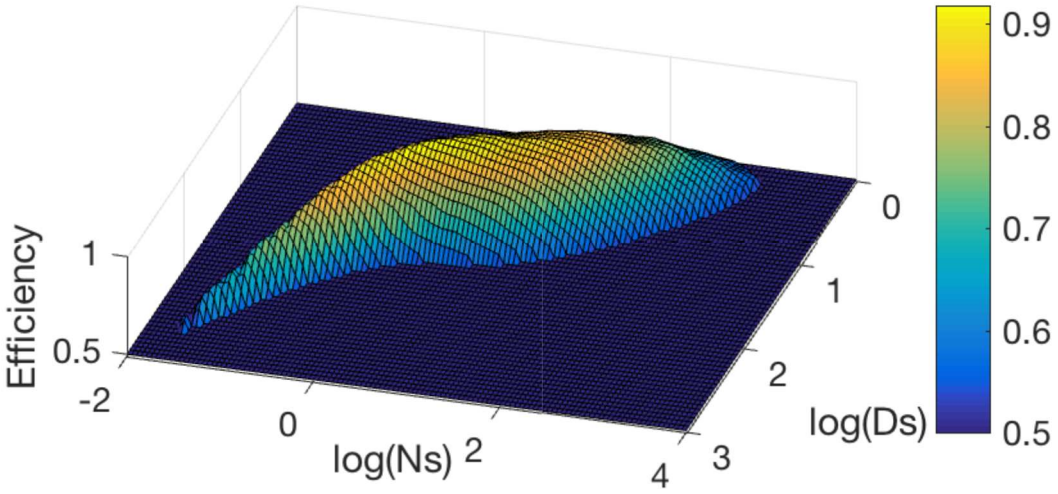


***Figure 3.16: Corrected data, digitize Balje map***

With respect to the previous corresponding chart (Figure 3.13), the efficiencies are higher to both the fixed and variable diameter method, with the expected value of 0.86 for the variable diameter method, the red one (Figure 3.17).

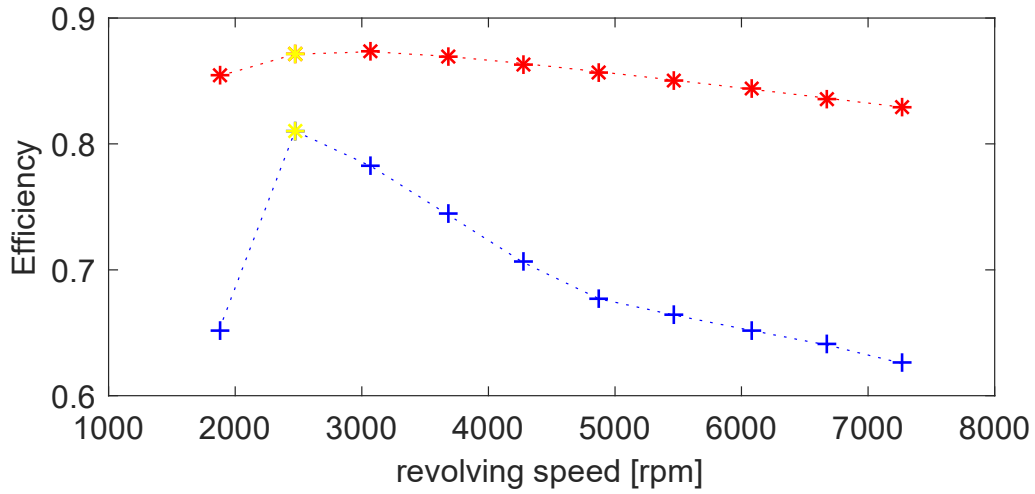


***Figure 3.17: Corrected Balje data, efficiency vs revolving speed in case of axial compressor, β = 12***

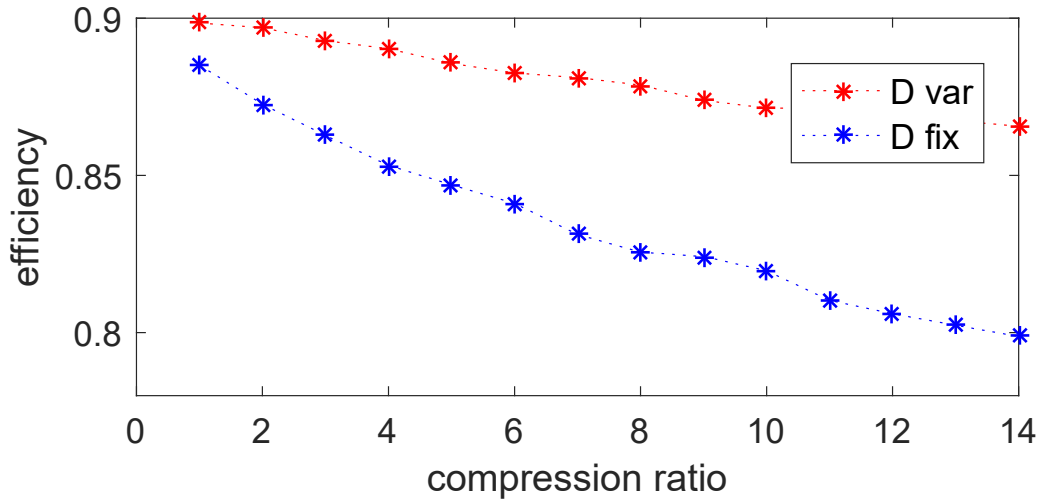


***Figure 3.18: Corrected Balje data, adiabatic compressor efficiency by varying the compression ratio***

As we can see from the Figure 3.18, while in the previous corresponding chart Figure 3.15, the efficiency trend, covered values in the range 0.75-0.85, now this range is changed into 0.8-0.9.

So, it could be possible to use the corrected data to have higher and more realistic values of compressor's efficiency, but the following analysis, that we are going to introduce, will keep the real Balje value, in order to provide more reliable results.

### 3.2.3. Optimized rotational speed

Even though the method has been validated for one compressor, to fit the considered system we have to take in consideration at least two axial compressors, and an additional centrifugal one in most of the cases.

Several kinds of configuration have been analysed with both the middle stage optimization methods:

1. One single shaft for the whole compression unit, but this case study will bring to too low efficiency due to the relevant changes in Ns along the compression stages. The results for this case will not be reported.

2. One single shaft for the two axial compressors and one other to the centrifugal one, that requires higher revolving speed. This configuration will be called 'Single shaft configuration'.

3. One single shaft for each compressor, in this way each compressor will be designed with its optimal speed. This configuration will be called 'Multiple shaft configuration'.

**Single Shaft Configuration**

The first idea to develop this configuration was to keep as optimal speed to the axial compressors shaft, the mean between the optimal speeds of the two compressors, with unsatisfactory results. As we can see, the efficiency that we are selecting as the best one is not really the maximum one, this method does not work (Figure 3.19).

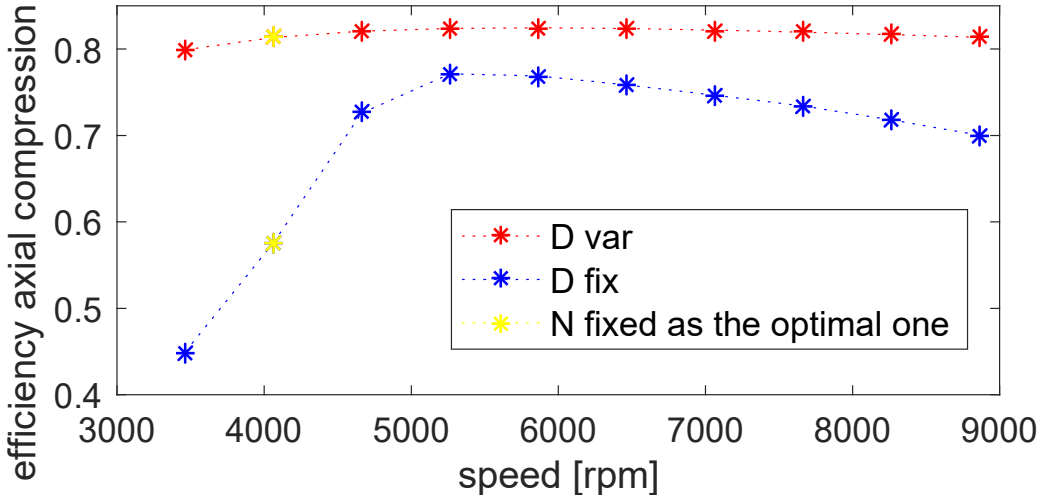


***Figure 3.19: mean optimal speed method with the single axial shaft***

At this point we decided to choose the optimal shaft speed as the optimal speed of the middle stage of the both axial compressors combination. In this example, we have a first compressor with 5 stages followed by an intercooler and 9 stages of the second compressors, so, the middle stage of the whole axial compressor will be the $7^{th}$, that is

physically, the second stage of the second axial machine. This method works only for the fixed diameter method, as shown in the figure below (Figure 3.20).

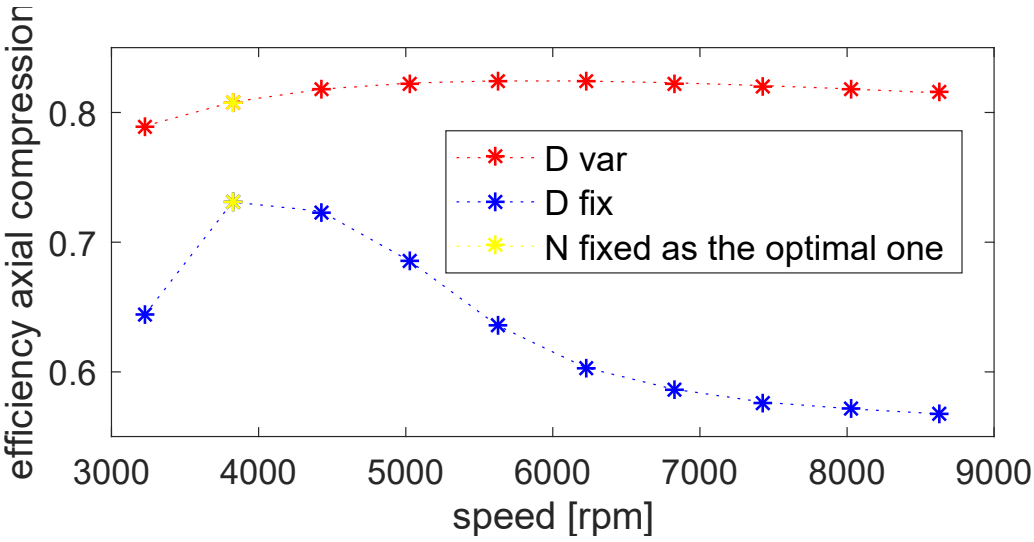


***Figure 3.20: middle axial compression stage method, one axial shaft***

After a sensitivity analysis we have found that, for the variable diameter method the stage that really optimizes the axial compression phase is not the middle one but the one at 70% of the compression already done. In this case of a totality of 14 stages it will be the 10$^{th}$ (Figure 3.21).

This solution, a single axial shaft with the variable diameter method and the 70% compression stage optimized, can guarantee good results in term of efficiency, comparable with the multiple shaft solution. This is a good point to underline, because this kind of solution gives the possibility to choose between the two configurations, taking into account just the economic aspects and the electrical and mechanical losses related to them.

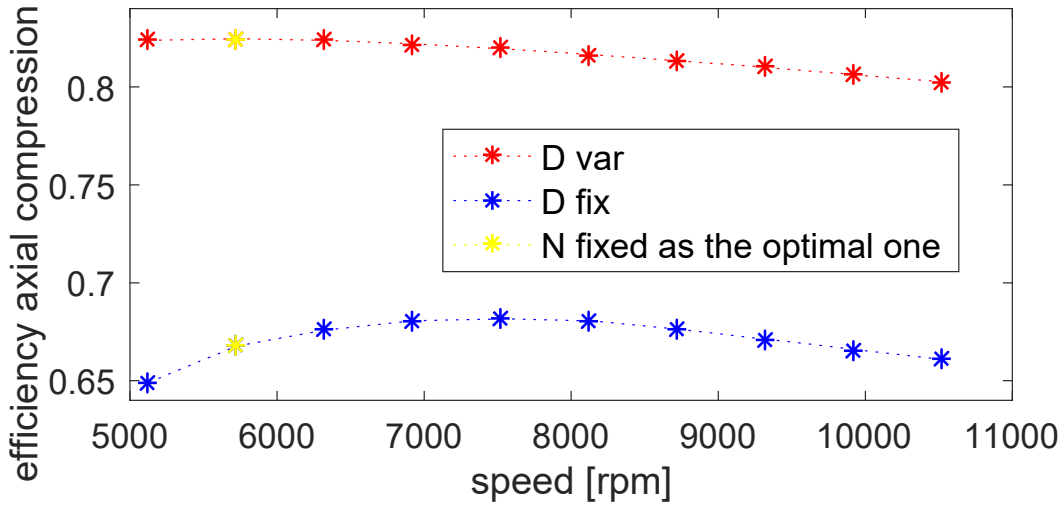


*Figure 3.21: stage at 70% of the axial compression, one axial shaft*

**Multiple Shaft Configuration**

The multiple shaft configuration has been already verified by the first analysis on the single compressor. Indeed, we are selecting the optimal speed for each compressor as the revolving speed of the middle stage for each machine. The following graph confirms again the validity of the middle stage method. It can be observed that the efficiency is the maximum one for both the axial compressors, and it will be the same for the centrifugal optimized compressor.

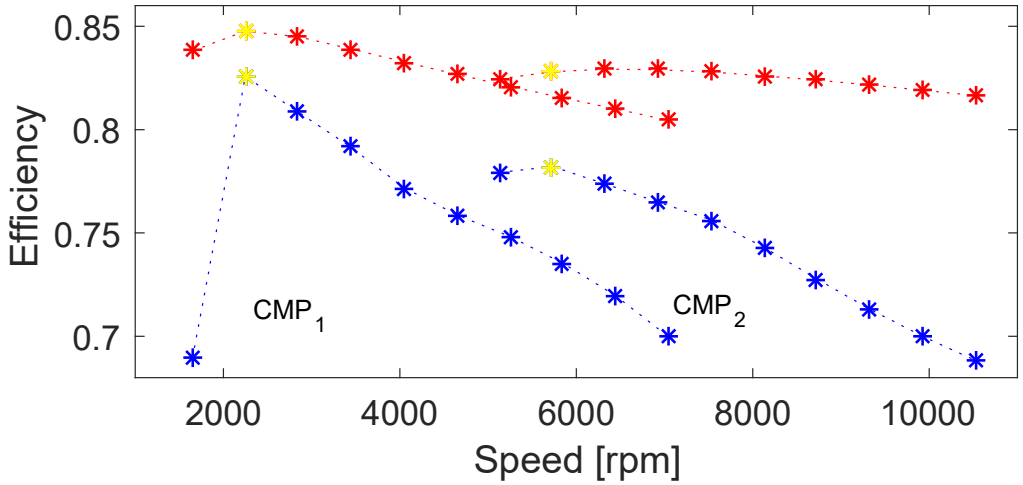


*Figure 3.22: : multiple shaft configuration, middle stage optimization method for the two axial compressors*

The "Multiple shaft configuration" can guarantee higher efficiencies and comparable losses with respect to the "Single Shaft Configuration". The choice to keep the Multiple shaft configuration is related to the wider developed system and to the possibility to maximize the compressors efficiencies in any conditions.

The Multiple shaft configuration could be made by either a motor to each shaft or a single motor with gear boxes to allow different revolving speeds to each compressor. Considering the possible future developments of this thesis, the configuration with one motor to each shaft can allow to wider the off-design application giving the possibility to work with variable revolving speed. So, the chosen configuration for our system is the multiple shaft one. Some global results in terms of adiabatic efficiencies are summarised in Table 3-2.

***Table 3-2: Adiabatic efficiencies for an a***pplication ***with storage pressure of 100 bar and nominal power of 80MW***

| | | First Axial CMP | Second Axial CMP | Axial compression with single shaft | Centrifugal CMP |
|---|---|---|---|---|---|
| Single shaft, D fixed, Middle stage optimization criteria | Standard Balje | 63.3% | 77.2% | 72.5% | 87.4% |
| | Corrected Balje | 67.3% | 82.5% | 77.27% | 91.6% |
| Single shaft, D variable, 70% compression stage optimization criteria | Standard Balje | 81.7% | 82.8% | 82.5% | 87.6 |
| | Corrected Balje | 86.4% | 88.4% | 87.8% | 91.8% |
| Multiple shaft, D fixed | Standard Balje | 82.5% | 78.8% | ~ | 87.4% |
| | Corrected Balje | 87.2% | 83.4% | ~ | 91.7% |
| Multiple shaft, D variable | Standard Balje | 84.7% | 82.8% | ~ | 87.6% |
| | Corrected Balje | 89.6% | 88.4% | ~ | 91.9% |

## 3.3. ULTIMATE OPTIMIZATION CRITERIA WITH APPLYING EXAMPLE

Now that all the configuration has been introduced, we can underline how, in all the studied cases, the variable diameter method can ensure higher values of adiabatic efficiency. So, the logical choose falls on the variable diameter criteria.

In order to understand better what happens in the design evaluation with the variable diameter criteria, together with the multiple shaft configuration, some relevant results can be introduced.

The example case study parameters are:

1. The pressure at the underwater tank equal to 100 bar;
2. The resulting configuration from the preliminary analysis provides for two axial compressors followed by the centrifugal one, with the compression ratio, respectively, of $\beta_1 = 3.1468$, $\beta_2 = 9.1436$, $\beta_3 = 3.5$;
3. The resulting single stage compression ratio for each compressor, respectively equal to $\beta_1^{ss} = 1.258$, $\beta_2^{ss} = 1.279$, $\beta_3^{ss} = 3.5$;
4. The resulting number of stage for each unit: $N_{stage,1} = 5$, $N_{stage,2} = 9$, $N_{stage,3} = 1$.

The main results, for variable diameter criteria with multiple shaft configuration, are summarised in the following Table 3-3 and Table 3-4.

***Table 3-3: Main results using the variable diameter criteria with the multiple shaft configuration with the standard Balje data***

| Standard Balje data | Adiabatic Efficiency | Revolving Speed [rpm] |
|---|---|---|
| Compressor 1 | 84,8 % | 2244 |
| Compressor 2 | 82,8 % | 5718 |
| Compressor 3 | 87,6 % | 44301 |

***Table 3-4: Main results using the variable diameter criteria with the multiple shaft configuration with the adjusted Balje data***

| Adjusted Balje data | Adiabatic Efficiency | Revolving Speed [rpm] |
|---|---|---|
| Compressor 1 | 89,6 % | 2160 |
| Compressor 2 | 88,4 % | 5493 |
| Compressor 3 | 91,4 % | 42415 |

From the previous tables it can be evident, how the adjusted value of the Balje data lead to higher adiabatic efficiency, while the required revolving speeds remains roughly the same. The following results, related to the machine's geometry, are the ones related to the standard Balje data, more restrictive and respectful of the reference values.

$$\dot{m} = \rho \cdot Va \cdot \pi \cdot Dm \cdot h \tag{3.12}$$

$$h = \frac{\dot{m}}{\rho \cdot Va \cdot \pi \cdot Dm} \tag{3.13}$$

$$u = \omega \cdot \frac{Dm}{2} \tag{3.14}$$

$$V_a = u \cdot \tan \alpha \tag{3.15}$$

To evaluate the geometry of the machine we have considered the optimized velocity triangle of an ideal reaction stage, with $\chi = 0.5 \; and \; \alpha_1 = 12$ °.

The diameter trend is directly derived by the specific diameter relation; the height of the blade by the fundamental equation of the mass conservation (3.12), from which we get the (3.13), where Va is the axial velocity component derived from the trigonometry equations (3.14) and (3.15).

Figure 3.23 represents the diameter decreasing trend in a range of value from 2.5 to 0.3 meters, with a stage by stage change in a percentage range of 1:5. The height of blade trend is decreasing too, with blade height from 20 to 5 cm as it is shown in Figure

3.24. The last one, Figure 3.25, represents the hub and tip diameter trend. All the outcomes are consistent.

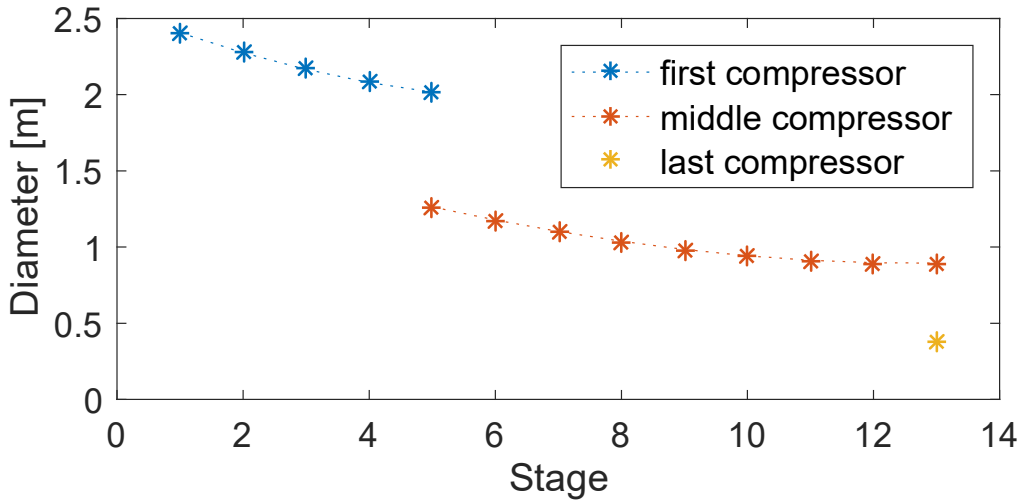


***Figure 3.23: Variable diameter trend with multiple shaft configuration, for the case study P=80 MW and Pressure at storage = 100 bar.***

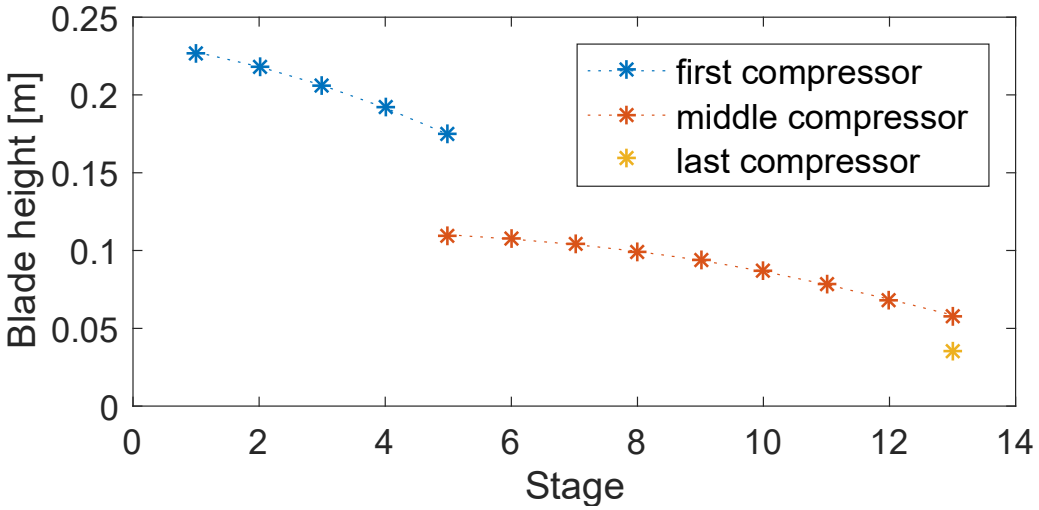


***Figure 3.24: Height of blade trend with multiple shaft configuration, for the case study P=80 MW and Pressure at storage = 100 bar.***

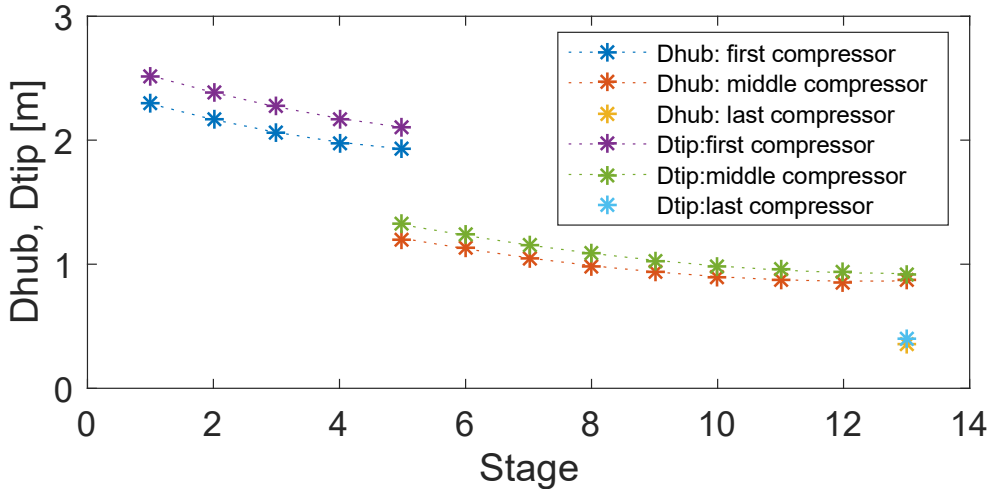


***Figure 3.25: Hub and tip diameter trend, for the case study P=80 MW and Pressure at storage = 100 bar.***

So, at the end of all these considerations, the chosen method is confirmed to be the variable diameter one, because it appears to be meaningful and it can ensure higher efficiency, so the risk to have an Outlet Compression Temperature that could overcame the maximum salt limiting temperature is better controlled.

### 3.3.1. Application to a reference CAES case

At the end, in the following Figure 3.26 we can see the overall behaviour of the system, with the nominal CAES efficiency optimized and the limiting salt temperature obeyed. It is possible to recognize in the compression phase the three units with different efficiencies and the intercooler in between, the heat exchange line in both the direction of cooling and reheating of the air flow, and the final expansion in the turbine. The current assumption is that all the air mass flow rate in input to the compression train is passing through the turbine. In a further analysis, the turbine will be dimensioned with relation to the wind farm.

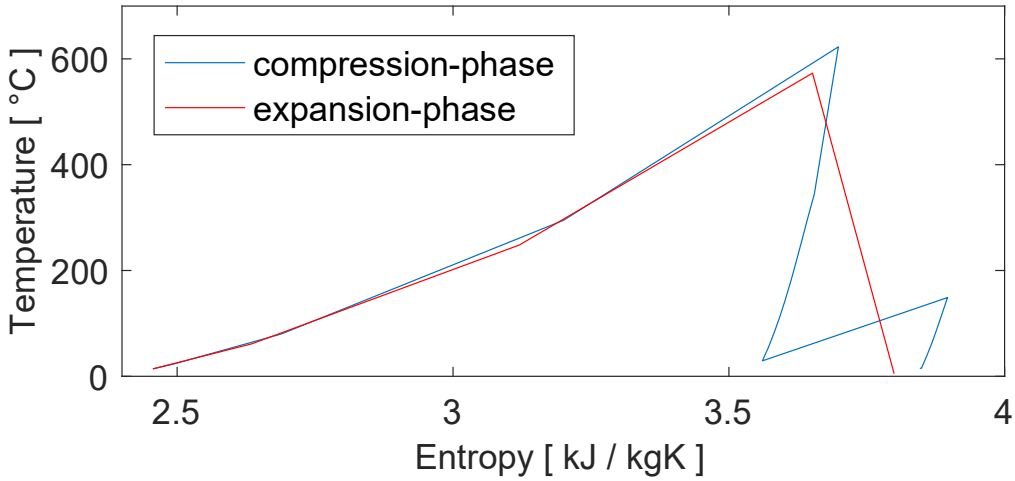


***Figure 3.26: T-s resulting diagram with "Variable diameter" criteria and "Multiple shaft Configuration", considering the case study with absorbed compression power of 80 MW and pressure at storage tank of 100 bar.***

The thermodynamic air conditions during the process are listed in Table 3-5. The case study introduced has been derived considering:

1. The nominal compression power of 80 MW.
2. The pressure at the air storage tank equal to 100 bar.
3. The Standard Balje data.
4. The "Variable Diameter" compression design criteria.
5. The "Multiple shaft" compression configuration.
6. The additional seawater heat recovery activated.
7. The discharging phase with the same air flow rate of the charging phase, the turbine size will be discussed in the 6$^{th}$ chapter.

***Table 3-5: Thermodynamic properties at the outlet of each component***

| *Air properties at the outlet of:* | | T [°C] | P [bar] | h [kJ/kg] | s [kJ/Kg K] | $\rho$ [kg/ $m^3$] |
|---|---|---|---|---|---|---|
| Environment conditions | | 15.00 | 1.01325 | 414.37 | 3.846 | 1.226 |
| Filter | | 15.0 | 1.0 | 414.38 | 3.849 | 1.213 |
| Axial Compressor | Stage 1 | 38.0 | 1.3 | 437.47 | 3.859 | 1.421 |
| | Stage 2 | 62.7 | 1.6 | 462.31 | 3.868 | 1.666 |
| | Stage 3 | 89.3 | 2.0 | 489.10 | 3.877 | 1.952 |
| | Stage 4 | 117.9 | 2.6 | 518.04 | 3.887 | 2.288 |
| | Stage 5 | 148.9 | 3.3 | 549.42 | 3.896 | 2.682 |
| Intercooler | | 29.0 | 3.2 | 427.97 | 3.561 | 3.714 |
| Axial Compressor | Stage 1 | 54.5 | 4.1 | 453.61 | 3.572 | 4.377 |
| | Stage 2 | 82.0 | 5.3 | 481.26 | 3.582 | 5.161 |
| | Stage 3 | 111.6 | 6.7 | 511.10 | 3.592 | 6.087 |
| | Stage 4 | 143.4 | 8.6 | 543.32 | 3.602 | 7.182 |
| | Stage 5 | 177.6 | 11.0 | 578.17 | 3.612 | 8.476 |
| | Stage 6 | 214.5 | 14.1 | 615.98 | 3.621 | 10.005 |
| | Stage 7 | 254.3 | 18.0 | 657.16 | 3.632 | 11.807 |
| | Stage 8 | 297.5 | 23.0 | 702.22 | 3.643 | 13.926 |
| | Stage 9 | 344.5 | 29.4 | 751.88 | 3.655 | 16.410 |
| Centrifugal Compressor | | 622.9 | 103.0 | 1060.09 | 3.699 | 38.664 |
| Salt HX | | 295.0 | 101.9 | 698.76 | 3.200 | 60.048 |
| Oil HX | | 80.0 | 100.9 | 466.29 | 2.689 | 97.711 |
| Water HX | | 24.0 | 99.9 | 402.89 | 2.496 | 118.178 |
| Under Water tank | | 14.0 | 99.9 | 391.15 | 2.456 | 123.252 |
| Water HX | | 61.5 | 98.9 | 445.90 | 2.635 | 101.793 |
| Oil HX | | 248.3 | 97.9 | 648.62 | 3.120 | 62.993 |
| Salt HX | | 573.1 | 96.9 | 1003.72 | 3.652 | 38.579 |
| Turbine | | 5.00 | 1.053 | 404.31 | 3.800 | 1.319 |

For this specific case study, the nominal CAES efficiency (3.16) results equal to 78%, and the compressor's specifications are shown in the Table 3-6.

$$\eta_{rt,standard\ Balje}^{nom} = \frac{\dot{m}\,\Delta h_T^{nom}}{\dot{m}\,\Delta h_C^{nom}} = 78.13\ \% \qquad (3.16)$$

***Table 3-6: Compressors Specifications for the introduced case study***

| *Standard Balje data* | $\eta_{CMP}$ | N [rpm] |
|---|---|---|
| First Axial Compressor | 0.8473 | 2305 |
| Second Axial Compressor | 0.8280 | 5832 |
| Centrifugal Compressor | 0.8756 | 45206 |

It could be interesting to note how, changing the Balje data with the adjusted one, that give higher and more realistic value of compressor's efficiencies (Table 3-8), the COT, obviously decreases, implying a reduction in the thermal storage and a slightly lower overall CAES efficiency (3.17). This consideration is related to the trade-off between the minimization of the compression work and the optimization of the thermal storage; however, in this case, the difference in CAES efficiency is mainly due to the lower limit on the TOT, Turbine Outlet Temperature, at the cost of a reduced expansion ratio. As already explained in chapter 2, the TOT is limited due to icing. In this specific case, the change in results at the compression and expansion outlet are shown in the Table 3-7. Nevertheless, it is relevant to underline how the whole CAES system will work coupled to the wind field, and often in off-design condition, so the COT will tend to increase but all the considerations on the CAES system efficiency are strongly related to the wind field production in time, and will be wider discussed in chapter 6.

***Table 3-7: Thermodynamic properties with adjusted Balje data, at the turbomachines outlet.***

| *Air properties at the outlet* | T [°C] | P [bar] | h [kJ/kg] | s [kJ/Kg K] | $\rho$ [kg/ $m^3$] |
|---|---|---|---|---|---|
| Centrifugal Compressor | 584 | 102.96 | 1016.1 | 3.6484 | 40.4 |
| Turbine | 5 | 1.3153 | 404.23 | 3.7355 | 1.64 |

$$\eta_{rt,adjusted\ Balje}^{nom} = \frac{\dot{m}\,\Delta h_T^{nom}}{\dot{m}\,\Delta h_C^{nom}} = 77.67\ \% \qquad (3.17)$$

***Table 3-8: Compressors Specifications for the introduced case study with the adjusted Balje data***

| *Adjusted Balje data* | $\eta_{CMP}$ | N [rpm] |
|---|---|---|
| First Axial Compressor | 0.8964 | 2219 |
| Second Axial Compressor | 0.8838 | 5603 |
| Centrifugal Compressor | 0.9194 | 43282 |

# 4. COMPRESSION PHASE IN OFF-DESIGN

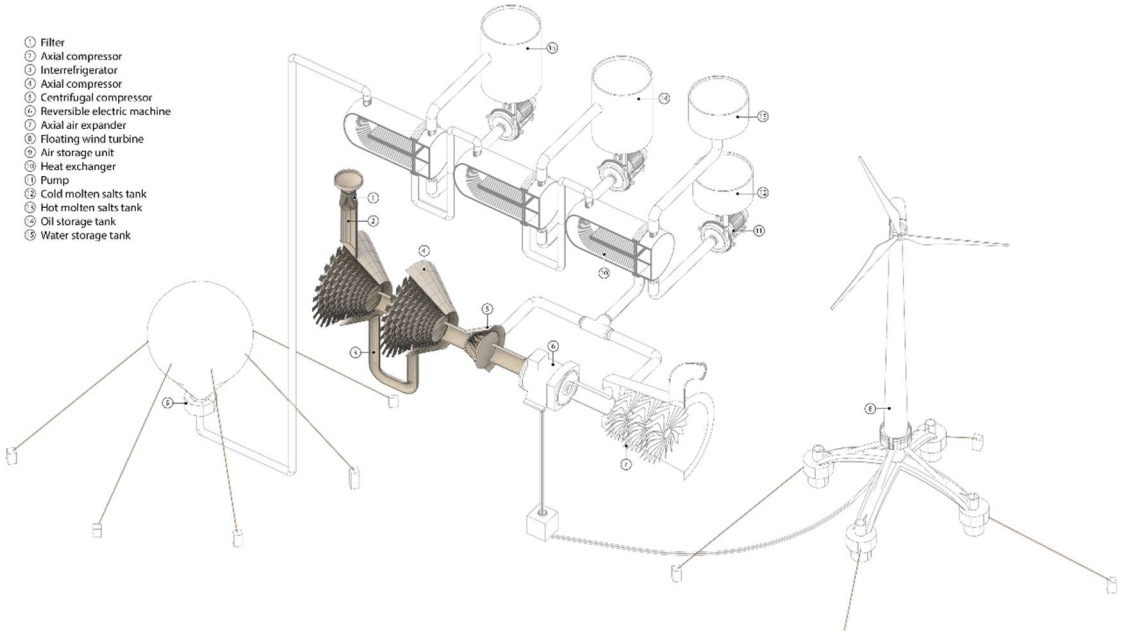


***Figure 4.1: Components of the CAES system addressed in the off-design of the compression phase***

In the present chapter the behaviour of the adiabatic CAES is studied when it is required a compression (Figure 4.1) with different conditions with respect to the ones considered in the design phase. In particular the algorithm employed is schematised, and its answer to the variation of input conditions is observed, highlighting the most significative parameters.

## 4.1. INTRODUCTION

Once established the design parameters necessary to define the working conditions of the compressor side of the CAES system, we have to consider also that most of the time it will work with values different from the ones considered until this moment. In particular, the main focus will be the possibility to modify the electric power absorbed, in order to vary the net electric output of the overall system, made up by more wind fields and the CAES itself. Furthermore, during the year both the surface

temperature of the sea and the air temperature, as shown in Figure 4.2, as well as the air pressure at sea level, represented in Figure 4.3, will change in a significative way from the design values.

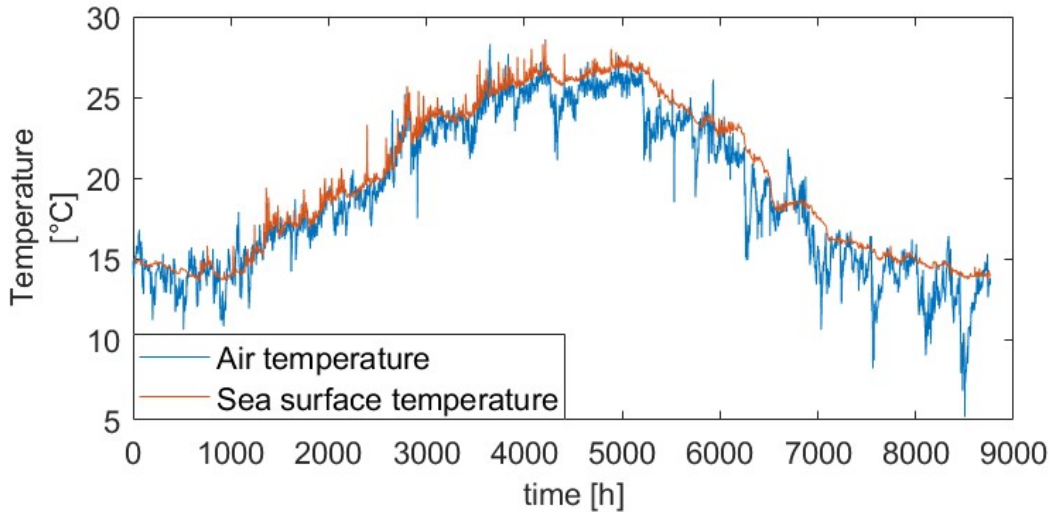


***Figure 4.2: Yearly air and sea surface temperature variation***

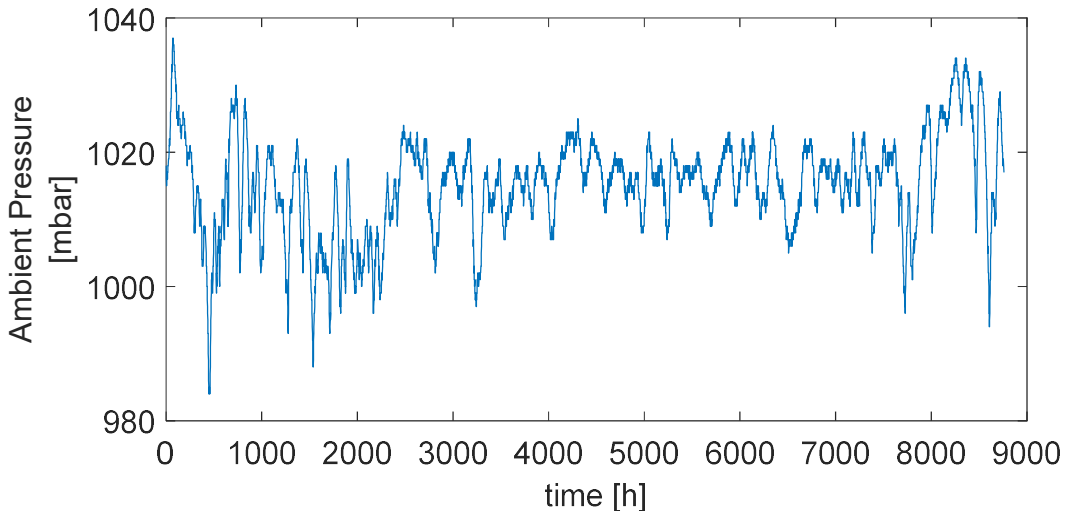


***Figure 4.3: Yearly air pressure at sea level variation***

It is now important to understand which values are fixed from the design conditions and which ones on the contrary will be different, either as input values, or as consequences of the variation of one or more parameters. As already mentioned, air temperature, air pressure, water surface temperature and power absorbed in the

compression phase are input parameters to our model, and in general can assume any feasible value. On the other hand the tank pressure is a fixed parameter, since is equal to the hydrostatic pressure of the water outside and the air storage unit is anchored at the sea ground and thus at fixed depth. Constant are also all the information about the layout such as compressors' nominal expansion ratios, the heat exchangers' surfaces, the pipes with the corresponding pressure losses as summarised from Table 4-1.

***Table 4-1: Main data used as input for the off-design***

| | | | |
|---|---|---|---|
| Nominal Power to the Compression Train | 75 MW | | |
| Pressure at the under-water storage | 80 bar | | |
| Compressor | Axial | Axial | Radial |
| Nominal compression ratio | 2.512 | 9.164 | 3.500 |
| Number of stages | 4 | 9 | 1 |
| Compressor efficiency (Balje standard) | 0.85 | 0.82 | 0.88 |
| COT standard | 617 °C | | |
| Compressor efficiency (Balje adjusted) | 0.89 | 0.88 | 0.91 |
| COT adjusted | 584 °C | | |
| Surface Heat exchanger Air-Salts | 1870 $m^2$ | | |
| Surface Heat exchanger Air-Oil | 2370 $m^2$ | | |
| Surface aftercooler Air Water | 2130 $m^2$ | | |
| Nominal air temperature | 15°C | | |
| Nominal ambient pressure | 1.01325 bar | | |
| Nominal sea surface temperature | 15 °C | | |

### 4.1.1. Degrees of Freedom and System Controllability

Now, the first thing worth noticing is that without any regulation system it is impossible to modify the electric power absorbed by the compression phase, since at fixed pressure difference and inlet conditions, both the mass flow rate and the work required are fixed, and thus their product. In order to gain a possible direction where to move it is then necessary at least one regulation method, and this can be done in two different ways:

- Applying a variable stator angle at the inlet of the first compressor, alias using Inlet Guide Vanes (IGV).

- Applying a variable rotational speed to the shaft, able to control the peripherical speed of the compressors.

However, in any of these ways we use the only degree of freedom available to follow the electric request, and consequently both temperature and compression efficiency are determined and cannot be optimised. However, how it will be explained better when dealing with the off-design of the heat exchangers, even a sensible increase in the air temperature at the compressor outlet will not result in a unacceptable consequent increase in the maximum salt temperature. This happens because the heat exchangers downstream will see lower air flow rates, and even if the inlet temperature increases, the possibility to control the molten salt flow rate avoids the reaching of the salt dissociation temperature.

Nevertheless, to enhance the controllability of the whole system, we can also think of installing variable inlet stator angles at all three the compressors, which for the centrifugal compressor means also the installation of variable angles in the diffuser (Diffuser Guide Vanes, DGV), in order to avoid an undesirable loss in efficiency. The equivalent method with the variable speed consists in using three different gear boxes or three independent shafts to control the speed of each machine. In such manner, we improve the degrees of freedom of the compression phase up to three, resulting at the price of a higher investment, in the possibility of obtaining lower charging time because of the increased mass flow rate, or higher overall efficiencies.

If we consider an analogy with a gas turbine, whose main degree of freedom consists in the regulation of the fuel flow rate while its objective is to follow a fixed peak demand, we can easily understand that the use of IGV allows higher efficiencies thanks to a variable intake of air. In the considered case, though, the possibility of variating the fuel rate is precluded, leaving the IGV as the only option to make the storage system follow the desired behaviour.

## 4.2. ALGORITHM

As previously introduced, the input data to the off-design of the compressors are the excess Power available from the wind source, the environmental conditions and the machinery designed and used, including one or more IGV components, while the outputs are the amount of air and heat that will be store, as summarised in Figure 4.4.

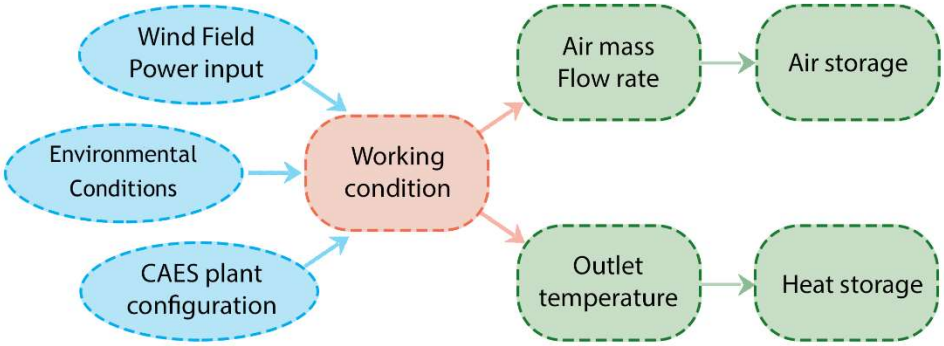


***Figure 4.4 Algorithm inputs and outputs***

On the other hand, the equations which have to be always verified are the conservation of the corrected (or volumetric) flow rate for the inlet of the axial compressors since choked conditions are usually reached. A typical working map for an axial compressor is schematised in Figure 4.5. The ellipses represented are the relative iso-efficiencies, referred to the nominal efficiency of the machine.

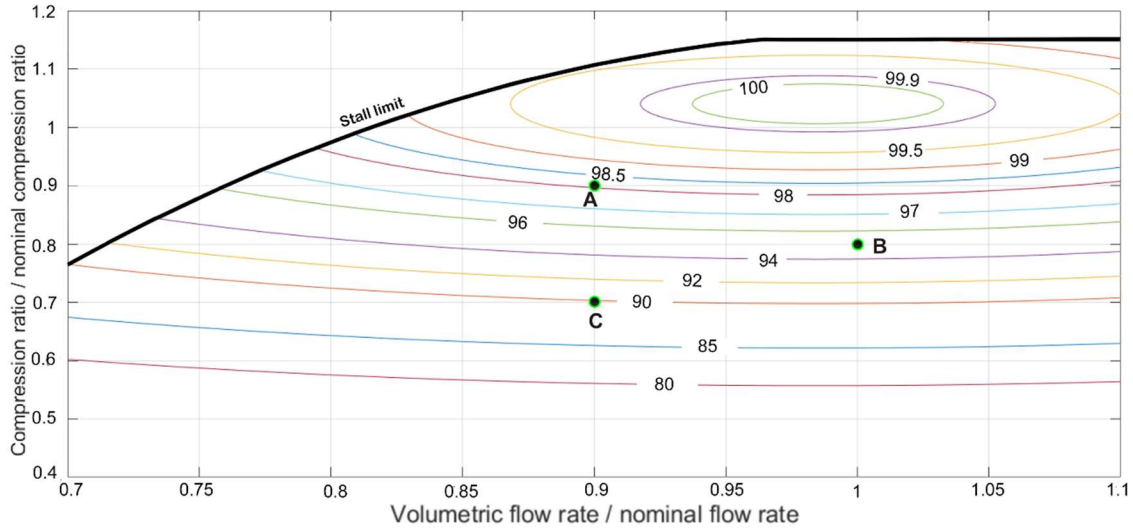


***Figure 4.5 Approximation employed in the algorithm for the axial compressors***

For the centrifugal compressor the restriction is more complicated, and regards fixed values of relative compression ratios as function of relative volumetric flow rates; in particular, without its inlet regulation system, the characteristic curve of the compressor can be considered as a parable in the compression ratio-volumetric rate diagram, as shown in Figure 4.6.

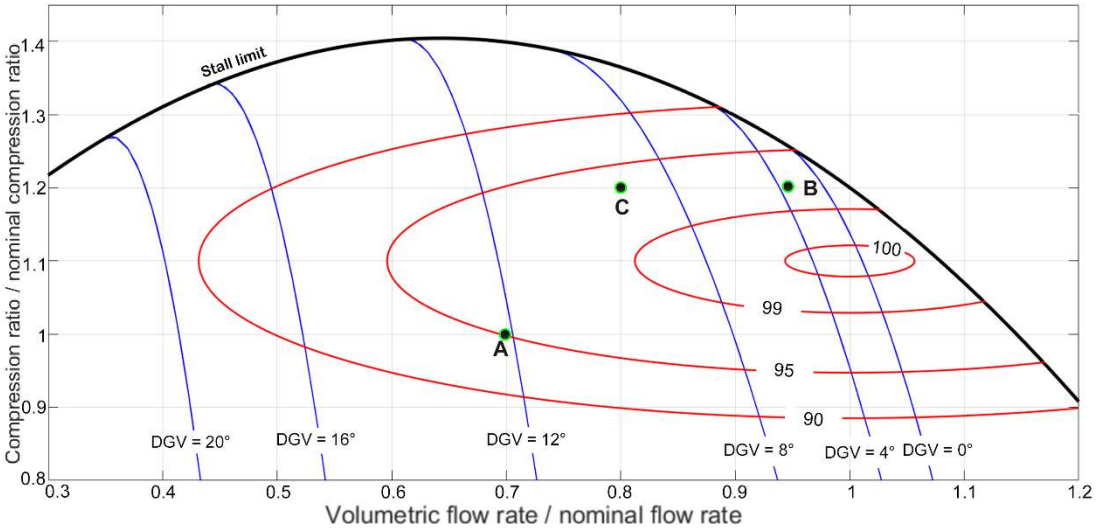


***Figure 4.6 Approximation employed in the algorithm for the centrifugal compressor***

Moreover also the efficiency curves of all compressors have to be coherent with both the relative ratios just introduced. The complexity of the problem of consuming the

exact amount of power lies behind the fact that all these equations are a function of the inlet mass flow rate in very non-linear ways, determining consequently also the variation of all the thermodynamics points of the compression.

$$\dot{m}_{corr} = \dot{m}\,\frac{\sqrt{R_g T_{in}}}{P_{in}} = const \tag{4.1}$$

Where $\dot{m}_{corr}$ is the corrected mass flow rate, $R_g$ is the gas constant, $T_{in}$ and $P_{in}$ are respectively the inlet temperature and pressure.

When evaluating the compressor performance away from the design condition, it is reasonable to suggest that machines optimised so keenly will perceive a drop in their efficiency. In order to better estimate such loss, different maps are available from literature that allow the calculation of the relative efficiency as a function of the compression ratio and volumetric flow rate, each relative to its design value. Maps from Figure 4.5 is implemented with an approximation from the information in [43] developed in a GECOS report [44], while the Figure 4.6 is implemented with an approximation from an Atlas Copco GT map [45].

To evaluate the error introduced with such approximation, in Table 4-2 and Table 4-3 three points have been chosen for each graph, and the relative error has been calculated:

***Table 4-2: Estimation of the relative error for three different points of the axial compressor map***

| *Axial compressor* | V rel | β rel | True value | Approximation | Error |
|---|---|---|---|---|---|
| Point A | 0,9 | 0,9 | 98,5% | 98,1% | **0,41%** |
| Point B | 1,05 | 0,8 | 94% | 94,9% | **0,96%** |
| Point C | 0,9 | 0,7 | 92% | 89,8% | **2,39%** |

***Table 4-3: Estimation of the relative error for three different points of the radial compressor map***

| *Radial compressor* | V rel | β rel | True value | Approximation | Error |
|---|---|---|---|---|---|
| Point A | 0,7 | 1 | 95% | 96,00% | **1,05%** |
| Point B | 0,95 | 1,2 | 99% | 98,73% | **0,27%** |
| Point C | 0,8 | 1,2 | 97% | 97,56% | **0,58%** |

The maximum error is about 2.5% and is located at the bottom left of the graphs, where both the relative compression ratio and the relative volumetric flow rate are low. However, the second and the third compressors will never work in that region, while the first one is expected to work there rarely. So, in the region where most of the time the compressors work, $\Delta\eta$ should be below 1%.

If only one IGV is used at the inlet of the first compressor, there is only one value of IGV that satisfies all the constrains, thus the algorithm reasons both as follows and as summarised from Figure 4.7:

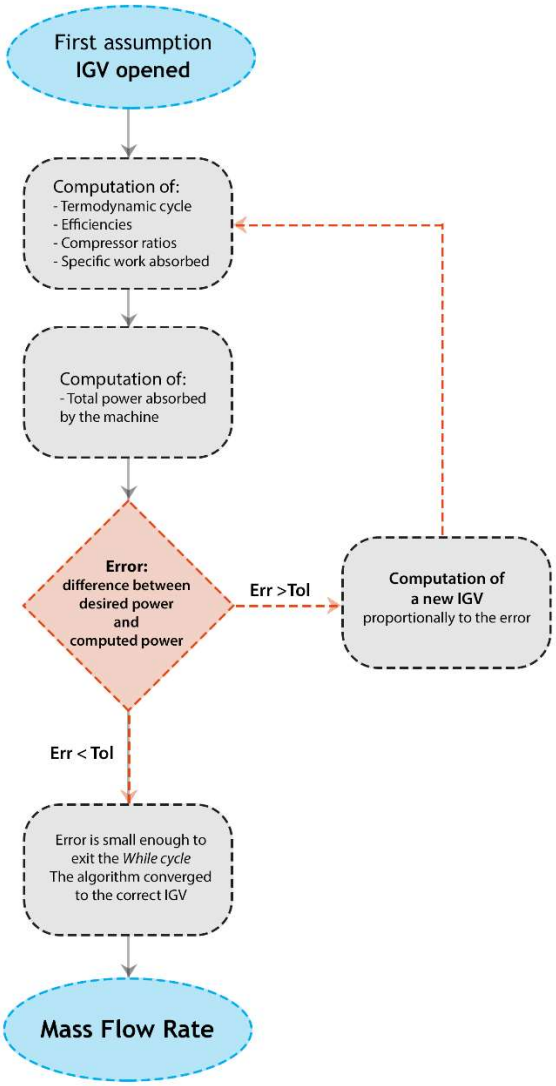


***Figure 4.7: Block scheme of the algorithm***

1. IGV opened (100%) is assumed as a first attempt value.
2. All the thermodynamic points of the compression are computed, with the relative efficiencies, compressor ratios and specific work absorbed.
3. The total power absorbed by the machine is then computed, and an error is obtained as a difference between the desired power and the computed one.
4. If the error is below the given tolerance, the algorithm has converged to the correct IGV value and the mass flow rate is obtained.
5. Otherwise a new value of IGV is then computed, differing from the previous one proportionally to the size of the error, and the cycle is repeated.

Instead, if each compressor has its own inlet module, there are more combinations of the IGV values that allow to obtain the same result, and among all of them, MATLAB's optimiser "Fmincon" chooses the one that maximises the air flow rate at the inlet. Moreover, a thermal constrain of 700°C has been set at the Compressor Outlet Temperature to limit the thermal stresses on the radial compressor, while the solar salts maximum temperature always stays below the thermal cracking point of 600°C.

However, the flexibility reached is just a partial one, since each IGV value can shift between 0.7 and 1.05, numbers representative of the ratio between the inlet section and the nominal inlet section. Moreover, for each compressor the region where it is possible to work is limited by the stall lines, producing an even more binding condition. All considered, the compressor side is able to work without any problem between 80% and 103% of the nominal power, reaching even wider values but only in particular environmental conditions.

## 4.3. OFF-DESIGN SIMULATIONS

### 4.3.1. Compression power variation

As previously introduced, the variation range of the power absorbed by the compression phase is limited in a very narrow region, independently of the number of freedom degrees. The cause is obviously due to the necessity of avoiding the stall region

in any of the compressor stages, which for the second axial compressor is a mild requirement, while both the first compressor and the last one have tighter working conditions.

To clarify graphically the directions where the stall condition limits the power variation of the system, the model is ran changing the electrical input, and for all compressors the working condition is mapped.

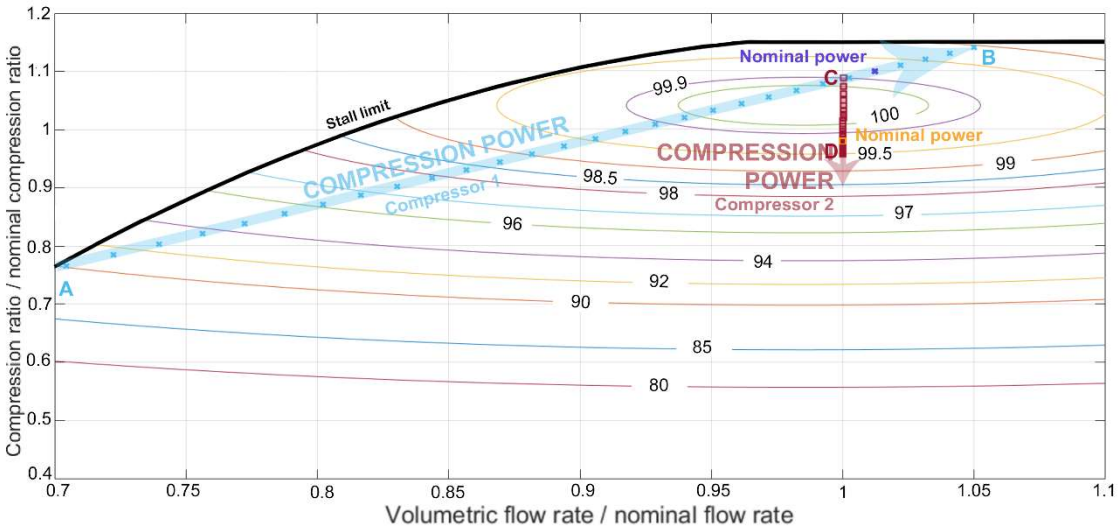


***Figure 4.8: Impact of the power increase on the relative compressor efficiency of the axial compressors.***

In Figure 4.8 the efficiency variation of both axial compressors is presented while the power input is modified along its whole range.

***Table 4-4: Main features in the extreme off-design working conditions***

| | $\frac{Compression\ Power}{Compression\ Power_{nom}}$ | $\dot{V}/\dot{V}_{nom}$ | $\beta/\beta_{nom}$ | $\eta/\eta_{nom}$ |
|---|---|---|---|---|
| Point A | 80 % | 71 % | 77 % | 90.0 % |
| Point B | 103 % | 105 % | 112 % | 99.0 % |
| Point C | 80 % | 100 % | 108 % | 99.9 % |
| Point D | 103 % | 100 % | 96 % | 99.5 % |

Table 4-4 shows the behaviour of the compressors in its extreme working points. As it can be noticed, at partial loads the compressor ratio of the second compressor reacts to the lower one imposed by the first one, increasing it as a consequence of the imposed pressure in the tank.

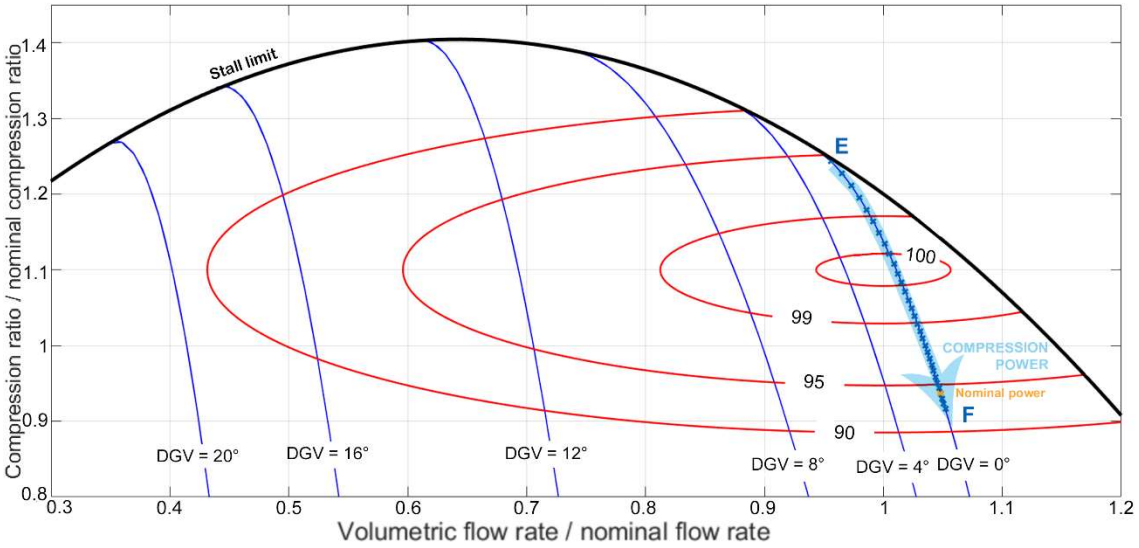


***Figure 4.9: Impact of the power increase on the relative compressor efficiency of the radial compressor.***

In Figure 4.9 the efficiency variation of the radial compressor is presented while the power input is modified along its whole range.

***Table 4-5: Main features in the extreme off-design working conditions***

| | $\frac{Compression\ Power}{Compression\ Power_{nom}}$ | $\dot{V}/\dot{V}_{nom}$ | $\beta/\beta_{nom}$ | $\eta/\eta_{nom}$ |
|---|---|---|---|---|
| Point E | 80 % | 97 % | 124 % | 96 % |
| Point F | 103 % | 106 % | 93 % | 92 % |

Table 4-5 shows the behaviour of the compressors in its extreme working points. As it can be noticed, the second compressor works with (almost) constant volumetric flow rate, very close to the corrected flow rate imposed as constant. Furthermore, its compressor ratio reacts to the lower one imposed by the first one, increasing as a consequence of the imposed pressure in the tank.

It is interesting to notice that, while the working points of the second compressor lie on a vertical line due to the fixed corrected mass flow rate, the first compressor is able to modify its working curve until the stall curve is reached. Also, the centrifugal compressor touches the limit function, even though unequipped of any regulation system, it is not able to modify its operative curve. Investigating more deeply the obtained result, the round-trip efficiency is plotted against the fraction of the nominal power absorbed, revealing an unexpected result, shown in Figure 4.10:

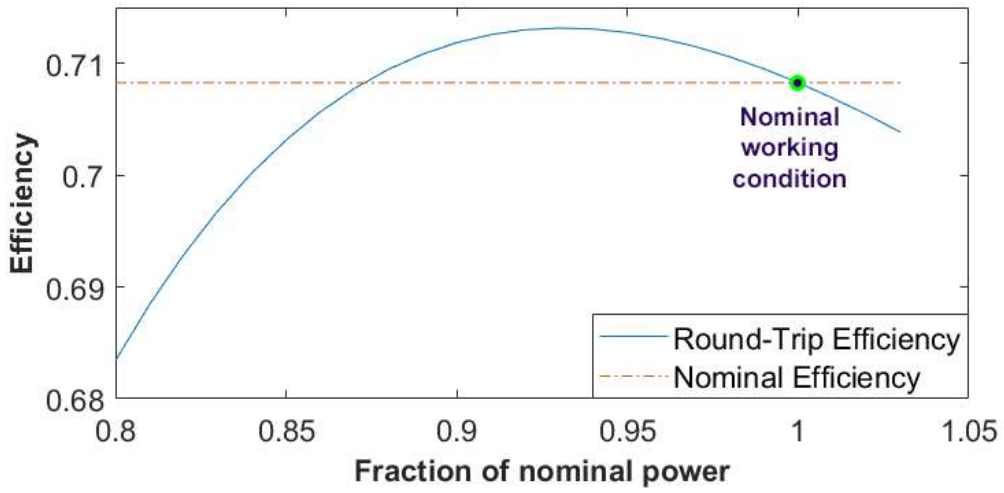


***Figure 4.10: Storage efficiency plotted together with its nominal value changing the load condition, for 80 bar, without aftercooler storage and for nominal environmental conditions***

In this context, it is useful to remind the expression of the round-trip efficiency, the reference parameter for all the storage processes, and generally defined as the maximum power (or energy) available in the discharging process over the one required to charge it.

$$\eta_{round-trip} = \frac{\dot{m}_T \, \Delta h_{exp}}{\dot{m}_C \, \Delta h_{comp}} \tag{4.2}$$

So, for a tank pressure of 80 bar, ambient temperature of 15°C, ambient pressure of 1 atm and nominal power of 75 MW, the nominal round-trip efficiency is about 70.8 %. However, most of the time such performance index is greater than the design value. If such factor can suggest an incorrect design optimisation, it is important to remember that with a one degree of freedom regulation system, the compressor outlet temperature

is impossible to control, as shown by Figure 4.11. Decreasing the inlet section such temperature rises, giving more heat to the thermal fluids, which in the heating from storage process it is returned back. As the analogy with the gas turbine model easily explains, in this way it carries up also the expansion work, as proven by Figure 4.12, and before the maximum is reached, exceeds the loss in efficiency of the compression process. On the contrary, for opening values of the inlet system that allow higher flow rates, the outlet temperature decreases and the thermal constrain is automatically satisfied.

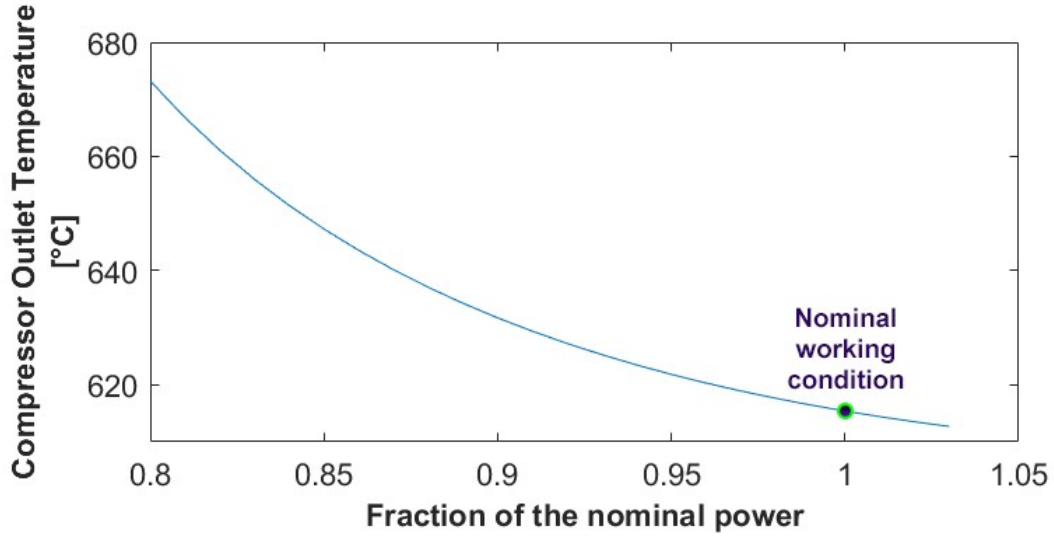


*Figure 4.11: Effect of the COT at the variation of the load condition*

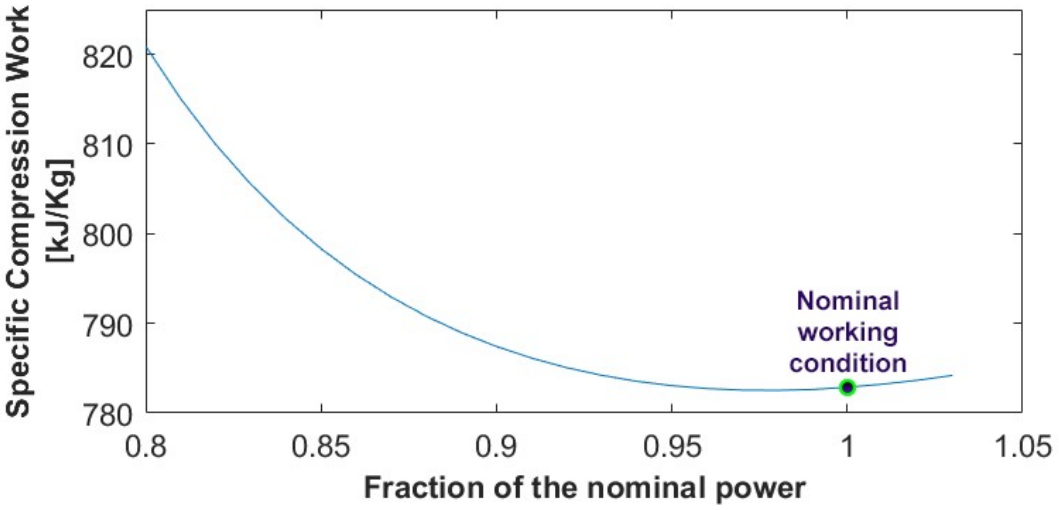


*Figure 4.12: Effect of the specific work at the variation of the load condition*

### 4.3.2. Variation of the ambient conditions ($P_{amb}$, $T_{amb}$)

The same considerations are valid for environmental conditions that differ from the nominal values. In particular, an increase in the local pressure due to meteorological events has the same effect of a decrease in the load condition, while the opposite happens for lower atmospheric pressure, as exposed in Figure 4.13. Coherently with the equation of the corrected mass flow rate, fluctuations in the ambient temperature result exactly in opposite direction with respect to the pressure, alias an increase in such variable moves towards higher flow rates, in the same way of lower pressures or higher load conditions.

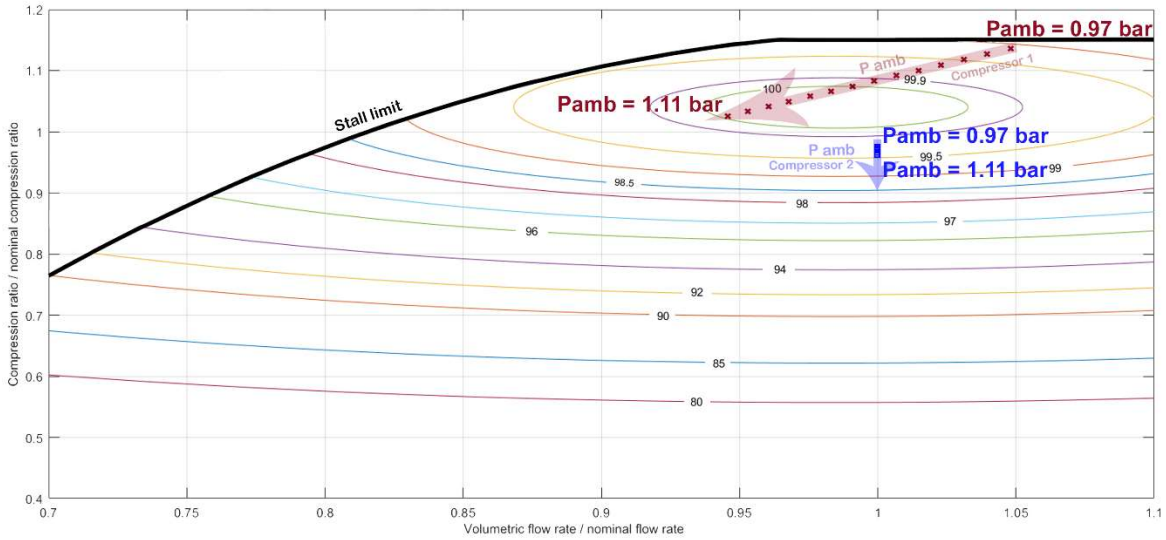


*Figure 4.13: Effect of ambient pressure variation, for the axial compressors*

The same variation is much less evident for the radial compressor, whose working values result almost unaffected by the changes in ambient conditions.

### 4.3.3. Inlet Guide Vanes for all compressors

In order to gain an increased controllability of the CAES system, all compressors are provided with an inlet variable stator angle, allowing both a better control on the thermal bound and the possibility to optimise a charging variable. Once satisfied all the constrains, the algorithm choses among infinite feasible solutions the one that maximises the mass flow rate, minimising the tank's charging time at fixed available

electrical power. Of course the price of such complication affects not only the investment cost, but also decreases the availability of the overall system, which has two more moving devices that can fail and require maintenance.

However, if the performances rise significantly by means of the improved system, the opportunity of increasing the efficiency of the process cannot be neglected. For this reason, the round-trip efficiency is plotted again, together with the previous result.

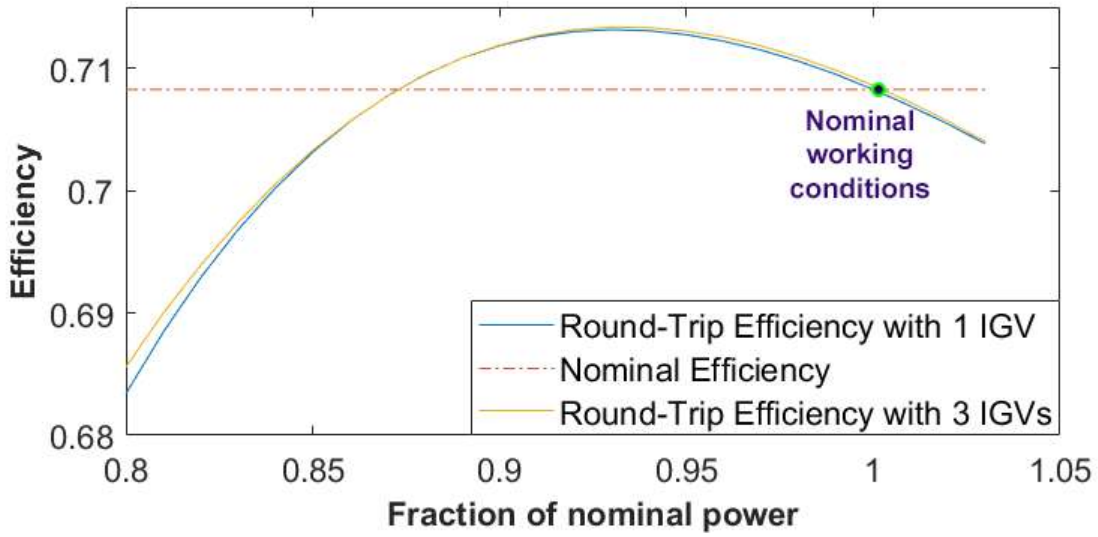


***Figure 4.14: Comparison between the efficiency with one or three controllable inlet components, for 80 bar, without aftercooler storage and for nominal environmental conditions***

As Figure 4.14 shows, even though the increase in efficiency is proven for any working power, this happens with very light improvement, reaching about 0.3 % for the minimum load condition. Accordingly, the possibility of employing more flexible systems as the one just presented, is kept only for application which will benefit more significantly from the better performances. However, it does not seem reasonable that the investment could compensate this small performance increase nor the slight increase in the mass flow rate, represented in Figure 4.15.

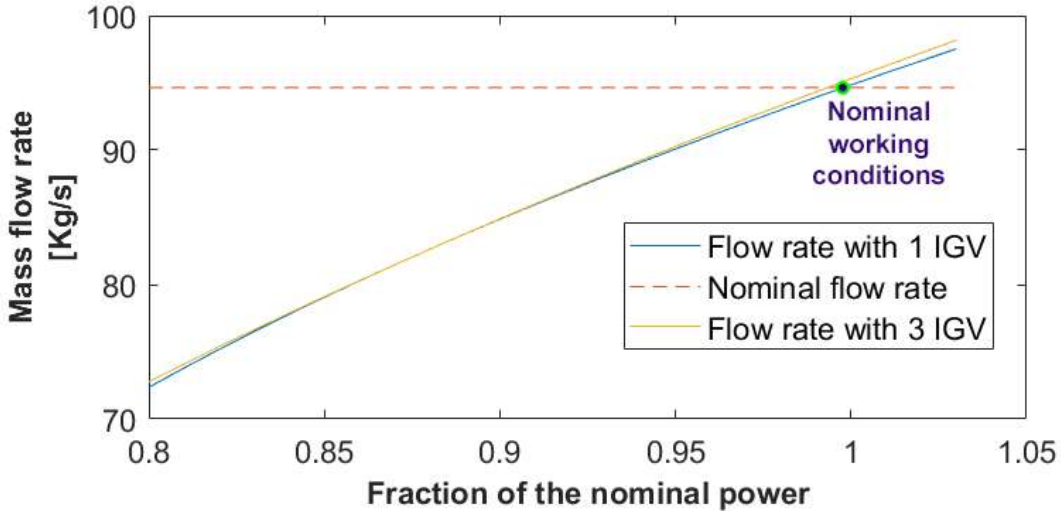


*Figure 4.15: Comparison between the mass flow rate with one or three controllable inlet components*

In the same direction, applications that allow the variation in the rotational speed of the shafts will not be considered, leaving to the following research the task of investigating them, as well as the combination with one or more IGVs.

### 4.3.4. Conclusion

The low flexibility of the CAES system does not allow a wide regulation region at partial loads, requiring a wise utilization logic behind its use. Besides using variable stator angles or rotational speed as suggested, the only alternative to increase such range implies more compression trains in parallel, each working with smaller mass flow rates and thus demanding a specific design process.

# 5. WIND TURBINE FIELD INTEGRATION

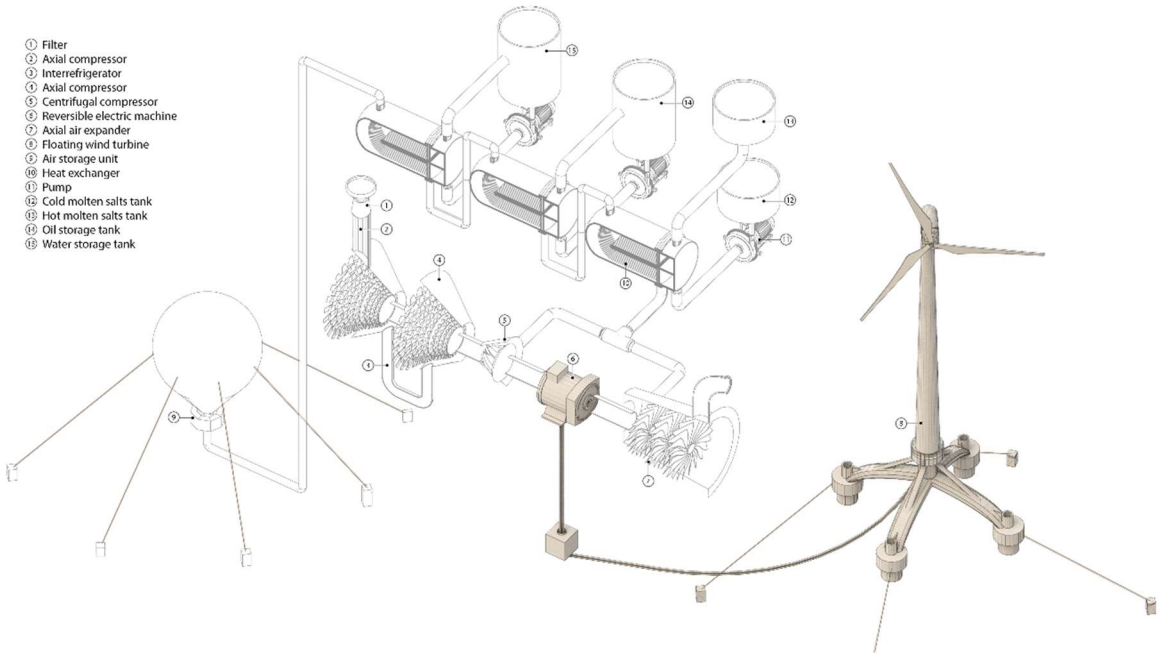


***Figure 5.1: Connection between wind field and CAES system***

Once that all the details of the turbomachinery are established, the CAES system is correctly working and the operative conditions are defined, the system is applied to a real-world application such as the coupling with different wind fields (Figure 5.1). The choice of the wind park is driven by the intrinsic features of the wind source, which allows higher powers, especially in large offshore environment, and which presents a very low degree of predictability.

## 5.1. SITE ASSESSMENT

In order to rely on the Italian regulation electric market, whose already high penetration of renewables is likely to furtherly increase, we imposed the place of our simulation in Italy. Moreover, we required an off-shore location with sea depth between 400 and 1200 m, corresponding to air storage pressure between 40 bar and 120 bar, and

this discarded all the Adriatic sea, not deep enough, as well as the centre of the Tirrenium sea and the east cost of Sicily, too deep, as it can be seen in Figure 5.2.

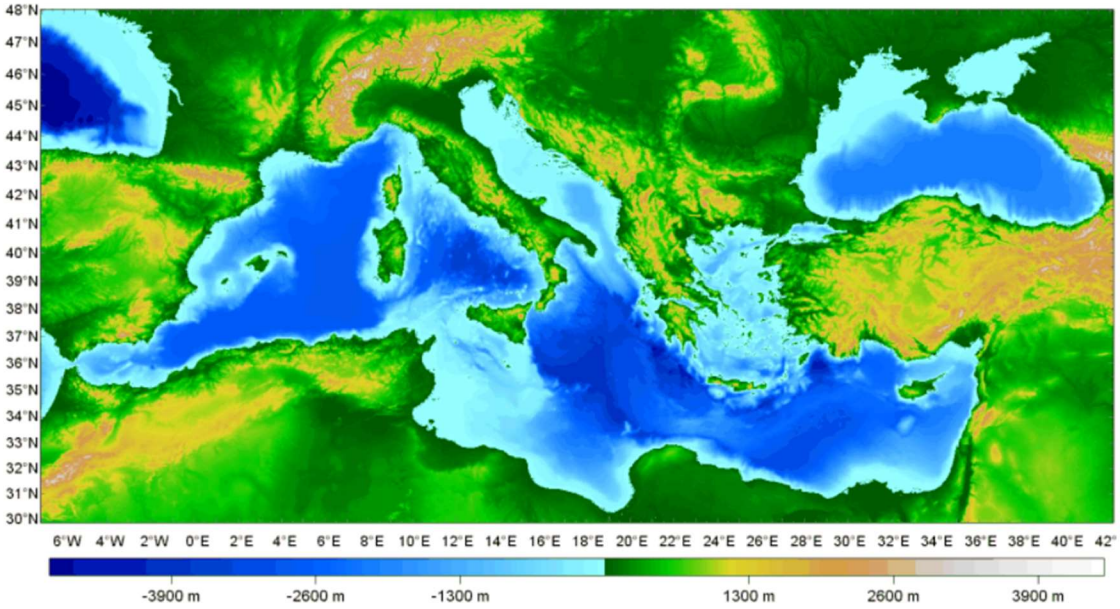


***Figure 5.2: Topographic and bathymetric map of the Mediterranean basin*** [46]

Finally, we crossed such result with the average wind data from the wind atlas, as done in Figure 5.3, in order to allow a favourable matching with an hypothetical wind turbine field. As we can notice, the most suitable places are either close to the island of Lampedusa, very far from the main national electric circuit, and in the west coast of Sardinia.

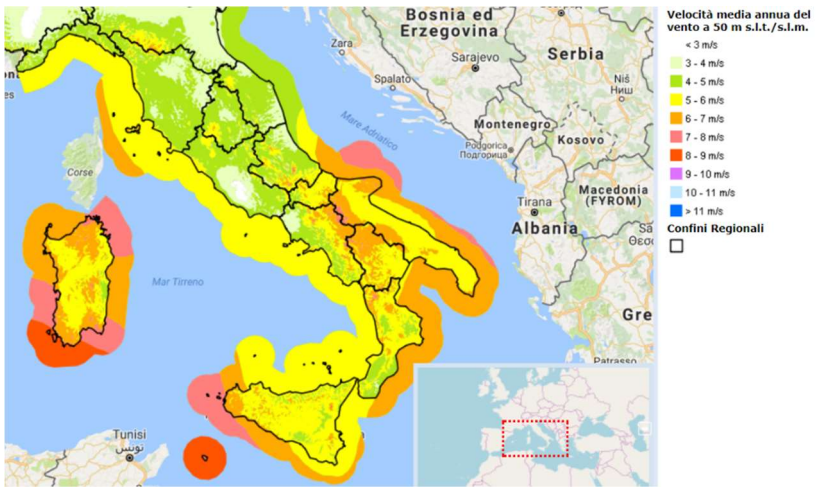


***Figure 5.3: Average wind speed estimated from the wind atlas*** [47]

The latter has been chosen as the position for our work, and in particular two different sites were spotted: the first one in the south-west corner of the island, while the second one in the middle of the western side. Furthermore, in both sites, the depth of the sea changes very steeply and in the surroundings varies from 200 m to 1800 m; in this way the storage pressure is still left as a free variable and not as an imposed condition. For both of these locations we obtained the hourly data of wind speed for four following years, thanks to the Spanish harbour weather forecast company, Puertos, which had two interesting datasets [19]. On the map represented in Figure 5.4 the positions of the sites where the wind data is taken are highlighted.

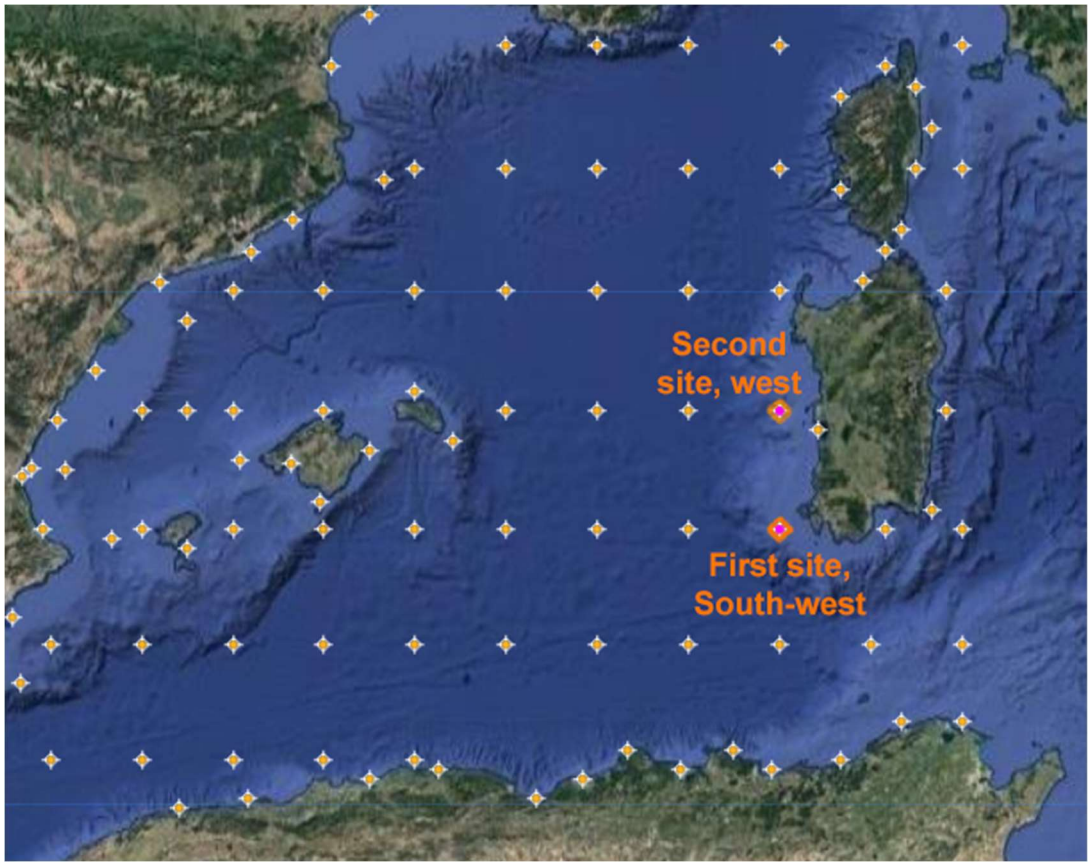


***Figure 5.4: Position of the considered locations among all the ones included in Puertos' data bank***

## 5.2. HORIZONTAL AXIS WIND TURBINE FIELD EVALUATION

### 5.2.1. Wind speed distribution and HAWT requirements

Once obtained the wind data, we had to decide the features of possible wind farms coupled with the designed system. The first decision regards the model of wind turbine that would be employed; in order to achieve such result, by means of the software System Advisor Model (SAM) [48], we obtained and compared the power curves of almost a hundred of Horizontal Axis Wind Turbines. However, the requirement of rated power bigger than 1.5 MW, mandatory to exploit scale economies, halved the number of candidates. Such condition is required since the offshore application needs expensive foundations, and thus large turbines are needed to lower the cost of energy. Furtherly investigating the features of the wind speed curves, we observed that the distribution of the first position, represented in Figure 5.5, has an average wind speed equal to 6.56 m/s with 9 hours in 4 years of wind blowing stronger than 20 m/s, while the latter one, in Figure 5.6, has an average wind speed of 6.05 m/s, but with 13 hours of very strong wind in the same period.

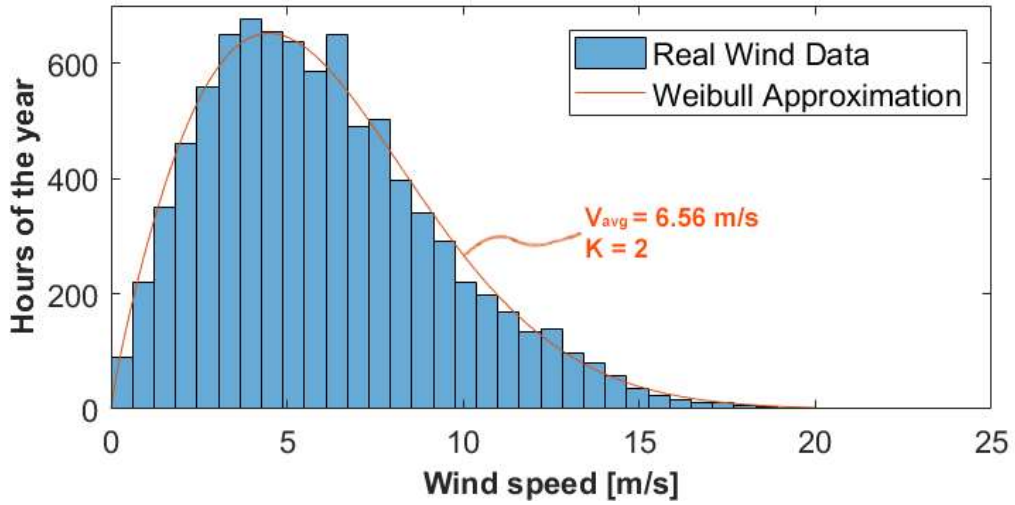


***Figure 5.5: Wind speed distribution and Weibull function approximation for the first site***

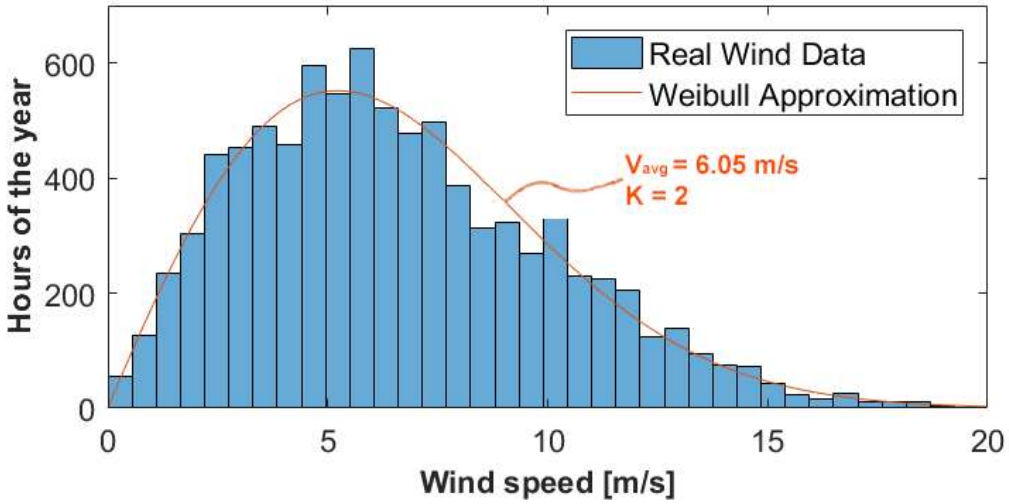


*Figure 5.6: Wind speed distribution and Weibull function approximation for the second site*

A second requirement we set was thus a cut-off speed of 20 m/s, since any increase from such value would be almost useless from the power production point of view, leading to complications both on the side of the mechanical stresses and on the one of the pitch angle required for the regulation, resulting in higher costs. Among the remaining ones, the best performing ones were compared directly on the SAM software, with the same structural and financial parameters and a Weibull wind distribution with the correct average speed and a shape factor K=2.

### 5.2.2. HAWT comparison

From SAM, we selected three possible wind turbines, whose power curves are shown in the following Figure 5.7.

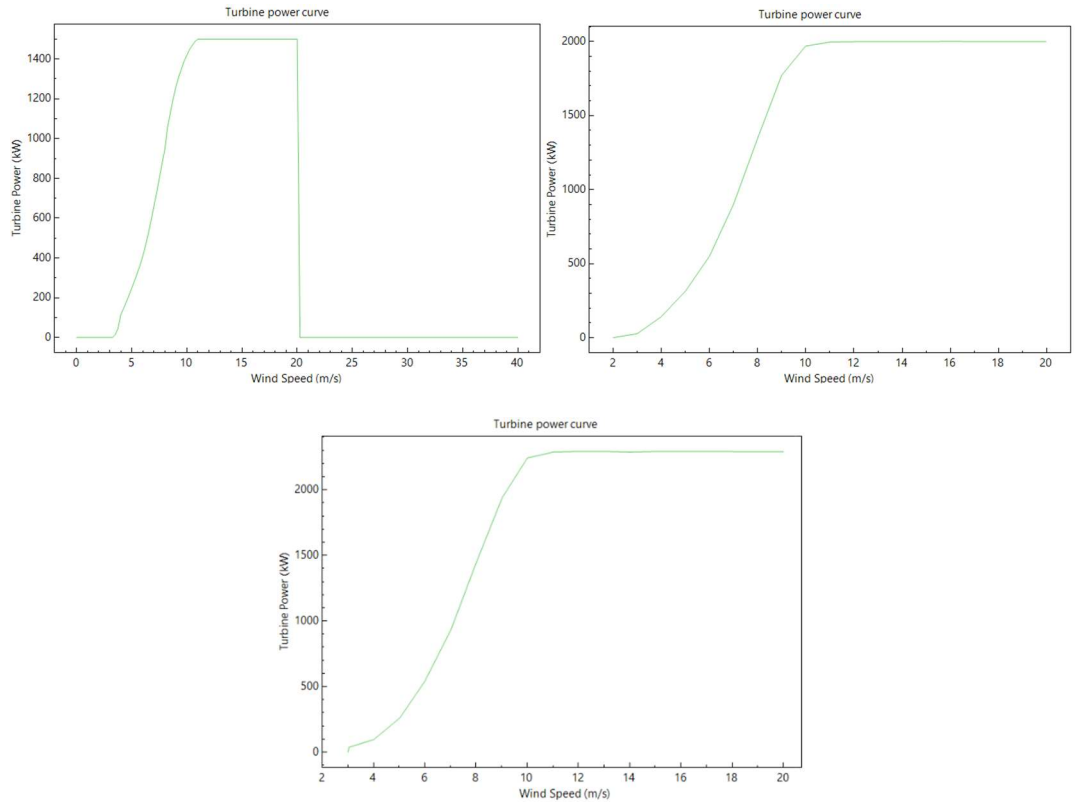


***Figure 5.7: General Electric's 1.5 MW power curve on the left, Vestas' 2 MW power curve on the right and Siemens' 2.3 MW power curve on the bottom***

In the following Table 5-1, it is possible to compare the main features of the power curves of these turbines.

***Table 5-1: Comparison among the most interesting data of the three considered wind turbines***

| | Rated Power | Cut-in speed | Cut-off speed | Rated speed |
|---|---|---|---|---|
| GE 1.5 xle | 1.5 MW | 4 m/s | 20 m/s | 11 m/s |
| Vestas V100-2.0 | 2 MW | 3 m/s | 20 m/s | 11 m/s |
| Siemens SWT 2.3 | 2.3 MW | 3 m/s | 20 m/s | 11 m/s |

These turbines come from three different firms, all huge players in the power generation sector. In order to identify the proper turbine for our application, we compared the three candidates, crossing both technical parameters, like the Annual Energy Produced or the Capacity Factor, and economic parameters, like the Net Present Value or the Levelized Cost of Electricity.

*Table 5-2: Comparison between the main technoeconomic indexes of different turbines for the first site*

| South-West site, with $v_{avg} = 6.56\ m/s$ | | GE 1.5 xle | Vestas V110-2.0 | Siemens SWT-2.3 MW-108m |
|---|---|---|---|---|
| Nominal Power | kW | 1500 | 2000 | 2300 |
| Annual Energy | MWh | 5964.9 | 8810.3 | 9578.8 |
| Capacity factor | % | 45.4 | 50.3 | 47.5 |
| Levelized cost | c$/kWh | 8.0 | 7.0 | 7.4 |
| Total installed cost | k$ | 5449.5 | 7266 | 8355.9 |
| Net present value | k$ | 630.4 | 829.4 | 944.6 |

*Table 5-3: Comparison between the main technoeconomic indexes of different turbines for the second site*

| West site, with $v_{avg} = 6.05\ m/s$ | | GE 1.5 xle | Vestas V110-2.0 | Siemens SWT-2.3 MW-108m |
|---|---|---|---|---|
| Nominal Power | kW | 1500 | 2000 | 2300 |
| Annual Energy | MWh | 5289.8 | 7928.6 | 8546 |
| Capacity factor | % | 40.3 | 45.3 | 42.4 |
| Levelized cost | c$/kWh | 9.2 | 7.9 | 8.5 |
| Total installed cost | k$ | 5449.5 | 7266 | 8355.9 |
| Net present value | k$ | 627.3 | 825.5 | 939.9 |

As we can notice from Table 5-2 and Table 5-3, the Siemens SWT-2.3 turbine has always the highest AEP and NPV, however when the wind speed decreases its LCOE increases a lot. On the other hand, the Vestas V110-2.0 turbine has a lower investment cost, resulting in the lowest LCOE in both cases, even though the energy production is lower. The GE 1.5-xle turbine is weaker according to any parameter, but simply because its inferior rated power (1.5 MW against 2 MW and 2.3 MW) is better suitable for power production from less windy regions. Another interesting observation is that very high values of CF are obtained: if this on one hand proves that the exploitation of the offshore wind source is well done, on the other hand may suggest that turbines with rated powers even higher could be employed. However, as we can notice from the following Table 5-4 and Table 5-5, such turbines have cut-off wind speeds of at least 25 m/s, and even for the first selected location would result in worse economic indexes, meaning that the increase in investment cost is not worth the value of the greater energy production. In particular we can notice that for both the bigger turbines considered the

capacity factors stick up to more conventional values. On the other hand, for different reasons, we can notice that the LCOEs are definitely higher than the corresponding value of the previous HAWTs.

***Table 5-4: Counter examples for the first site***

| **South-West site, with $v_{avg} = 6.56\ m/s$** | | **Siemens SWT-2.3 MW-108m** | **Nordex N80-2500** | **Leitwind LTW101m-3** | **Enercon E-126 127 m 7.5** |
|---|---|---|---|---|---|
| Nominal Power | kW | 2300 | 2500 | 3000 | 7500 |
| Annual Energy | MWh | 9578.8 | 5871.4 | 9636.55 | 18693.2 |
| Capacity factor | % | 47.5 | 26.8 | 36.7 | 28.4 |
| Levelized cost | c$/kWh | 7.4 | 14.2 | 9.9 | 13 |
| Total installed cost | k$ | 8355.9 | 9082.5 | 10899 | 27247.5 |
| Net present value | k$ | 944.6 | 1002.5 | 1205.7 | 2922.9 |

***Table 5-5: Counter examples for the second site***

| **West site, with $v_{avg} = 6.05\ m/s$** | | **Vestas V110-2.0** | **Nordex N80-2500** | **Leitwind LTW101m-3** | **Enercon E-126 127 m 7.5** |
|---|---|---|---|---|---|
| Nominal Power | kW | 2000 | 2500 | 3000 | 7500 |
| Annual Energy | MWh | 7928.6 | 4886.7 | 8327.1 | 15781.4 |
| Capacity factor | % | 45.3 | 22.3 | 31.7 | 24 |
| Levelized cost | c$/kWh | 7.9 | 17.4 | 11.8 | 15.7 |
| Total installed cost | k$ | 7266 | 9082.5 | 10899 | 27247.5 |
| Net present value | k$ | 825.5 | 998 | 1199.8 | 2909.8 |

So, at the light of such reasoning, the Siemens turbine has been considered for the first site, while the turbine produced by Vestas will be used for the second one. The choice of using different turbines for the two locations has been guided by the desire of using different power curves that will lead to an increase of variability in the electric power input, and consequently to make generally applicable the results. Nevertheless, for the purpose of this research, it is not relevant the energy production of a single HAWT, but what really matters is the production of the whole wind farm.

### 5.2.3. Offshore Wind farm

At the moment there is only one offshore wind farm already under construction in Italy, and it is located close to Taranto. It should start commissioning in 2018, and it

will be made up of 10 wind turbines of 3 MW each, for a total of 30 MW[49]. Moreover, the first floating wind farm has just been delivering its energy in Scotland, and it is made up of 5 turbines of 6 MW each, for an entire rated power of, again, 30 MW [50]. Since our need is to think about a floating offshore wind farm in Italy, it seems reasonable to think at wind farms of the same order of magnitude. Accordingly, we decided to pick up 15 Horizontal Axis Wind Turbines for each kind, in order to reach 30 MW of rated field power in the least favourable location, while an amount of 34.5 MW for the more fortunate one. However, both values have to be corrected since aerodynamic interaction between wind turbines cannot be neglected; furthermore, each wind turbine may have a slightly different rotational speed. Considering the correction of the latter effect and an array efficiency of the former, defined as the ratio between the power produced by the field and by each of the $N_{turbines}$ separately, we can consider that the power produced by the find farm is equal to the 95% of that produced by each single wind turbine [51].

$$P_{nom,field} = P_{nom,turbine} * N_{turbines} * Correction\ Factor \tag{5.1}$$

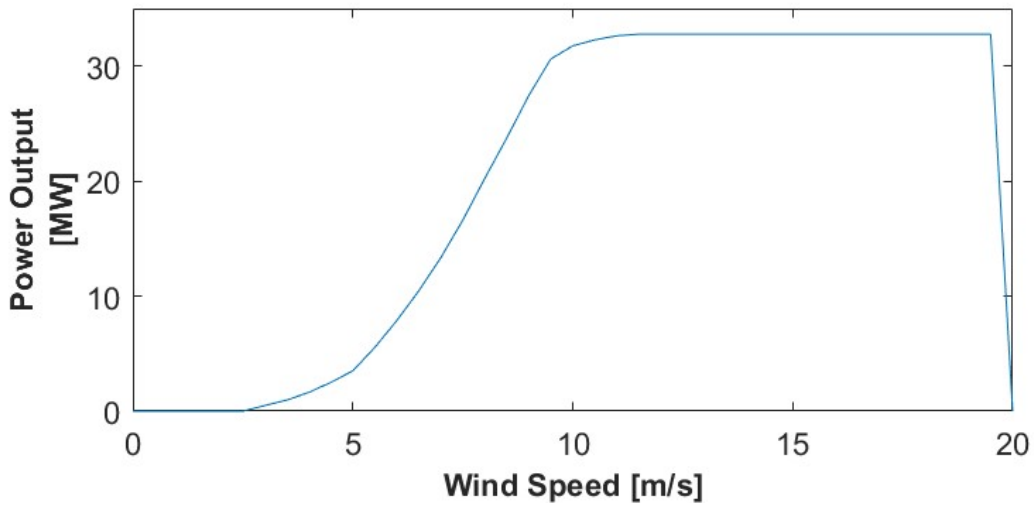


***Figure 5.8: Power produced by the whole wind field as a function of the wind speed***

In Figure 5.8 the production of the considered wind field for the first site is shown. Along a year with the considered wind distribution it works for 3360 equivalent hours.

## 5.3. COUPLING WITH THE CAES SYSTEM

When connecting the behaviour of an unpredictable renewable energy source to a storage device, scale economies should correctly be taken into account, since the investment cost is usually extremely high due to the complications implicit in the transformation of energy from one form to another one. Consequently CAES systems (but the same can be said about dams, the other potential energy form of storage) are considered only as large scale devices, and their purpose is accordingly related to peak shaving and load levelling. For this reason, it seems improbable to link just one wind farm to a storage unit, but it is more likely to do so with more than one; thus, to enrich the results of our simulation, we supposed to connect the southern site to four different wind farms, while the western one only to two farms, all of them of the previously considered size.

In order to ensure a correct matching between the production and storage systems, different logics can be followed:

- Strategy 1: Peak Shaving. The most extreme 13.5 % top and bottom values are flattened.
- Strategy 2: Optimised Peak Shaving. The levelling of the distribution is made in order to maximise the most relevant parameters
- Strategy 3: Arbitrage. The storage system charges or discharges itself following the most profitable logic.

### 5.3.1. Peak Shaving: reference case

The concept of peak shaving stands on the fact that maximum values of power very distant from the average value, both on the supply and on the demand side, are badly tolerated by the electric system. Also situations with a steep gradient in the power curve are preferably avoided. In the considered case this means that the maximum values of electricity obtained over a certain threshold will be stored, and then released in any moment where the production is enough below the average. So, as previously observed, being the compressor side flexible to fluctuate between the 80% and the

103% of the nominal power, the peak shaving will be dimensioned accordingly and, at least at the beginning, referring to the mean value.

First of all we ran the wind simulation in order to understand the hourly average power produced in one full year of plant activity, and to do so we used the wind data from year 2014, data that will be used for all the present chapter. Since it would be optimistic to suppose that all the HAWT will be working all year without problems nor maintenance, a certain availability has been considered, and in particular the availability factor multiplies the average value by 97% [52]. The hypothesis behind this process is that being impossible to know exactly when each turbine will be curtailed, for the central limit theorem and for a huge number of hours it is possible to assume that the shut-down will be flattened among all the hours, and thus affecting in the same way the mean value too.

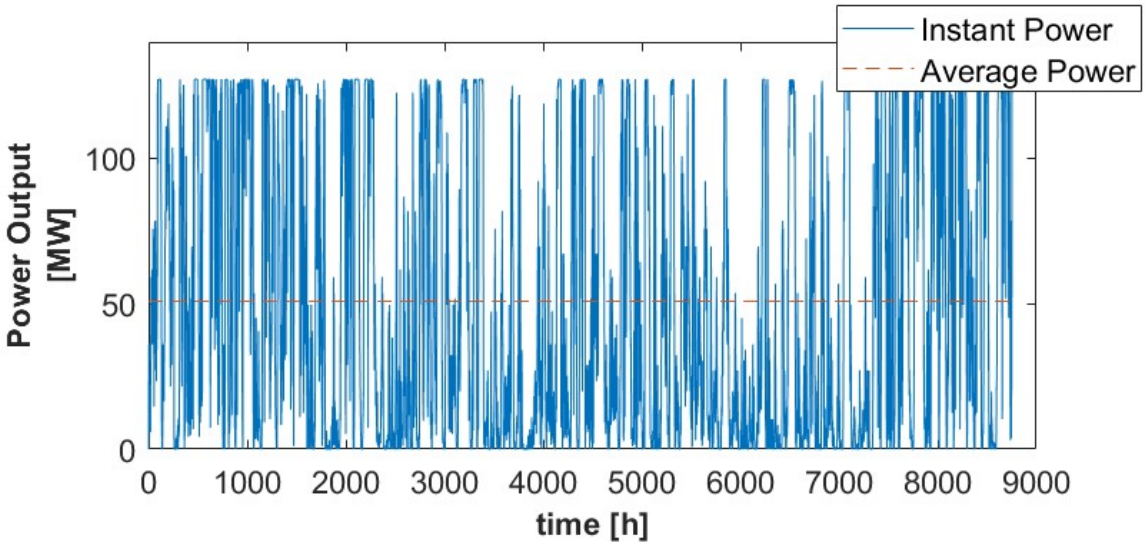


***Figure 5.9: Power generated by the entirety of the four power fields considered, with the average value marked as the red dashed line***

Figure 5.9 represents the yearly fluctuating power, and the following results are obtained. The standard deviation is highlighted, since it will be used to compare the fluctuations from the average for each of the following cases; a reduction of peaks means also a decrease in the standard deviation, with a strong influence when extreme values are reduced. For the same reason the Annual Energy Produced is computed, and

in particular it will be used in order to understand the relative loss of energy because of the CAES efficiency.

$\overline{P_{field}} = 50{,}9\ MW, \qquad AEP = 445{,}6\ GWh, \qquad \sigma\ (standard\ deviation) = 48{,}6MW$

Furthermore, we know how much is the maximum power generated by the wind farms, and if we subtract the average power considered as reference, we obtain the highest power the compressor should be able to absorb, defining this as the Maximum Load Condition ($P_{\%,Max}$), and being this the 103% of the design value, the nominal power of the compressor is so obtained. Moreover, since the flexibility range spans only down to the 80% of the design value, the minimum load condition ($P_{\%,min}$), and defining consequently this as the minimum load condition, also the threshold of the peak shaving is fixed.

$$P_{nom,CAES} = \frac{(P_{max,field} - P_{avg,field})}{Maximum\ Load\ Condition} \tag{5.2}$$

Where $P_{nom,CAES}$ is equivalent to the nominal power of the compressor train.

$$P_{\%,min} * P_{nom,CAES} \leq P_{CAES} \leq P_{\%,Max} * P_{nom,CAES} \tag{5.3}$$

Theoretically, the size of the compressor and of the turbine are not linked, as they never work at the same time. Nevertheless, as a first attempt the turbine dimensioning leads to a configuration with the same mass flow rate as the compressor, activated for a bandwidth coherent with the one in compression. In such way, both the extreme 13.5% top and bottom power values are avoided, decreasing the width of the electricity function sold to the grid.

As a reference case we considered data from the first site, a tank pressure of 80 bar, no additional heat recovery from the aftercooler system, IGV equipped only at the first compressor, a turbine dimensioned on the nominal mass flow rate of the compression phase and unlimited capacity for each storage unit. It is interesting to notice that the initial state of charge of the storage units is obtained running the model

for the last two months of the previous year, in order to avoid boundary effects that could affect significantly the results.

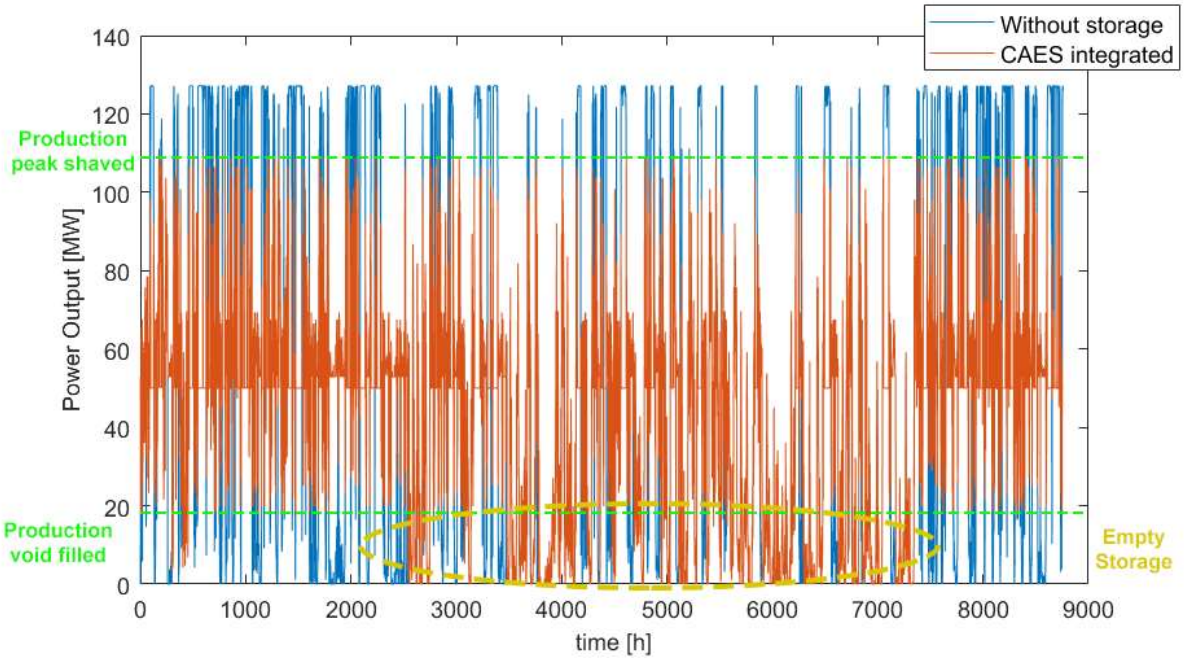


***Figure 5.10: Power given to the grid, both with (red) and without (blue) storage system***

As we can notice from Figure 5.10, the extension of the yearly fluctuations is reduced with respect to its original value, and with the exceptions of when the state of charge is not able to satisfy the higher demand of power, the bandwidth of power released to the grid is always contained between the compression activation power and the turbine activation power. The main results are visible in Table 5-6; however, some dynamics are immediately self-evident, and will consequently require particular attention.

First of all, it can be easily observed the strong seasonality in the energy generation, with greater production in winter, both at the beginning and at the end of the year. In order to tackle this issue, a better analysis could use the moving mean instead of the integral meal. The physical reasoning behind such choice lies behind the possibility to predict under certain limits such periodic fluctuation, and thus avoid as much as possible deviations from the so-built function.

$$moving\ mean: \bar{P}(t) = \frac{\sum_{i=t-\frac{N}{2}}^{t+\frac{N}{2}} P(i)}{N} \tag{5.4}$$

Where N=2190 is the number of hours in a season, the time span considered

***Table 5-6: Main numerical results of the reference peak shaving case***

| | | |
|---|---|---|
| Charging hours | 2015 | h |
| Equivalent compressor hours | 2007 | h |
| Discharging hours | 1673 | h |
| Unavailable expansion hours | 1804 | h |
| Turbine Power | 53 | MW |
| Energy to Compression | 150,5 | GWh |
| Energy from Turbine | 88,96 | GWh |
| Round-trip efficiency | 59,1 | % |
| Corrected efficiency | 63,5 | % |
| Standard deviation | 25,78 | MW |

A second consideration is deserved by the state of charge of the reservoirs along the year, shown in the following Figure 5.11 and Figure 5.12, whose final value is way higher than the beginning one. On the other hand, a certain number of hours at which the turbine could have worked persist, limited by the oil storage unit whose state of charge does not allow any further expansion. Since the bottleneck is represented by the oil thermal storage, the intuition of regenerating the final discarded heat of the cooling to storage to preheat the air before the oil heat exchanger seems very reasonable. In order to correct such difference in the state of charge, the initial values are increased coherently, while the presence of the aftercooler, the heat recovery at the end of the cooling process stored by means of a water tank, is guaranteed.

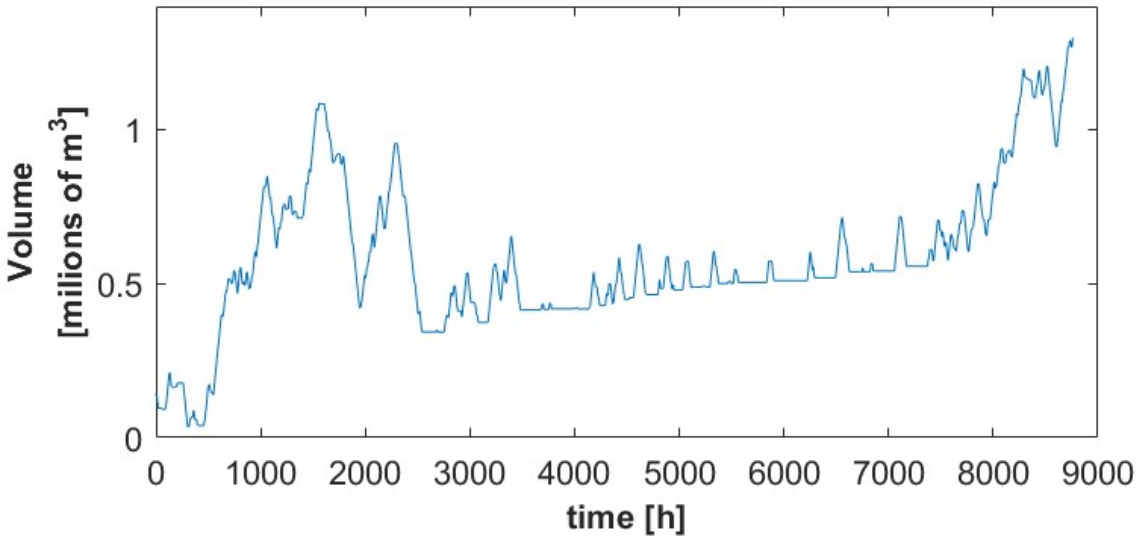


*Figure 5.11: Variation of the air stored volume in the underwater tank along the year (reference case)*

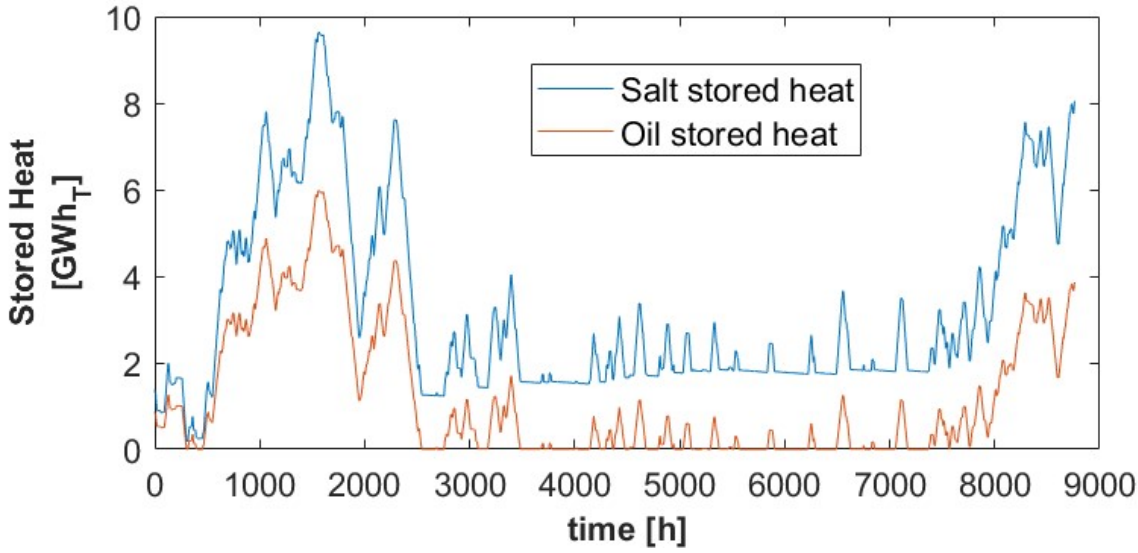


*Figure 5.12: Variation of the amount of heat stored in each unit along the year (reference case)*

Finally, the difference in the state of charge between the end of the year and its beginning is calculated, and accordingly the round trip efficiency corrected, imagining an hypothetic expansion in nominal conditions that stops when the first tank reaches its initial condition. Furthermore, the nominal power of the turbine is an output of the model, since it is dimensioned to produce the power obtained expanding the same mass

flow rate previously compressed. Its size can be approximated to the product of the nominal efficiency of the CAES with the nominal compression power.

### 5.3.2. Peak shaving improvement

As a first correction, the aftercooler storage system is activated, and its initial state of charge is obtained from the result of a whole year simulation, as well as the equivalent values of the other two reservoirs. In this way the hours at which the expansion is desirable but impossible to achieve should decrease. However, as it can be noticed from the following results in Table 5-7, the unavailable expansion hours increase instead of decreasing, as it will be explained at the light of a deeper qualitative thermodynamic analysis.

***Table 5-7: Main numerical results for the corrected peak shaving case***

| | | |
|---|---|---|
| Charging hours | 1645 | h |
| Equivalent compressor hours | 1546 | h |
| Discharging hours | 1634 | h |
| Unavailable expansion hours | 1843 | h |
| Turbine Power | 53 | MW |
| Energy to Compression | 115,9 | GWh |
| Energy from Turbine | 86,82 | GWh |
| Round-trip efficiency | 74,9 | % |
| Corrected efficiency | 74,9 | % |
| Standard deviation | 31,01 | MW |

Running the model again allows a wider view on the dynamics of an adiabatic Compressed Air Energy Storage system. In particular, now that the aftercooler is present, the scarce resource is shifted from the oil heat reservoir to the heat stored in the water tank, leaving a considerable amount of time where such tank is empty. The reason is probably to seek considering the charge and discharge processes together: under the assumption of a rigid discharge process, working only in design condition for the turbine, and with fixed off-design for the heat exchangers resulting in constant mass flow rates for the thermal fluids, the rulers are the air side temperature differences. This means that equal temperature differences between charge and discharge result in a

symmetrical process, while alterations lead to unbalances that in the long run will stop the system. In particular this will happen because the air volume decreases only when the turbine works proportionally to the charging process, while the state of charge of the thermal reservoirs, besides suffering an hourly self-discharge of 0,1 %, is a consequence of the thermal boundaries imposed. In practice, when the system is charged, the temperature differences are imposed and thus are given values. On the other hand, during the discharge process the temperature difference reduces and the heat cannot be recovered.

Without the additional heat recovery system, the heat embedded in the oil system spans the range between 270°C and 65°C in the cooling to storage phase, while in the heating from storage the air inlet temperature is of the order of the tenth of degrees Celsius, depending on the depth of the air tank, and reaches 245°C. The asymmetry between these two phases results, for equal air flow rates, in an increase in the relative discharging of the oil system with respect to the salt or the air storages. When the aftercooler is introduced, the problem is reduced, since part of such unbalance is absorbed by the new device. However, since an unevenness remains, the bottleneck becomes the heat in the water tank. Moreover, the growth in the number of hours of unsatisfied expansion demand can be linked to the increased relative asymmetry in a heat exchanger. In fact, even though the global balance between charging and discharging processes is levelled, focusing on the single element the relative disparity is pumped by the much smaller temperature differences. In order to avoid this problem, the aftercooler should present a bypass valve that allows the system to work even when this tank is empty. Another option could be the free variation in the mass flow rate of the thermal fluids, in order to have a heat power free variable. In fact, the mass flow rate changes only to assure fixed temperature differences in the thermal fluid side.

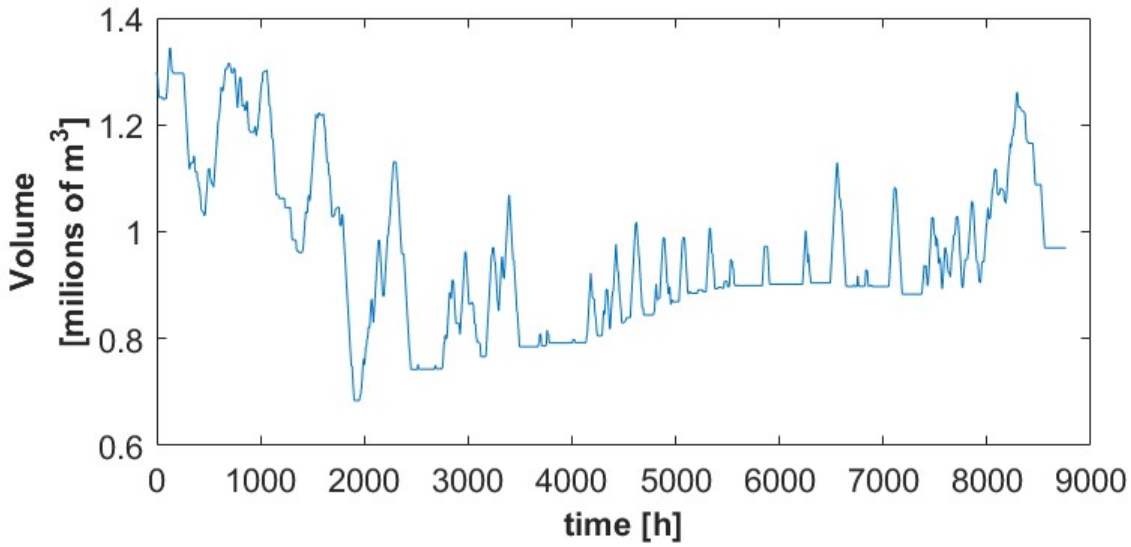


***Figure 5.13: Variation of the volume of air stored in the underwater tank along the year***

Comparing Figure 5.13 and Figure 5.14, it is important to observe that, while the air stored has decreased along the year, and so did the heat stored in the water and salt tanks, the heat in the oil tank increased, as a consequence of the imbalance already introduced.

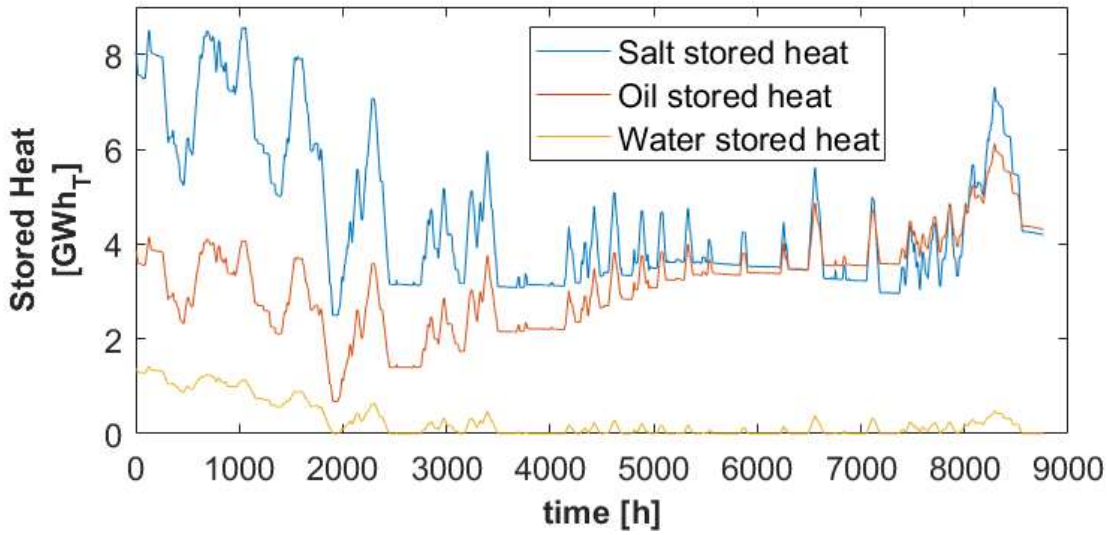


***Figure 5.14: Variation of the amount of heat stored in each unit along the year***

Furthermore, the moving mean, clearly visible in Figure 5.15, built by hourly values from a quarter of year, is used instead of a constant value, to take care of the

seasonality of the wind resource. The purpose is to avoid an unjustified charging of the CAES during months when the production is high for a wide period, resulting in an over-dimensioning of the reservoirs. However, in order to exploit the same logic also for the discharge side, a different approach has to be employed, decreasing either the compression power or the relative size of the turbine with respect to the compressor.

As shown in Table 5-7, this reduces the compression time, and drops down even more the number of equivalent hours, limiting the improvement in the standard deviation, which remains higher. This is due to the time in the most windy period at which the compressor has to work at partial load in order to reach the higher reference value.

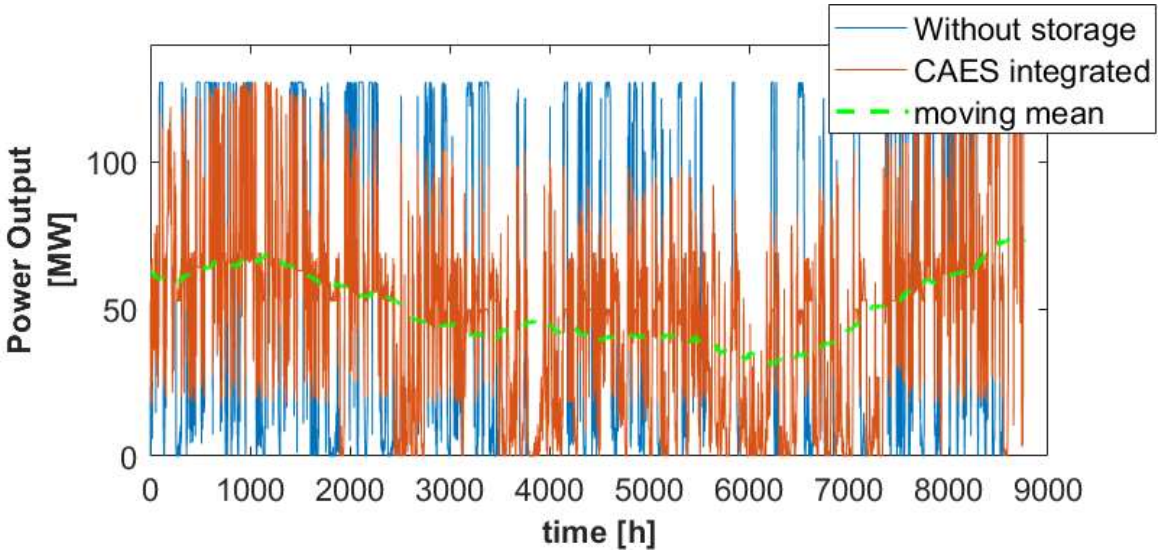


***Figure 5.15: Power given to the grid, both with (red) and without (blue) storage system; it is highlighted the average value considered for the distribution, alias the moving mean***

Finally, the most significative result is the huge rise in the round-trip efficiency, which gains more than 10 points percentage: in particular, despite what has been said before, the energy expanded by the turbine along the year suffers only a small reduction. The cause is partially the better matching between hot and cold fluids, that allows an improved exergetic exploitation. Nevertheless, another important reason that explains such escalation is the increased temperature in the turbine inlet, that as well as increasing the turbine efficiency, as the gas turbine theory explains well, avoids the

thermal curtailment of the turbine. The latter occurs when the temperature inside the machine reaches 5°C and, to avoid ice formation on the blades, stops the expansion and laminates the air until ambient condition is reached, but thanks to the aftercooler such process never happens.

### 5.3.3. Bypass valve for the aftercooler

The impressive increase in the round-trip efficiency obtained by means of an aftercooler storage tank suggests to consider different solutions able to embank its weaknesses and to exploit its great exergetic advantage. The simplest configuration adopts a bypass valve that allows the discharge of the system even if the water storage is empty. This new configuration on one hand allows to level the aforementioned asymmetry between two different reservoirs, the oil and the water ones, while on the other hand permits many more working hours reducing the constraints required for the expansion phase.

***Table 5-8: Main numerical results for the bypass at the aftercooler case***

| | | |
|---|---|---|
| Charging hours | 1645 | h |
| Equivalent compressor hours | 1546 | h |
| Discharging hours | 1787 | h |
| Unavailable expansion hours | 1690 | h |
| Turbine Power | 53 | MW |
| Energy to Compression | 115,9 | GWh |
| Energy from Turbine | 94,97 | GWh |
| Round-trip efficiency | 81,92 | % |
| Corrected efficiency | 76,34 | % |
| Standard deviation | 30,48 | MW |

The first thing worth noticing from Table 5-8 is the decrease in the hours during which the expansion is stopped because the constrains allowing the discharge are not satisfied, the main purpose of the current simulation. In particular, focusing on the state of charge of each single tank, as suggested by Table 5-9, the situation appears much more balanced, with all reservoirs uniformly charged and discharged during the year.

***Table 5-9: Yearly empty thermal storage time, with reported also the useful time of bypassed aftercooler***

| **Heat storage** | | |
|---|---|---|
| At least 1 empty tank | 1843 | h |
| At least empty aftercooler | 1298 | h |
| At least empty oil storage | 176 | h |
| At least empty salt storage | 1514 | h |
| Aftercooler bypassed in discharge | 151 | h |

Another consequence is the further improvement in the round-trip efficiency, which exceeds the threshold of 75 %; in this case the correction lowers such index, since at the end of the year all tanks are emptier with respect to the beginning of the year, as we can notice from the following Figure 5.16 and Figure 5.17. However, the impact of the beginning conditions on the round-trip efficiency must not be neglected, lowering such value of at least five percentage points.

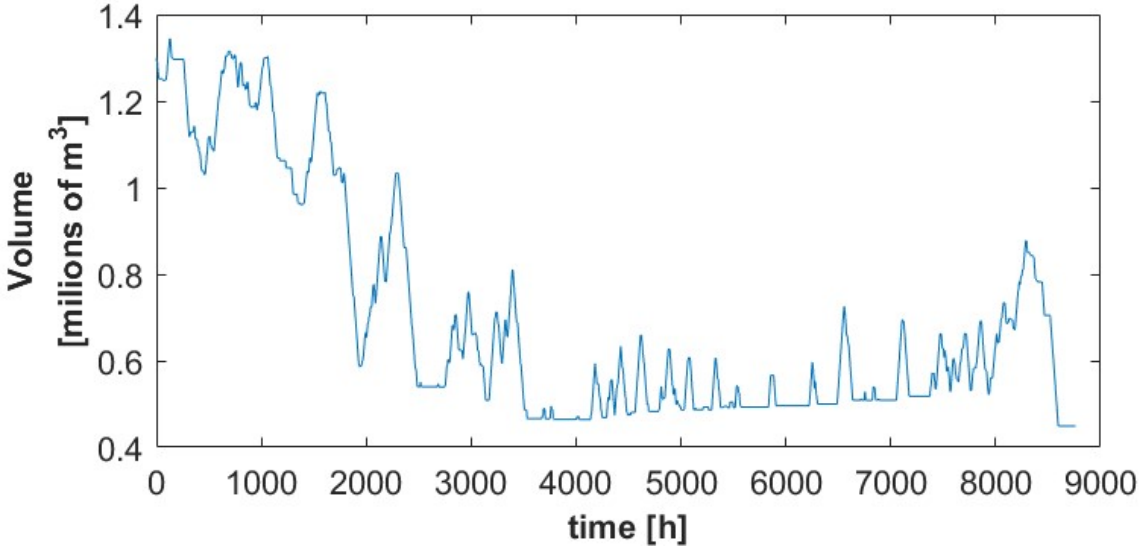


***Figure 5.16: Variation of the volume of air stored in the underwater tank along the year***

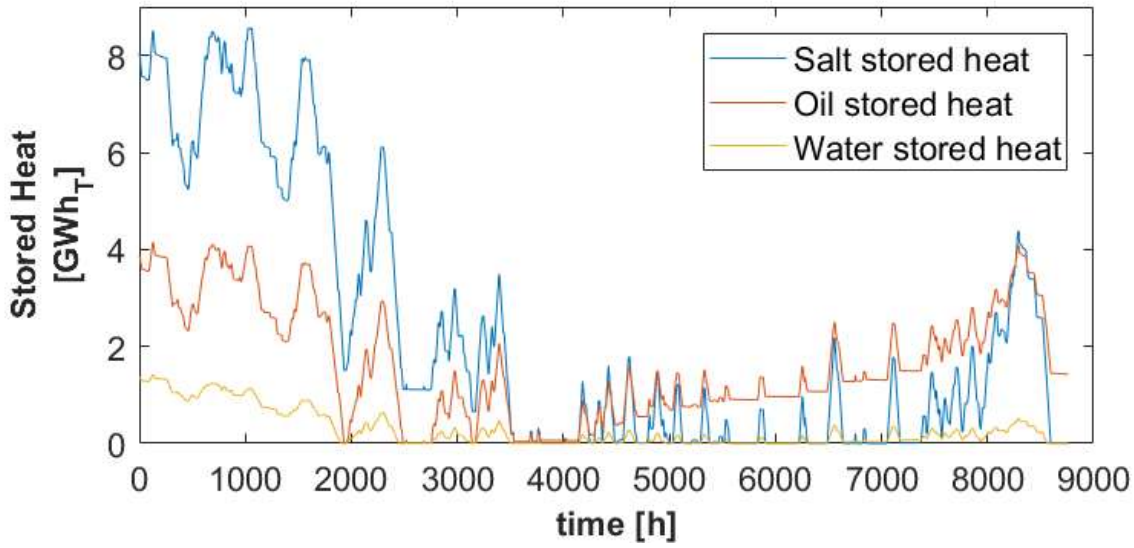


***Figure 5.17: Variation of the amount of heat stored in each unit along the year***

It is of paramount importance noticing from Figure 5.17 that finally there is alignment among the state of charge of all the reservoirs, allowing a continuative use of the system even after the considered period of time. Finally, because of the increase in the effectiveness of the expansion process, the standard variation slightly decreases with respect to the previous case, proving that the resulting power function is closer to its average value.

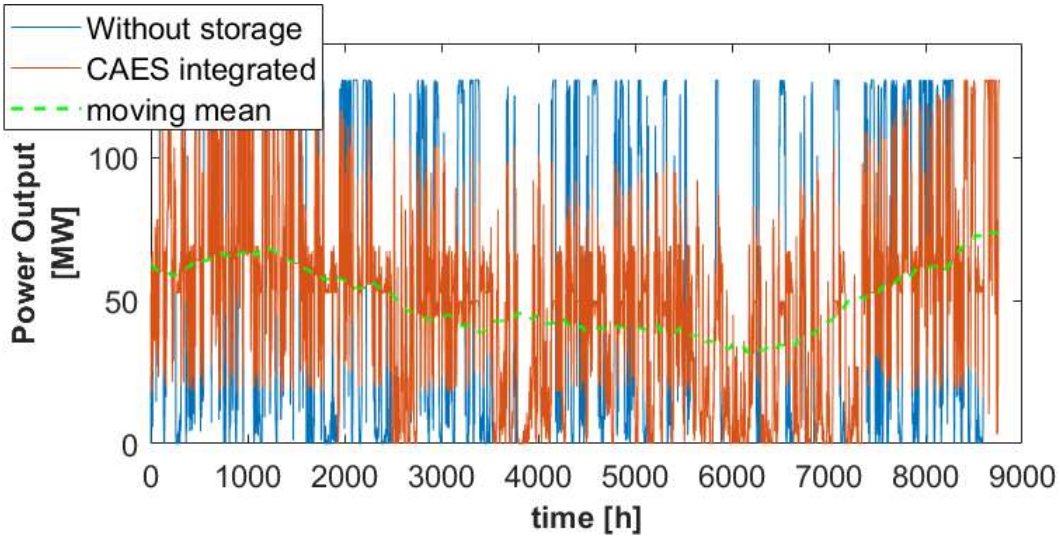


***Figure 5.18: Power given to the grid, both with (red) and without (blue) storage system; it is highlighted the average value considered for the distribution, alias the moving mean***

# 6. PLANT LAYOUT OPTIMIZATION

Once chosen the best configuration among the given possibilities (IGVs only at the inlet of the first compressor, additional aftercooler heat storage recovery system, equipped with a bypass valve that allows the air to bypass it), a deeper analysis is required to validate the mathematical model used for the simulation of an underwater adiabatic CAES system. In particular, both the compression and expansion turbomachines needs a careful dimensioning, indeed because they shape the profile of the electricity function sold to the grid, but also because they will define the size of all the storage units, and consequently the investment cost of the system. Since the results obtained from the present chapter will be used for the economic analysis too, the wind data for the simulation were chosen from the year 2015, in order to use energy prices from a context closer to the present one. Finally, since the chosen configuration is decided as the desired one, from this moment on the state of charge of each tank at the beginning of the year is turn to zero, in order to avoid interactions with the model itself even though the difference is negligible.

## 6.1. SENSITIVITY TO TURBINE SIZE

It is of paramount importance now to consider the correct dimensioning of the expansion side: an expander of the same size of the compressor, as previously shown, or even bigger will definitely result in higher investment costs and will be functioning either exceeding the moving average or working only very few hours. However, a turbine which is too small will not be able to exploit the stocked energy in the available time and will thus require an useless over dimensioning of all the storage units. Nevertheless, in order to dimension correctly the turbine, a sensitivity analysis is performed, keeping the dimension of the compressor side fixed to the value previously considered (75 MW) in order to avoid a non-optimal matching with the compression side.

### 6.1.1. Equation setup

First of all it is required to the turbine to avoid an overall electric power above the moving average value at its hourly value *i*. Consequently, the power at which the turbine may start working each hour is only a function of the nominal power of the turbine, as showed in the following equation.

$$P_{T,i}^{activation} + P_T^{nom} = P_{average,i} \tag{6.1}$$

Furthermore, the turbine's nominal power can be expressed as a function of the system's nominal efficiency and of the ratio between the nominal mass flow rates of the turbine and compressor; such ratio is defined as the Turbine Dimension Factor.

$$TDF(Turbine\ Dimension\ Factor) = \frac{\dot{m}_T^{nom}}{\dot{m}_C^{nom}}, \tag{6.2}$$

$$\eta_{CAES}^{nom} = \frac{\dot{m}_T^{nom} * \Delta h_T^{nom}}{\dot{m}_C^{nom} * \Delta h_C^{nom}} \tag{6.3}$$

This parameter allows to unlink results from the specific system size, giving the relative power of the machines. And finally, since where the nominal efficiency is computed both mass flow rates are equal, the maximum discharge power is expressed as a function of the Turbine Factor as the only free parameter.

$$P_T^{activation} = P_{average,i} - P_C^{nom} * \eta_{CAES}^{nom} * TDF \tag{6.4}$$

The range of values assumed by TDF in the following analysis spans between 0.45 and 1; in particular, lower values were forbidden because of the heat exchangers. Actually they are dimensioned on the nominal case and halving the air flow rate passing after the compression, making the heat exchange unbalanced both in terms of velocities and of heat exchange coefficients. On the other hand higher values meant extremely low turbine working hours, requiring a different and *ad hoc* approach to the problem. However, the great advantage that arises following this path is the possibility to follow the trend imposed by the moving average not only in the charging process, but also on the discharge side.

### 6.1.2. Power output

It is clear from its definition that increasing the Turbine Dimension Factor, the size of the turbine increases and thus its cost, but the operative number of hours will reduce. Consequently also the standard deviation (i.e. the average distance of the actual production from a controlled profile) will rise, as shown in Figure 6.1 since the storage system is acting only on extreme values, accepting increasing deviations from the average values. In practice, with TDF ~ 1 the turbine is activated only when huge amounts of energy are missing and not during many hours next to the average

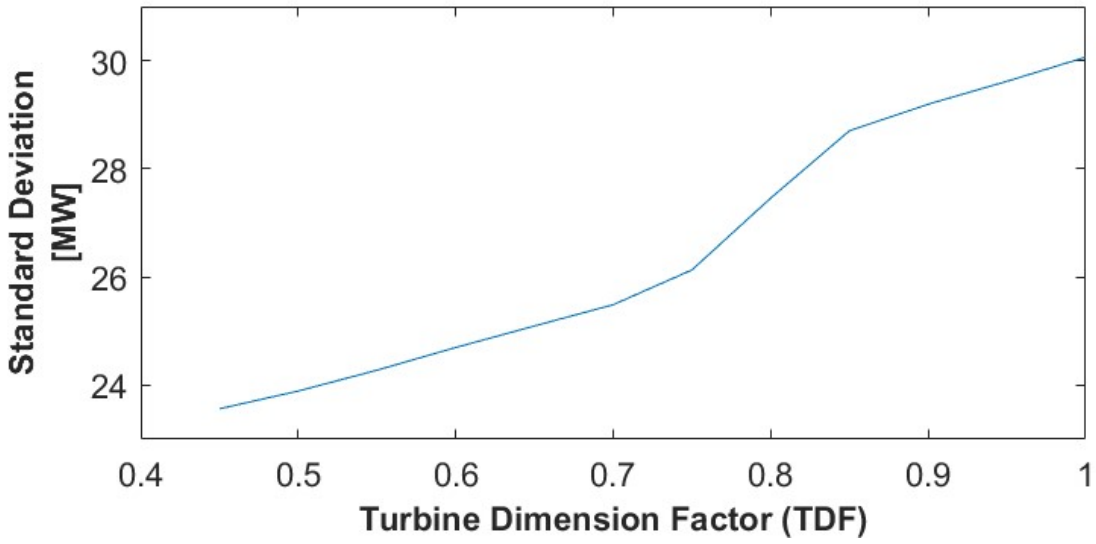


***Figure 6.1: Standard deviation as a function of the Turbine Dimension Factor***

Anyway, the standard deviation is much lower (about halved) than the one of the same distribution without the CAES system ($\sigma = 48{,}97 MW$ for the considered year), meaning that the desired outcome of flattening the production is well achieved, as we can also notice from the following Figure 6.2, Figure 6.3 and Figure 6.4. In these graphs, the moving average is immediately noticeable between 60 MW and 40 MW, while the compression remains untouched since is not influenced by the turbine dimensioning.

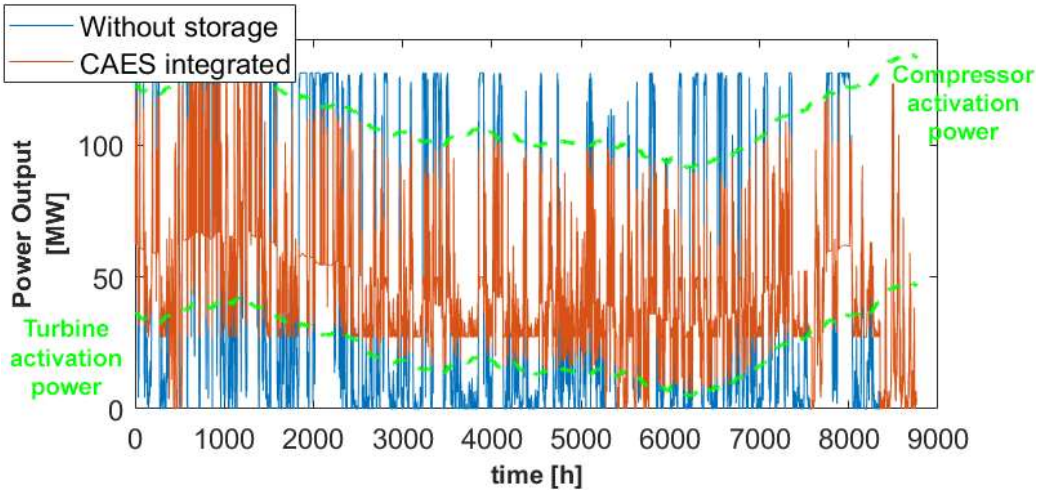


*Figure 6.2: Power output for a TDF of 0.5 both with (red) and without (blue) storage system.*

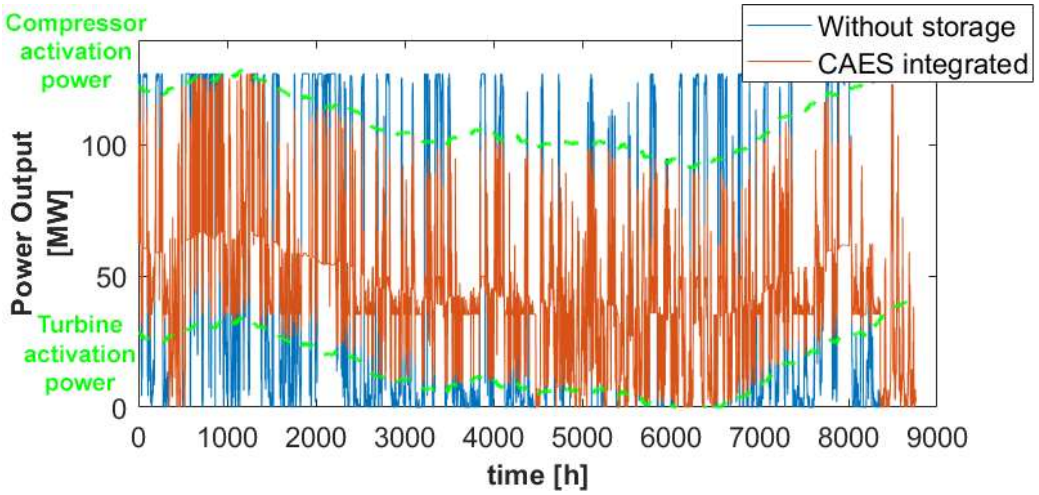


*Figure 6.3: Power output for a TDF of 0.65 both with (red) and without (blue) storage system*

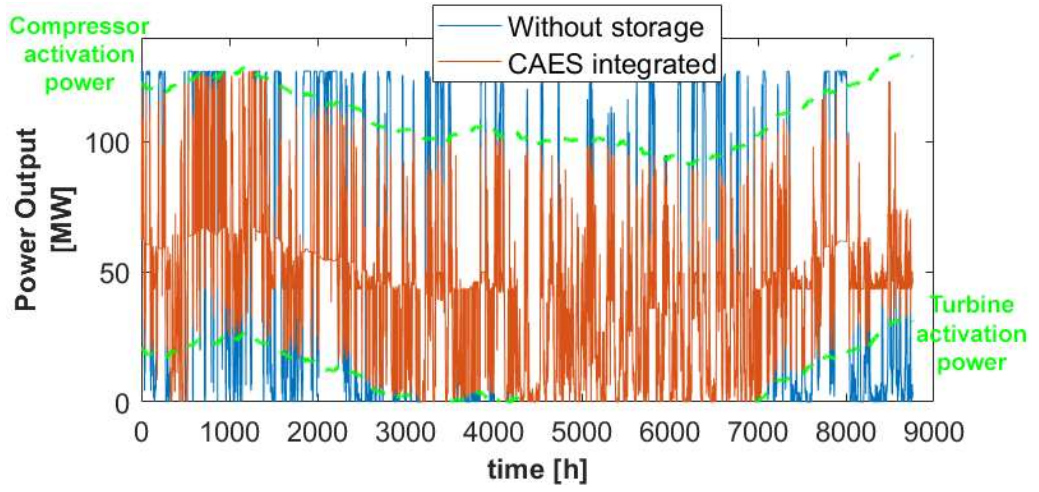


*Figure 6.4: Power output for a TDF of 0.8 both with (red) and without (blue) storage system*

It is interesting to notice that, if possible, the power given to the grid will always lie between the turbine and compressor activation powers. However, at the beginning of Figure 6.2 it can be noticed a region where such bound is not respected, even though the turbine is working. The reason is that such a turbine has a nominal power of only 26.5 MW, too small to allow the fulfilment of the constrain in zero wind condition. In practice, the turbine is active also when the missing power needed to reach the desired bandwidth, included between the turbine and compressor activation powers, is higher than the turbine's nominal power. Increasing the Turbine Dimension Factor, this does not happen anymore, and if the power released is outside its bandwidth, the reason is only that the storage is empty. Finally, comparing these figures, it can be then immediately observed that values below the average are hardly accepted for low a TF, but well tolerated when such value reaches its upper limit

On the other hand, as proven by Figure 6.5 the turbine operative hours will drop down for high Turbine Dimension Factors, reducing the possibility to reach the breakeven. However, in most of the graph the power production in the two cases are the same, and in particular this occurs for central values. The exceptions lie, as already observed, where the state of charge of the storage unit do not allow to increase the lower peaks (i.e. fulfil missing energy demand), although for TDF > 0.8 this hardly happens.

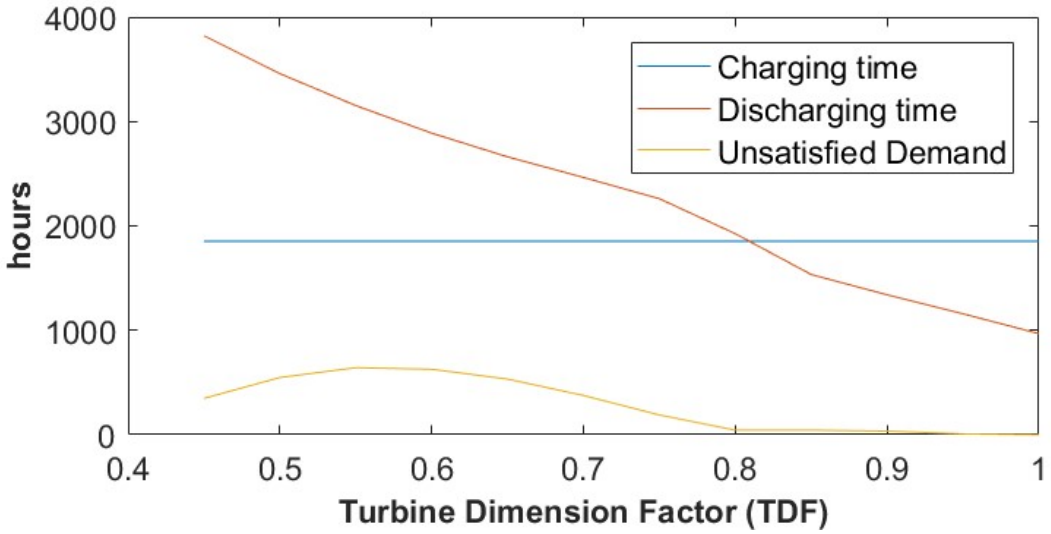


***Figure 6.5 Compression and Turbine working hours as a function of the Turbine Dimension Factor***

### 6.1.3. Storage utilization

If the focus is now directed to the storage units, another family of parameters can be investigated, and in particular the difference between the maximum and the minimum state of charge of each reservoir (in the corresponding measure units) during the yearly simulation. If such operation is useful to have a first idea of the size of the accumulators in each case, the actual dimensions will probably be reduced to all the redundant elements. However, since the cost function of these elements takes their size as the most relevant input (as it will be discussed in the economic section, Chapter 7), and the cost of the storage components is not negligible at all, the consequent minimization is an objective that should be pursued.

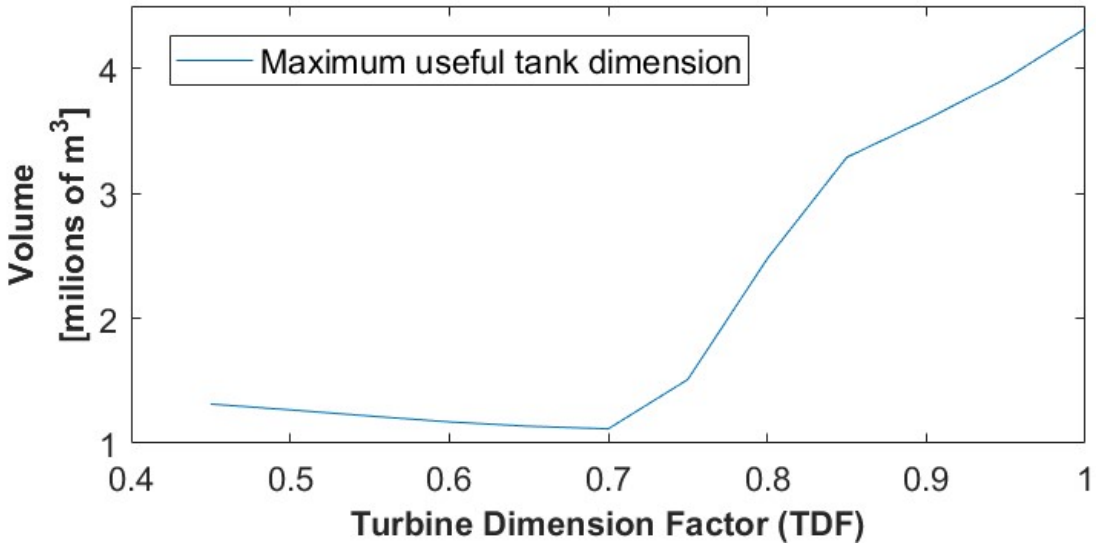


***Figure 6.6: Maximum useful dimension of the air tank as a function of the Turbine Dimension Factor***

As it can be noticed in Figure 6.6, the air tank size has an optimum value, as expected from the previous considerations, for TDF=0.7. Indeed, for smaller Turbine Dimension Factors, the possibility to exploit the air reservoir is limited by the turbine itself, leading to store more air than necessary; for higher values the air volume rises, since the average residence time inside the tank increases due to the lower turbine operative hours. It is useful to introduce already the modularity of the air storage

system, requiring more tanks to obtain the desired capacity, and leading to an almost linear cost function.

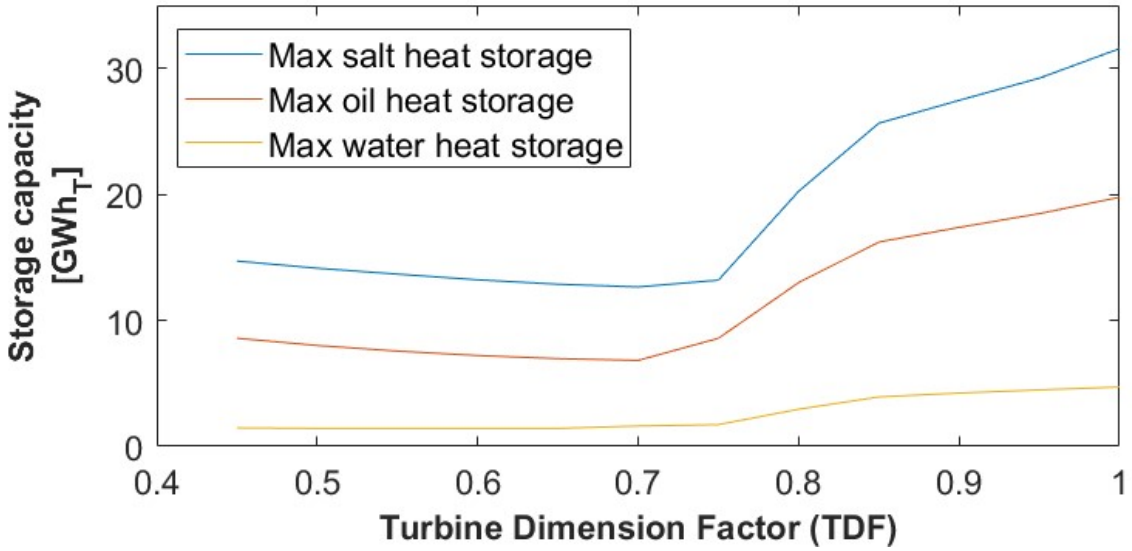


***Figure 6.7: Maximum useful dimension of the molten salts, of the oil and of the water thermal storage as a function of the Turbine Dimension Factor***

***Table 6-1: Energy density both on a mass and volume basis for the thermal fluids***

| | $kWh\ /\ kg$ | $kWh\ /\ m^3$ |
|---|---|---|
| Molten salts | 0,137 | 260,4 |
| Diathermal oil | 0,136 | 122,3 |
| Water | 0,064 | 63,9 |

Looking at Figure 6.7, it is important to notice that the measure unit of all the thermal storage components is $GWh_T$, and thus not the physical volume occupied by the module. The latter can be addressed by means of Table 6-1. Secondarily, even though the water thermal trend seems monotone, it actually presents a minimum too, for TDF=0.65. The minimum of the other two tanks is for TDF=0.7, last value before all functions strongly increase. The reason behind this trend can be better understood observing the state of charge of the heat tanks during the year, as shown in the following Figure 6.8, Figure 6.9 and Figure 6.10.

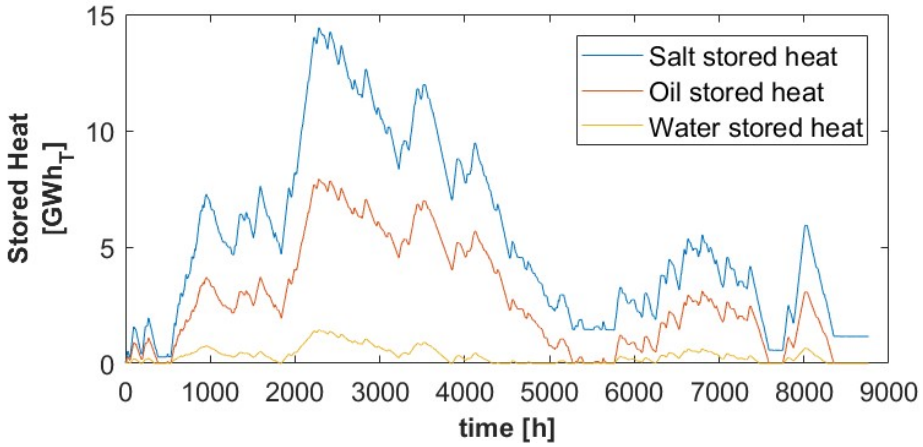


***Figure 6.8: State of Charge of the thermal storage units for a Turbine Dimension Factor of 0.5***

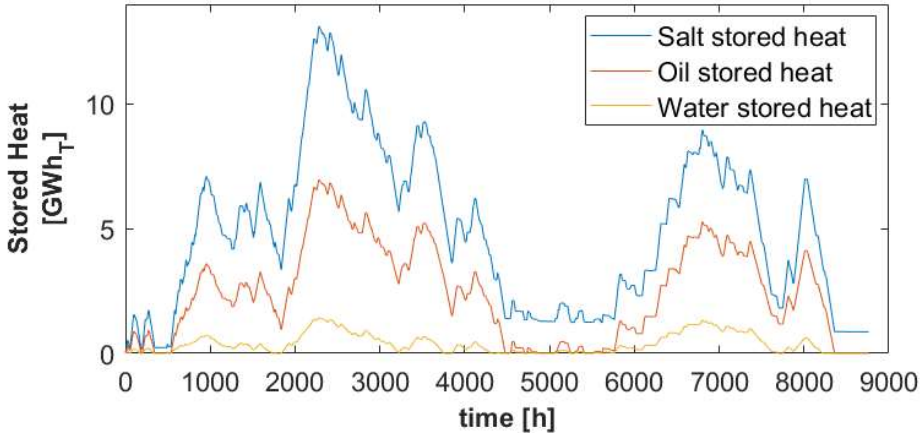


***Figure 6.9: State of Charge of the thermal storage units for a Turbine Dimension Factor of 0.65***

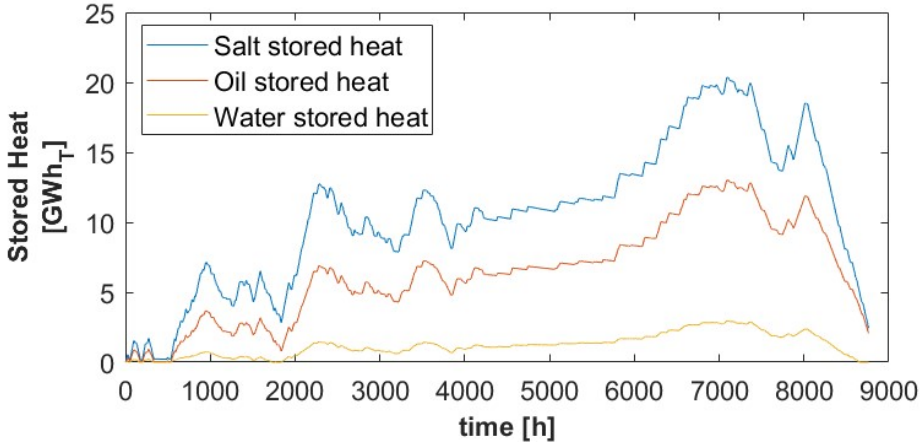


***Figure 6.10: State of Charge of the thermal storage units for a Turbine Dimension Factor of 0.8***

For the last case, the comparison is made with the same simulation but with the previous initial condition and, as it can be immediately noticed in Figure 6.11, the difference is negligible. The only parameter affected by the initial condition is the round-trip efficiency, even though once it has been corrected as previously explained, such difference is only of the order of a couple percentage points.

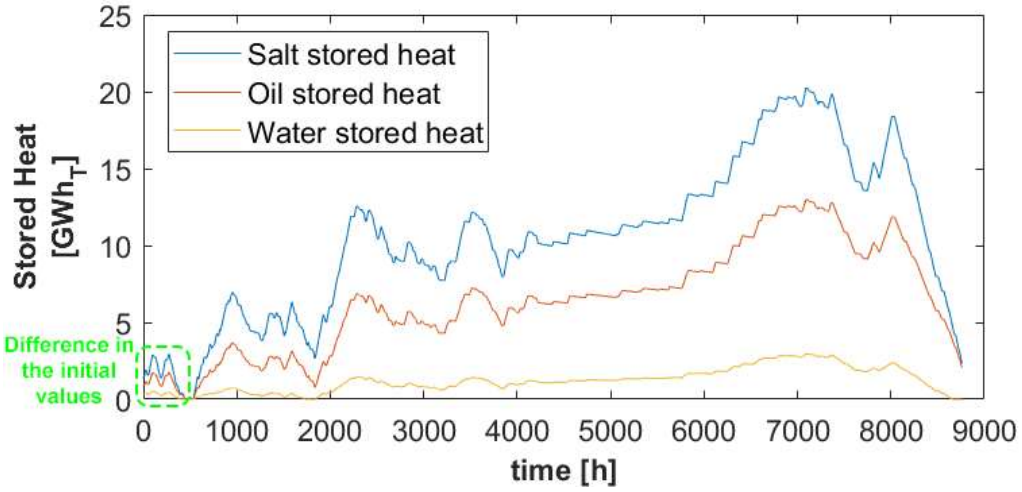


***Figure 6.11: State of Charge of the thermal storage units for a Turbine Dimension Factor of 0.8, for the previous considered initial condition: the difference can be slightly noticed only at the beginning***

The continuous use of small turbines avoids stagnation in the thermal reservoirs, resulting in reasonable storage maximum capacities. Increasing the size of the turbine, the energy used in every discharge step increases proportionally to the decrease of working hours of the turbine, keeping an almost constant energy output. With a TDF of 0.65, the proportion between the charge and the discharge of the CAES results balanced, with an optimal use of the maximum size of the heat storage units. For even bigger turbines, the seasonality of the wind source strongly affects the behaviour of the storage system, affecting strongly the size of the heat reservoirs. However, only in the latter case the hours of unsatisfied expansion drop down to zero, making possible the expansion in the final part of the year, as it can be seen in Figure 6.11.

### 6.1.4. Round-trip efficiency

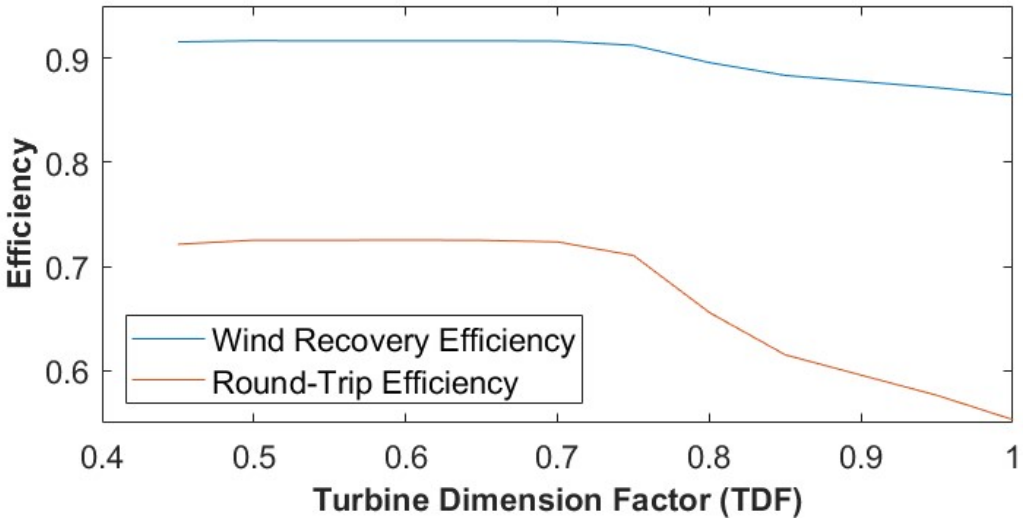


***Figure 6.12: Round-trip and Wind Recovery efficiencies as a function of the Turbine Dimension Factor***

Last but not least, the ratio between the electric output with the CAES system and without it is computed, resulting in a value, the Wind Recovery Efficiency, which is an overall index of the effectiveness of the energy conversion from the wind turbine. Such value has nothing to do with the Round-Trip efficiency, the ratio between the energy expanded in turbine over the energy used in compression, which is represented too in Figure 6.12, but considers the final electricity sold to the grid with respect to the wind generated power.

$$\eta_{WR} = \frac{E_{with\ CAES}}{E_{without\ CAES}}, \qquad \eta_{RT} = \frac{E_T}{E_C}, \qquad \eta_{WR} = \frac{E_{to\ grid} + E_{to\ CAES} * \eta_{RT}}{E_{without\ CAES}} \tag{6.5}$$

The WRE can be seen as a weighted average of the energy that enters the storage system for the average input-output efficiency, and the energy given directly to the grid with 1 as an efficiency. An increase in such value must not be necessarily associated to an increase in the average round-trip efficiency, but can simply mean that less energy is given to the CAES. However, with its limits, such index is very useful when comparing

different solutions among the others, because of its strict relation with the RTE, as very clear in the present case.

The reason of the final drop in the efficiency has to be sought on one side in the increased thermal losses due to the higher mean amount of heat stored, while on the other side in the asymmetry already introduced in the state of charge of the tanks. The latter involves in particular a certain amount of energy imprisoned in a tank but useless alone. Such "Trapped" energy becomes more important when the conditions necessary to the expansion become more restrictive. Furthermore, all the efficiencies are corrected taking into account the difference in the state of charge of the reservoirs between the first and the last hour of the year, pretending to compress or expand air restoring the initial most binding condition.

A turbine dimension factor of TDF=0.65 seems to be the optimising result from the sensitivity analysis preformed; not only is the value which maximises the round-trip efficiency, but all components present a minimum in their dimensioning for very close values with respect to the chosen one. However, it would be only a partial result to consider such value without an analogous analysis regarding the compressor side. Since the nominal efficiency of the CAES is known, consequently the nominal power of the turbine is known and equal to 35 MW.

$$P_T^{nom} = P_C^{nom} * \eta_{CAES}^{nom} * TF = 75\ MW * 0.72 * 0.65 \approx 35\ MW \tag{6.6}$$

## 6.2. SENSITIVITY TO COMPRESSOR SIZE

Now that the optimal ratio between the nominal power of the turbine and the compressor seems to be obtained, a further optimisation has to involve the ratio between the latter and the rated power of the wind farms nearby. It is important to underline that even though the relative dimension of the turbine side is fixed with respect to the compressor one, increasing the latter also the former will result proportionally bigger, accordingly with the fixed Turbine Dimension Factor.

### 6.2.1. Equation setup

Consistently with the previous analysis on the turbine, such ratio will be defined as the Compressor Dimension Factor and will be the independent variable of the following study.

$$CDF(Compressor\ Dimension\ Factor) = \frac{P_C^{nom}}{P_{max,field}} \tag{6.7}$$

In the present circumstance, we assume to limit this value between 0.25 and 0.6. While the lower bound was chosen in order to avoid air mass flow rates that would be troublesome for the compressor to manage, and thus meets a turbomachinery limit, the upper bound is fixed by the maximum acceptable distance from the moving average, e.g. the maximum excess with respect to the average "flat" production. Such value, which in particular is CDF=0.59, is the one necessary in order to perform the genuine peak shaving as exposed in the previous chapter. As an output of the previous analysis, the selected TDF is equal to 0.65, although afterwards this hypothesis will be integrated in a more general context.

### 6.2.2. Power output

The first parameter addressed is the standard deviation of electricity injection in the grid, parallelly with what was previously done.

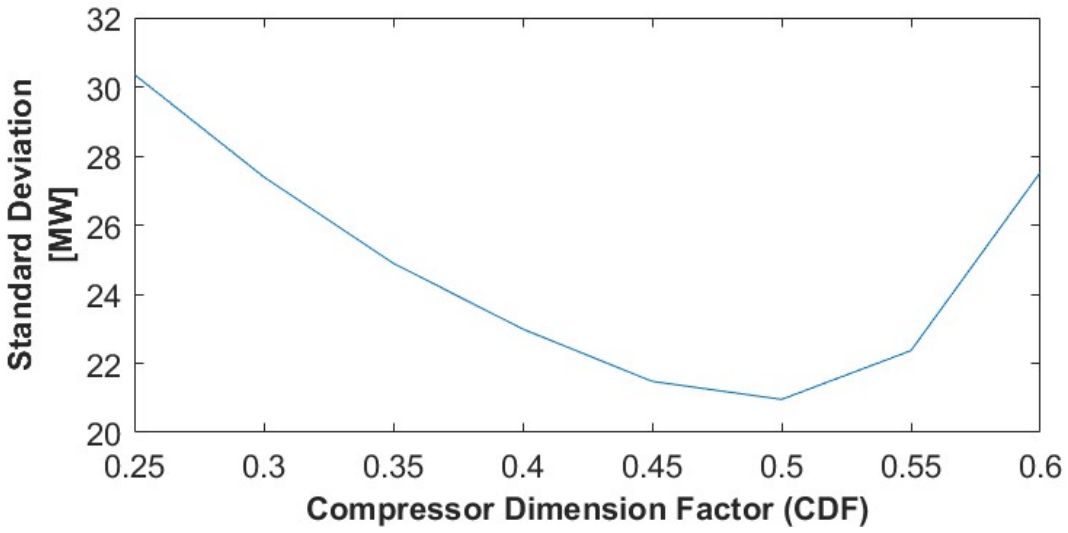


*Figure 6.13: Standard deviation as a function of the Compressor Dimension Factor, TDF=0.65*

This time a minimum is present in the distribution, as shown by Figure 6.13. The reason has to be found once again in two opposite trends occurring increasing with the compressor size. The former is the "strength" of the compressor to flatten the energy released to the grid when activated, as well as its absolute energy flexibility range. The latter is the decreasing number of hours at which the compressor is activated, as shown by the following Figure 6.14.

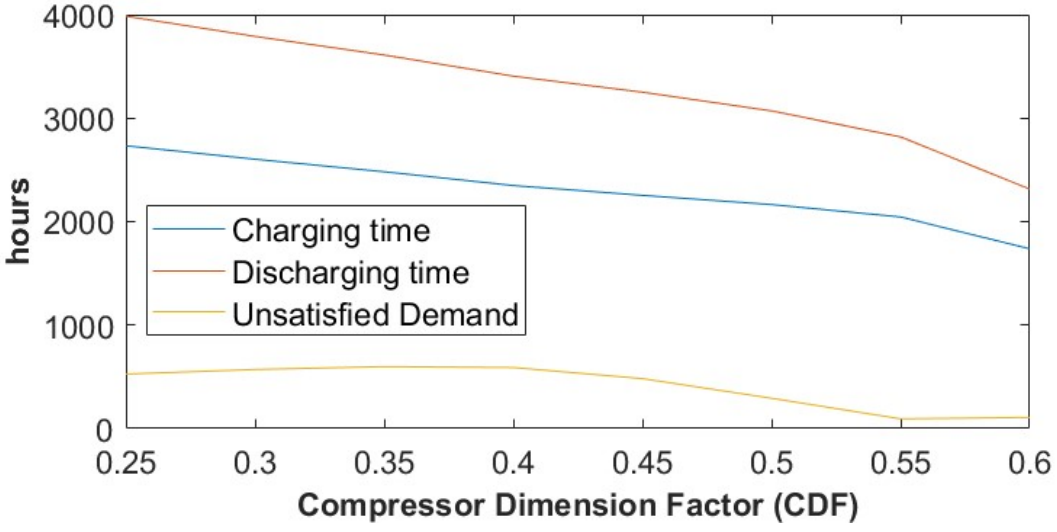


*Figure 6.14: Working hours as a function of the Compressor Dimension Factor, TDF=0.65*

In particular the combination of these two effects can be better observed focusing on the power released to the grid for two different values (Figure 6.15 and Figure 6.16).

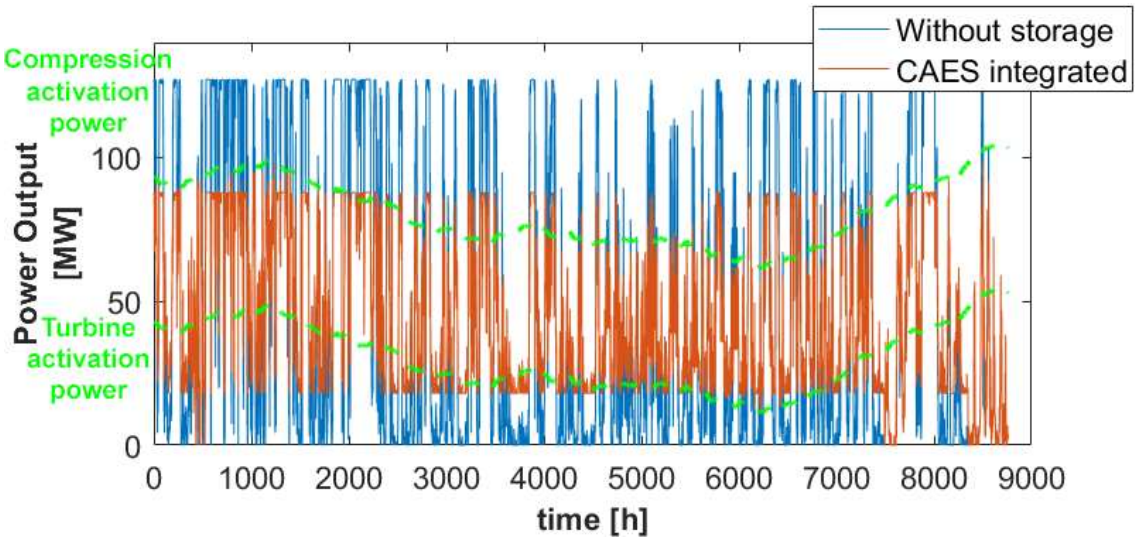


***Figure 6.15: Power output for a Compression Dimension Factor of 0.3 both with (red) and without (blue) storage system***

It is worth noticing that with small turbomachinery, as in Figure 6.15, the attempt to follow the moving average is almost useless, since their size is sufficient only to damp the most extreme values.

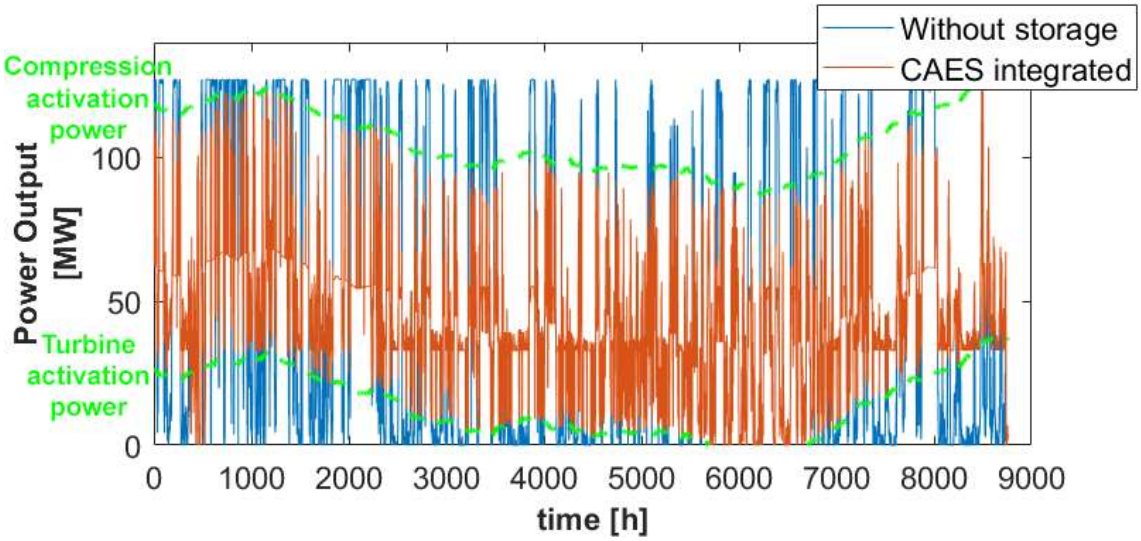


***Figure 6.16: Power output for a Compression Dimension Factor of 0.55 both with (red) and without (blue) storage system***

On the other hand, with values of CDF near to the minimisation of the standard deviation of the power released to the grid, as in Figure 6.16, the moving average is

followed much more accurately. The resulting profile of power injected to the grid is more flattened

### 6.2.3. Storage utilization

Turning the attention to the storage units, it is easy to believe that with the increase of the CDF, and thus of the mass flow rate involved, the heat stored per hour increases, leading to capacities that are about twice the ones necessary for small machines, as proven by the following Figure 6.17 and Figure 6.18.

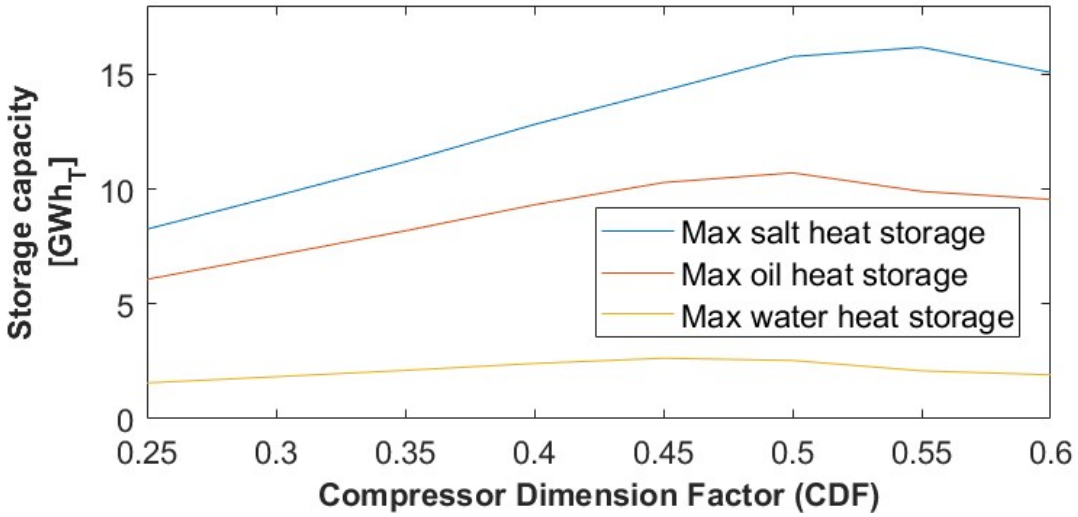


***Figure 6.17: Maximum useful dimension of the molten salts, of the oil and of the water thermal storage, TDF=0.65***

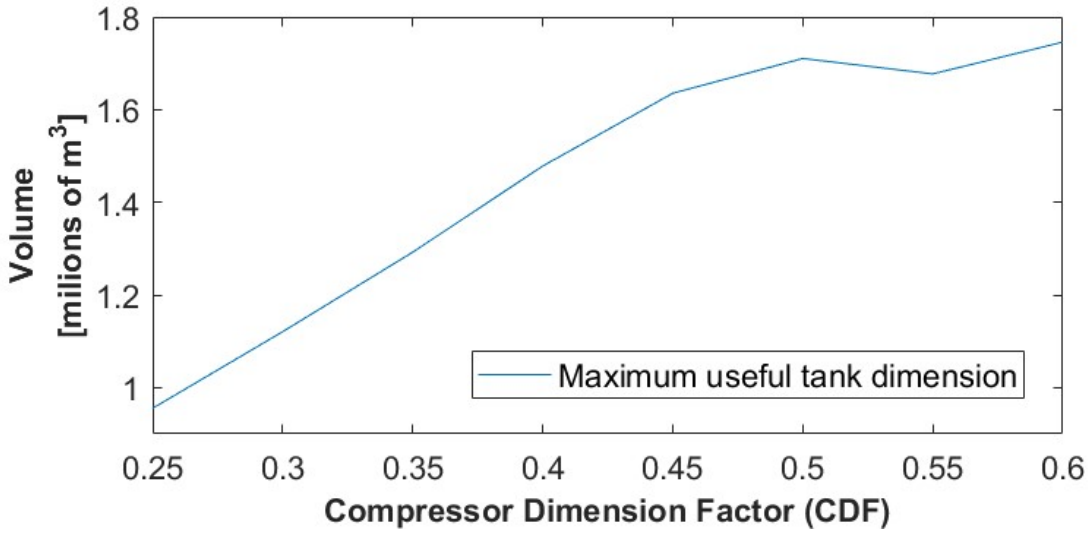


***Figure 6.18: Maximum useful dimension of the air tank as a function of the CDF, TDF=0.65***

All the considerations made for the thermal storages can be extended also to the underwater tank. Furthermore, the maximum is directly dependent on the maximum stored and recovered electrical energy, as proved by the following Figure 6.19.

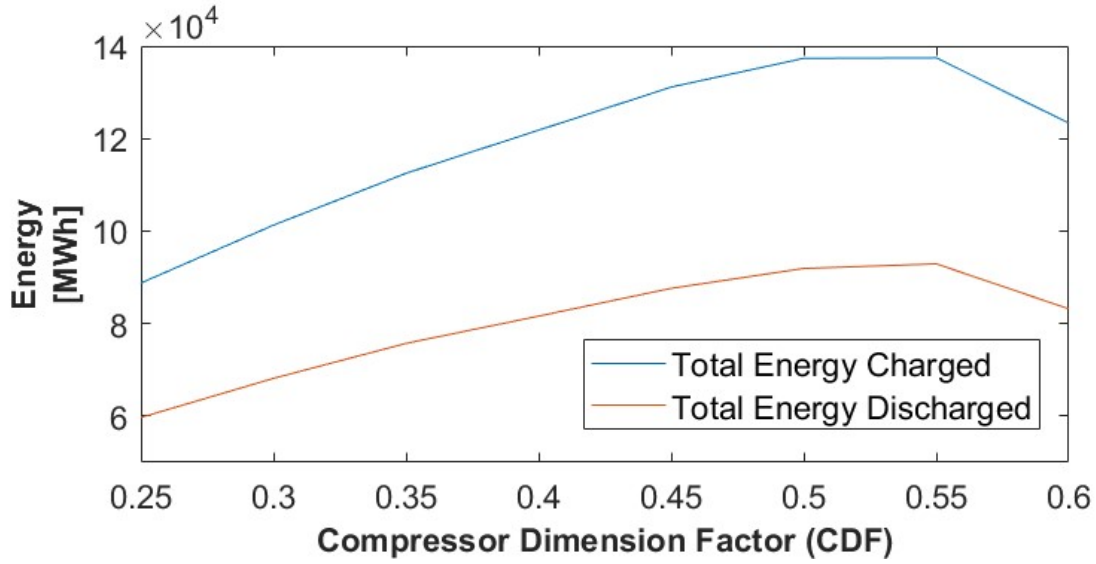


***Figure 6.19: Energy charged and discharged as a function of the Compressor Dimension Factor, TDF=0.65***

### 6.2.4. Round-trip efficiency

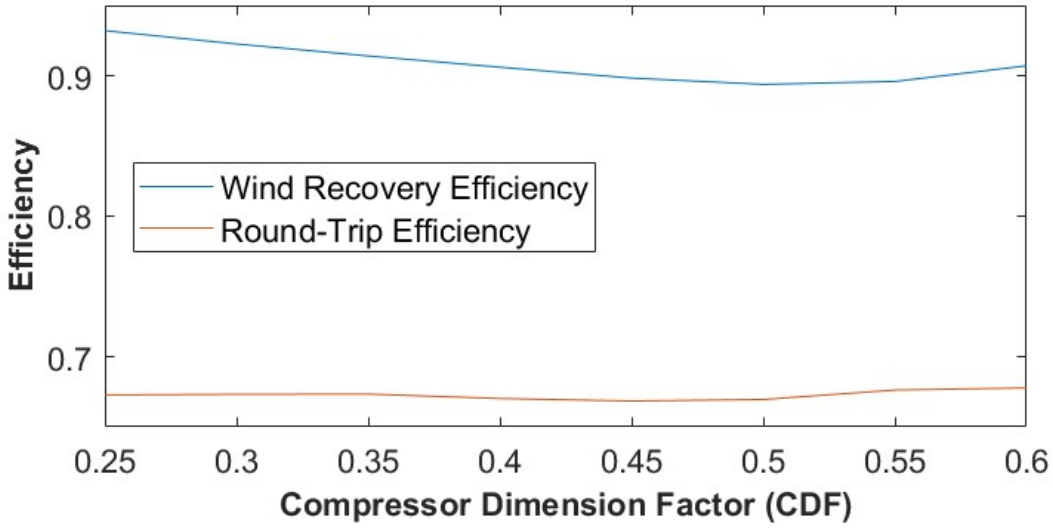


***Figure 6.20: Round-trip and Wind Recovery efficiencies as a function of the Turbine Dimension Factor, TDF=0.65***

Finally, the variation of the round-trip efficiency and of the wind recovery efficiency can be computed and represented in Figure 6.20. It is interesting to notice that this time, the decrease in the latter is not influenced by the former, almost constant (i.e. decoupled from a real power input), but only to the increase of the utilization of the storage. Another consideration of paramount importance is the value of the round-trip itself, slightly lower than the 70% expected from the previous preliminary optimization process. The explanation is that the maximum is hidden between the last two values of the simulation, as only a more general view can reveal.

Finally, to ensure the technical feasibility of all the proposed configurations, the number of times the turbine is activated from a cold start up is checked, obtaining usually very reasonable results, between 230 and 270 times a year.

## 6.3. COMPLETE OPTIMIZATION

As proven by the previous results, a separate analysis on the dimensions of turbine and compressor is not sufficient to optimise the whole CAES configuration, since these two parameters are strictly related. For the following optimisation, both analysis were

performed several times, and the results were crossed in order to have a complete map of the matching between compressor and turbine.

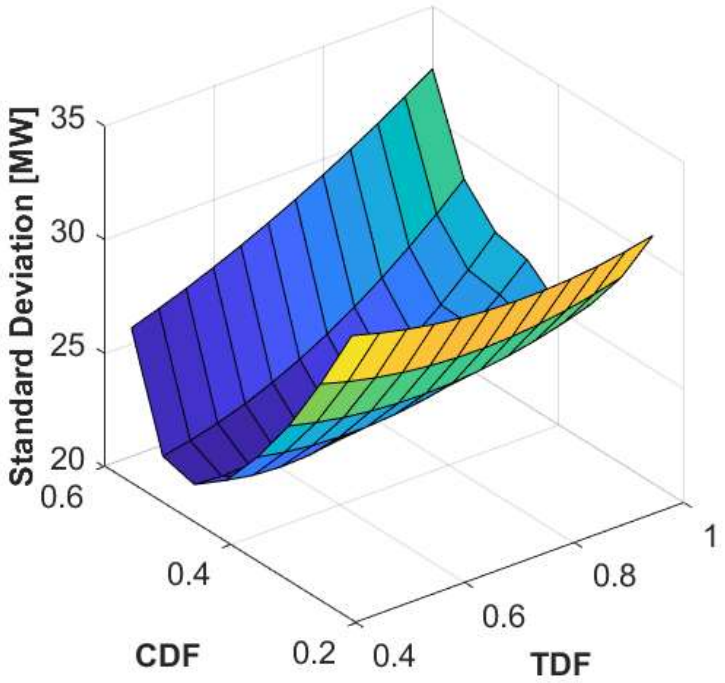


***Figure 6.21 Standard deviation mapped crossing CDF = [0.25 0.6] with TDF = [0.45 1]***

Figure 6.21 shows the standard deviation of electricity injection into the grid in all the function domain, highlighting together the two already delineated parallel trends: the constant increase of the standard deviation with the size of the turbine and the presence of a minimum with the growth of the size of the compressor. It is useful to remember that the standard deviation of the wind field without any enhancement is of 48.97 MW. It can be seen as the mould of the energy produced, remembering that the turbine always works to flatten the distribution.

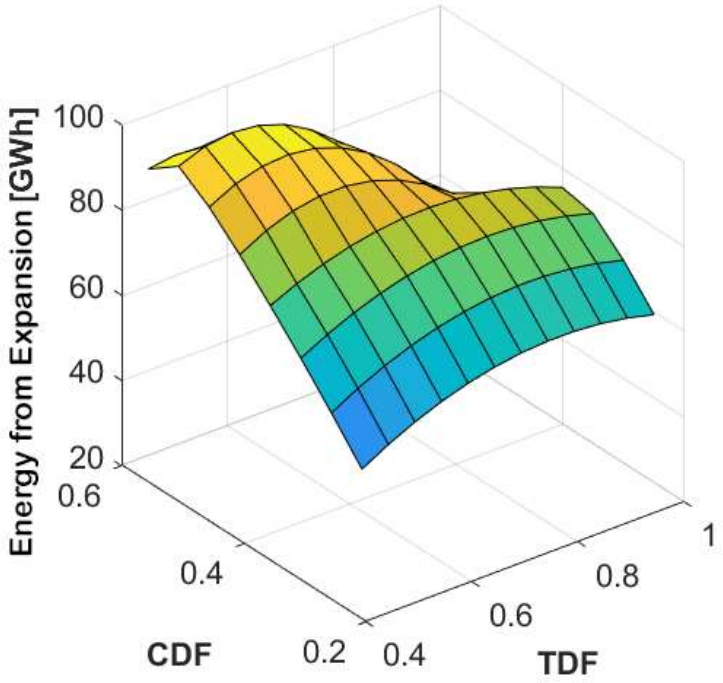


***Figure 6.22: Energy from the turbine mapped crossing CDF = [0.25 0.6] with TDF = [0.45 1]***

It is interesting to notice in Figure 6.22 that such surface presents a drop where both machines are huge, due to the combined effect of less often compression and expansion. Nevertheless its minimum is where both machines are small, resulting in smaller energy fluxes, i.e. an efficient system that manages small amounts of energy.

Finally, in Figure 6.23, the round-trip efficiency can be investigated. In this case we can notice a diagonal line where the efficiency is maximum. Any departure from this optimal line will result in unbalances between the thermal units that lead to non-optimal values in such performance parameter.

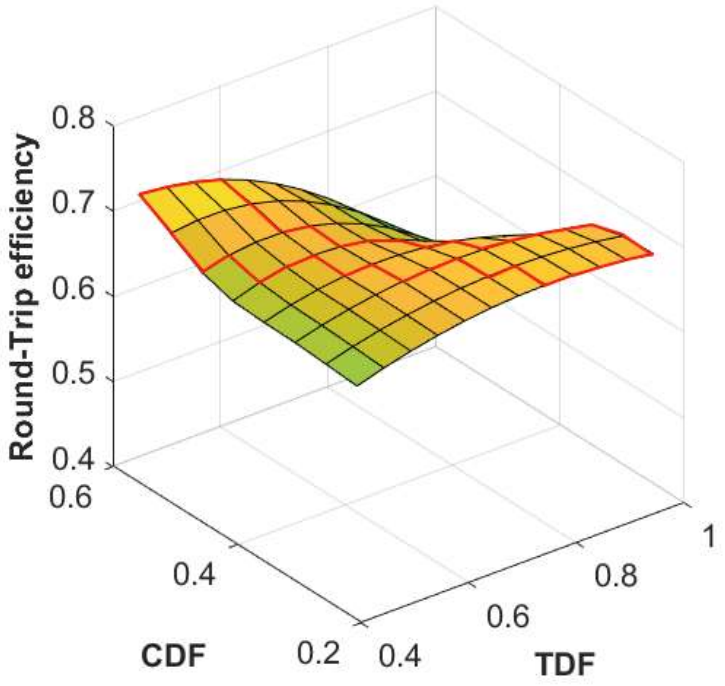


***Figure 6.23: Round-Trip efficiency mapped crossing CDF = [0.25 0.6] with TDF = [0.45 1]***

# 7. ECONOMIC ANALYSIS

In order to allow an innovative technology to spread out, the financial aspects cannot be neglected. If energy storage will become or not an essential element in power systems, this depends a lot on the economic feasibility of the considered solution. For this reason it has to be clarified which are the most expensive elements and if it is possible to reduce them in a cost effective way. In the present chapter these aspects are taken into account, always in a differential analysis with respect to the wind fields without the CAES system. However, before a detailed analysis will try to give an answer to such question, it is important to presume some preliminary considerations.

## 7.1. INTRODUCTION

First of all it is important to understand that the possibility to store electric energy like any other kind of good, is a very precious service and that should be accordingly rewarded. Furthermore, the whole system considered will be very expensive: not only the turbomachinery and the thermal storage units will represent together an important cost, but also the floating structure and the air pipe connected to the bottom of the sea are equally important. Moreover, as any energy transformation device, there is a round-trip efficiency to consider, implying that a part of the energy that was stored and thus not payed will simply be dissipated, wasting the possibility to sell it.

Such clarification is needed in order to understand that without pursuing the economic result from the beginning, it is impossible to achieve cash flows higher than those obtained without CAES. The main reason is that the considered wind farms are small enough to not affect with their production the zonal energy cost, and consequently there is no relation between wind source availability and price of electricity. Of course, such reasoning will be valid until the number of energy production devices relying on the same source can still be neglected compared to the whole electricity generation. However, since the number of wind farms is increasing exponentially, it seems reasonable that in a near future such assumption could fall. On the other hand, the

Transmission System Operator (TSO) could pay less unpredictable energy producers and give the delta to those who can control it, either as a function of the standard deviation or proportionally to the instantaneous difference with the moving mean of the production. Or finally, the MSD market will extend the possibility to dispatch well payed ancillary services also to storage systems [53].

These and many other storage incentive solutions could be employed, but they all require huge investments that will consequently and reasonably be subtracted from the renewable sector. Nevertheless, there is only one possibility where there is no need for such financial effort, and this is doing arbitrage on the electricity market. In this way, which has nothing to do with the technical advantage of employing a storage unit, electricity can be stored when the price is low and sold when the price is high, exploiting the natural fluctuations in the energy market caused by unbalances in the grid.

The following analysis will compare these two main alternatives, the economic benefits coming from arbitrage activity with the incentives funding flattening the electricity distribution. Nevertheless, the first step has to present at least a rough estimation of the investment cost of the Underwater Adiabatic CAES system.

## 7.2. COST ANALYSIS

The total investment cost is made up by all its component, some of which are fixed for all the considered configurations, while others change accordingly with the characteristic dimension of the component. In order to perform a correct analysis, not only were required the prices of the fixed elements like the heat exchangers, but also the cost functions of those parts most affected by changes in the different configurations, like the compression train or the thermal capacity of the reservoirs. The variable costs will partially depend too on the configuration adopted, but have to be corrected considering the inflation and actualization rate. The final objective is thus to have a capital expenditure that depends strongly on the case study considered, in order to choose the most cost-effective solution.

### 7.2.1. Turbomachinery

For each axial compressor, the following equation can be considered valid:

$$Cost\ [€] = 450 * \frac{P\ [kW]}{\dot{m}^{0.31}} \tag{7.1}$$

Where the mass flow rate $\dot{m}$ is expressed in $[kg/s]$. As it can be noticed, the exponent of the denominator takes into account the size factor, making such function non-linear [44].

For the centrifugal compressor, another cost function was used, made on purpose for radial compressors, and considering their much smaller size with respect to the power absorbed:

$$Cost\ [€] = 6490 * (P\ [HP])^{0.62} \tag{7.2}$$

Where in this case the power refers to British Horse Power. Also here the non-linearity is assured by the power exponent. However, even though the functions are quite different, for the considered range of mass flow rate, for comparable power we obtain similar costs [54].

For the expander, since we considered an axial turbine, the cost function is very similar to the one of the axial compressor, and in particular [18]:

$$Cost\ [€] = 500 * \frac{P\ [kW]}{\dot{m}^{0.363}} \tag{7.3}$$

### 7.2.2. Heat storage

The heat storage represents certainly the most important voice in the total investment cost. First of all, starting from the requirements on each thermal unit, knowing the specific heat at constant pressure and the temperature difference, the amount of all the fluids required is computed and consequently their cost, as summarised in Table 7-1.

***Table 7-1: Main thermal and economic features of the thermal fluids and their accumulators***

| **Molten salts** | | |
|---|---|---|
| *Fluid cost* | 0,7 | €/kg |
| *Specific heat* | 1,55 | kJ/Kg K |
| *Accumulator cost* | 26 | $/kWh |
| *Density* | 1900 | kg/m$^3$ |
| **Diathermal oil** | | |
| *Fluid cost* | 1,5 | €/kg |
| *Specific heat* | 2,39 | kJ/Kg K |
| *Accumulator cost* | 625 | €/m$^3$ |
| *Density* | 770 | kg/m$^3$ |
| **Water** | | |
| *Fluid cost* | negligible | €/kg |
| *Specific heat* | 4,186 | kJ/Kg K |
| *Accumulator cost* | 500 | €/m$^3$ |
| *Density* | 1000 | kg/m$^3$ |

Afterwards, the size of each accumulator is obtained, either directly from the required heat capacity, or by means of the density of the fluid in order to obtain the volume necessary to store the fluid. It is useful to remember that, while oil and water make use of a thermocline system to operate, for the molten salts two different tanks are required, doubling their overall cost. Furthermore, some correction factors are used, either to convert from dollars to euros (1.15 $/€), to take into account the variation in the specific heat at constant pressure (+30% for oil in the considered range) and last but not least to consider a scale factor (0.7) for the correlations regarding the size of the tank. Finally, the cost of each heat storage unit is further incremented of 10% to consider piping, fixed-speed pumps and electric equipment[55][56][57].

### 7.2.3. Underwater air tank

The cost evaluating procedure for the main element of the underwater CAES system is probably also the most difficult to assess. Both solutions previously introduced, the polymeric balloon and the concrete structure, have to be designed for this application and thus very few references are available in literature. However, a

trustworthy analysis considers modular concrete tanks of an inner capacity of 10000 $m^3$, at the price of 40 €/$m^3$ of useful volume each.

### 7.2.4. Heat exchangers

Since the heat exchangers are defined from the design case, their cost depends only on the nominal mass flow rate in compression, and can be evaluated without any function cost that has to consider the model output. In particular, since two different datasheets were available, one for an air-salt heat exchanger and another one for an air-oil heat exchanger, these were considered as reference cases able to estimate the cost of the respective components, shown in Table 7-2.

***Table 7-2: Main thermal and economic features of the heat exchangers***

| **Air-Salt Reference case** | | | **Air-Oil Reference case** | | |
|---|---|---|---|---|---|
| *Surface* | 3580 | $m^2$ | *Surface* | 5390 | $m^2$ |
| *Thermal power* | 66,9 | MW | *Thermal power* | 46,2 | MW |
| *Cost* | 7160 | k€ | *Capital cost* | 1942 | k€ |
| *Heat Transfer coefficient* | 0,7 | $kW/m^2\ K$ | *Heat Transfer coefficient* | 0,4 | $kW/m^2\ K$ |

To relate the cost of the required elements with the original values, once again a scale factor has been assumed, but since the cost of the heat exchangers is strictly related to the useful surface, this time such vale is assumed as 0.9, accordingly with the following:

$$C = C_{ref} * \left(\frac{A}{A_{ref}}\right)^{scale\ factor} \tag{7.4}$$

Finally, since the aftercooler and the inter-refrigerator are much simpler air-water heat exchangers, their cost can be assumed as 40 \$/$m^2$. However, since their $\Delta T_{m,l}$ is less than half the analogous value of the previous two, the surface will result of the same order of magnitude, ensuing nevertheless much cheaper components.

### 7.2.5. Electric and mechanic equipment

Further costs are required for all the electrical converters and cables needed, each scaled with the previous equation (7.5). The reference 80 MW transformer has an investment cost of $800\ k€$, while the chosen 80 MVA alternator costs $3000\ k€$. For the grid connection devices, the mechanical shafts and the transmission system, an overall cost of $20\ k€$.

### 7.2.6. Variable costs

When thinking at variable costs, the main concern is for the Operation and Maintenance (O&M), which is assumed equal to 0.5 €/MWh. Moreover, also some staff is needed, assuming a personnel cost of 100 k€/year, sufficient for up to five workers. Finally, since the risk embedded in the project is huge, an insurance in considered, with an annual premium of 0.5% of the total investment cost.

It is worth remembering that these costs have to be considered for all the lifetime of the CAES systems, and thus will be incremented accordingly with the inflation rate, assumed for Italy equal to 2% coherently with the most updated values coming from the ministry.

### 7.2.7. Other costs

Now that the cost functions of all component are known, a consideration of paramount importance is the physical location of the system itself, supposed on a floating platform on the sea. However, according to references [58], the extra cost resulting from doing so is about half of the sum of all costs considered up to this point. Such cost does not take into account only the piping down to the underwater air tank, the chains down to the bottom of the sea and the floating platform itself, but also the engineering, the start-up costs as well as all the expenses related to the transport of the whole structure of the size of a containership.

### 7.2.8. Total cost

As easily understandable, the overall cost is of the order of magnitude of hundreds of millions of euros. However, as the following Figure 7.1 shows, among the different options in the variation range for both the turbine and the compression size, such value can change hugely.

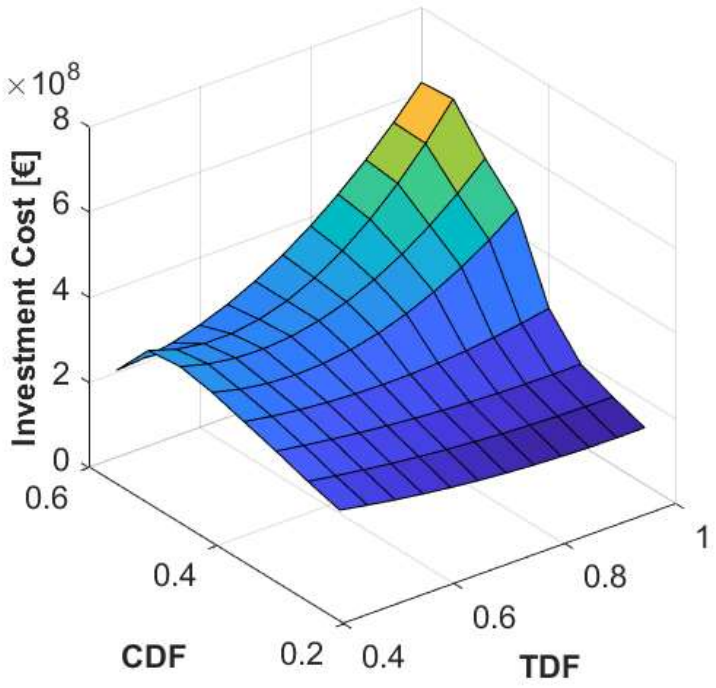


***Figure 7.1: Total investment cost mapped crossing CDF = [0.25 0.6] with TDF = [0.45 1]***

In particular, it is worth noticing from the following Figure 7.2 and Figure 7.3 the cases with smallest and biggest turbomachinery respectively, that one third of the obtained value is due to the floating platform, while of the remaining part about 80% of the cost is due to the raw materials of oil and molten salts. This has to be accounted to the massive amount of these fluids required, of the order of magnitude of the ten thousands of tons. If on one hand this results suggests that the heat storage system is widely over dimensioned, on the other hand there are CSP systems already existing that for eight hours of thermal storage are equipped with even bigger molten salt storage tanks [25].

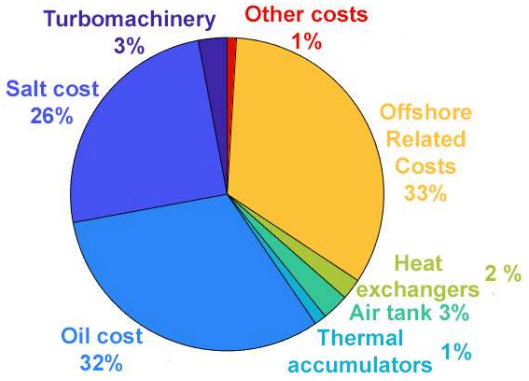


*Figure 7.2: Share of the investment costs for CF=0.25, TF=0.45. Total cost: 198 M€*

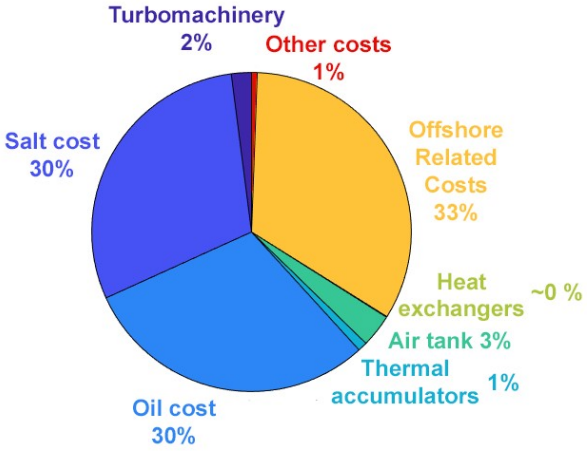


*Figure 7.3: Share of the investment costs for CF=0.6, TF=1. Total cost: 622 M€*

Moving towards the highest investment cost, the relevance of the technical components disappears compared with the cost of the thermal fluids and the offshoring costs. The enormous amount of salt and oil required for the system suggests a possible under-dimensioning of the heat storage units.

## 7.3. REVENUES

Aware of the giant investment cost needed to build the Underwater CAES, the primary concern is to assess the order of magnitude of the revenues obtained either using an arbitrage logic, or relying on different incentives that will become more and more important in the future scenario with increasing unpredictable production and decreasing incentives for the renewables. In particular, it is probable that, similarly to what happened in 2012 [59], in the following years not only renewable energy will be

bought at market price, but rewards and penalties will become common in regulating clean energy production too.

So, in order to perform the following analysis, the hourly data of the electricity price in the Sardinia region is used as input data, assuming that the relative revenues will remain unchanged for the whole lifetime, considering the electricity price constant along the years.

### 7.3.1. Net Present Value

Once all the costs are known and the revenues type defined, the profitability of the investment has to be tested. In particular, cash flows occurring in different years require actualisation before summing them together; positive revenues will be taxed, but until a certain year, an amortisation value equal to a fraction of the initial investment will be considered; at the end of its life the components will be sold, recovering a fraction of the beginning investment. In the following Table 7-3, the indexes used to consider all these effects are summarised.

***Table 7-3: Main economic indexes employed for computing the NPV***

| | | |
|---|---|---|
| *Actualisation factor* | 3 | % |
| *Inflation rate* | 2 | % |
| *Lifetime* | 30 | years |
| *Amortisation limit* | 20 | years |
| *Amortisation amount* | 80 | % |
| *Taxation rate* | 32 | % |
| *Dismission value* | 25 | % |

The result of the presented calculation is an overall actualised cash flow, solution of the following equation:

$$NPV = \sum_{t=0}^{Life\ Time} \frac{Net\ Cash\ Flow_t}{(1 + Actualisation\ factor)^t} \tag{7.6}$$

As we can notice from the following Figure 7.4, all values are in absolute value slightly higher than the investment cost, meaning that not only the system is very

expensive, but making it following the profile levelling logic it does not even produce positive cash flows, coherently with what previously written. Exactly for this reason then, either an arbitrage logic is required or a continuous support from incentives is needed.

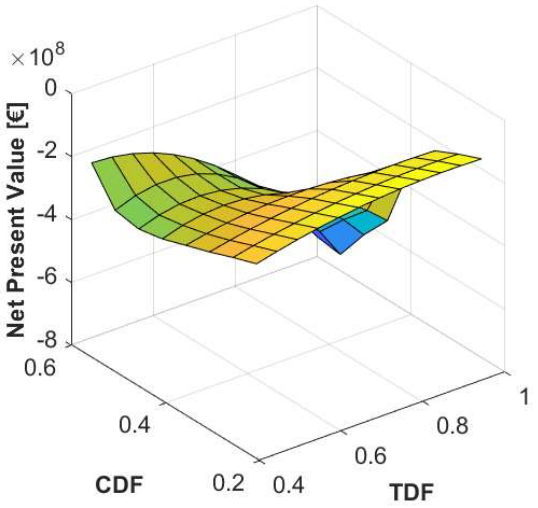


***Figure 7.4: Net Present Value mapped crossing CDF = [0.25 0.6] with TDF = [0.45 1]***

Finally, in the following Figure 7.5, the yearly revenue needed to reach the breakeven at the end of the life is computed, revealing that some tens of millions are required in order to reach such ambitious objective.

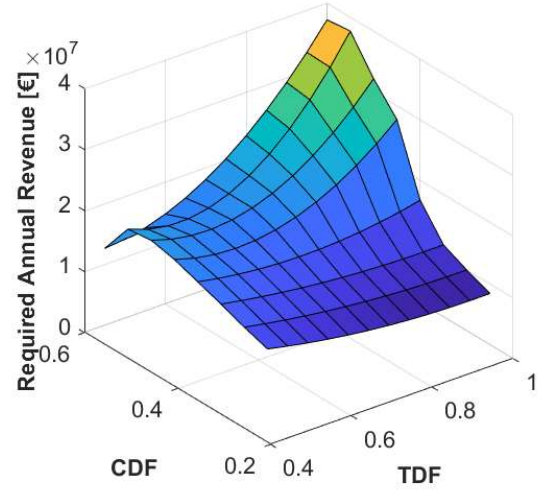


***Figure 7.5: Annual Revenue Required mapped crossing CDF = [0.25 0.6] with TDF = [0.45 1]***

### 7.3.2. Arbitrage

The general definition for arbitrage refers to it as buying and selling the same product to the same market at different times, exploiting a good's price variation to generate a profit. Applying it to the electric market, this means that energy produced by the wind field will be normally sold to the grid if the hourly regional price will fall inside a certain bandwidth. Above such boundary the price is high enough to exploit also the energy stored in the CAES, expanding air and selling also the extra energy. Under the inferior limit, if the wind energy allows it, the electricity will be compressed and only the remaining part will be sold to the grid. Following this logic, however, will not stabilise the grid, but will result in a wider fluctuation range. Nevertheless, since to perform the compression process the wind source availability is needed, this will still slightly abate the standard deviation of the distribution.

First of all, it is important to discover the correct amplitude of the bandwidth to exploit for the electricity market. In other words, the extra-price value of k that maximises the annual cash flow, activating the storage system according to the following equations:

$$Charge\ if: \qquad Zonal\ Price \leq Average\ price - k \tag{7.7}$$

$$Discharge\ if: \qquad Zonal\ Price \geq Average\ price + k \tag{7.8}$$

To do so, in order to avoid an analysis with three degrees of freedom, not only expensive from a computational point of view, but also difficult to understand in its results, one particular cases is chosen. This simulation was performed in order to have a general overview on the variables interested by k, however the order of magnitude of the results does not encourage any deepening at all. To obtain the most general results, a compressor and turbine matching is chosen near to the centre of the region, with $CDF_2 = 0.4$ , $TDF_2 = 0.6$. As confirmed by the following results, a maximum is found. This is due to the increase in the marginal revenues with k, as well as a decrease in the energy stored and expanded by the system.

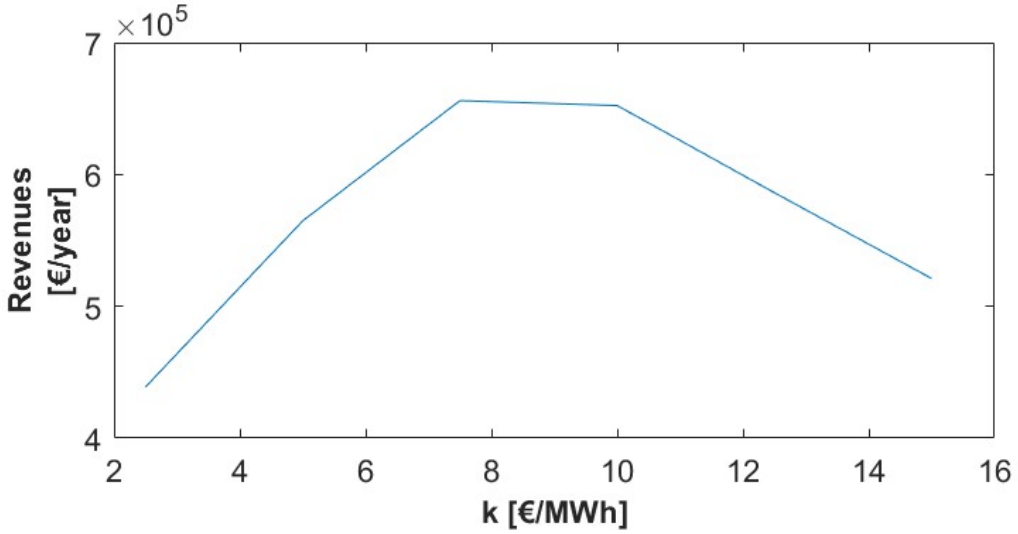


***Figure 7.6: Yearly revenues obtained by arbitrage changing the activation extra-price, CDF=0.4, TDF=0.6***

The optimum value for equations (7.9) and (7.10) is found for $k = 7.5\ €/MWh$, and chosen for the following analysis in order to evaluate the profitability for some possible configurations.

At the beginning, the compressor size is varied, keeping constant the turbine relative dimension. Figure 7.7 shows the obtained results, consequence of the fact that with bigger turbomachinery it is possible to exploit more intensively the oscillations in the price of electricity, and consequently increase the incoming revenues.

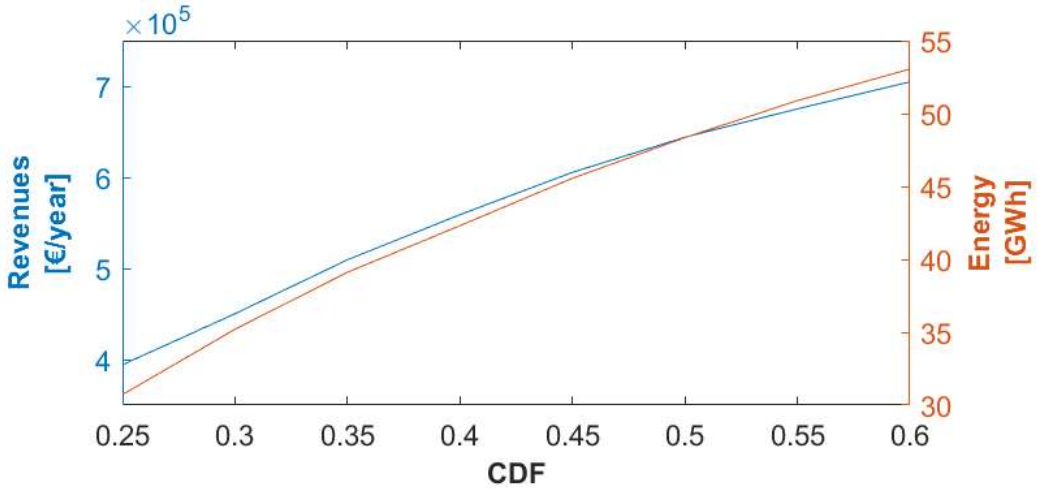


***Figure 7.7: Energy output plotted together with the yearly revenues obtained by arbitrage changing the Compressor Dimension Factor. TDF=1***

On the other hand, a second analysis can be performed increasing the relative dimension of the turbine. The value of the compressor is chosen accordingly with the one that maximised the previous study (CDF=0.6), and the results are shown in Figure 7.8. In this case a maximum is present; for bigger turbines the system is empty for most of the time, because of the unbalances between thermal reservoirs, losing the possibility to exploit the few extremely profitable situations in the second part of the year. In particular it can be noticed how the energy obtained from expansion stops growing and then even decreases, sign that even though the turbine is bigger and thus has the possibility to obtain more energy from expansion, this opportunity cannot be exploited.

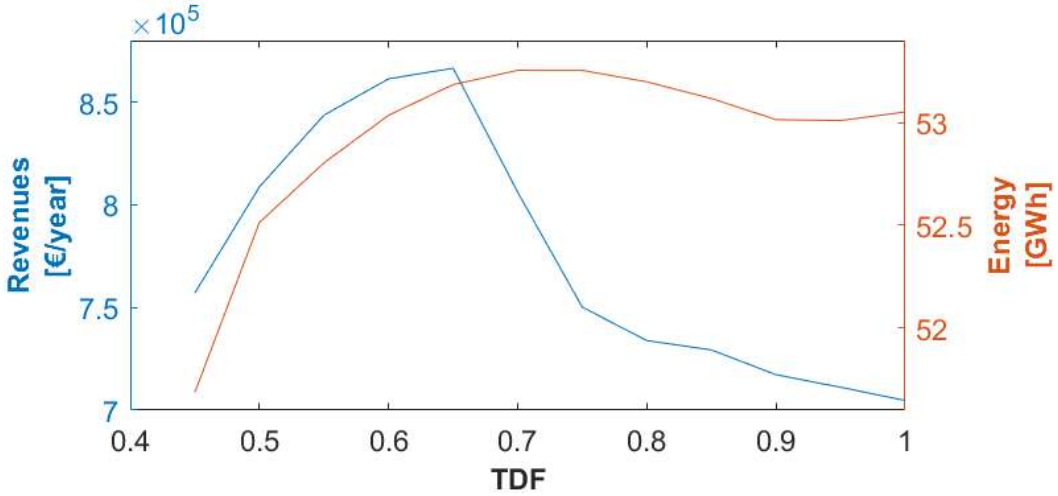


***Figure 7.8: Yearly revenues obtained by arbitrage changing the Turbine Dimension Factor, CDF=0.6***

Unfortunately, as it was expected, there is no possibility to reach the breakeven, even if the overall maximum is slightly higher than the computed values. Since the revenues are almost one order of magnitude below the necessary values leading to the outcome that incentives are the only alternative able to make the CAES technology cost-effective.

### 7.3.3. Incentive

It is now possible to estimate the smallest incentive necessary to pay the service that the CAES offers to the grid. There are many ways then to spread such amount of money on the particular aspect that is appreciated, either the effectiveness in reducing the standard deviation or the closer the final distribution gets to the moving average. For

clearness it was chosen an incentive on the energy produced by the system, a very understandable parameter, which increments its market value.

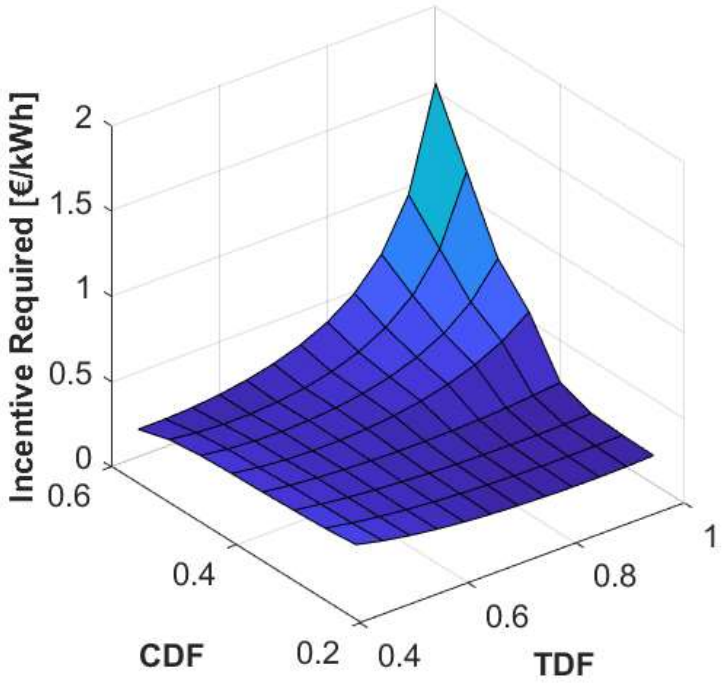


***Figure 7.9: Incentive required mapped crossing CDF = [0.25 0.6] with TDF = [0.45 1]***

As revealed by Figure 7.9, for most of the cases the extra price payed by the TSO on the energy produced by the turbine is about 0.16 $€/kWh$, with minimum values of 0.155 $€/kWh$, comparable with values used to incentive renewable energy [60]. However, when the turbomachinery is big and the thermal storage requires huge investments, such value can rise up to 1.38 $€/kWh$, an order of magnitude more.

## 7.4. COST ABATEMENT

Once understood that the main cost is due to the amount of thermal fluid employed, a possible solution could be to limit the size of the thermal storage units. In fact, with the current configuration, the maximum heat stored is enough to discharge the system for about 650 hours. If it may be consequently seen as over dimensioned, it is useful to remember that it was almost always exploited down to zero, with also hours of

forbidden expansion. Nevertheless, the behaviour of the system can be studied when the number of consecutive hours is reduced down to different values.

### 7.4.1. Storage limited to 250 hours

The first limitation imposed to the whole system is a maximum consecutive discharge time of 250 hours. Now the limitations impose a boundary not only to the expansion, when the CAES is empty, but also to the compression, when at least one thermal reservoir is full. The size of the underwater tank is still on output of the model, and not a further constrain.

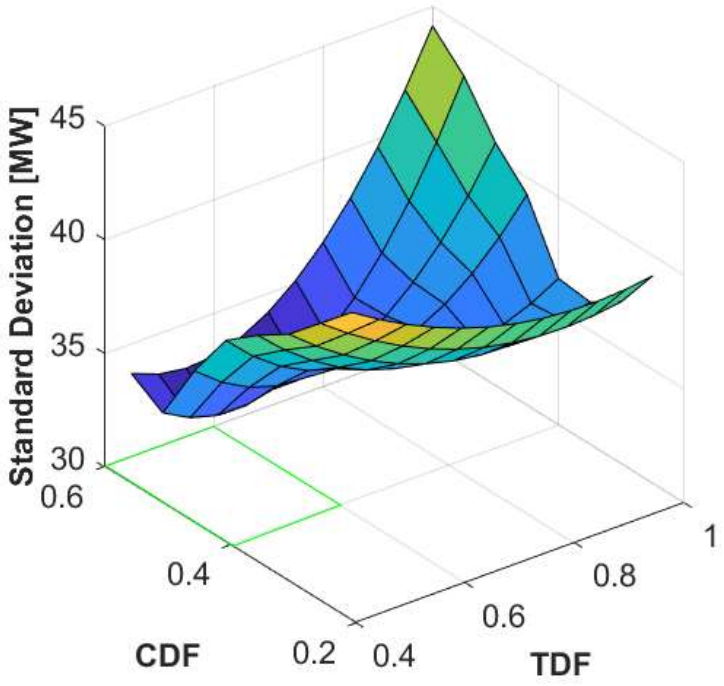


***Figure 7.10: Standard deviation limited to 250 discharge hours mapped crossing CDF = [0.25 0.6] with TDF = [0.45 1]***

Figure 7.10 shows the distortion occurred to the standard deviation. It is of paramount importance to remember now that without any storage, the standard deviation is equal to 48.97 MW. So with the exception of the region highlighted in green, in the rest of the mapped area the standard deviation abatement is very limited.

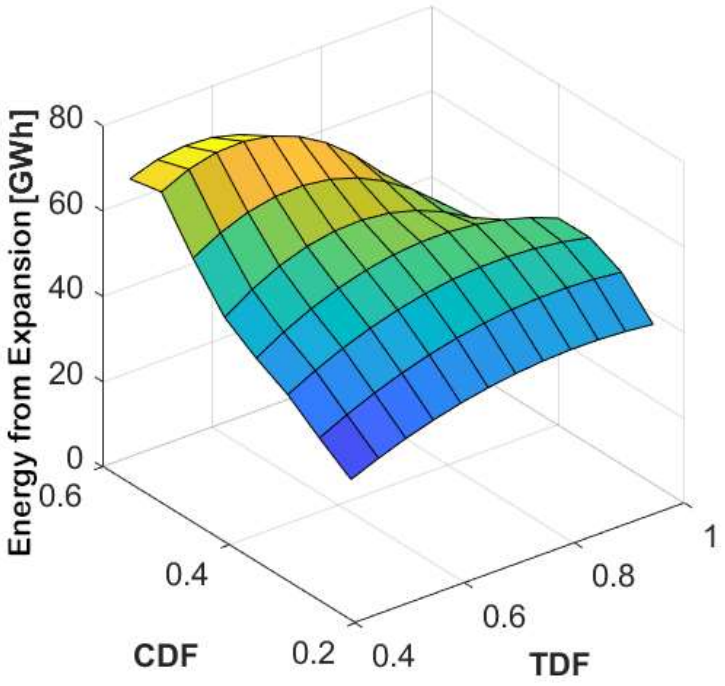


***Figure 7.11: Energy from the turbine limited to 250 discharge hours mapped crossing CDF = [0.25 0.6] with TDF = [0.45 1]***

The reason is proven by Figure 7.11, which shows an almost constant 20 GWh reduction with respect to the analogous unbounded graph. This means that the effectiveness of the distribution flattening is strongly mined by the under dimensioning of the thermal reservoirs. However, the performance indicator that resents most of this limitation is the round-trip efficiency, plotted in Figure 7.12.

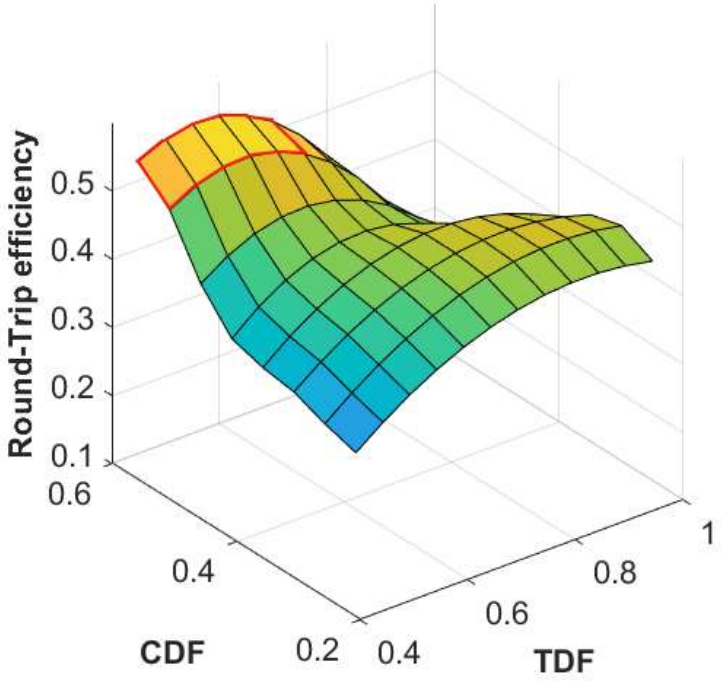


***Figure 7.12: Round-trip efficiency limited to 250 discharge hours mapped crossing CDF = [0.25 0.6] with TDF = [0.45 1]***

The highlighted area is the only region where the energy obtained from the turbine is more than half of the one consumed in compression. The reason for a drop in the round-trip efficiency of at least 20 percentage points is due to the increase in the thermal unbalances introduced by this further limitation. The comparison between the following two yearly thermal profiles explains very well why in some cases the system reaches a condition where it is not able to work anymore (Figure 7.13), dropping down the efficiency. On the other hand in other cases, the thermal limitation works well (Figure 7.14), allowing a correct charge/discharge of the system.

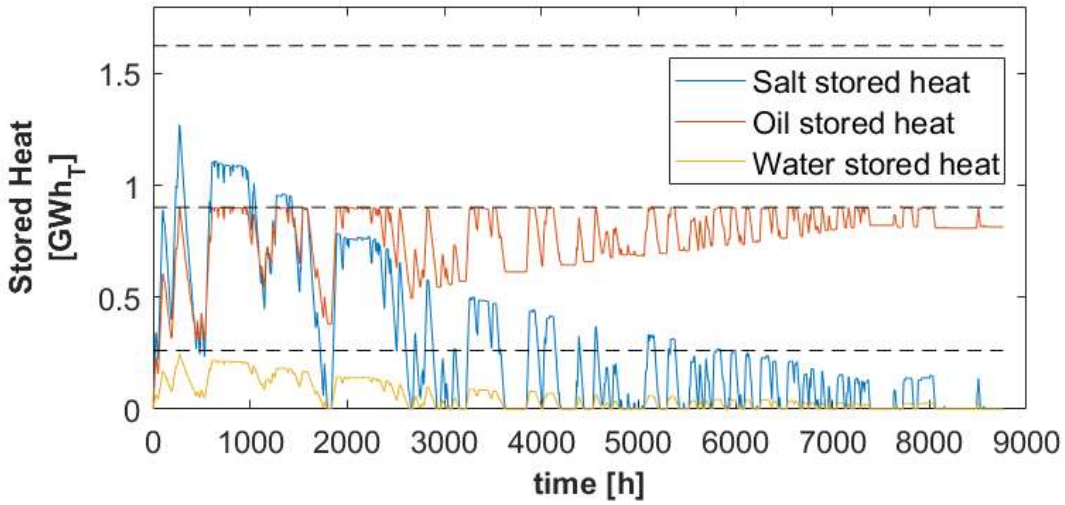


***Figure 7.13: State of Charge of the thermal storage units when $\eta_{RT}$ is low (30.2%), obtained with CDF=0.25, TDF=0.45. The dashed lines are the thermal limit for each unit***

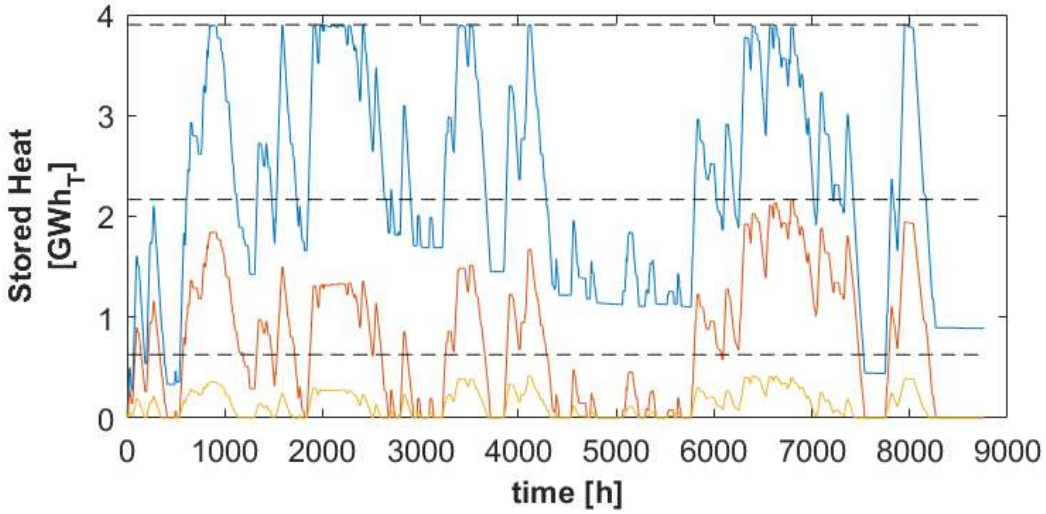


***Figure 7.14: State of Charge of the thermal storage units when $\eta_{RT}$ is high (52.9%), obtained with CDF=0.6, TDF=0.45. The dashed lines are the thermal limit for each unit***

If the investment cost is now considered, as in Figure 7.15, a reduction of one order of magnitude can be appreciated, achieving the purpose of the present study. The straight shape of the surface is a consequence of the linearization in the size of the thermal reservoirs, the most relevant cost.

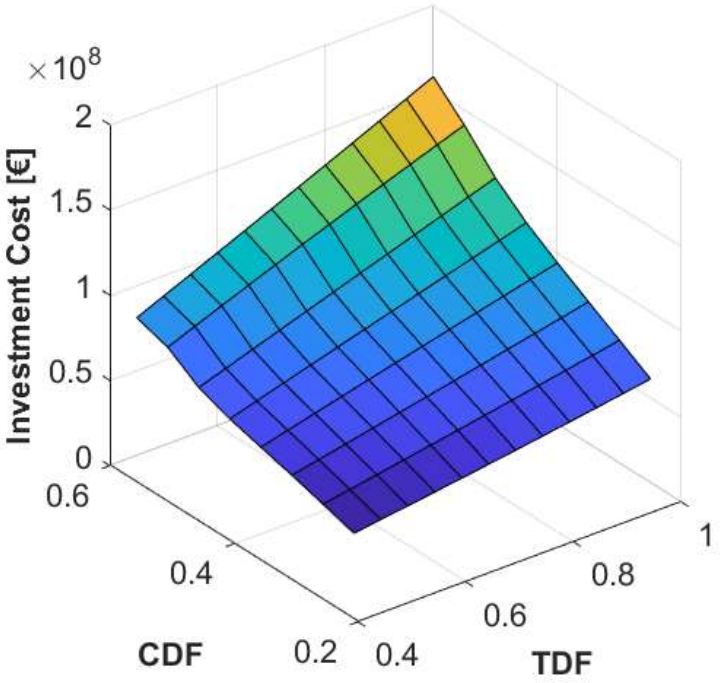


*Figure 7.15: Investment cost limited to 250 discharge hours mapped crossing CDF = [0.25 0.6] with TDF = [0.45 1]*

In particular, if each voice cost is observed for the same cases considered in the previous case, as in Figure 7.16 and Figure 7.17, it can be noticed as the investment cost is split in a much more even way among the components.

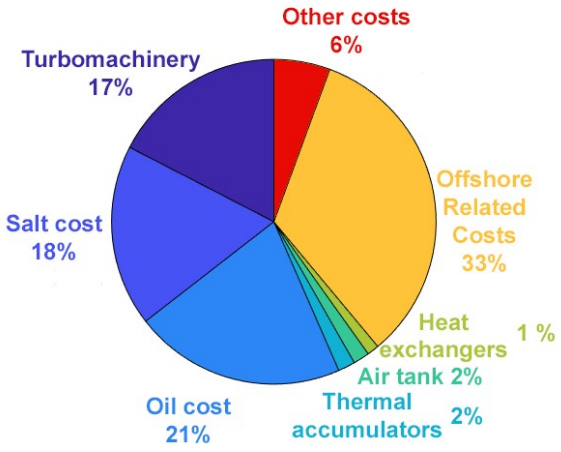


*Figure 7.16: Share of the investment costs for 250 storage hours, CDF=0.25, TDF=0.45. Total: 34.7 M€*

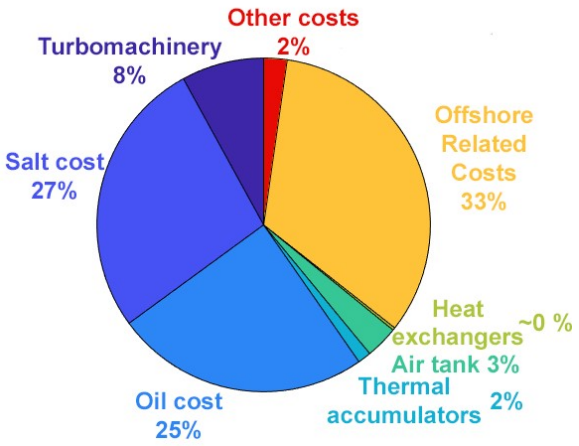


*Figure 7.17: Share of the investment costs for 250 storage hours, CDF=0.6, TDF=1. Total: 158 M€*

Finally, it has to be evaluated if such a reduction in the investment cost will improve the overall situation. So, the incentive required to reach the breakeven is computed again, as shown by Figure 7.18.

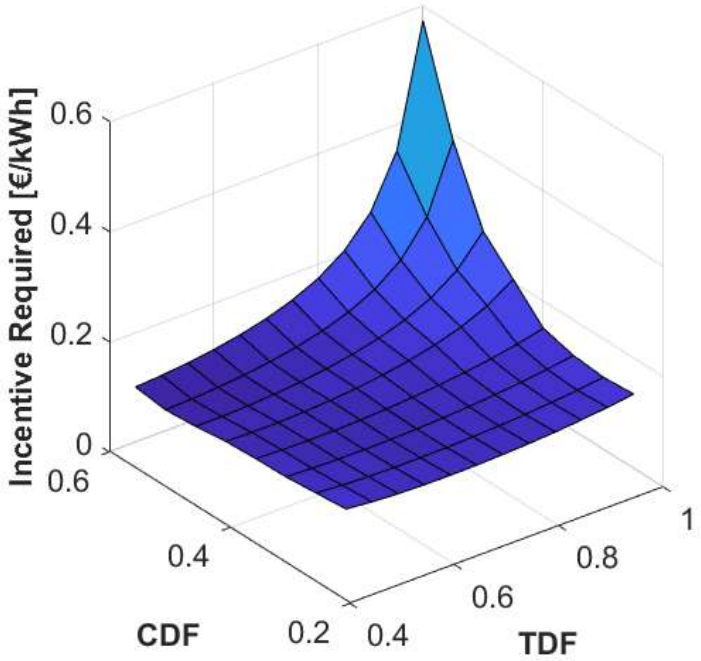


*Figure 7.18 Incentive required limited to 250 discharge hours mapped crossing CDF = [0.25 0.6] with TDF = [0.45 1]*

We can notice an overall improvement, since the extra-price on the energy expanded by the turbine is of 0.11 $€/kWh$, with respect to about 0.16 $€/kWh$. The

minimum values reach now even lower incentives, of 0.093 $€/kWh$ instead of 0.155 $€/kWh$. However, the most significative improvement results for big turbomachinery, where such value rises up to 0.574 $€/kWh$, halving the previous value of 1.38 $€/kWh$.

### 7.4.2. Variation of the storage capacity

The last paragraph explained how it has been possible to lower the amount of an hypothetic incentive used to sustain economically the projected underwater CAES. In order to be sure that the cost effectiveness is maximised, a final analysis was performed, where the size of the thermal storage was modified. Such parameter, expressed in maximum consecutive discharge hours, has been chosen to evaluate the variation of the most important parameters.

First of all two particular cases were chosen, among those who performed better with under dimensioned storage tanks, and in particular the compressor was fixed at CDF=0.6, while two different turbine sizes were considered, for TDF={0.45, 0.65}. Afterwards, their round-trip efficiencies, the most relevant performance parameter, are compared for different storage capacities, and as shown in Figure 7.19, decrease with the possibility to store thermal energy.

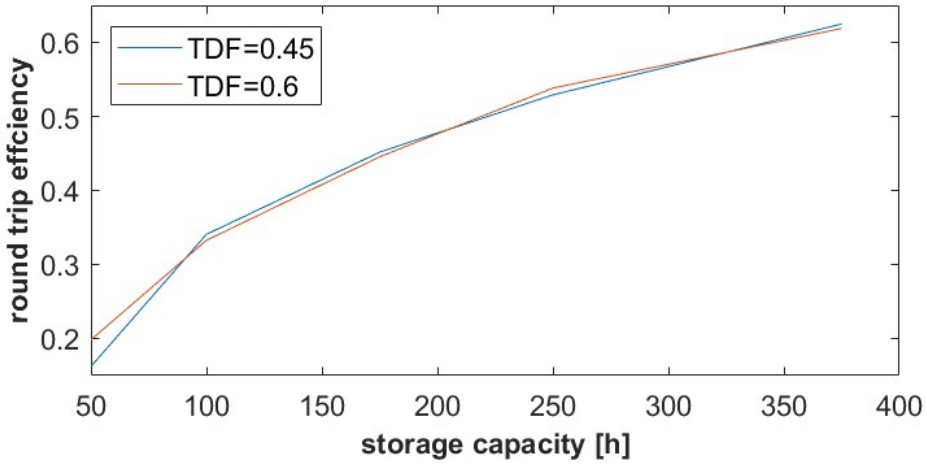


***Figure 7.19: Round-trip efficiency for increasing storage capacities, measured in consecutive discharge hours, CDF=0.6***

The same trend is shown by the energy obtained by the turbine, in Figure 7.20, which is the cause of the drop in the efficiency.

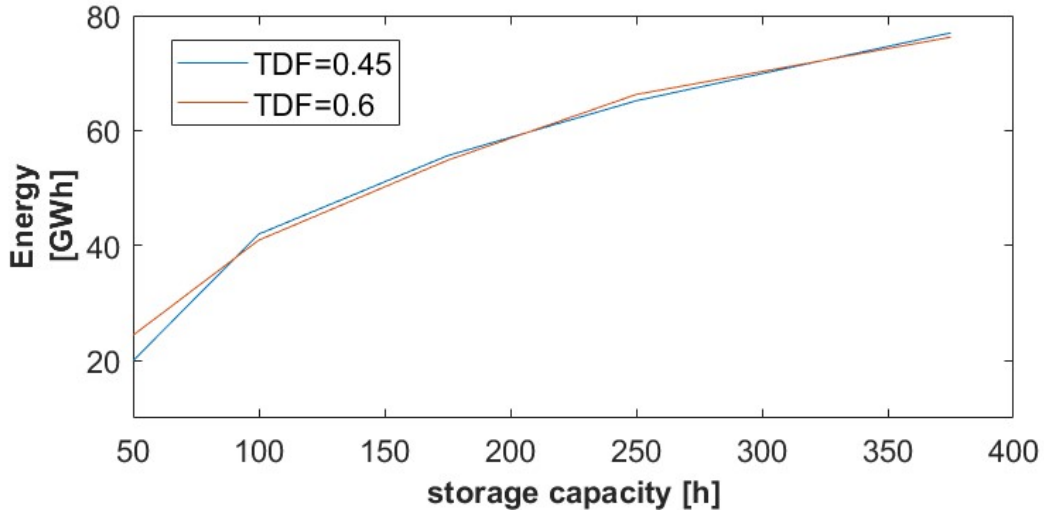


***Figure 7.20: Energy obtained from the expansion in turbine, for increasing storage capacities, measured in consecutive discharge hours, CDF=0.6***

On the other hand, the standard deviation of the electricity given to the grid increases reducing the storage capacity, as a consequence of the lower utilisation of the CAES system (Figure 7.21), reaching for very small storage tanks almost the same value that the wind field had without any storage at all.

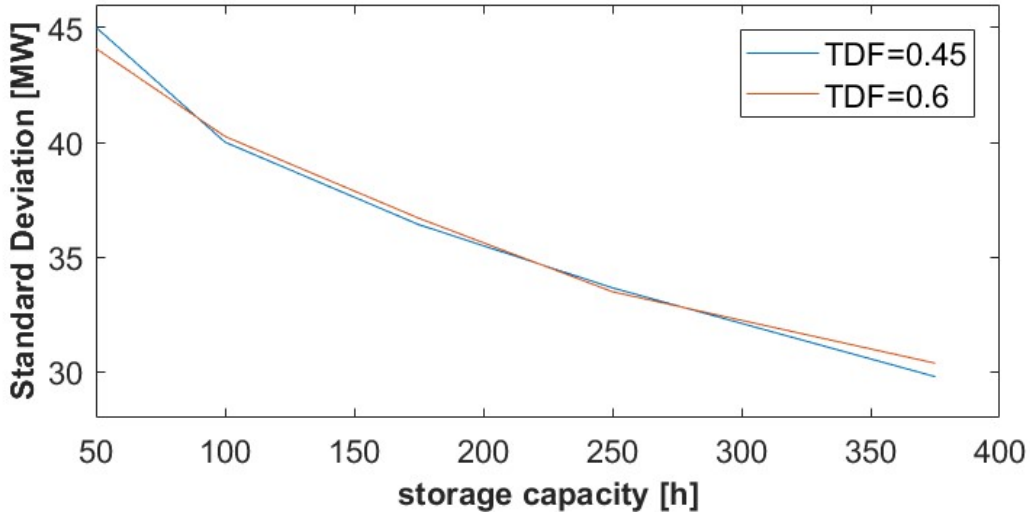


***Figure 7.21: Standard deviation of the power released to the grid, for increasing storage capacities, measured in consecutive discharge hours, CDF=0.6***

Nevertheless, the objective of reducing the investment cost is well achieved, as proven by the following Figure 7.22. It is interesting to notice the different slope of the

curves: this is due to the different air flow rate between the two cases, that implies proportional amounts of thermal fluid that, even for equal hours of storage, results in diverse sizes of the storage units.

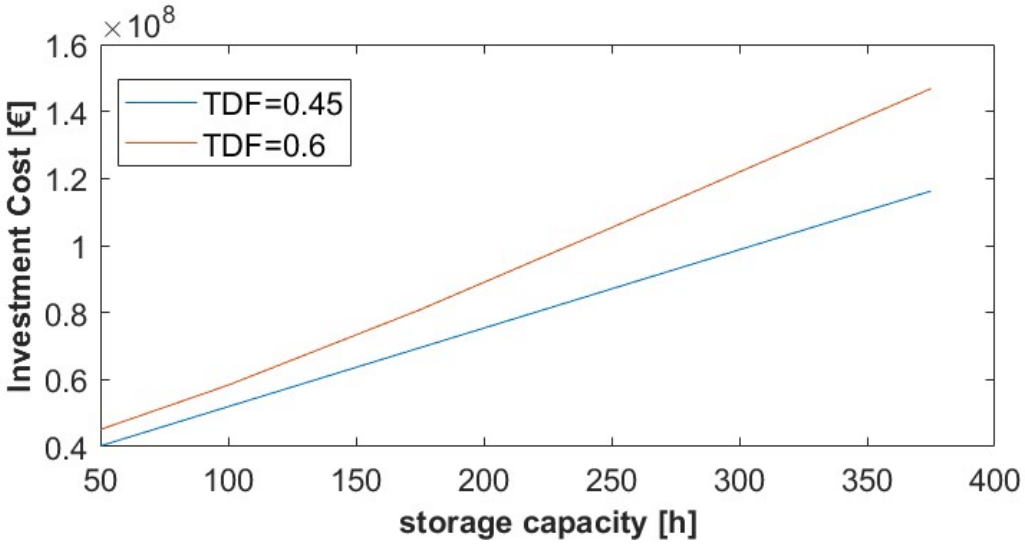


***Figure 7.22: Investment cost of the whole system, for increasing storage capacities, measured in consecutive discharge hours, CDF=0.6***

Finally, as a consequence of all the abovementioned results, the incentive required to reach the breakeven at the end of the plant's lifetime, is plotted in the following Figure 7.23.

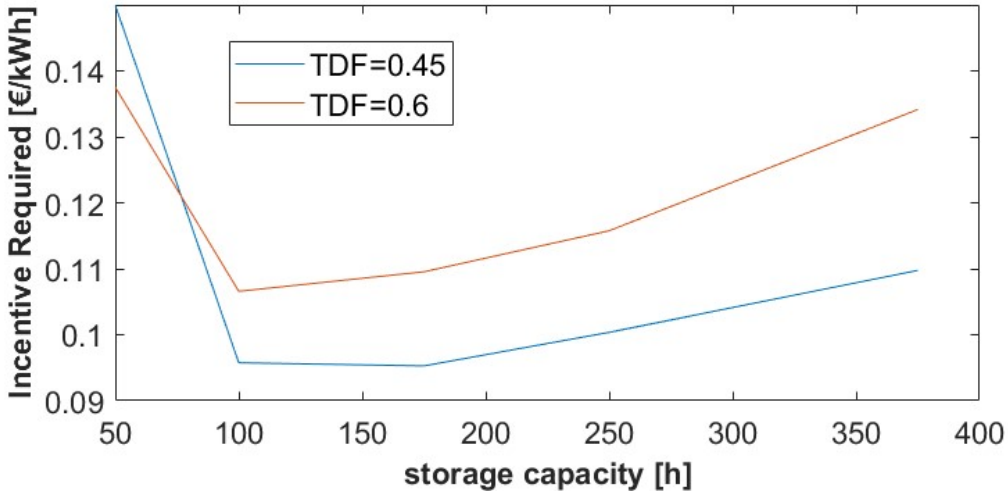


***Figure 7.23: Incentive required for the breakeven, for increasing storage capacities, measured in consecutive discharge hours, CDF=0.6***

It is worth noticing the minimum, present for both curves, due to the trade-off between the decreasing investment cost on one hand, and the worsening of all the technical indexes on the other one. In particular, the minimum incentive necessary to make profits from an adiabatic Compressed Air Energy Storage system, according to the current analysis, is of 0.095 $€/kWh$. Such value is achieved for a compressor of 76.5 MW, a turbine of 34.5 MW and a storage able to heat up the air flow directed to the turbine for 175 consecutive hours. However, the minimum of the surface obtained with 250 hours of storage showed a minimum incentive of 0.093 $€/kWh$. If on one side this means that these analysis should not be conducted independently one from the others, on the other side shows that for values lower than 0.1 $€/kWh$ the breakeven can be gained for different configuration. Among these, the preferred arrangement should be the one that allows the best performances under the desired point of view, either the maximisation of the round-trip efficiency or the minimisation of the standard deviation.

# 8. MODEL VALIDATION

In this last chapter, the model validity will be verified, trying to understand if the conclusions obtained until this point will remain valid changing the boundary conditions. In particular, the storage capacity variation analysis will be performed, changing alternatively the reference year for the wind data, the site where the CAES system is located with the respective wind turbine, and the depth of the underwater tank with the related storage pressure. Finally, the values found in each case will be compared and the consequent conclusions will be drawn.

## 8.1. DIFFERENT YEAR WIND DATA

In the previous two chapters, the wind data used for the simulations came out from the measurements done in year 2015. To widen the amplitude of the outcomes of this work, data from years 2013, 2014 and 2016 was used to change the maximum storage capacity accordingly with what previously done. It can be noticed in Figure 8.1 that the round-trip efficiencies are always immediately comparable.

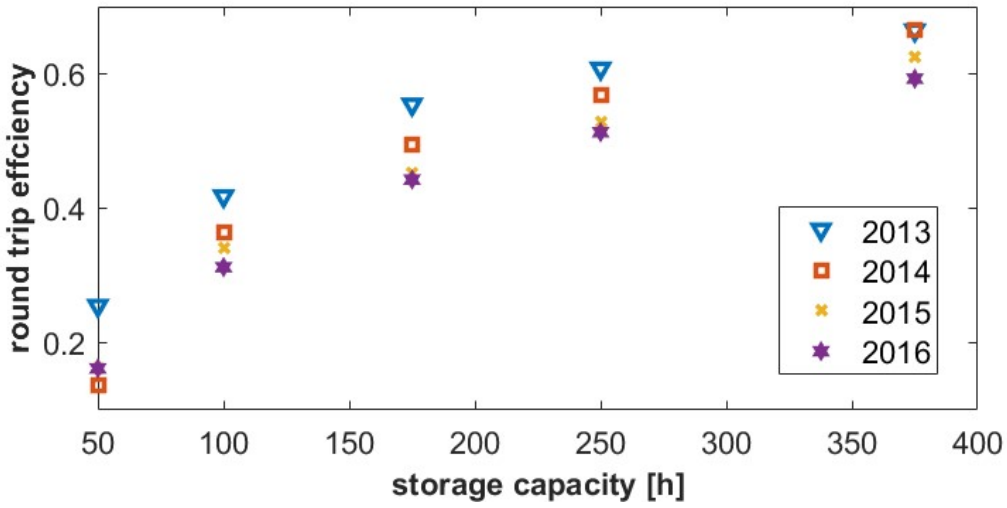


***Figure 8.1: Round-trip efficiency for increasing storage capacities, measured in consecutive discharge hours, for different years, CDF=0.6, TDF=0.45***

On the other hand, since the standard deviation of the electricity given to the grid depends on the wind distribution, to plot them together, each one was divided by the standard deviation of the same year without the CAES system (Figure 8.2).

$$Relative\ Standard\ Deviation = \frac{\sigma\ (with\ CAES)}{\sigma\ (without\ CAES)} \tag{8.1}$$

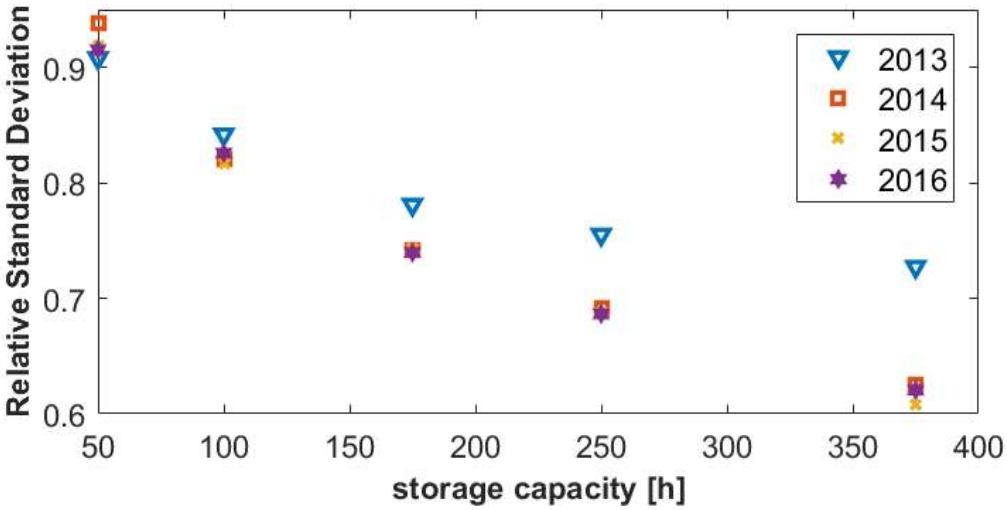


***Figure 8.2: Relative standard deviation for increasing storage capacities, measured in consecutive discharge hours, for different years, CDF=0.6, TDF=0.45***

Finally, the incentive required to reach the breakeven in 30 years of lifetime is computed, highlighting in Figure 8.3 the common presence of a minimum.

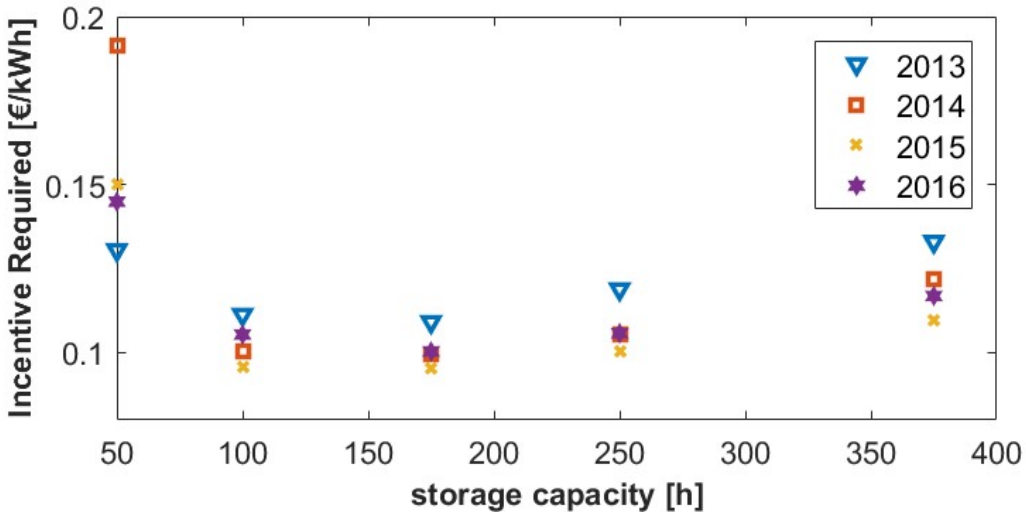


***Figure 8.3: Incentive required for increasing storage capacities, measured in consecutive discharge hours, for different years, CDF=0.6, TDF=0.45***

As it can be observed, if data measured in year 2013 was used as a reference one, the outcomes would not be exchangeable, while all other years show very similar values. In particular such year is characterised by a very long period of strong wind in January and February, obtaining a moving mean so high that it does not allow the activation of the system until March. However, the similarity among the results can also be attributed to the small difference with respect to the previous data, since the wind data come from the same place, and all the structural parameters are unchanged.

## 8.2. DIFFERENT SITE AND TURBINE

As introduced in chapter 5, also a second site was considered to install the underwater CAES system. In this case, two fields of 30 Vestas 2 MW turbines were chosen, and also the wind speed probability function is different (see paragraph 5.1 Site assessment and following). Now the input data see a substantial change, leading already to a lower investment cost related to the smaller wind net power (55.6 MW instead of 127.2 MW) that determines a consequent under dimensioning for all components as plotted in Figure 8.4.

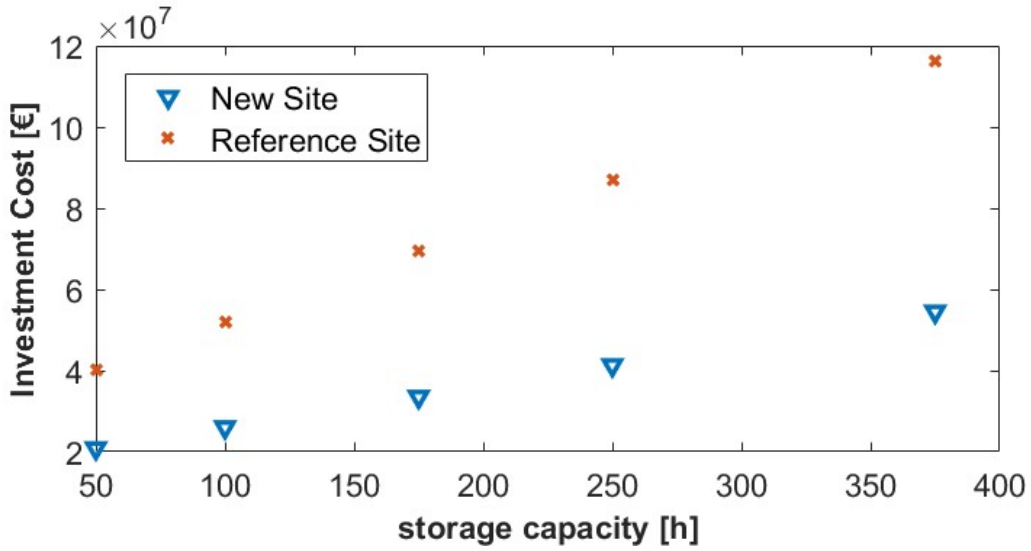


***Figure 8.4: Investment costs for increasing storage capacities, measured in consecutive discharge hours, for the two different sites, CDF=0.6, TDF=0.45***

The main consideration regards now the different exploitation of the scale economies, because if on one side the investment costs are halved, on the other side also the energy stored and recovered is less (Figure 8.5).

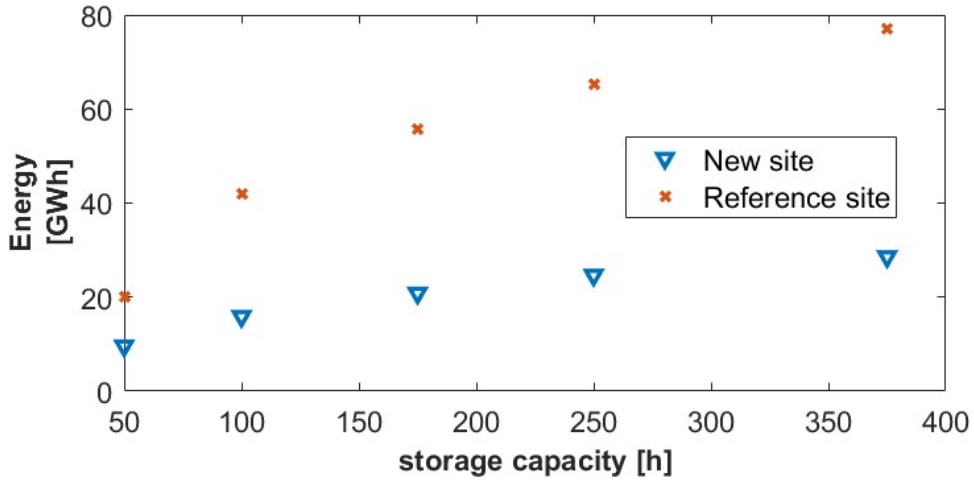


***Figure 8.5: Energy obtained from expansion for increasing storage capacities, measured in consecutive discharge hours, for the two different sites, CDF=0.6, TDF=0.45***

However, independently of the fluctuation of the wind and the consequent power production, the relative reduction in the standard deviation of the electricity released to

the grid is almost the same (Figure 8.6), meaning that the main objective of the system is still achieved.

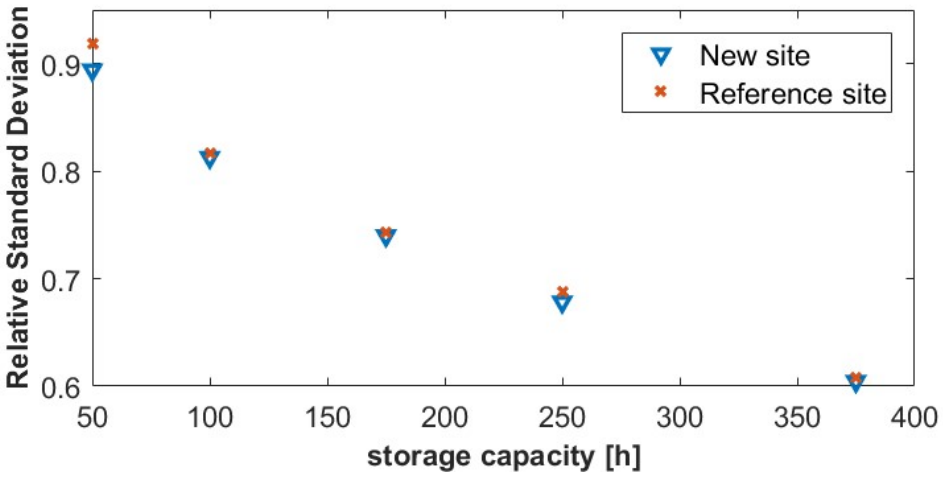


***Figure 8.6: Relative standard deviation for increasing storage capacities, measured in consecutive discharge hours, for the two different sites, CDF=0.6, TDF=0.45***

Also the round-trip efficiency shows, in Figure 8.7, a small effect due to the size, although for little capacities the unbalances affect less the performances, while for huge thermal storage systems, the higher efficiency of the single elements is noticeable.

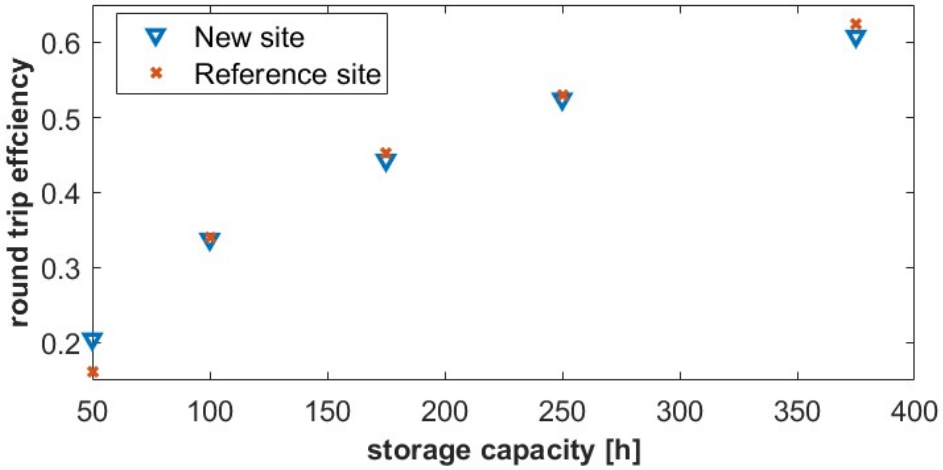


***Figure 8.7: Round trip efficiency for increasing storage capacities, measured in consecutive discharge hours, for the two different sites, CDF=0.6, TDF=0.45***

Nevertheless, the scale economies seem to reward also the CAES systems: as shown by Figure 8.8, the incentive needed to reach the breakeven is less. Such outcome

seems obvious if compared to many other power plants, but it is not generally valid for most energy storage devices, which usually use many small units to obtain the desired capacity.

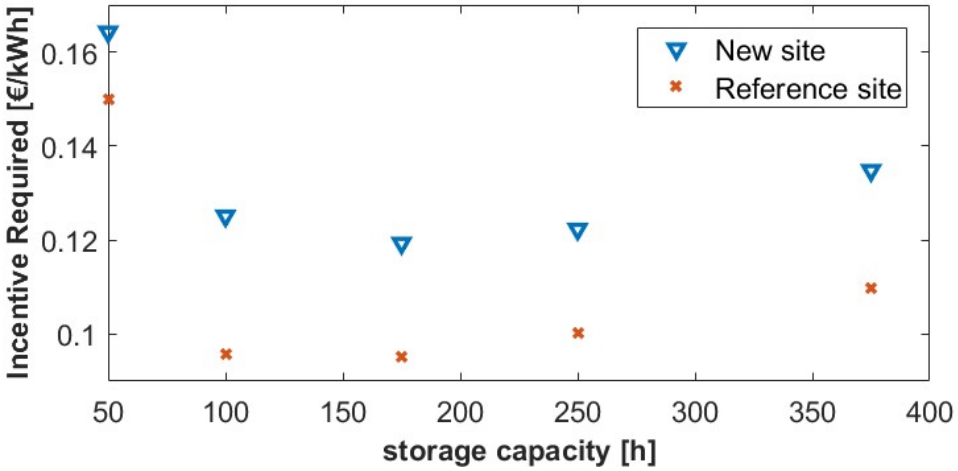


***Figure 8.8: Incentive required for increasing storage capacities, measured in consecutive discharge hours, for the two different sites, CDF=0.6, TDF=0.45***

## 8.3. DIFFERENT DEPTH AND TANK PRESSURE

Finally, two new air storage pressures are tested, meaning that the underwater tank is posed at different depths. In this case the differences are even more, since affect the dimensioning of each component of the system. As shown by Figure 8.9, increasing the pressure the total investment cost decreases; if this behaviour seems unexpected, it is important to remember that the higher the final pressure imposed by the marine water outside the tank, the higher is also the specific enthalpy increase in compression.

So, at constant nominal power, the mass flow rate during both charge and discharge is lower, implying lower thermal reservoirs required. As previously observed, since the huge amounts of thermal fluids are the most important costs, their decrease is more important than the increase in turbomachinery costs and in the underwater pipes.

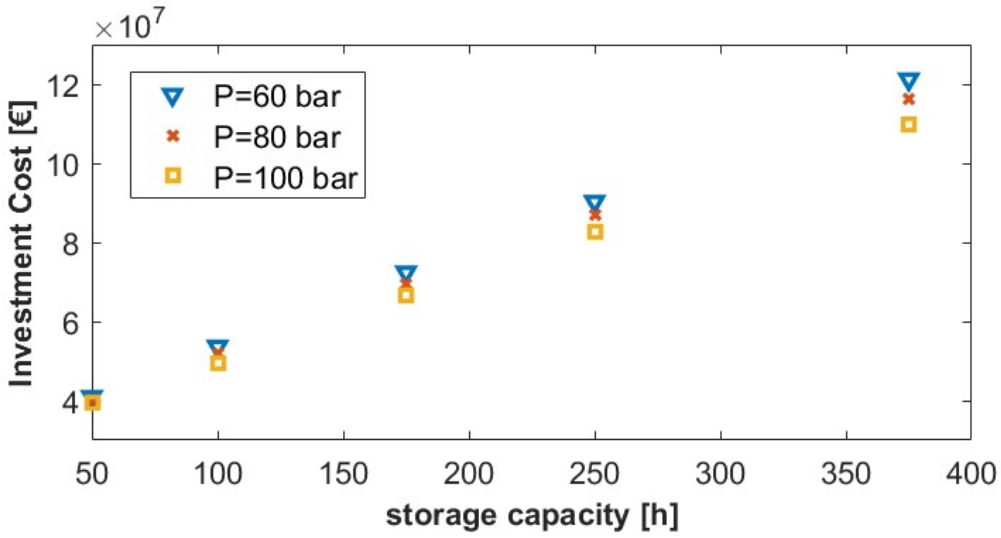


***Figure 8.9: Investment costs for increasing storage capacities, measured in consecutive discharge hours, for three different tank pressures, CDF=0.6, TDF=0.45***

On the other hand, Figure 8.10 illustrate the behaviour of the round-trip efficiency, which is much less straightforward to understand, since it is a result of different compressors and consequent efficiencies, different unbalances in the thermal coupling between charge and discharge phases, and last but not least different heat released in the intercooler.

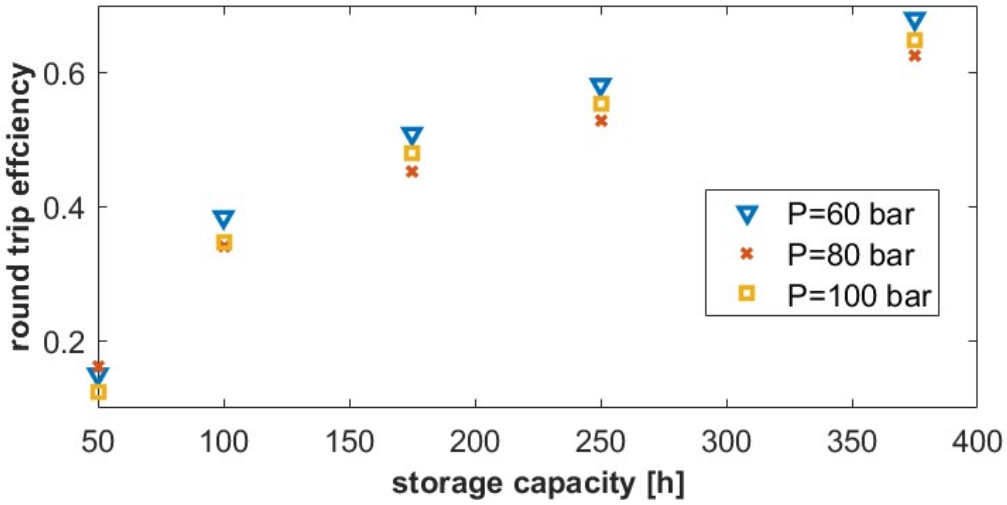


***Figure 8.10: Round-trip efficiencies for increasing storage capacities, measured in consecutive discharge hours, for three different tank pressures, CDF=0.6, TDF=0.45***

Nevertheless, the purpose of delivering a less fluctuating power function to the grid is fulfilled once again, as proven by the following Figure 8.11.

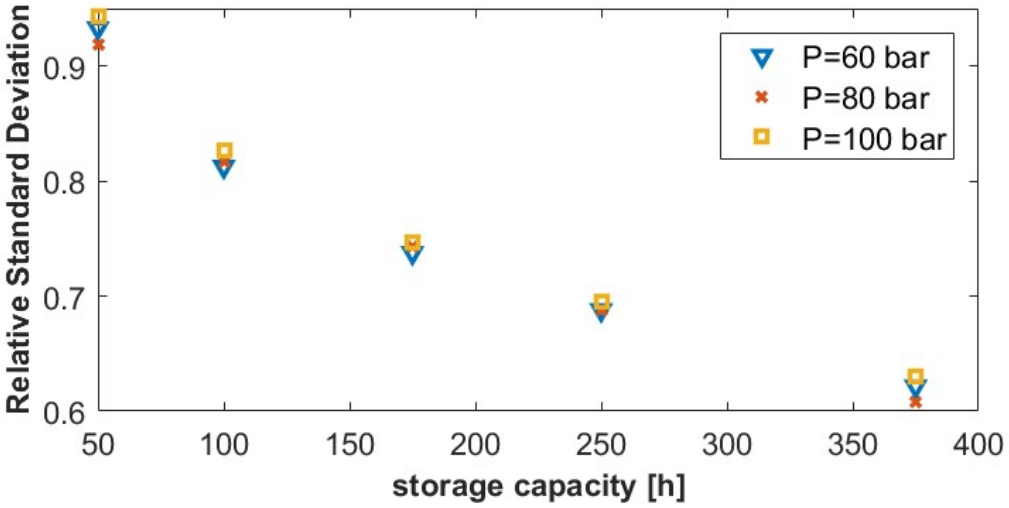


***Figure 8.11: Relative standard deviation for increasing storage capacities, measured in consecutive discharge hours, for three different tank pressures, CDF=0.6, TDF=0.45***

Finally, the incentive necessary to reach the breakeven is computed and plotted in Figure 8.12, showing that in all these cases it is possible to achieve values around 0.1 €/kWh.

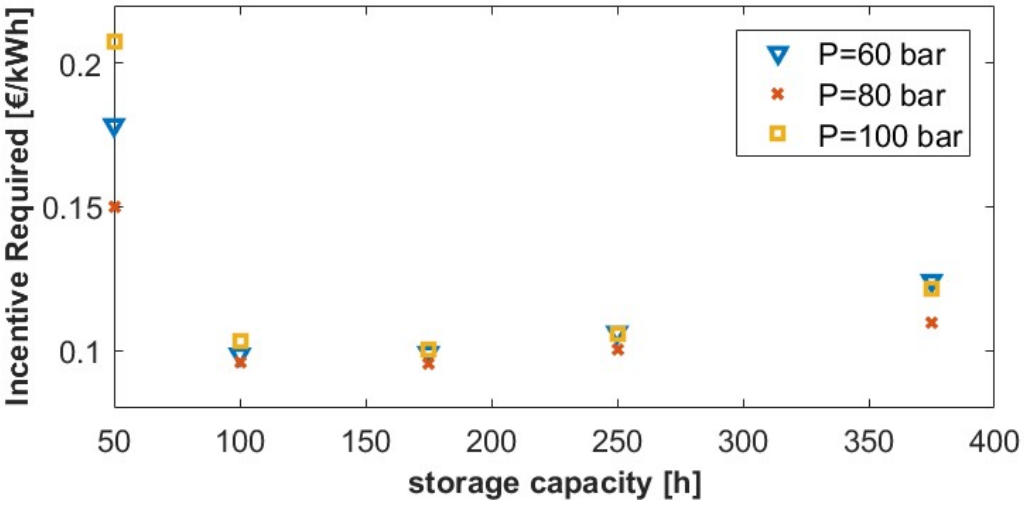


***Figure 8.12: Incentive required for increasing storage capacities, measured in consecutive discharge hours, for three different tank pressures, CDF=0.6, TDF=0.45***

So, at the end of this final analysis, the results obtained in this work can be generalised to most of the existing situations. The versatility of CAES storage systems allows applications in a very broad range of circumstances, different sea bed depths, plant sizes and wind profiles without affecting significantly the results.

# 9. CONCLUSIONS

In a society with the growing need of storing energy because of the increasing share of renewables, most existing storage devices use technologies with low or no scale economies at all. Among other large scale facilities, Compressed Air Energy Storage systems seem to be a suitable solution to be coupled, where possible, with dams, the unique assessed large scale storage system for balancing purposes. Furthermore, since the escalation in energy production from renewables pursues the reduction of carbon emissions, adiabatic CAES arrangements, not requiring any fuel consumption, are definitely preferred. Together with the increasing number of offshore wind fields, the underwater air storage reveals itself as an opportunity to localise storage facilities close to the source without overloading the transmission lines, beyond the abovementioned advantages guaranteed by the isobaric storage through the hydrostatic pressure.

The advantage of such technology consists in the use of well-known elements, such as turbomachinery, heat exchangers and thermal storage units, with the underwater air tank as the only component requiring a specific design. However, the opposite logic leading the compressor train, which has to be able to change as freely as possible its absorbed power, needs a specific approach. In this thesis, a careful analysis has been performed on compressor design. Three different machines were designed stage by stage and, referring to the Balje diagram, their efficiencies were computed. In order to update the results in accordance with the most recent technologies, corrective factors have been taken into account, resulting in top adiabatic efficiencies (about 87%) for a standard axial compressor with compression ratio equal to 12, to which the state of art technology can refer to. Moreover, different configurations were studied to join together the turbomachinery with the shaft, improving the existing optimisation procedure:

- A two-shafts axial/centrifugal compression, with fixed diameter optimized on the middle stage and adiabatic efficiencies around 77% for the axial compressors and 87% for the single shaft-single stage centrifugal one;

- A two-shafts axial/centrifugal compression, with variable diameter, optimized on the stage at 70% of the compression with adiabatic efficiencies around 88% for the axial compression and 87% for the single shaft-single stage centrifugal one;
- A three shafts axial/centrifugal compressor, optimized on middle stage of each unit with adiabatic efficiencies around 88-91% for each one;

The final result suggests a compression made by two axial compressors, assembled preferably with variable diameter, and a single-stage centrifugal compressor, each unit driven by its motor.

Once designed the compressor, its off-design behaviour has been considered and the limits necessary to avoid the stall condition were understood, resulting as the critical component of the storage plant because of such strict restriction. In practise, the use of IGV for mass flow rate control yields an off-design operating power range between 80% and 103% of the nominal value. This observation suggests the investigation of additional strategies, such as more parallel compressor trains or variable rotational speed, for increasing the operating range. Consequently, in order to work between the so imposed boundaries, some adjustments were considered with the aim of refining the coupling between the charging and the discharging phases of the system. The most effective outcome recommends a single degree of freedom regulation method, the IGV system at the inlet of the first compression stage, with three levels of thermal storage, molten salts, (about 600°C - 265°C), diathermal oil (about 265°C - 55°C), and water (about 70°C - 15°C), the latter equipped with a bypass valve that allows the discharge when it is the only empty reservoir.

The CAES contextualisation was then outlined, as well as its integration with a reasonable off-shore wind turbine field. Thanks to the hourly wind data made available to us, the power profile generated was then computed and a year-working flexible model of the storage plant was created. Two main directions were chosen, either the flattening of the power profile given to the grid (peak shaving) or the economic benefits obtained from arbitrage on the electricity market, being this last the maximum possible

revenue for the park owner. However, once computed the investment cost, the latter was rejected because of the too low revenues obtainable, and the former was deeply investigated. In fact this last path also requires an incentive to be economically sustainable, but reasonably it will be paid in order to improve grid stability.

The size of each component resulted of paramount importance, not only for the cost associated, but also for the balance among the thermal reservoirs. In particular, a correct matching between the dimension of turbine and compressor side leads to better performance parameters as well as to an accurate capacity required to the thermal storage. Accordingly, the yearly behaviour of the CAES was mapped as a consequence of the variation of two free parameters, defined respectively as the Turbine Dimension Factor (ratio between turbine and compressor nominal mass flow rate) and the Compressor Dimension Factor (ratio between compressor and wind park nominal power). As a result, the model prefers configurations with big compressors and small turbines (e.g. TDF around 0.45 and CDF around 0.6), even though also the opposite combination is worth some interest (e.g. TDF around 0.9 and CDF around 0.25). In practice, the first allows to store large peaks of available wind energy and discharge in long periods, while the latter reduces the investment costs and increase the availability of the tanks that are often discharged by the large turbine. All the other combinations do not allow an equilibrated heat storing process, resulting in unbalances in the state of charge of the reservoirs that in the short period lower the working hours and the round-trip efficiency, while in the long run paralyse the system.

Of course, the need for incentives to sustain the economic feasibility of the system is undiscussed, assigned proportionally to the energy obtained from expansion. The reason of such incentive is to pay the grid-balancing service offered from the system, which counterbalances the effect brought by unpredictable renewables.

Once defined the features of the storage system, the investment cost of each component was obtained, starting from functions based on the characteristic dimension of each component. Since the major cost voices, excluded the one linked to the offshore location, resulted accountable to the thermal storage, and especially to the huge amounts

of thermal fluid required, down-scalable solutions have been performed with smaller thermal capacities.

Since the performance of the cases with limited storage capacities would obviously be lower, in order to compare all these alternatives, the minimum incentive required to reach the breakeven at the end of the lifetime was computed, and the so-obtained values were compared. Smaller thermal tanks result in lower investment costs, but also in lower efficiencies and less efforts in the grid balancing service. The outcomes are often lower than 0.1 $€/kWh$, comparable with the ones received from the renewable sector. More in detail, the analysis evidenced that:

- A reduction in fluctuations of energy injection in the grid (measured as standard deviation) to about 70% of the initial value can be obtained;
- Yearly averaged round-trip efficiencies higher than 55% are assessed, reaching 72% for the best performing plants;
- Incentives of the order of 0.093-0.095 $€/kWh$.

The same analysis has been performed also in different contexts, in order to generalise the conclusions obtained. In particular, changing the reference year for wind profiles, air tank pressure and depth, offshore wind park location does not influence significantly the observed results described above.

Finally, it is important to underline that many future developments could be introduced in the simulation of an adiabatic UW-CAES. First of all, it would be interesting to analyse the system behaviour in an even broader range of locations and boundary conditions. Another direction of possible improvement would be the implementation of parallel compression trains. In this way, it would be possible to work in a wider operative range, without the limitations imposed to the absorbed power. In particular, if the number of parallel sections would be five or more, working with only some lines could drop down the compression power to less than 20 % of the nominal one. Furthermore, if combined with more parallel turbine lines, an almost flat profile could be obtained, reducing the standard deviation of the electricity given to the grid

down to zero. Anyway, from the previous analysis the most limiting components seems to be the energy storage, so the improved flexibility of the compressor train should be coupled with more flexible heat storage management. A last considered development was the possibility of reducing the investment cost with different installation options. In particular, installing the turbomachinery and thermal storage system on ground, connected with offshore deep tanks could reduce the costs from 20 % to 25 %. However, a challenging underwater pipeline sizing process would be necessary, due to the fluctuation in the charging phases and the consequent pressure stresses.

Nevertheless, in the near future, when offshore wind fields will produce an important fraction of the energy mix, they will reasonably have to pay for the consequent unbalance given to the grid. In this context, when wind farms will be without any kind of incentive, the fields linked to underwater CAES or any other large-scale energy storage unit will take advantage from the possibility to avoid economic losses. If the opportunity cost will be higher than the extra price of the system, the most cost-effective technology will spread out, enhancing the grid stability and allowing a further increase in renewable penetration. Advantages could be outlined also thinking to a carbon emission taxation forward-looking perspective.

In conclusion, if the decline of the advantages currently owned by renewable sources will be properly managed, not only it could determine a new dawn for large-scale energy storage, but could free the power system from fossil fuel reliance.

# *Nomenclature and acronyms*

## *Nomenclature*

| | | |
|---|---|---|
| **v** | *m/s* | Velocity |
| **ρ** | $kg/m^3$ | Density |
| **ṁ** | *kg/s* | Mass flow rate |
| **$\dot{V}$** | $m^3/s$ | Volumetric flow rate |
| **P** | *kW* | Power |
| **Q** | *kJ* | Heat exchanged |
| **η** | - | Efficiency |
| **χ** | - | Reaction Grade |
| **β** | - | Compressor ratio |
| **Ns** | - | Specific speed |
| **Ds** | - | Specific diameter |
| **Re** | - | Reynolds' Number |
| **T** | *°C* | Temperature |
| **p** | *bar* | Pressure |
| **h** | $m^2/s^2$ | Specific enthalpy |
| **s** | *kJ/kg K* | Specific entropy |
| **D** | *m* | Diameter |
| **N** | *rpm* | Revolving speed |
| **ω** | *rad/s* | Rotational speed |
| **u** | *m/s* | Peripheral speed |
| **Rg** | *kJ/kg K* | Gas constant |
| **μ** | *kg/m s* | Viscosity |
| **k** | *€/MWh* | Extra-price in arbitrage |
| **cp** | *kJ/kg K* | Specific heat at constant pressure |
| **ΔTm,l** | *°C* | Mean logaritmic temperature difference |

## *Acronyms*

| | |
|---|---|
| **CAES** | Compressed Air Energy Storage |
| **TDF** | Turbine Dimension Factor |
| **CDF** | Compressor Dimension Factor |
| **LCOE** | Levelized Cost Of Electricity |
| **AEP** | Annual Energy Production |
| **IGV** | Inlet Guide Vanes |
| **DGV** | Diffuser Guide Vanes |
| **COT** | Compressor Outlet Temperature |
| **TIT** | Turbine Inlet Temperature |
| **UW** | Underwater |
| **TES** | Thermal Energy Storage |
| **LP** | Low Pressure |
| **HP** | High Pressure |
| **LAES** | Liquid Air Energy Storage |
| **CTS** | Cooling To Storage |
| **HFS** | Heating From Storage |

# *References*


[1] United Nations, “World Population Prospects 2017,” *United Nations*, 2017. [Online]. Available: https://esa.un.org/unpd/wpp/.

[2] BP, “BP Energy outlook 2017,” *BP Stat. Rev. World Energy*, p. 52, 2017.

[3] NASA, “Climate Change and Global Warming.” [Online]. Available: https://climate.nasa.gov/.

[4] J. Cook, “Consensus on consensus: a synthesis of consensus estimates on human-caused global warming,” 2016.

[5] T. . Boden, G. Marland, and R. J. Andres., “Global, Regional, and National Fossil-Fuel CO2 Emissions. Carbon Dioxide Information Analysis Center, Oak Ridge National Laboratory, U.S. Department of Energy, Oak Ridge, Tenn, U.S.A.” 2010.

[6] IPCC and UNFCCC, “Climate Change, Synthesis Report Summury for Policymaker.” 2014.

[7] “NASA’s Goddard Institute for Space Studies, NOAA National Climatic Data Center, Met Office Hadley Centre/Climatic Research Unit and the Japanese Meteorological Agency.” .

[8] “Finding ways to fix the climate before it is too late, Global Carbon Project, The Norwegian University of Science and Technology (NTNU),” 2017.

[9] IRENA, “Renewable Power Generation Costs in 2014,” 2015.

[10] British Petroleum, “BP Statistical Review of World Energy 2017,” *Br. Pet.*, no. 66, pp. 1–52, 2017.

[11] S. Brian and M. J.Kaiser, “Ecological and economic cost-benefit analysis of offshore wind energy.” 2008.

[12] “European Association for Storage of Energy (EASE).,” 2016. [Online]. Available: http://ease-storage.eu/.

[13] B. Li and J. F. Decarolis, “A techno-economic assessment of offshore wind coupled to offshore compressed air energy storage,” *Appl. Energy*, vol. 155, pp. 315–322, 2015.

[14] Lena and P. A. Lombardi, “Adele-ing: workshop grid plus storage.” 2016.

[15] J. Wang, X. Luo, M. Dooner, J. Clark, and C. Krupke, “Overview of current development in compressed air energy storage technology,” 2014.

[16] G. Venkataramani, P. Parankusam, V. Ramalingam, and J. Wang, “A review on compressed air energy storage – A pathway for smart grid and polygeneration,” *Renew. Sustain. Energy Rev.*, vol. 62, pp. 895–907, 2016.

[17] F. A. Tiano, G. Rizzo, and N. Feo, “Study and Optimization of an Under-Water Compressed Air Energy Storage System Coupled with Renewable Energy Plants .,” no. July, 2016.

[18] G. F. Carbone, “Simulazione di funzionamento e dimensionamento preliminare di sistemi CAES sottomarini ( UW-CAES ) connessi a centrali eoliche offshore,” 2016.

[19] “Puertos del Estado.” [Online]. Available: http://www.puertos.es/en-us.

[20] G. Lozza, *Turbine a Gas e Cicli Combinati*. 2016.

[21] RWE, “Adele – Adiabatic Compressed-Air Energy Storage For Electricity Supply,” p. 12, 2010.

[22] J. Trahan, “Thermal energy storage technologies and systems for concentrating solar power plants,” no. August 2013, 2017.

[23] G. G. Nrel, “Summary Report for Concentrating Solar Power Thermal Storage Workshop Summary Report for Concentrating Solar Power Thermal Storage Workshop,” no. August 2011.

[24] P. Dolado, A. Gil, M. Medrano, I. Martorell, A. La, and L. F. Cabeza, “State of the art on high temperature thermal energy storage for power generation . Part 1 — Concepts , materials and modellization,” vol. 14, pp. 31–55, 2010.

[25] NREL and SENER Ingenieria y Sistemas S.A., “The Andasol Solar Power Station Project 1&2,” no. March. 2007.

[26] “Heat Exchanger Thermal Design,” in *Heat Exchanger Design Handbook, Second Edition*, 2013, pp. 117–144.

[27] M. De Jong, “Commercial grid scaling of Energy Bags for underwater compressed air energy storage underwater compressed air energy storage,” *Int. J. Environ. Stud.*, vol. 7233, no. November, pp. 1–8, 2017.

[28] “Hydrostor launches compressed air power storage system off toronto island.” [Online]. Available: https://www.theglobeandmail.com/report-on-business/industry-news/energy-and-resources/hydrostor-launches-compressed-air-power-storage-system-off-toronto-island/article27306527/.

[29] C. Lay and G. Andreas, “STENSEA -Stored Energy in the Sea- 7th international Renewable Energy Storage Conference and Exhibitions,” no. November 2012, 2015.

[30] S. Koren, “Under Water Caes Arothron,” 2011. [Online]. Available: http://arothron-es.com/Technology.aspx.

[31] P. E. Smith, “3 – Design and specification of marine concrete structures,” in *Marine Concrete Structures Design, Durability and Performance*, 24 June 20., .

[32] STL, “Oil & Gas piping.” [Online]. Available: http://www.stlitalia.com/oil-gas/.

[33] Wickens Rupert, “Offshore pipe size selection, LFF Group Engineering,” 2017. .

[34] “Dimensioning principles of tubomachinerery,” in *ENERGY CONVERSION COURSE, Politecnico di Milano*, 2017, pp. 1–81.

[35] M. P. Boyce, “Design Characteristics,” in *Centrifugal Compressors*, 1997, pp. 237–237.

[36] T. Wright, *FLUID MACHINERY Performance, Analysis and Design*. 1999.

[37] E. Kenneth and P. Nichols, “How to Select Turbomachinery For Your Application.”

[38] G. Turbine and E. Handbook, *7 Axial-Flow Compressors*. 2012.

[39] G. Turbine and E. Handbook, *6 Centrifugal Compressors*. 2012.

[40] F. Palazzi, F. Marechal, and J. Van Herle, “Thermo-Economic Optimization of a Solid Oxide Fuel Cell , Gas Turbine Hybrid System,” 2017.

[41] “Amsterchem Scanit.” [Online]. Available: https://www.amsterchem.com/scanit.html.

[42] W. Collins and T. Passions, *Axial-Flow Compressors and Ducted Fans 5*. 2010.

[43] Royce and Brown, *Compressors Selection and Sizing*, 2nd editio. 1997.

[44] P. Chiesa, “Stato dell ’ arte e prospettive dei sistemi di accumulo energetico basati sulla tecnologia CAES Committente : Enipower SpA Autori : Sommario,” pp. 1–125, 2014.

[45] “Catalogo Atlas Copco.” [Online]. Available: https://www.atlascopco.com/content/dam/atlas-copco/compressor-technique/gas-and-process/documents/driving-centrifugal-compressor-technology.pdf.

[46] “Oceanmap, Università degli studi di Pavia,” 2005. .

[47] “AtlaEolico,” 2017. [Online]. Available: http://atlanteeolico.rse-web.it/.

[48] A. Sluiter *et al.*, “NREL, National Renewable Energy Laboratory.,” *LAP, Laboratory Analytical Procedure. Technical Report NRL/TP-510-42618*, 2012. [Online]. Available: http://www.nrel.gov.

[49] “Eolico off-shore, parte la realizzazione del primo parco in Italia,” 2017. [Online]. Available: http://www.qualenergia.it/articoli/20170616-eolico-shore-parte-la-realizzazione-del-primo-parco-italia.

[50] “World’s first floating windfarm to take shape off coast of Scotland,” 2017. [Online]. Available: https://www.theguardian.com/business/2017/jun/27/hywind-project-scotland-worlds-first-floating-windfarm-norway.

[51] S. Li, “WIND ARRAY PERFORMANCE EVALUATION MODEL FOR LARGE WIND,” 2014.

[52] “Huronwind,” 2017. [Online]. Available: http://huronwind.com/.

[53] “MSD, al via progetti pilota per la partecipazione delle rinnovabili,” 2017. [Online]. Available: http://www.rinnovabili.it/energia/fotovoltaico/rinnovabili-

accumulo-msd-progetti-pilota/.

[54] R. Ja. Couper, W. P. Roy, R. F. James, and W. M. Stanley, "Costs of individual equipment," in *Chemical Process Equipment*, vol. 11, no. 8, 1988, pp. 663–669.

[55] D. Cocco and F. Serra, "Performance comparison of two-tank direct and thermocline thermal energy storage systems for 1 MWe class concentrating solar power plants," *Energy*, vol. 81, pp. 526–536, 2015.

[56] M. M. Conceição and J. C. O. Santos, "Comparative study of specific heat capacities of some vegetable oils obtained by DSC and microwave oven," 2005.

[57] R. Serrano-lópez, J. Fradera, and S. Cuesta-lópez, "Molten salts database for energy applications," 2013.

[58] Entec UK Ltd, "Cost estimation methodology,The Marine Energy Challenge approach to estimating the cost of energy produced by marine energy systems," 2006.

[59] G. Guandalini, "Power-to-gas systems for hydrogen-based renewable energy storage in the natural gas infrastructure," Politecnico di MIlano, 2016.

[60] Gse, "Incentivazione della produzione di energia elettrica da impianti a fonti rinnovabili diversi dai fotovoltaici," *Ww.Gse.It*, vol. 2016. pp. 1–97, 2016.